A WHOLE-CORE THERMAL HYDRAULIC MODEL FOR PIN-FUELED FLUORIDE-SALT-COOLED REACTORS

A Dissertation
Presented to
The Academic Faculty

by

Sriram Chandrasekaran

In Partial Fulfillment
of the Requirements for the Degree
Doctor of Philosophy in the
School of Mechanical Engineering

Georgia Institute of Technology
August 2022

A WHOLE-CORE THERMAL HYDRAULIC MODEL FOR PIN-FUELED FLUORIDE-SALT-COOLED REACTORS

Approved by:

Dr. Srinivas Garimella, Chair
G.W. Woodruff School of Mechanical Engineering
Georgia Institute of Technology

Dr. Farzad Rahnema
G.W. Woodruff School of Mechanical Engineering
Georgia Institute of Technology

Dr. Bojan Petrovic
G.W. Woodruff School of Mechanical Engineering
Georgia Institute of Technology

Dr. S. Mostafa Ghiaasiaan
G.W. Woodruff School of Mechanical Engineering
Georgia Institute of Technology

Dr. Thomas Fuller
School of Chemical and Biomolecular Engineering
Georgia Institute of Technology

Date Approved: July 19, 2022

To my family

ACKNOWLEDGEMENTS

I am grateful to my advisor, Dr. Srinivas Garimella, for his generous support, encouragement, and guidance through this research and graduate school. I would like to thank my Ph.D. committee members: Dr. Farzad Rahnema, Dr. Bojan Petrovic, Dr. S. Mostafa Ghiaasiaan, and Dr. Thomas Fuller for their valuable guidance and suggestions.

I would also like to thank all the present and past members of the Sustainable Thermal Systems Laboratory for their technical and moral support throughout my time at Georgia Tech. In particular, I would like to thank Dr. Alexander Huning, Dr. Daniel Kromer, Dr. Daniel Boman, Dr. Bachir El Fil, Dr. Girish Kini, Christy Green, Matthew Hughes, and Roland Crystal for their help during this process.

Finally, I would like to thank my family and friends for their unwavering support and constant encouragement throughout this journey.

TABLE OF CONTENTS

LIST OF TABLES

LIST OF FIGURES

LIST OF SYMBOLS AND ABBREVIATIONS

A	area	(m^2)
B	channel pressure drop linear constant	(Pa)
C	friction factor constant, channel pressure drop linear slope, or total heat capacity	(-, Pa s kg^{-1}, or W K^{-1})
CN	friction factor correlation exponent	(-)
CAT	closest approach temperature	(K)
c	specific heat capacity	(J kg^{-1} K^{-1})
D_h	hydraulic diameter	(m)
D_{pin}	pin diameter	(m)
D_v	volumetric hydraulic diameter	(m)
F^*	subchannel geometry factor	(-)
f_{axi}	axial friction factor	(-)
f_{gap}	gap friction factor	(-)
G	mass flux	(kg m^{-2} s^{-1})
g	acceleration due to gravity	(m s^{-2})

h	enthalpy	(J kg^{-1})
i	specific internal energy	(J kg^{-1})
I	total internal energy	(J)
k	thermal conductivity	(W m^{-1} K^{-1})
K'_{form}	form resistance per unit length	(m^{-1})
K_{gap}	gap or lateral resistance	(-)
L	axial subchannel length	(m)
l	length of lateral control volume	(m)
m	axial mass flow rate	(kg s^{-1})
N_{gap}	number of gaps in the pin bundle	(-)
Nu	Nusselt number	(-)
P	pressure	(Pa)
PE_w	wetted perimeter	(m)
PT	pin pitch	(m)
Pr	Prandtl number	(-)
q'	linear heat transfer rate	(W m^{-1})

q'''	volumetric heat generation rate	(W m^{-3})
q_{gen}	heat generated by the core	(W or MW)
q_{HX}	heat exchanger capacity	(W or MW)
q_{ideal}	ideal heat exchanger capacity	(W or MW)
R	thermal resistance	(K W^{-1})
Re	Reynolds number	(-)
r	radial distance	(m)
s	gap between the pins	(m)
T	temperature	(°C)
T^{+}	non-dimensional temperature	(-)
t	time	(s)
u	axial velocity	(m s^{-1})
u^{+}	non-dimensional axial velocity	(-)
V	volume	(m^3)
v	lateral velocity	(m s^{-1})
w	lateral mass flow rate per unit length	(kg m^{-1} s^{-1})

w'^{H}	turbulent mixing rate for energy	(kg m^{-1} s^{-1})
w'^{M}	turbulent mixing rate for momentum	(kg m^{-1} s^{-1})
X	flow split parameter	(-)
y^{+}	non-dimensional wall distance	(-)
z	axial distance	(m)

Greek Symbols

α	time step reduction factor	(-)
β	mixing Stanton number or mixing coefficient	(-)
γ	friction factor interpolation exponent	(-)
Δ	change/difference	(-)
δ	change/difference	(-)
ε	eddy diffusivity or heat exchanger effectiveness	(m^{2} s^{-1}, or -)
ϵ	convergence tolerance	(-)
θ	azimuthal angle	(rad)
κ	$k_{particle}/k_{matrix}$	(-)

μ	dynamic viscosity	(kg m^{-1} s^{-1})
ρ	density	(kg m^{-3})
σ	$(\kappa - 1)/(\kappa + 2)$	(-)
φ	volumetric packing fraction	(-)
ψ	friction factor intermittency factor	(-)
ω	specific dissipation rate	(s^{-1})

Abbreviations

AGR	advanced gas reactor
AHTR	advanced high temperature reactor
BSL	baseline
BWR	boiling water reactor
CAT	closest approach temperature
CFD	computational fluid dynamics
CFS	cold flow split
CIET	compact integral effects test
CTC	carbonate thermochemical cycle

CTF	COBRA two fluids
DHX	DRACS heat exchanger
DNS	direct numerical simulation
DRACS	direct reactor auxiliary cooling system
FHR	fluoride salt-cooled high-temperature reactor
FHR-DR	FHR demonstration reactor
FSG	freestream grid
HEM	homogenous equilibrium model
HTGR	high temperature gas-cooled reactor
HX	heat exchanger
IAEA	International Atomic Energy Agency
KP-FHR	Kairos power FHR
LES	large eddy simulation
LMFBR	liquid metal fast breeder reactor
LMR	liquid metal-cooled reactor
MHTGR	modular HTGR

MSR	molten salt-cooled reactor
ORNL	Oak Ridge National Laboratory
PHX	primary heat exchanger
P-LOFF	protected loss of forced flow
P-LOHS	protected loss of heat sink
PWR	pressurized water reactor
PyC	pyrolytic carbon
RANS	Reynolds-averaged Navier-Stokes
RMS	root mean squared
RSM	Reynolds stress model
SmAHTR	small modular advanced high temperature reactor
SMR	small modular reactor
SST	shear stress transport
TFHR	transportable FHR
TRISO	tristructural isotropic
UCO	uranium oxy-carbide

U-TOP	unprotected transient overpower
WG	wall grid

SUMMARY

Fluoride-salt-cooled high-temperature reactors (FHRs) are an emerging category of reactors that combine the graphite-matrix coated-particle fuel developed for high temperature gas reactors (HTGRs) with a high heat capacity, single-phase molten salt coolant. One of the potential configurations for the FHR core includes the pin bundle configuration in which the molten salt coolant flows parallel to an array of fuel and non-fuel pins.

A thermal hydraulic modeling tool that can perform fluid flow and heat transfer analyses in the core region of the reactor during normal operation and under different postulated accident scenarios is essential to enable the further development of pre-conceptual pin-fueled FHR designs. To enable multiphysics coupling and the analysis of several different core design iterations for this FHR, the thermal hydraulic model must provide detailed (pin-level) resolution across the entire core while incurring a modest computational overhead and providing fast simulation turnaround times. This requirement is addressed in the present study. A comprehensive thermal hydraulic model is developed for the solid pin-fueled design to analyze the steady-state and transient behavior of the core. A finite volume model is used to compute temperatures in the solid regions in the core. The coolant flowing through the pin bundles in the core is modeled using the conventional subchannel methodology. For the solid pin fuel configuration, a steady-state computational fluid dynamics (CFD) model is developed for 1/12th of a single fuel assembly. The results from the CFD model are compared with the subchannel-based model to perform code-to-code comparison and preliminary verification of the subchannel model. Whole-core steady-state temperature, pressure, and flow profiles for different power profiles and flow rates are presented and discussed. The subchannel-based thermal hydraulic model is then extended to analyze the annular pin-fueled core configuration for steady-state scenarios. A transient CFD model is developed for the solid pin-fueled configuration to perform code-to-code comparison with the subchannel-based model. The transient thermal hydraulic model is then used to analyze accident scenarios that involve high (forced circulation) as well as low (natural circulation) coolant flow rates into the core. For the two protected accident scenarios involving loss of heat sink and loss of forced flow investigated in this study, the peak fuel and coolant temperatures are generally well within the allowable safety limits for this FHR configuration. The results from the unprotected transient over power accident simulation with an assumed power profile show that the peak fuel temperature during the transient is within the maximum allowable temperature for the coated particle TRISO fuel. However, for accident scenarios with more severe power excursions, the peak fuel temperature could exceed the maximum allowable TRISO temperature, and an optimization of core design might be necessary to provide better thermal margins against more severe U-TOP accidents. Insights from these simulations can guide the optimization of core design, and analysis of core safety during accident scenarios.

CHAPTER 1. INTRODUCTION

In 2021, nuclear energy accounted for ~19% of the electricity generated in the U.S. (EIA, 2022), representing ~48% of the carbon-free electricity. With the increasing focus on reducing carbon emissions, the role of nuclear energy is now more important than ever. However, the current generation of nuclear reactors faces significant economic challenges that inhibit the growth of nuclear power. In fact, as shown in Figure 1.1, with continuing retirement of more nuclear power plants, the nuclear electricity generation capacity in the U.S. is expected to significantly decline in the next few decades.

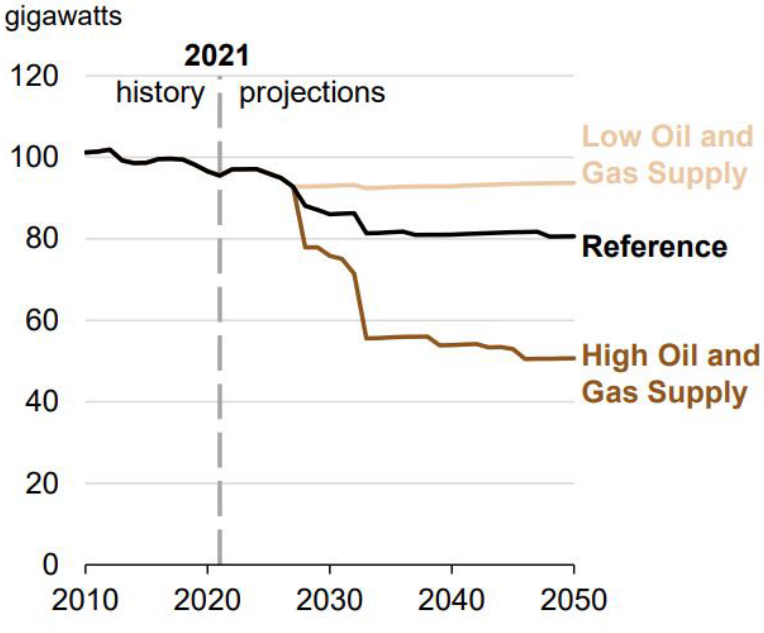

Figure 1.1: U.S. nuclear electricity generation capacity (EIA, 2022)

In addition to the economic challenges, the public's confidence in the safety of nuclear energy has been severely undermined after the 2011 meltdown of three boiling water reactors (BWRs) in Fukushima, Japan due to the failure of backup cooling systems following a tsunami (Kim et al., 2013).

The next generation of nuclear reactor technologies, collectively known as Generation IV reactors, have the potential to mitigate these economic and safety challenges associated with the current generation of reactors, while also addressing the issues related to nuclear waste, proliferation resistance, and physical security (US DOE and GIF, 2002), and to increase the role of nuclear energy in providing carbon-free electricity.

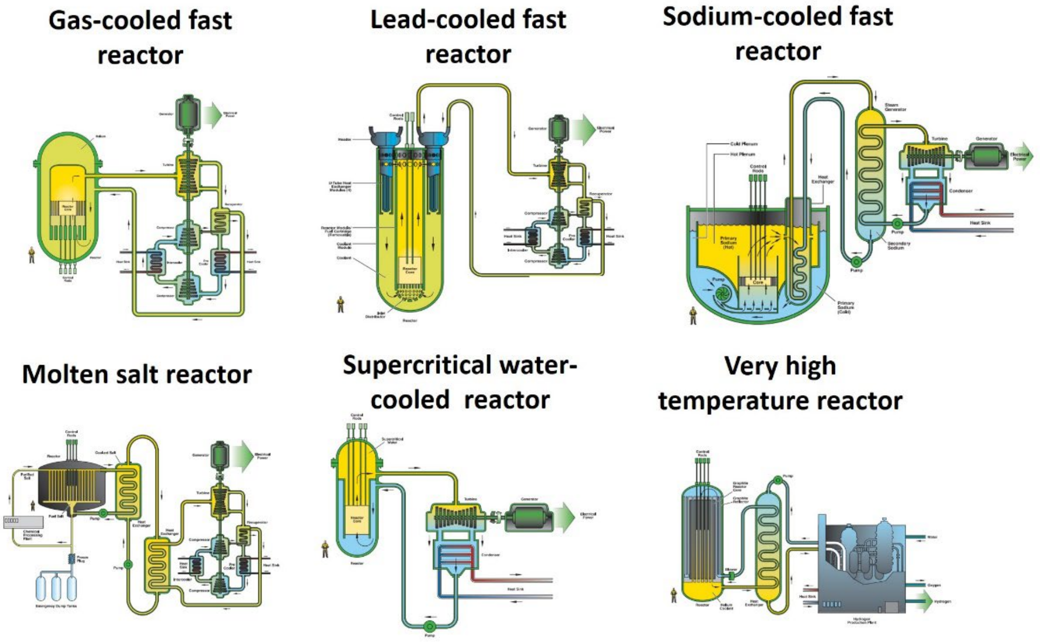

Figure 1.2: Generation IV reactors (US DOE and GIF, 2002)

The six Generation IV concepts shown in Figure 1.2 include reactors both in the thermal and fast neutronic spectrum, and a variety of coolants, including liquid sodium and lead, helium, supercritical water, and molten salt (Kamide et al., 2021). The molten salt reactors (MSRs) are primarily divided into two subcategories – liquid fueled and solid fueled designs. In the liquid fueled MSRs, the fissile elements are mixed into the molten salt. When the liquid fuel salt enters the core, fission occurs within the salt, and the heat generated in the fuel salt is then transferred to the secondary coolant through the primary-to-secondary heat exchanger (PHX). In the solid fueled MSRs, the molten salt serves as the coolant while the core is fueled with the solid coated-particle tristructural-isotropic (TRISO) fuel similar to that employed by the high temperature gas-cooled reactors (HTGRs). To enable easier identification of the reactor types, the MSRs with solid fuel design are commonly referred to as fluoride salt-cooled high temperature reactors (FHRs) (Serp et al., 2014).

FHRs have several economic and safety benefits due to higher core power densities compared to HTGRs, near-atmospheric pressure operation, higher cycle efficiencies due to high secondary-coolant temperatures, less demanding reactivity control compared to light water reactors (LWRs), higher margin for fuel failure temperature and coolant boiling, and passive decay heat removal using natural circulation. The FHR concepts currently being considered include the pebble bed design (Scarlat and Peterson, 2014; Zhang et al., 2018; Blandford et al., 2020), prismatic design (Wang et al., 2016a; Brown et al., 2017), plate/plank design (Greene et al., 2011; Varma et al., 2012), and pin bundle design (Greene et al., 2011).

Parallel to the development of the different Generation IV reactor systems, there is a growing interest in the development of small modular reactors (SMRs). The International Atomic Energy Agency (IAEA) defines SMRs as *"newer generation reactors designed to generate electric power up to 300 MW, whose components and systems can be shop fabricated and then transported as modules to the sites for installation as demand arises"*

(IAEA, 2014). Several SMR designs that use coolants including water, liquid metal, gas, and molten salt, in both the thermal and fast spectrum, are currently under development (IAEA, 2014). This growing interest is due to the improved safety, economics, availability, utility, and proliferation resistance that SMRs could offer in comparison to the conventional large-scale nuclear power plants (Boldon et al., 2014). The enhanced utility of SMRs is due to the ability to not only support electricity production, but also a variety of other applications including desalination, hydrogen production, and industrial process heating.

The small modular advanced high temperature (SmAHTR) is a fluoride-salt-cooled reactor concept that combines the advantages of the FHR and SMR technologies mentioned above, and is designed to be transported and assembled at remote sites to deliver high temperature process heat and electricity. The pre-conceptual design for the SmAHTR was developed by the Oak Ridge National Laboratory (ORNL) (Greene et al., 2011). The fuel configurations considered for SmAHTR include two different pin bundle configurations (solid pin and annular pin) and a plate/plank type configuration (Figure 1.3).

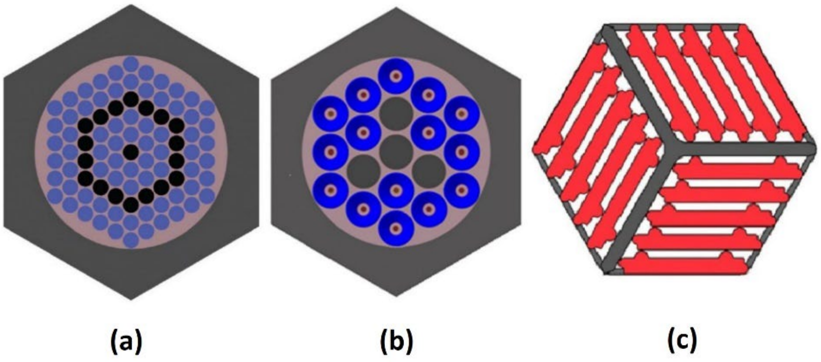

Figure 1.3: SmAHTR fuel configurations (a) solid cylindrical pin , (b) annular pin, and (c) plate/plank (Greene et al., 2011)

To aid the further development of FHR designs that are still in the pre-conceptual or early design stages, it is essential to develop a thermal hydraulic computational tool for optimizing the core design, and for analysis of the safety aspects of the core. The computation of temperatures and densities for the fuel, graphite and coolant regions in the core is critical for performing neutron transport calculations, analyzing the stresses in the different core elements, and in other multiphysics analyses. To facilitate coupling with other multiphysics tools, the thermal hydraulic model must provide detailed flow and temperature information across the entire core. This precludes the use of system-level codes such as RELAP (INL, 2012). While those codes can perform whole-core analysis and offer coupling to neutronic codes such as Rattlesnake (Wang et al., 2021), they typically cannot provide the fuel element (pin/pebble/plate)-level resolution needed for multiphysics studies. On the other hand, computational fluid dynamics (CFD) codes such as ANSYS Fluent (ANSYS, 2021) can provide very detailed flow fields and temperatures across the different core elements. However, these CFD codes require large computational overheads. This leads to a limitation where only a fraction of the core can be considered when the CFD approach is applied for core thermal hydraulic analysis. Whole-core, medium fidelity thermal hydraulic modeling tools that can provide the required fuel element-level (or even single TRISO fuel particle-level) resolution have been developed for certain FHR configurations such as the pebble fueled FHRs. However, there is currently a lack of thermal hydraulic modeling tools for analyzing pin bundle FHR configurations (such as the solid and annular pin-fueled SmAHTRs shown in Figure 1.3a and Figure 1.3b) that achieve the appropriate balance between fidelity, resolution and computational runtime, while providing the capability to model the entire core. This is addressed in the present work.

1.1 Literature review

1.1.1 FHR thermal hydraulic modeling

Figure 1.4 shows the reactor vessel schematic for a typical pebble bed FHR.

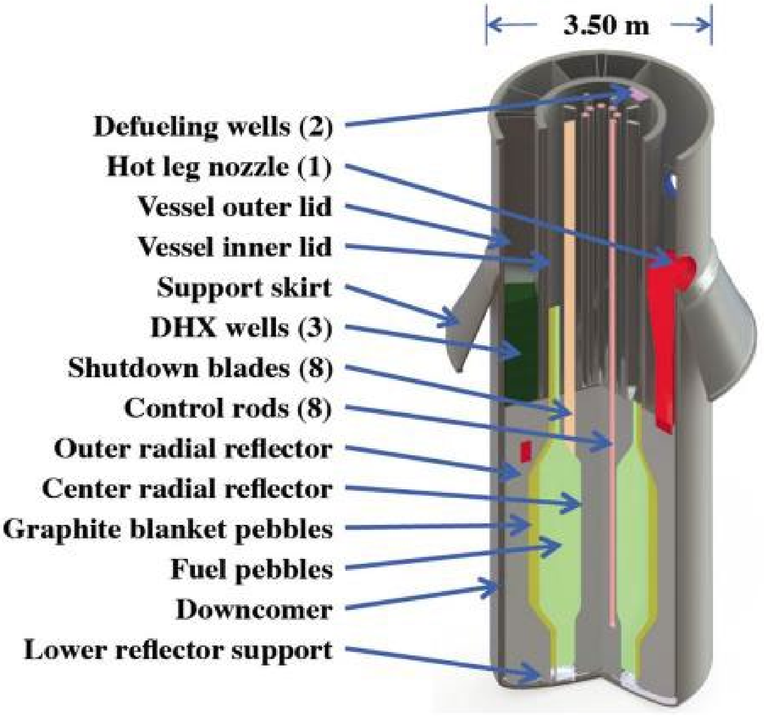

Figure 1.4: Mark-1 pebble bed reactor (Andreades et al., 2016)

The reactor core is annular, and is filled with the fuel and graphite pebbles. These pebbles slowly but continuously circulate through the reactor core. Each fuel pebble has an outer diameter of 30 mm, with a low-density solid graphite core at the center and a high-density outer graphite coating. Between the core and the coating, the coated-particle TRISO fuel is embedded within a graphite matrix. Each TRISO particle is ~1 mm in diameter.

For the pebble bed FHR design, several CFD studies have been performed to characterize the pressure loss and convective heat transfer in the pebble bed, conjugate heat transfer, and the flow of granular pebbles inside the reactor core (Wang et al., 2014; Ge et al., 2016; Liu et al., 2017; Dave et al., 2018; Blandford et al., 2020). Medium-fidelity computational tools with fast turnaround times have also been developed to enable scoping calculations and rapid thermal hydraulic computations. One such computational tool is Pronghorn (Novak et al., 2021), a multi-scale finite element thermal hydraulic model that uses the conventional porous media approach (Todreas and Kazimi, 2001). This coarse mesh tool can model the thermal and flow physics in the complex pebbled bed geometry at different length scales ranging from macroscale (core-level), through mesoscale (a single fuel pebble), and down to the microscale (a single coated particle fuel). KP-AGREE is another coarse-mesh core-level thermal hydraulics code that is currently being developed to analyze the Kairos Power pebble bed FHR (KP-FHR) (Blandford et al., 2020). Both Pronghorn and KP-AGREE have been benchmarked with the data from the SANA experiments (Stocker and Niessen, 1997). For system-level analyses of pebble bed FHRs, several studies (Andreades et al., 2016; Blandford et al., 2020) have employed existing codes such as RELAP (INL, 2012), TRACE (NRC, 2010), SAM (INL, 2017), and Flownex (M-Tech Industrial, 2013). Some of these system-level pebble bed FHR models have been validated using the data from the compact integral effects test (CIET) facility (Zweibaum, 2015).

For the advanced high temperature reactor (AHTR) (Varma et al., 2012) that uses a plate type fuel configuration similar to that shown in Figure 1c, Yoder et al. (2014) performed CFD studies on a single coolant channel as well as 1/3rd symmetric section of a single fuel assembly. In addition to the baseline model, multiple sensitivity studies were conducted to investigate the impact of varying the thermal conductivity values of the different solid materials on the temperature profile of the fuel assembly. These sensitivity studies were performed as the current thermal conductivity correlations for these solid regions have large uncertainties. Based on these simulations, multiple recommendations were provided to improve the fuel assembly design. Avigni and Petrovic (2020) developed a novel methodology that coupled CFD, system-level code, and reduced-order model for pressure drop through coolant and bypass channels to simulate the on-line refueling for the AHTR. They also developed a medium fidelity finite volume model that calculated the temperature profile for both a single fuel plate as well as 1/3rd of the plate fuel assembly. System-level models for the AHTR have been developed in RELAP by Avigni and Petrovic (2014), and in TRACE by Yoder et al. (2014), to simulate the loss of forced flow (LOFF) accident. For the plate type SmAHTR, Greene et al. (2011) developed a RELAP model and reported steady-state maximum fuel temperatures for a range of core inlet mass flow rates.

Figure 1.5 shows the fuel assembly configuration for the fluoride salt-cooled engineering demonstration reactor (FHR-DR) (Brown et al., 2017), which uses a prismatic block-type fuel design. In this design, the cylindrical fuel compacts are inserted into a hexagonal graphite block. The graphite block also has channels for other non-fuel elements, and for coolant flow.

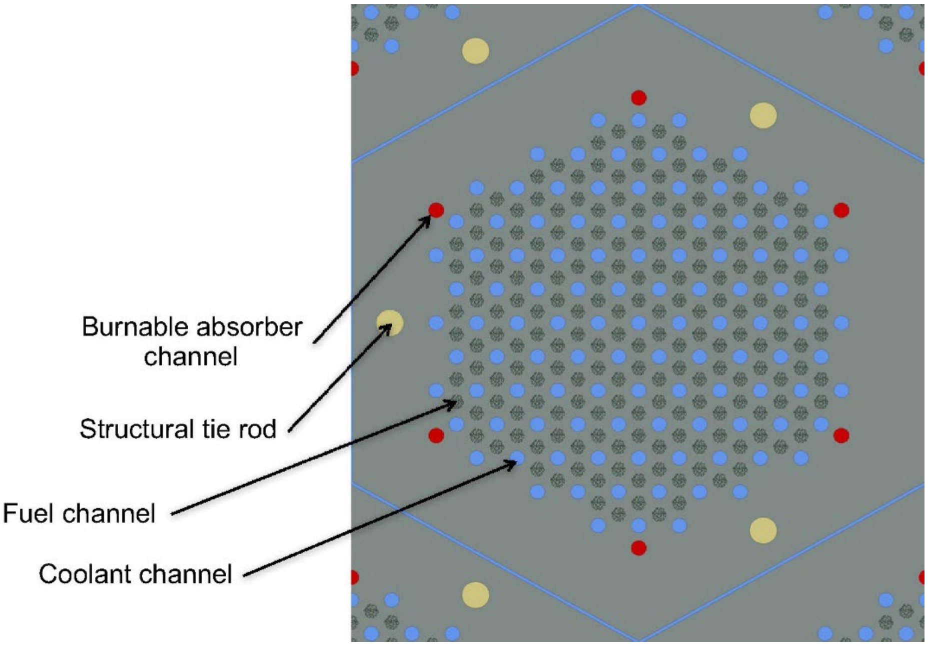

Figure 1.5: FHR-DR fuel assembly design (Brown et al., 2017)

For the FHR-DR, Brown et al. (2017) developed a finite element model for 1/6th of a fuel assembly to determine the thermal hydraulic performance of this prismatic design. Wang et al. (2016a) performed CFD studies on a 1/12th fraction of the core for the prismatic transportable FHR (TFHR) design. From this analysis, it was determined that the design would not be able to meet all the safety requirements in the event of 20% overpower, and recommendations to improve the TFHR design were provided. System-level models were developed for both FHR-DR (Brown et al., 2017) and TFHR (Wang et al., 2017) designs to analyze off-normal conditions including LOFF with and without scram, overcooling transients, reactivity-initiated accidents, and loss of heat sink (LOHS) without scram.

For the solid and annular pin bundle FHR designs similar to that shown in Figure 1.3a and Figure 1.3b, Greene et al. (2011) developed a system-level model in RELAP, and reported the maximum fuel temperatures for both the solid and annular pin fueled

SmAHTR designs for different core inlet mass flow rates. They also performed a transient simulation of the LOFF with the scram accident scenario for the solid pin bundle configuration. No medium fidelity or CFD models have been developed thus far to study core thermal hydraulics in pin bundle FHR designs. Table 1.1 summarizes the key FHR core thermal hydraulic modeling studies discussed in this section.

Table 1.1: Summary of key FHR core thermal hydraulic modeling studies

FHR Configuration	Low core resolution (system-level models)	Intermediate core resolution (medium fidelity models)	High core resolution (CFD models)
Pebble bed	Andreades et al. (2016) Blandford et al. (2020)	Blandford et al. (2020) Novak et al. (2021)	Wang et al. (2014) Ge et al. (2016) Liu et al. (2017) Dave et al. (2018) Blandford et al. (2020)
Prismatic	Brown et al. (2017) Wang et al. (2017)	Brown et al. (2017)	Wang et al. (2016a)
Plate/plank	Greene et al. (2011) Avigni and Petrovic (2014) Yoder et al. (2014)	Avigni and Petrovic (2014)	Yoder et al. (2014)
Pin bundle	Greene et al. (2011)		

1.1.2 Subchannel modeling for pin bundle reactors

Figure 1.6 shows a typical pin bundle fuel assembly design. In this design, the coolant flows parallel to an array of fuel and non-fuel pins arranged either in hexagonal, square, or circular layout. The interstitial gap between the solid pins through which the coolant flows is referred to as the pin bundle region. In addition to the pin bundle region, coolant can also flow through regions such as the guide tube (typically provided for inserting control rods or instrumentation) shown in Figure 1.6, or the fuel pin annulus in case of the annular fuel design. Spacer grids or wire wraps are added to the pin bundle assembly to provide structural support, promote mixing, and maintain the gap between the fuel and non-fuel pins in the assembly. These pin bundle configurations are commonly encountered in water-cooled reactors such as pressurized water reactors (PWRs) and BWRs, and liquid metal-cooled reactors (LMRs).

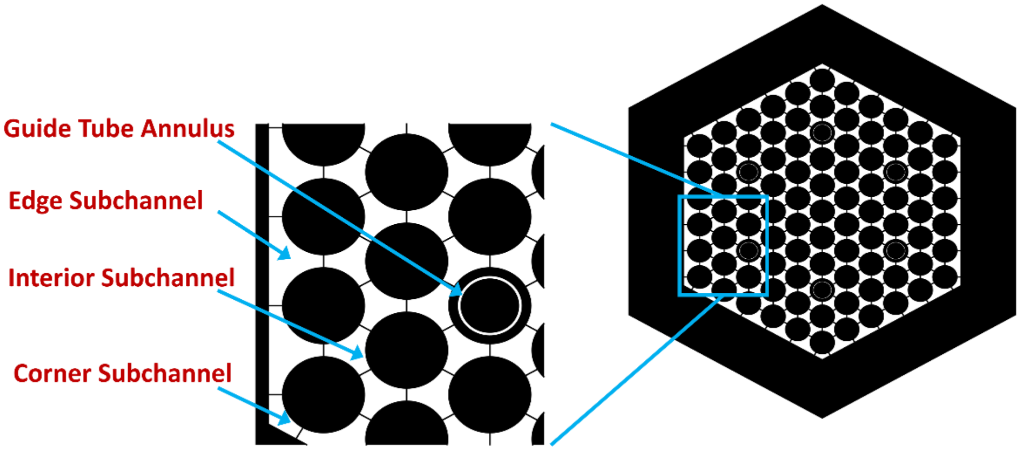

Figure 1.6: Hexagonal pin bundle design and subchannel discretization

The subchannel approach is commonly used in pin bundle designs to enable the development of medium fidelity coarse mesh thermal hydraulic models. In this approach, the pin bundle region in each fuel assembly is divided into finite volumes called ‘subchannels’. These subchannels are identified as interior, edge, and corner subchannels based on their geometry and their location in the pin bundle (Figure 1.6). While this model accounts for the lateral exchange between adjacent subchannels, it is assumed that the flow through the gap between the adjacent subchannels loses its sense of direction after leaving the gap region. This allows for the subchannels to be connected arbitrarily without requiring a fixed lateral coordinate system. The appropriate forms of mass, energy, axial and lateral momentum equations resulting from the subchannel discretization are systematically solved to obtain the flow and temperature profiles for the coolant region. The heat conduction equations for the fuel and non-fuel regions in the core are typically solved using a finite volume approach. Heat transfer from the solid to the fluid region is quantified using Newton's law of cooling. Closure relations from the literature are used to quantify axial and lateral flow resistances, heat transfer from solid to fluid, and turbulent mixing. The combination of using a coarse mesh and empirical relations to characterize the transport phenomena in the fluid region render this approach with a substantially lower computational overhead compared to the CFD approach. This subchannel approach, therefore, can be used for developing whole-core thermal hydraulic models.

Several subchannel-based thermal hydraulic codes have been developed for water and liquid-metal cooled reactors. These include the COBRA family of codes (Stewart et al., 1977), VIPRE family of codes (Stewart et al., 1989), and the SUPERENERGY family of codes (Basehore and Todreas, 1980). Codes such as COBRA-IV (Stewart et al., 1977), VIPRE-01 (Stewart et al., 1989) and MATRA (Yoo and Hwang, 1998) use a relatively simple homogenous equilibrium model (HEM) to characterize the one-dimensional, two-phase flow within the subchannels during coolant boiling. On the other hand, codes such as COBRA-TF (CTF) (Salko et al., 2019) use a more complex two-fluid (liquid and vapor), three-field (fluid film, fluid drops, and vapor) approach to model two-phase flow in subchannels. The codes based on the HEM approach can also be used for simulating single-phase flow in liquid metal-cooled reactors. In addition to the HEM-based codes, codes such as COBRA-WC (George et al., 1980), SUPERENERGY (Basehore and Todreas, 1980), and ANTEO+ (Lodi et al., 2016) have been specifically developed for single-phase liquid metal-cooled reactor applications. Some of these codes can perform multi-fuel assembly modeling and account for inter-assembly heat transfer, which are significant considerations for reactors such as the sodium-cooled liquid metal fast breeder reactor (LMFBR). Table 1.2 summarizes the key subchannel codes discussed in this section.

Table 1.2: Summary of subchannel codes

Subchannel code	Fluid region formulation	Reactor application
CTF (Salko et al., 2019)	Two fluid, three field	PWR, BWR
COBRA-IV (Stewart et al., 1977)	HEM	PWR, BWR, LMR
VIPRE (Stewart et al., 1989)	HEM	PWR, BWR
MATRA (Yoo and Hwang, 1998)	HEM	PWR, BWR, and LMR (MATRA-LMR)
ANTEO+ (Lodi et al., 2016)	Single-phase	LMR
SUPERENERGY (Basehore and Todreas, 1980)	Single-phase	LMR
COBRA-WC (George et al., 1980)	Single-phase	LMR

It must be noted that except for a few subchannel codes such as CTF, a majority of the available subchannel codes neglect axial and azimuthal conduction in the fuel pins, and compute the temperature profile by solving the 1-D radial conduction equation. Neglecting azimuthal pin temperature variations is a reasonable assumption if the subchannels surrounding each fuel pin have similar mean temperatures and heat transfer coefficients. However, this assumption might not be valid for the fuel pins in the outer periphery of the bundle, which are surrounded by subchannels (edge, corner and interior) that have significantly different geometries. Moreover, the mean temperature for interior subchannels that are connected to three fuel pins can be significantly different compared to interior subchannels that are connected to one fuel pin and two non-fuel pins. The azimuthal subchannel variations therefore could be important in calculating the fuel pin temperature profile.

1.1.3 CFD modeling for pin bundle geometries

Subchannel-based models can provide the capability to analyze the whole-core thermal hydraulics for different normal operation and accident scenarios. On the other hand, CFD modeling can provide insights into complex transport phenomena in the pin bundle such as coolant mixing, turbulence-driven secondary flows, large scale flow oscillations, and also the local wall temperature distribution around the circumference of the fuel rods. In the absence of experimental data for code validation, CFD models could also serve as a high-resolution benchmark to perform preliminary verification of medium fidelity subchannel-based models, especially for single-phase flows.

Due to the large computational cost and runtime associated with CFD modeling, only a fraction of a single fuel assembly in the core is typically modeled. Several CFD studies have been conducted in the past to characterize the heat transfer and fluid flow through water cooled and liquid-metal cooled pin/rod bundles (Shang, 2009; Fricano and Baglietto, 2014; Manservisi and Menghini, 2015; Chang et al., 2016; Podila and Rao, 2016; Sohag et al., 2017; Chen et al., 2018). In rod bundle heat transfer modeling, many studies primarily focus on the coolant region, with a heat flux applied at the fuel pin/coolant interface to simulate the heat input from the fuel pins in the core. Fuel pins in an actual fuel assembly could have large circumferential variations in coolant temperatures and heat transfer coefficients, which could result in a significant departure from an azimuthally uniform heat transfer condition. Some CFD studies in the literature (EPRI, 2015; Podila and Rao, 2018; Palomino and El-Genk, 2019a) include conjugate heat transfer, which results in a more realistic characterization of heat transfer between the solid and fluid regions in the bundle.

As the computational overheads associated with the direct numerical simulation (DNS) and large eddy simulation (LES) approaches are very large, a majority of the CFD studies for typical pin bundle geometries employ the Reynolds averaged Navier-Stokes (RANS) approach for turbulence modeling. For the RANS approach, the choice of turbulence model is often very important, as it heavily influences the transport phenomena in the coolant region, which in turn influences the temperature, flow and pressure profiles in the CFD model domain.

Within the RANS approach, many studies have employed the *k-ω* shear-stress transport (SST) model. This two-equation model has been used in several rod bundle CFD studies (Sohag et al., 2017; Podila and Rao, 2018; Palomino and El-Genk, 2019a; Zhang et al., 2020) as it combines the accuracy of the original *k-ω* model in the near wall region with the freestream independence of the *k-ε* model in the bulk fluid flow region. In addition, a recent work by Palomino and El-Genk (2019b) applied the *k-ω* SST model for predicting pressure drop in rod bundle geometries and showed good agreement with the experimental data by Rehme (1972) for a wide range of bundle geometries and flow conditions. While these studies point to the potential applicability of the *k-ω* SST model, it must be noted that there is no single turbulence model recommended for fluid flow through rod bundles, and many CFD studies in literature have applied other two-equation turbulence models (such as the *k-ε* family of models) (Zhu et al., 2014) as well as anisotropic Reynolds stress transport models (Cheng and Tak, 2006). Table 1.3 shows a summary of a few different pin bundle CFD studies for water and liquid metal coolants and the different turbulence models employed in these studies.

Table 1.3: Pin bundle CFD studies and turbulence models

Coolant	Study	Turbulence modeling
Supercritical water	Zhu et al. (2014)	Multiple k-ε models (standard two-layer k-ε model recommended)
Water (single-phase)	Podila and Rao (2018)	k-ω SST model
	Sohag et al. (2017)	Multiple models (k-ω SST model recommended)
Liquid sodium	Chang et al. (2016)	Anisotropic cubic k-ε model
Liquid sodium	Chen et al. (2018)	Realizable k-ε model
Liquid sodium	Fricano and Baglietto (2014)	Multiple models (no significant difference was observed between different turbulence models)
Liquid sodium	Palomino and El-Genk (2019a)	k-ω SST model
Lead-bismuth eutectic	Cheng and Tak (2006)	Multiple models (SSG Reynolds stress model recommended)

1.2 Research needs and scope of present work

The literature survey in the previous sections reveals several important insights. It is clear from the summary presented in Table 1.1 that while some CFD and/or medium fidelity models have been developed to characterize the detailed thermal hydraulic behavior for pebble bed, plate type and prismatic fuel designs, there is a lack of medium/high resolution models for the pin bundle type FHRs.

It is also evident that the medium fidelity models for water and liquid-metal cooled reactors that employ the pin bundle design have been developed based on the subchannel methodology. While there are several subchannel codes for analyzing PWRs, BWRs and LMRs, as shown in Table 1.2, none of these codes can be readily utilized for the FHR design. It is also seen that except for a few codes such as CTF, a majority of the subchannel codes neglect azimuthal pin temperature variations in the fuel pins, which might not always be a reasonable assumption. In addition, due to the combination of high heat capacity and a very high boiling point, the subchannel codes for FHRs only need the single-phase form of the conservation equations, and not the general two-phase HEM or the more complex two-fluid, three-field form considered by many subchannel codes. A single-phase formulation for the subchannel model results in a substantially simpler code architecture. It also aids in minimizing the inputs that must be specified by the code user, which in turn would reduce the potential for errors that can arise due to incorrect user inputs. A thermal hydraulic code based on single-phase subchannel formulation, which accounts for azimuthal pin temperature variations, and tailored for the thermophysical properties of the FHR fuel and coolant, can address the issues associated with current subchannel codes, and enable pin-by-pin, whole-core analysis of pin bundle FHRs.

It is also seen that while several CFD studies have addressed the flow of water and liquid metal through pin/rod bundles, there is a lack of studies that characterize the heat transfer and fluid flow of molten salt flowing through a pin bundle. Molten salts have relatively higher Prandtl numbers (*Pr*) of ~10-15, compared to liquid metals (~0.01) and water (~7) (Shams et al., 2019), and therefore, have different transport characteristics and a non-negligible thermal entrance effect. In addition, due to the high viscosity, the bundle Reynolds number (*Re*) for molten salts in typical rod bundle geometries is substantially lower than that of liquid metals or water. In addition, many studies in the literature do not model conjugate heat transfer and consider a uniform heat flux at the fuel pin/coolant interface, which might not be a realistic assumption. Hence, it is important to study the thermal hydraulics of molten salt flow through pin bundles while also accounting for the effects of conjugate heat transfer. Also, as shown in Table 1.3, there is currently no consensus on the choice of RANS turbulence model to be used in the simulation of pin bundles. Therefore, it is also essential to quantify the effect of different turbulence models on the thermal hydraulic behavior of FHR pin bundles.

1.3 Research objectives

The primary objective of the proposed work is the development and initial verification of a whole-core, medium fidelity thermal hydraulic model that can be used for coupled, multi-physics analyses of both normal operation and postulated accident scenarios for FHRs with pin bundle configurations. The main focus of this proposed work will be on solid pin-fueled FHR configuration. However, to demonstrate that the proposed modeling framework can also be extended to analyze other variants of pin-fueled FHR configurations, a whole-core, steady-state, thermal hydraulic model is developed and presented for the SmAHTR with annular pin fuel configuration. The following tasks are conducted to accomplish these objectives.

1. Development of whole-core, steady-state subchannel model for the solid pin-fueled FHR designs.
2. Steady-state CFD modeling for a 1/12th fuel assembly in the solid pin-fueled FHR (SmAHTR) design, and code-to-code comparison with the subchannel-based model.
3. Extension of steady-state subchannel methodology for the annular pin-fueled FHR designs and code-to-code comparison with a 1/6th annular fuel assembly CFD model.
4. Development of transient subchannel model for the solid pin-fueled FHR designs, and CFD model comparison.
5. Modifications to the transient subchannel model for solid pin-fueled FHR designs to analyze accident scenarios that involve natural circulation cooling.

1.4 Thesis organization

This dissertation is organized as follows:

- Chapter 2 presents the development of a comprehensive subchannel-based thermal hydraulic model that can be used for both steady-state and transient analysis of solid pin-fueled FHRs.
- Chapter 3 discusses the studies performed to verify the steady-state version of the subchannel thermal hydraulic model developed in Chapter 2. The verification studies performed to test the key sub-models in the subchannel model are first described. This is followed by the discussion of a conjugate CFD model for 1/12th fuel assembly for the solid pin-fueled SmAHTR. The results from the code-to-code comparison between subchannel and CFD models are then presented.
- Chapter 4 shows the whole-core, steady-state results for the solid pin-fueled SmAHTR. The temperature, pressure, and flow profiles for the core for different power profiles, flow rates, inlet boundary conditions are presented and discussed.
- Chapter 5 presents the extension of the subchannel-based thermal hydraulic modeling framework for annular pin-fueled FHRs for the analyses of steady-state scenarios.
- Chapter 6 discusses the application of the subchannel-based thermal hydraulic model for transient scenarios that involve forced circulation cooling of the core. The results from a transient code-to-code comparison study with a CFD model are presented, along with the results from two postulated accident scenarios -- protected loss of heat sink (P-LOHS) accident and unprotected transient overpower (U-TOP) accident.

- Chapter 7 presents and discusses the results for accident scenarios involving low flow rates into the core such as the protect loss of forced flow (P-LOFF) accident.
- Chapter 8 summarizes the important conclusions of this study and provides recommendations for future work in this area.

CHAPTER 2. WHOLE-CORE THERMAL HYDRAULIC MODEL FOR SOLID PIN-FUELED SMAHTR

The development of the whole-core thermal hydraulic model is discussed in this chapter. The details of the SmAHTR reactor, modeling of solid and fluid regions in the core, closure relations, and the overall model structure are described next.

2.1 SmAHTR description

The vessel configuration for the SmAHTR is shown in Figure 2.1a. FLiBe and FLiNaK are employed as the primary and secondary coolants respectively. The FLiBe salt flows into the core from the bottom, moves upwards, and leaves the core through the top. The primary FLiBe coolant then enters the PHX, where it transfers the heat to the secondary FLiNaK coolant. This relatively colder FLiBe coolant is then pumped back to the bottom of the core. The decay heat from the core post scram shutdown is removed using a direct reactor auxiliary cooling system (DRACS). Three DRACS heat exchangers (DHXs) are co-located with the PHXs inside the reactor vessel to enable the passive natural circulation cooling of the core. The core cross-section is shown in Figure 2.1b. The core consists of 19 hexagonal fuel assemblies. The hexagonal and radial graphite reflectors and the coolant channels in the radial reflector are also shown in Figure 2.1b.

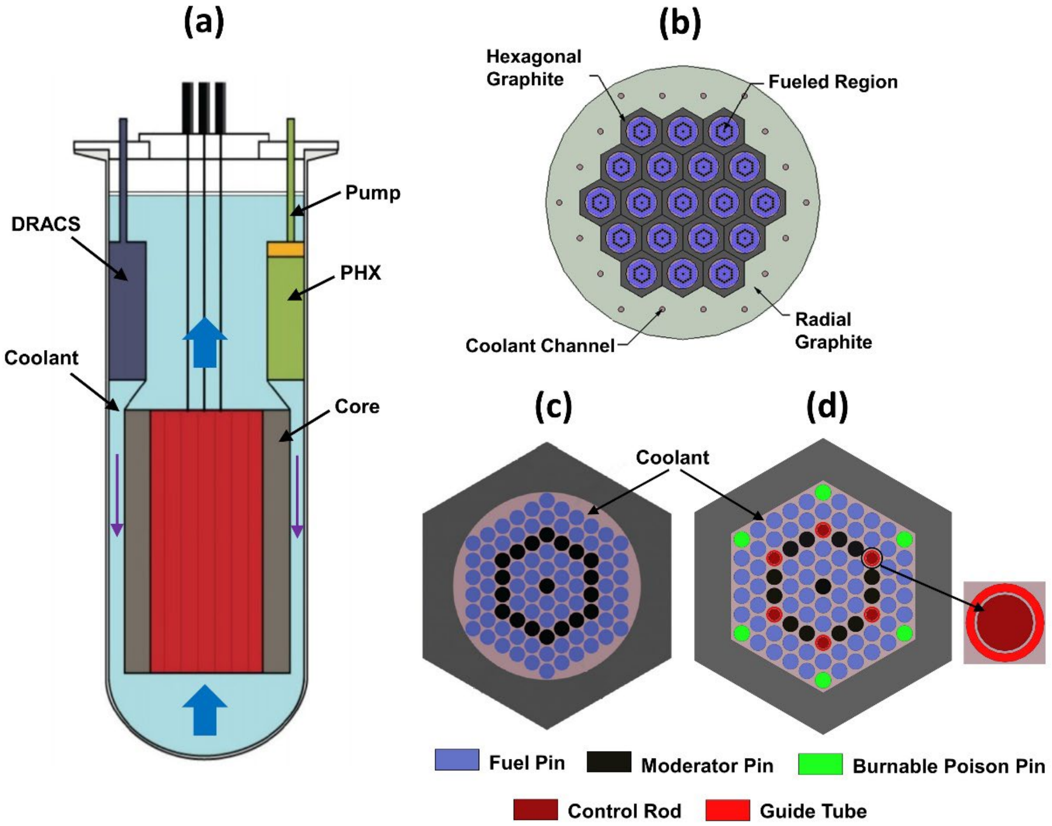

Figure 2.1: SmAHTR: (a) reactor vessel layout, (b) core cross-section, (c) original fuel assembly design, and (d) modified fuel assembly design

A single fuel assembly for the solid pin-fueled design considered in this study is shown in Figure 2.1c. The original pre-conceptual design had an inner cylindrical housing, which resulted in a significant flow bypass through the large, unobstructed gap between the cylindrical house and the pin bundle periphery. To mitigate this unfavorable flow bypass and ensure sufficient coolant flow rates through the interior of the pin bundle, the inner cylindrical housing is replaced with an inner hexagonal housing in the present study. The modified fuel assembly is shown in Figure 2.1d. The pin pitch is increased from 30.8 mm to 32.9 mm to maintain the same coolant volume in the fuel assembly as the original pre-conceptual design, as the FLiBe coolant also provides neutron moderation in the core. The fuel assembly in the pre-conceptual design also only included fuel pins and moderator pins. In the modified fuel assembly, the fuel pins in the six corners of the hexagonal bundle are replaced with burnable poison pins, and six of the moderator graphite pins in the assembly are replaced with control rod assemblies. In this preliminary control rod assembly, the control rod is extended/retracted inside a guide tube. A small gap exists between the control rod and guide tube, which is filled by the coolant. When the control rod is extended or retracted, it displaces the FLiBe coolant inside the guide tube, similar to the control blade arrangement in the plate type AHTR design (Varma et al., 2012). Additional details of the fuel assembly modifications can be found in the work of Reed (2021).

Each fuel assembly shown in Figure 2.1d has 66 fuel pins. Each fuel pin has an active fuel region in which TRISO particles with uranium oxy-carbide (UCO) fuel kernels are loaded with a volumetric packing density of 50% into a graphite matrix. The active fuel region is surrounded by a graphite sleeve or coating, referred to as the cladding region. Each fuel assembly also has 13 moderator pins, six poison pins, and six control rods. Five layers of fuel assemblies, each 0.8 m in height, are stacked for a total core height of 4 m. The key dimensions for the SmAHTR fuel assembly are shown in Table 2.1.

Table 2.1: SmAHTR fuel assembly key dimensions

Parameter	Value (mm)
Fuel pin: active fuel region radius	11.0
Fuel pin: cladding radius	14.0
Moderator pin radius	14.0
Poison pin radius	14.0
Control rod assembly: control rod radius	10.0
Control rod assembly: guide tube inner radius	11.0
Control rod assembly : guide tube outer radius	14.0
Pin pitch (original)	30.8
Pin pitch (modified)	32.9
Wall pitch (pin center to bundle wall distance)	18.9

2.2 Core thermal hydraulic model

The modeling approach followed to obtain the whole-core temperature distribution for the fuel, graphite and the coolant, and flow distribution and pressure drop for the coolant region is discussed in this section. The model is subdivided into two parts: (1) a conduction model for the computation of energy balance and heat transfer in the various solid regions in the core including the fuel and non-fuel pins, and the graphite reflectors; (2) a subchannel model for the coolant to compute the mass, momentum and energy balances in the fluid region. Empirical correlations are used in quantifying friction and form loss, solid-to-fluid heat transfer and other mixing phenomena in the fluid domain.

2.2.1 Solid region model

The solid regions in the core include fuel and non-fuel pins as well as the hexagonal and radial graphite reflectors. The representative discretization and node placement for the fuel pin is shown in Figure 2.2a. A magnified view for a control volume with center node P is shown in Figure 2.2b.

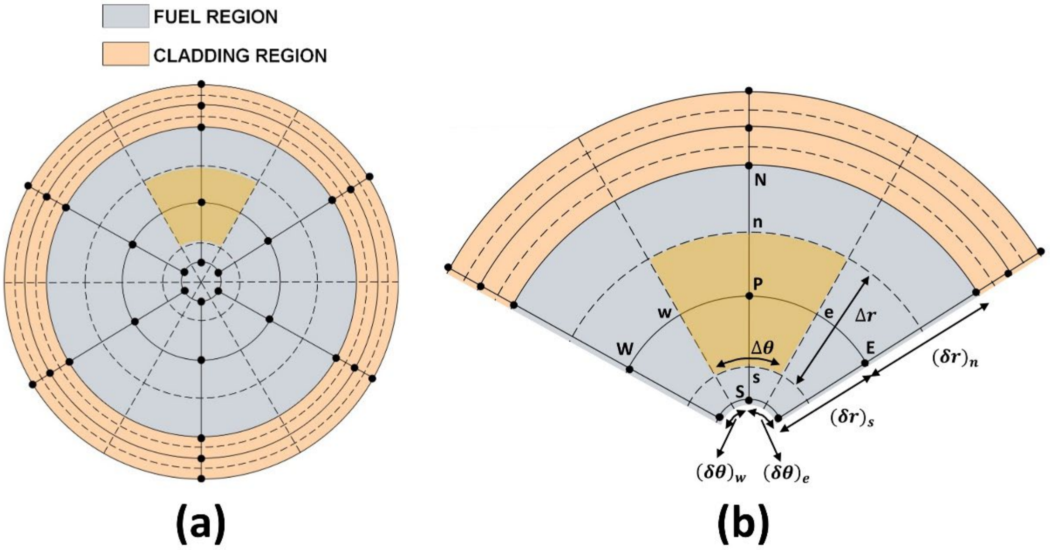

Figure 2.2: Fuel pin (a) representative discretization, and (b) detailed view of a control volume with center node ‘P’

The neighboring nodes are identified using the ‘east’, ‘west’, ‘north’, ‘south’, ‘top’ and ‘bottom’ terminology. Figure 2.2b shows the radial and azimuthal control volume dimensions as well as node-to-node distances. It must be noted that in the present model, each pin can have up to six azimuthal segments, depending on its position within the pin bundle. The fuel pins in the bundle periphery have five azimuthal segments, whereas the interior fuel pins have six azimuthal segments. This type of discretization is chosen such that each azimuthal in the pin is connected to a subchannel in the coolant domain. An energy balance for the control volume in Figure 2.2b results in an equation of the form shown in Equation 2.1, which provides the temperature for node *P*.

$$\rho \cdot c \cdot \Delta r \cdot r_P \cdot \Delta\theta \cdot \Delta z \cdot \frac{T_P^0 - T_P}{\Delta t} + \frac{k_e \cdot \Delta r \cdot \Delta z}{r_e \cdot (\delta\theta)_e} \cdot (T_E - T_P) + \frac{k_w \cdot \Delta r \cdot \Delta z}{r_w \cdot (\delta\theta)_w} \cdot (T_W - T_P) +$$

$$\frac{k_n \cdot r_n \cdot \Delta\theta \cdot \Delta z}{(\delta r)_n} \cdot (T_N - T_P) + \frac{k_s \cdot r_s \cdot \Delta\theta \cdot \Delta z}{(\delta r)_s} \cdot (T_S - T_P) + \frac{k_t \cdot \Delta r \cdot r_P \cdot \Delta\theta}{(\delta z)_t} \cdot (T_T - T_P)$$

$$+ \frac{k_b \cdot \Delta r \cdot r_P \cdot \Delta\theta}{(\delta z)_b} \cdot (T_B - T_P) + q''' \cdot \Delta r \cdot r_P \cdot \Delta\theta \cdot \Delta z = 0 \qquad (2.1)$$

The upper case subscripts (*E, W, N, S, T, B* and *P*) in Equation 2.1 correspond to the nodal values, whereas the lower case subscripts (*e*, *w*, *n*, *s*, *t* and *b*) represent the corresponding control volume interface. It must be noted that the volume of the control volume shown in Figure 2.2b is represented by the term $\Delta r \cdot r_P \cdot \Delta\theta \cdot \Delta z$ in Equation 2.1 as the node *P* lies midway between control volume interfaces *n* and *s*. For cases in which the node *P* does not lie between *n* and *s*, the volume should be calculated as $\Delta r \cdot (r_n + r_s) \cdot 0.5 \cdot \Delta\theta \cdot \Delta z$. A similar consideration also applies for the area terms that appear in the heat flow equations in the top and bottom directions. The key assumptions in the conduction model include (1) fuel is homogenous, (2) constant heat generation in the active fuel control volumes shown in Figure 2.2a, and (3) thermal conductivity is only dependent on temperature. It can also be noted from Equation 2.1 that a fully-implicit formulation is used to calculate the temperature of node *P*. All the temperatures of the neighboring nodes in Equation 2.1 are current time step values (indicated without any superscript), while the temperature of node *P* from previous time step appears in the first term (indicated with a 0 superscript.) The computations start with initial guesses (or previous time step values) for thermal conductivities, which are updated based on the calculated temperatures. Iterations are performed until the maximum difference in temperatures between successive iterations is less than 10^{-6}°C. A similar modeling procedure is used for the non-fuel pins (moderator, poison, etc.) in the pin bundle. A simplified representation of a fully inserted control rod is used for all the cases presented in this study, and the relative position or the insertion/retraction of control rods is not modeled. This control rod simplification is not expected to significantly change the temperature, pressure and flow rate predictions, or the core transient response predicted by the thermal hydraulic model.

For the layered TRISO fuel particle, the dimensions of the UCO fuel kernel, buffer, inner pyrolytic carbon (PyC), silicon carbide and outer PyC regions, along with the associated density values are shown in Table 2.2.

Table 2.2: TRISO fuel dimensions and density values

Material	Inner radius (micron)	Outer radius (micron)	Density (kg m^{-3})
UCO	0	250	10970.0
Buffer	250	350	1050.0
Inner PyC	350	390	1900.0
Silicon carbide	390	425	3190.0
Outer PyC	425	465	1900.0

All the dimensions, and all the density values except that of the (UCO) kernel shown in Table 2.2 are from the pre-conceptual design report (Greene et al., 2011). Based on the recommendation from the core design benchmark study for the modular high-temperature gas-cooled reactor (MHTGR) (OECD, 2018), the density of uranium dioxide (UO_2) is used instead of UCO in the present study, as UCO properties are not currently available. The UO_2 density shown in Table 2.2 is from the MHTGR benchmark study.

Using a volumetric packing fraction of 0.5 as indicated in the pre-conceptual design report for this SmAHTR configuration, and the density of the graphite matrix as 1740 kg

m^{-3} (OECD, 2018), the effective density of the active fuel region in the fuel compact is calculated using Equation 2.2.

$$\rho_{eff} = \frac{\int \rho \cdot dV}{\int dV} \tag{2.2}$$

The effective specific heat capacity for the active fuel region in the fuel compact is calculated using Equation 2.3.

$$c_{eff} = \frac{\int \rho \cdot c \cdot dV}{\int \rho \cdot dV} \tag{2.3}$$

The temperature-dependent specific heat correlations for all regions shown in Table 2.2 are taken from the MHTGR benchmark study (OECD, 2018). The specific heat correlation for the graphite matrix is taken from the study of Johnson et al. (2009).

The effective thermal conductivity for the homogenous TRISO fuel is determined using the methodology described in the advanced gas reactor (AGR) fuel development report (Collin, 2015). In this approach, the thermal conductivity of the graphite matrix obtained from the work of Gontard and Nabielek (1990) as shown in Equation 2.4 is combined with the homogenized TRISO particle thermal conductivity from the work of Folsom (2012) using the approach outlined by Gonzo (2002) as shown in Equation 2.5. The neutron fluence and density correction terms for the graphite matrix are neglected. The effect of neutron fluence is neglected as the analyses in this study pertain to the fresh core. However, the effects of burnup on the thermal conductivity of the graphite can be readily incorporated by including the neutron fluence correction term in Equation 2.4.

$$k_{matrix} = 47.4 \cdot \{1 - 9.7556 \cdot 10^{-4} \cdot (T - 100) \cdot \exp(-6.036 \cdot 10^{-4} \cdot T)\} \qquad (2.4)$$

$$\frac{k_{eff}}{k_{matrix}} = \frac{1 + 2 \cdot \sigma \cdot \varphi + (2 \cdot \sigma^3 - 0.1 \cdot \sigma) \cdot \varphi^2 + 0.05 \cdot \varphi^3 \cdot \exp(4.5 \cdot \sigma)}{1 - \sigma \cdot \varphi} \qquad (2.5)$$

Apart from the fuel pins, the thermophysical properties for Graphite H-451 are used for all other graphite regions in the core. The density and thermal conductivity of Graphite H-451 are taken from the MHTGR benchmark study (OECD, 2018). The specific heat capacity of Graphite H-451 is from the work of Johnson et al. (2009).

The discretization for the hexagonal graphite reflectors is shown in Figure 2.3. A control volume, along with an interior node and a boundary node are also highlighted in the figure.

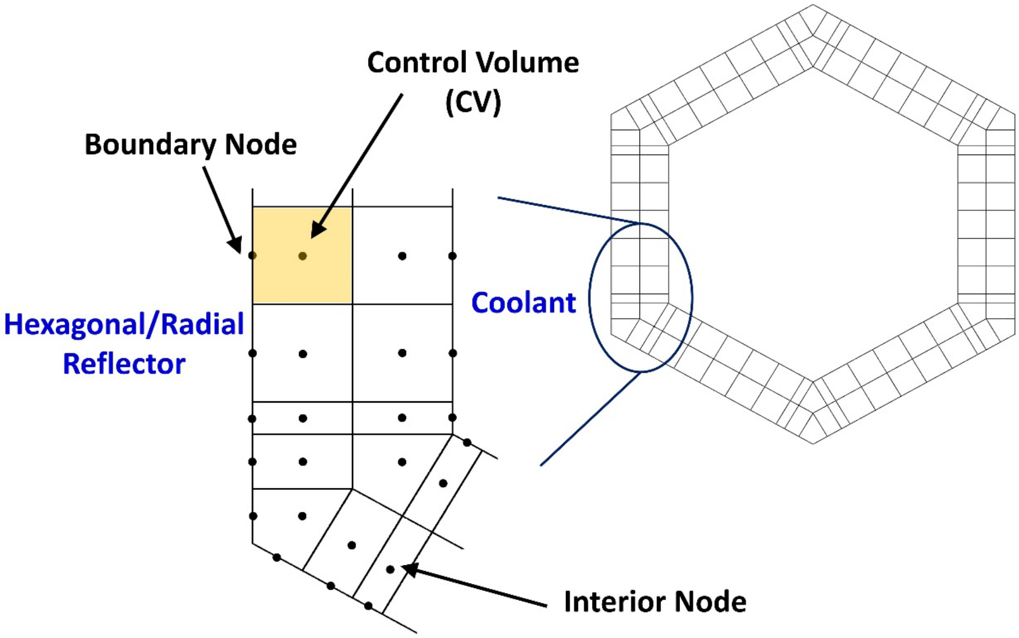

Figure 2.3: Hexagonal reflector discretization

The inner surfaces of each hexagonal reflector face the coolant subchannels, while the outer surfaces are in contact with the neighboring hexagonal reflector or the radial reflector. The contact resistance between adjacent hexagonal reflectors and between radial and hexagonal reflectors is also addressed, using a nominal contact conductance value of 10,000 W m^{-2} K^{-1}, which is chosen based on the general range for contact conductance values in Bergman et al. (2011). Performing an energy balance on each control volume shown in Figure 2.3 results in an equation similar to that of Equation 2.1. It must be noted that the nodes on inner and outer boundaries of the hexagonal reflector represent control volumes with zero thickness, and therefore do not have any storage and generation terms. The energy balance for the boundary control volumes therefore reduces to a surface energy balance. Also, while the non-fuel regions including moderator pins and the reflector regions would have heat generation due to phenomena such as gamma heating, this is not considered in the present study, and all the energy generated due to fission is assumed to be deposited on the fuel pins. The fission energy deposited on moderator, coolant, and other core supporting structures is typically ~2-3% for light water reactors (Masterson, 2019), and is expected to be in the similar range for FHRs. Assuming 100% energy deposition on fuel pins will provide conservative estimates for the peak fuel temperatures during both normal and the postulated accident scenarios.

Figure 2.4a shows the radial reflector from the pre-conceptual design. To enable the use of simple control volume geometries, a modified form of the radial reflector (Figure 2.4b) is considered in the present study. The density of the radial reflector material (graphite) is adjusted in the new design such that the thermal mass of the modified radial reflector ($\rho \cdot V \cdot c$) is the same as that of the original design. Figure 2.4c shows the discretization for the radial reflector. A control volume, an interior node, and a boundary node are also highlighted in the figure. The inner surfaces of the radial reflector face the hexagonal reflectors while the outer surfaces of the radial reflector region face the coolant in the downcomer region. For laminar heat transfer in the downcomer region, the Nusselt number value for the annulus from the work of Lundberg et al. (1963) is used. For the turbulent flow regime, the Dittus and Boelter correlation (Bergman et al., 2011) is used. A logarithmic interpolation is performed to calculate the Nusselt numbers in the transition flow regime.

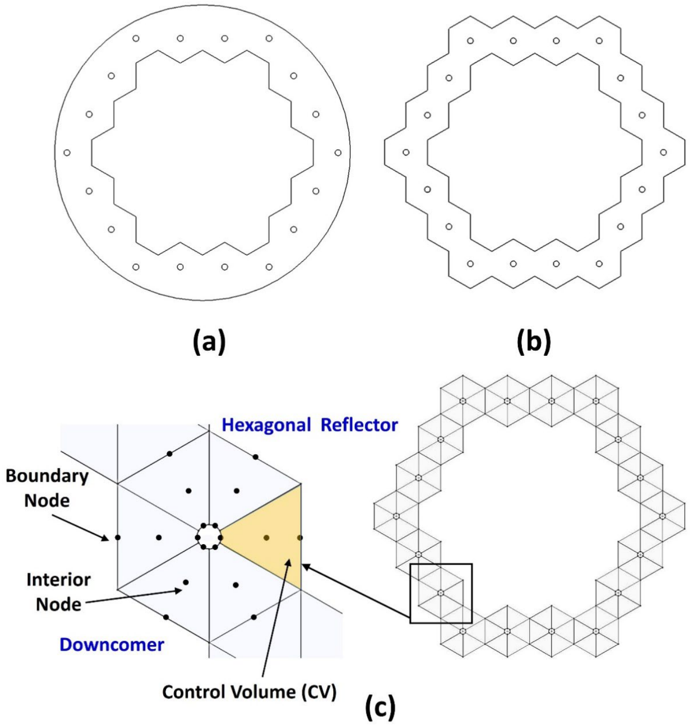

Figure 2.4: Radial reflector (a) original design, (b) simplified design, and (c) discretization

Performing an energy balance for each control volume results in an equation similar to that of the form of Equation 2.1 (the heat generation term is not included in the present study, as all the fission power is assumed to be deposited on the active fuel region of the fuel pins.)

Figure 2.4c also shows the coolant channels in the radial reflector region. The heat transfer from/to each coolant channel is calculated using the nearest radial reflector node temperature, the mean temperature of the coolant through the radial reflector channel, and heat transfer coefficient through the radial reflector coolant channel. For the forced flow cases for the solid pin-fueled configuration in the present study, the total coolant flow rate through the channels in the radial reflector region is set to a nominal value of 20 kg s^{-1} (this is ~1-2% of the core inlet flow rates considered in this study.)

2.2.2 Fluid region model

The fluid region model provides the temperature, flow, and pressure profiles for the FLiBe coolant region in the core. The coolant flowing through the pin bundles is modeled using the conventional subchannel approach, in which the pin bundle channel is subdivided into coolant-centered 'edge', 'corner', and 'interior' subchannels, and the resulting conservation equations are systematically solved. In this approach, closure models are needed to quantify the different momentum and energy transport phenomena and close the system of equations. The details of the discretization, conservation equations and the closure models are discussed in this subsection.

The coolant region discretization for a single fuel assembly is similar to the one shown in Figure 1.6. The appropriate forms of mass, energy, axial momentum and lateral momentum equations, derived based on assumptions applicable to the subchannel model (Stewart et al., 1977) are discussed next.

The transient mass conservation equation is shown in Equation 2.6.

$$A_i \cdot \frac{\partial}{\partial t}(\rho_i) + \frac{\partial m_i}{\partial z} + \sum_{j=1}^{J} w_{ij} = 0 \qquad (2.6)$$

In the above equation, t is time, A_i and ρ_i are the flow area and density of the fluid in subchannel *i* respectively, *z* is the axial coordinate, m_i is the axial mass flow rate of coolant in subchannel i, and w_{ij} is the lateral flow rate per unit length from subchannel i to neighboring subchannel *j*.

The transient energy conservation equation is shown in Equation 2.7.

$$A_i \cdot \frac{\partial}{\partial t}(\rho_i \cdot h_i) + \frac{\partial}{\partial z}(m_i \cdot h_i) + \sum_{j=1}^{J} (w \cdot h^*)_{ij} + \sum_{j=1}^{J} w_{ij}'^{H} \cdot (h_i - h_j) - \sum_{k=1}^{K} q'_{solid,k} = 0 \qquad (2.7)$$

The energy equation includes energy storage in subchannel *i*, axial transport of enthalpy, lateral transport of energy due to crossflow and turbulent exchange, and heat transfers from/to solid structures connected to the subchannel. In Equation 2.7, h_i is the enthalpy of the coolant in subchannel i, $w_{ij}'^{H}$ is the turbulent mixing rate for energy between subchannels *i* and *j*, and $q'_{solid,k}$ is the linear heat rate from solid *k*. The heat transfer from solid to fluid is quantified using Newton's law of cooling. The enthalpy transported due to crossflow is taken to be the enthalpy of the subchannel at which the crossflow originates (denoted by the starred term). The axial conduction term is neglected in Equation 2.7 as the product of *Re* and *Pr* numbers is typically large due to the relatively high *Pr* for the FLiBe salt. The viscous dissipation term is neglected as the heat input to the subchannel from fuel pins and other heat transfers (due to cross flow and mixing) are significantly larger than the heat generation due to viscous dissipation. Similarly, the terms representing the pressure-volume work for the fluid as well as work terms due to viscous and body forces are also neglected due to these values being substantially lower than the heat input from the fuel pins and other heat transfers.

$$A_i \cdot \frac{\partial}{\partial t}(\rho_i \cdot u_i) + \frac{\partial}{\partial z}(m_i \cdot u_i) + \sum_{j=1}^{J}(w \cdot u^*)_{ij} + \sum_{j=1}^{J} w_{ij}'^{M} \cdot (u_i - u_j)$$

$$+A_i \cdot \left\{\frac{\partial P_i}{\partial z} + \frac{\rho_i \cdot u_i \cdot |u_i|}{2} \cdot \left(\frac{f_{axi}}{D_{h,i}} + K'_{form}\right) + \rho_i . g\right\} = 0 \qquad (2.8)$$

The axial momentum conservation in Equation 2.8 includes temporal acceleration due to axial velocity change, momentum fluxes in axial and lateral directions due to motion in the axial direction along with turbulent exchange, pressure and body forces, and frictional losses. In Equation 2.8, for subchannel i, u_i is the axial velocity of the coolant, $w_{ij}'^{M}$ is the turbulent mixing rate for momentum between subchannels i and j, P_i is the coolant pressure, f_{axi} is the axial friction factor, $D_{h,i}$ is the subchannel i hydraulic diameter, K'_{form} is the form loss coefficient per unit length (this is set to zero for the bare rod bundle considered in this study), and g is acceleration due to gravity. The axial velocity transported due to crossflow is denoted by the starred term. The change in subchannel flow area in the axial direction is not included in the present model.

$$s \cdot \frac{\partial}{\partial t}\left(\rho_{ij}^* \cdot v_{ij}\right) + \frac{\partial}{\partial z}(u^* \cdot w)_{ij} - \frac{s}{l}\left(P_i - P_j\right) + \frac{1}{2} \cdot K_{gap} \cdot \frac{w_{ij} \cdot |w_{ij}|}{\rho_{ij}^* \cdot s \cdot l} = 0 \qquad (2.9)$$

The lateral momentum conservation in Equation 2.9 includes temporal acceleration due to crossflow velocity change, lateral momentum flux due to axial motion, the lateral pressure gradient, and flow resistance terms. In Equation 2.9, s is the gap between the pins, v_{ij} is the crossflow velocity of flow through the gap connecting subchannels i and j, l is the length of the lateral control volume, and K_{gap} is the lateral resistance. The axial velocity and coolant density transported due to crossflow are denoted by the starred terms. For crossflow at an axial location z, the pressures for subchannels i and j shown in Equation 2.9 correspond to the values at an axial location of z-1.

The subchannels are discretized in the axial direction with a finite axial length Δz, and the differential equations (Equations 2.6-2.9) are converted into their finite difference forms. Figure 2.5 shows an axially discretized interior subchannel control volume used in deriving the finite difference equations for mass, energy, and axial momentum.

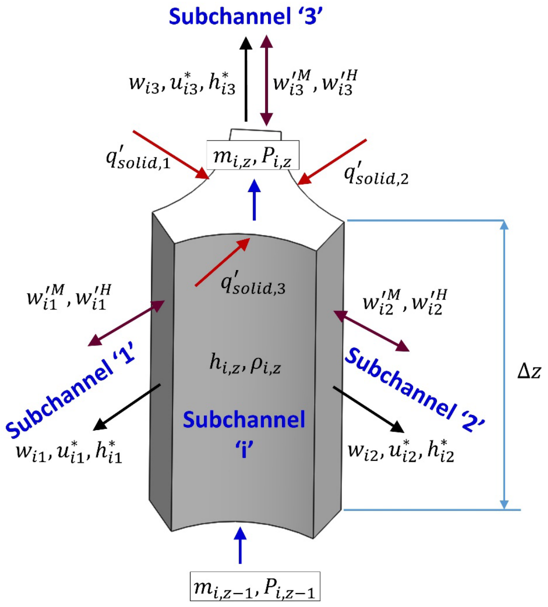

Figure 2.5: Subchannel axial control volume

The terms for crossflow, turbulent mixing, and linear heat rate shown in Figure 2.5 correspond to the axial location *z*. It should be noted that Equations 2.6-2.9 are already discretized in the lateral direction. The finite difference form of these equations is derived using appropriate area- and volume-averaged terms, employing backward spatial derivatives and an upwind scheme (Patankar, 2018) for the convective terms. A fully implicit formulation is used for the temporal discretization of Equations 2.6-2.9.

The lateral control volume for the subchannel is shown in Figure 2.6.

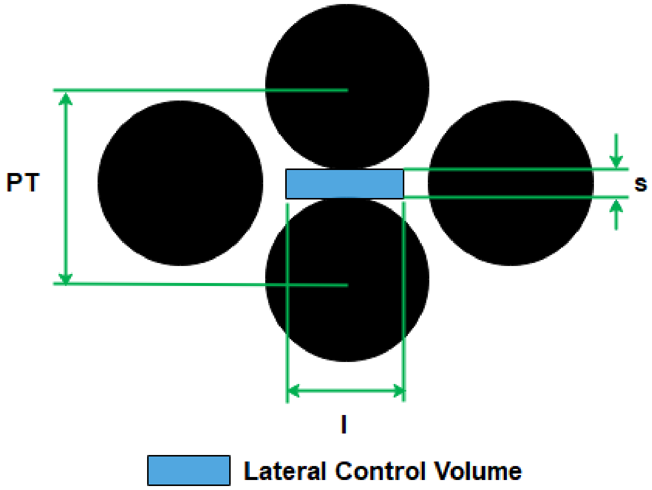

Figure 2.6: Subchannel lateral control volume

The boundary conditions for the subchannel model are zero inlet crossflow, zero radial pressure gradient at the exit, and specified subchannel mass flow rate and enthalpy at the inlet. The individual subchannel mass flow rates can be determined from the total core mass flow rate by using a uniform mass flux condition at the inlet of the core. The total flow rate into all the control rod annulus regions in the core is set to a small fraction (~0.1 %) of the total core inlet flow rate. The present model also has the option to determine the flow distribution by enforcing equal pressure drop across all the fuel assemblies in the core. This mass flow distribution procedure is discussed in Section 2.2.2.6. For the other fluid regions in the core (control rod guide tube annulus, and the radial reflector coolant channels shown in Figure 1), the 1-D version of the fluid region thermal hydraulic model described in this subsection is solved.

In addition to the thermophysical properties of the FLiBe coolant, the subchannel-based fluid region model requires closure relations for axial friction factor, heat transfer coefficient, lateral resistance, and turbulent mixing to close the system of equations. These are discussed next.

2.2.2.1 FLiBe thermophysical properties

The thermophysical properties of the FLiBe coolant recommended in the work of Romatoski (2017) are employed. The values and correlations of key properties are listed in Table 2.3.

Table 2.3: FLiBe thermophysical properties (temperatures in °C)

Property	Correlation/Value
Density (kg m^{-3})	$2413 - 0.488 \cdot (T + 273.15)$
Dynamic viscosity (kg m^{-1} s^{-1})	$0.000116 \cdot \exp\{3755/(T + 273.15)\}$
Thermal conductivity (W m^{-1} K^{-1})	1.1
Specific heat capacity (J kg^{-1} K^{-1})	2386

2.2.2.2 Axial friction factor

For the different subchannels in the pin bundle, the application of friction factor, heat transfer and mixing correlations requires the knowledge of whether the axial flow is in the laminar, transition or turbulent regime. The critical Reynolds numbers for each type of subchannel is calculated from an empirically determined transition *Re* for the pin bundle using the approach of Cheng and Todreas (1986). In this approach, the critical transition Reynolds numbers for laminar-to-transition flow and transition-to-fully turbulent flow for the pin bundle are first determined using the empirical correlations shown in Equations 2.10 and 2.11.

$$\log_{10}\left(\frac{Re_{b,L}}{300}\right) = 1.7 \cdot \left(\frac{PT}{D_{pin}} - 1\right) \tag{2.10}$$

$$\log_{10}\left(\frac{Re_{b,T}}{10000}\right) = 0.7 \cdot \left(\frac{PT}{D_{pin}} - 1\right) \tag{2.11}$$

In the above equations, $Re_{b,L}$ and $Re_{b,T}$ are the critical bundle Reynolds numbers for laminar-to-transition and transition-to-fully turbulent flow, respectively. The term PT is the pin pitch, and D_{pin} is the pin diameter. The critical transition *Re* values for each type of subchannel (corner, edge, and interior) are then determined using Equations 2.12 and 2.13.

$$Re_{s,L} = Re_{b,L} \cdot \frac{D_{h,s}}{D_{h,b}} \cdot X_{s,L} \tag{2.12}$$

$$Re_{s,T} = Re_{b,T} \cdot \frac{D_{h,s}}{D_{h,b}} \cdot X_{s,T} \tag{2.13}$$

where s is the type of channel (corner, edge, or interior), $D_{h,s}$ and $D_{h,b}$ are the hydraulic diameters of the subchannel and bundle, and $X_{s,L}$ and $X_{s,T}$ are the 'flow split parameters'. The flow split parameter for a subchannel of type s is defined as

$$X_s = \frac{u_s}{u_b} \tag{2.14}$$

Where u_s is the axial coolant velocity of the subchannel, and u_b is the axial velocity of the bundle. The values of $X_{s,L}$ and $X_{s,T}$ for the three different types of subchannels (corner, edge, and interior) are determined by assuming that all the subchannels are in the same flow regime as that of the pin bundle, enforcing equal pressure drop across all the subchannels in the bundle, and using mass continuity. The expressions for determining the flow split parameters for the laminar and fully turbulent flow regimes are provided in Cheng and Todreas (1986).

The subchannel friction factors for the laminar and turbulent flow regimes are determined using Equations 2.15 and 2.16 respectively.

$$f_{axi,s,L} = \frac{C_{s,L}}{Re_s} \tag{2.15}$$

$$f_{axi,s,T} = \frac{C_{s,T}}{Re_s^{0.18}} \tag{2.16}$$

The constants $C_{s,L}$ and $C_{s,T}$ are calculated using the methodology from Cheng and Todreas (1986) for corner, edge, and interior subchannels. For the transition flow regime, the friction factor correlation is given by

$$f_{axi,s,TR} = f_{axi,s,L} \cdot (1 - \psi_s)^{\gamma} + f_{axi,s,T} \cdot \psi_s^{\gamma} \tag{2.17}$$

where γ is the exponent (with a value of 1/3), and the value of ψ_s, the intermittency factor for subchannel s, is given by

$$\psi_s = \frac{\log_{10}(Re_s) - \log_{10}\left(Re_{s,L}\right)}{\log_{10}\left(Re_{s,T}\right) - \log_{10}\left(Re_{s,L}\right)} \tag{2.18}$$

The isothermal friction factors obtained from the above correlations are then corrected to account for wall property variations using the correlations from Kakac et al. (1987).

It should be noted that the present model considers a bare pin bundle, as the pre-conceptual design for SmAHTR does not include specifications for spacers and other core support structures. However, the subchannel model described here can be readily extended to include the impact of spacers and other structures on the thermal hydraulic performance of the core. To include grid spacers along the length of the core, a coefficient or a correlation for the form loss needs to be specified at the appropriate subchannel axial control volumes. For wire wrap spacers, the axial friction factor model from Cheng and Todreas (1986) model used in the present study can be readily modified to include the additional flow resistance due the spacer wire.

2.2.2.3 Heat transfer coefficient

Due to the lack of subchannel-specific heat transfer correlations for the subchannel geometry, correlations originally developed for circular tubes are typically used in subchannel models. The heat transfer correlations in this study also include the impact of thermal development length, as the Prandtl number of the FLiBe salt at the inlet of the core is ~15. These heat transfer correlations for the different flow regimes are based on the recommendations from the work of Romatoski (2017) for the circular channels in the prismatic FHR design. For the laminar flow regime, the Sieder and Tate (1936) correlation is used.

$$Nu_s = 1.86 \cdot \left\{ Re_s \cdot \mathrm{Pr}_s \cdot \left(\frac{D_{h,s}}{L_s} \right) \right\}^{\left(\frac{1}{3}\right)} \tag{2.19}$$

where Re_s and Pr_s are the subchannel Reynolds and Prandtl numbers, $D_{h,s}$ and L_s are the hydraulic diameter and axial distance from the inlet for the subchannel. To ensure that the laminar flow *Nu* correlation reduces to the fully developed laminar flow value for long axial lengths from the inlet, the following logical statement is implemented.

$$Nu_s = \max(\text{Equation } 2.19, 4.36) \tag{2.20}$$

For the transition flow regime, the subchannel model has two different options for the heat transfer correlation. The first option is the Hausen correlation (Romatoski, 2017).

$$Nu_s = 0.116 \cdot \left(Re_s^{\left(\frac{2}{3}\right)} - 125 \right) \cdot \mathrm{Pr}_s^{\left(\frac{1}{3}\right)} \cdot \left[1 + \left(\frac{D_{h,s}}{L_s} \right)^{\left(\frac{2}{3}\right)} \right] \tag{2.21}$$

The second option is to use the Gnielinski (1976) correlation, with the term to account for the thermal entrance effect in the Gnielinski (1976) correlation taken from the work of Romatoski (2017).

$$Nu_s = \frac{\left(\frac{f_{axi,s}}{8} \right) \cdot (Re_s - 1000) \cdot \mathrm{Pr}_s}{1 + 12.7 \cdot \left(\frac{f_{axi,s}}{8} \right)^{\left(\frac{1}{2}\right)} \cdot \left(\mathrm{Pr}_s^{\left(\frac{2}{3}\right)} - 1 \right)} \cdot \left[1 + \left(\frac{D_{h,s}}{L_s} \right)^{\left(\frac{2}{3}\right)} \right] \tag{2.22}$$

Equation 2.22 is also used for the fully turbulent flow regime. The axial friction factors in the above equation are calculated using the Cheng and Todreas (1986) model discussed in the previous section. It should be noted that the transition from laminar flow for circular tubes occurs at a substantially higher Reynolds number (2300) compared to the subchannels, while it can be as low as 250 for the rod bundle pitch-to-diameter ratio of 1.175 investigated in this study. The Hausen and Gnielinski correlations shown in Equations 2.21 and 2.22 in fact will yield negative *Nu* values when the *Re* values are less than ~1400 and 1000, respectively. To ensure that there are no physically unrealistic *Nu* (such as negative values or values lower than the laminar flow *Nu*), logical statements are implemented in the model to return the maximum of laminar and transition *Nu* values for *Re* values up to 2300. The isothermal heat transfer coefficients obtained from the above correlations are then corrected to account for wall property variations using the correlations from Kakac et al. (1987). For the circular coolant channels in the radial reflector region, the Sieder and Tate correlation (Equation 2.19) is used for the laminar flow regime. For the transition and turbulent flow regimes, the Gnielinski correlation (Equation 2.22) is used. For the guide tube annulus in the control rod assembly, the laminar Nusselt number from the work of Lundberg et al. (1963) is used, and the Gnielinski correlation (Equation 2.22) is used for the transition and turbulent flow regimes, but without the thermal entrance term. The thermal entrance effects are neglected for the guide tube annulus as the hydraulic diameter of the annulus is small (0.001 m).

2.2.2.4 Lateral crossflow resistance

There are two options for quantifying the lateral crossflow resistance between adjacent subchannels. The first option is the Gunter and Shaw (1945) correlation without the viscosity correction. The gap resistance in this model is defined as

$$K_{gap} = f_{gap} \cdot \left(\frac{l}{D_v}\right) \cdot \left(\frac{D_v}{PT}\right)^{0.4} \cdot \left(\frac{l}{s}\right) \tag{2.23}$$

where f_{gap} is the crossflow frictional resistance for the gap between the pins, l is the length of the lateral control volume, D_v is the volumetric hydraulic diameter, PT is the pin pitch distance, and s is the gap between the pins. The volumetric hydraulic diameter is given by

$$D_v = \frac{4 \cdot V_{free}}{A_{fric,surf}} \tag{2.24}$$

Where V_{free} is the free volume of the coolant and $A_{fric,surf}$ is the frictional surface area. The gap frictional resistance is given by

$$f_{gap} = \begin{Bmatrix} 180/Re_{D_v} & ; Re_{D_v} \leq 200 \\ 1.92/Re_{D_v}^{0.145} & ; Re_{D_v} > 200 \end{Bmatrix} \tag{2.25}$$

The other option for modeling crossflow resistance is to set the value to a constant of 0.5, similar to the approach used in the COBRA-IV model (Stewart et al., 1977). For the predominantly axial flow situations encountered in the conditions investigated in the present study, the actual value of crossflow resistance is expected to have an insignificant impact on quantities of interest such as peak fuel temperatures, core pressure drop, etc. This is demonstrated in Section 4.2, in which the steady-state results for a case with crossflow resistance calculated from the Gunter and Shaw correlation are compared with the results from a case in which the crossflow resistance is set to a constant value of 0.5 is used. Using a constant value of crossflow resistance aids in reducing the computational effort expended in computing the crossflow resistances, which is especially advantageous while running transient simulations.

2.2.2.5 Turbulent mixing

For turbulent mixing between interior subchannels, the turbulent mixing rate is determined using the correlation suggested in the work of Kawahara et al. (2006), due to its applicability for the transition flow regime and tight rod bundles. In this model, the total turbulent mixing rate is calculated as the sum of turbulent diffusion (w'_{TD}) and convective transfer (w'_{CT}) components, as shown in Equation 2.26.

$$w' = w'_{TD} + w'_{CT} \tag{2.26}$$

The turbulent diffusion component is a function of coolant density (ρ), eddy diffusivity (ε), and subchannel geometry factor (F^*) as depicted in Equation 2.27.

$$w'_{TD} = \frac{\rho \cdot \varepsilon}{2 \cdot F^*} \tag{2.27}$$

The convective component is calculated using Equation 2.28, which is a function of the mixing Stanton number (β), and the subchannel mass flux (G). The values for the eddy diffusivity, subchannel geometry factor, and mixing Stanton number are calculated using the expressions from Kawahara et al. (2006).

$$w'_{CT} = \beta \cdot s \cdot G \tag{2.28}$$

For turbulent mixing rate for the wall bound subchannels, no specific correlation could be identified, and the Petrunik (1973) correlation (Equation 2.29) is used in the present work following the methodology suggested in the work of Eiff and Lightstone (1997) for non-identical subchannel geometries.

$$w' = 9 \cdot 10^{-3} \cdot \mu \cdot Re^{0.827} \tag{2.29}$$

In the above equation, μ is the dynamic viscosity. It is also assumed that the turbulent mixing rates for momentum and energy are identical, without any correction factor to account for the imperfect analogy between the turbulent transport of energy and momentum. For the thermal mixing between adjacent subchannels, the transport due to molecular diffusion is also included, although the contribution from molecular diffusion is expected to be low due to the relatively low thermal conductivity of the FLiBe coolant (compare to high conductivities of liquid metals such as sodium).

In addition to the molecular and turbulent transport, the presence of elements such as wire wraps will also induce a forced mixing between the subchannels. While forced mixing is not present for the bare rod bundle investigated here, the forced mixing in the presence of wire wrap spacers can be modeled using the correlations provided in the work of Cheng and Todreas (1986).

2.2.2.6 Equal pressure drop scheme for flow distribution

The present model employs a procedure that iteratively adjusts the fraction of the inlet-flow split among the hexagonal pin bundles to achieve equal pressure drop across all channels in the core. The average pressure drop for the pin bundle is determined using the subchannel pressure drops as shown in Equation 2.30.

$$\Delta P_{pin\ bundle} = \frac{\sum \Delta P_{subchannel} \cdot A_{subchannel}}{\sum A_{subchannel}} \tag{2.30}$$

Therefore, the entire pin bundle region in each fuel assembly is treated as a single channel in this procedure. The total inlet mass flow rate through the bundle is the sum of the individual subchannel mass flow rates. This leads to a total of 19 channels (1 channel for each fuel assembly) in the core. In this flow rate adjustment procedure, the total pressure drop is calculated for two different inlet mass flow rates, $m_n^{(0)}$and $m_n^{(1)}$, where subscript n refers to channel number and superscripts (0) and (1) refer to mass flow rate value. A linear relationship between the pressure drop and mass flow rate is established as shown in Equation 2.31.

$$\Delta P_n^{(k)} = B_n + C_n \cdot m_n^{(k)} \tag{2.31}$$

The system of linear equations is solved for each channel to obtain B_n and C_n values. If a channel pressure drop value $\Delta P_n^{(2)}$ is known, the mass flow rate for each channel $m_n^{(2)}$ can be estimated using Equation 2.31. Summing Equation 2.31 for all the channels, assuming equal channel pressure drops ($\Delta P_1^{(2)} = \Delta P_2^{(2)} = \cdots = \Delta P_N^{(2)} = \Delta P^{(2)}$), and using the total mass flow rate into the core ($\sum_{n=1}^{N} m_n^{(2)} = m_{total}$), leads to the relation for pressure drop shown in Equation 2.32. The channel mass flow rates estimated using this procedure are then used in the appropriate momentum equations for the subchannels to determine the actual pressure drop. This procedure repeats until all the actual channel pressure drops are within 1 Pa of each other.

$$\Delta P^{(2)} = \frac{m_{total} + \sum_{n=1}^{N} \frac{B_n}{C_n}}{\sum_{n=1}^{N} \frac{1}{C_n}} \tag{2.32}$$

2.2.3 Overall core model

Figure 2.7 shows the model structure for the overall core model. The present model is implemented in the MATLAB (2020) platform. The overall model begins with the specification of the geometry and discretization parameters (number of axial segments, radial segments in the fuel pin, etc.) The numbering of fuel assemblies, as well as fuel and non-fuel pins, and the coolant subchannels within each assembly is then performed. The connections between the different subchannels, and between subchannels and other solid regions (fuel and non-fuel pins, and graphite reflectors) within each fuel assembly are then established. The connections between adjacent hexagonal graphite reflectors, as well as between the hexagonal and radial graphite regions are also established at this stage. The pertinent guess (for steady-state simulations) or initial (for transient simulations) values for the core temperatures, pressures, flow rates, etc., are then specified. The model then enters the transient solver. If a steady-state simulation is to be performed, the time step size is set to a very high value (such as 10^{10} seconds). If a transient simulation is to be performed, an appropriate time step size is used. The model also has the capability to automatically adjust the time step size over the course of the simulation, which is discussed in a later chapter (Section 6.1). With the specification of the time step size, the model then enters an iterative solver, in which computations are performed for all the solid regions in the core to determine the temperature profile and heat input to the subchannels. Parallelization is enabled in MATLAB so that computations can be simultaneously performed for the 19 fuel assemblies (when solving for fuel pin, non-fuel pin and hexagonal reflector temperatures) and the 18 radial reflector control volumes (Figure 2.4). These are also denoted in Figure 2.7.

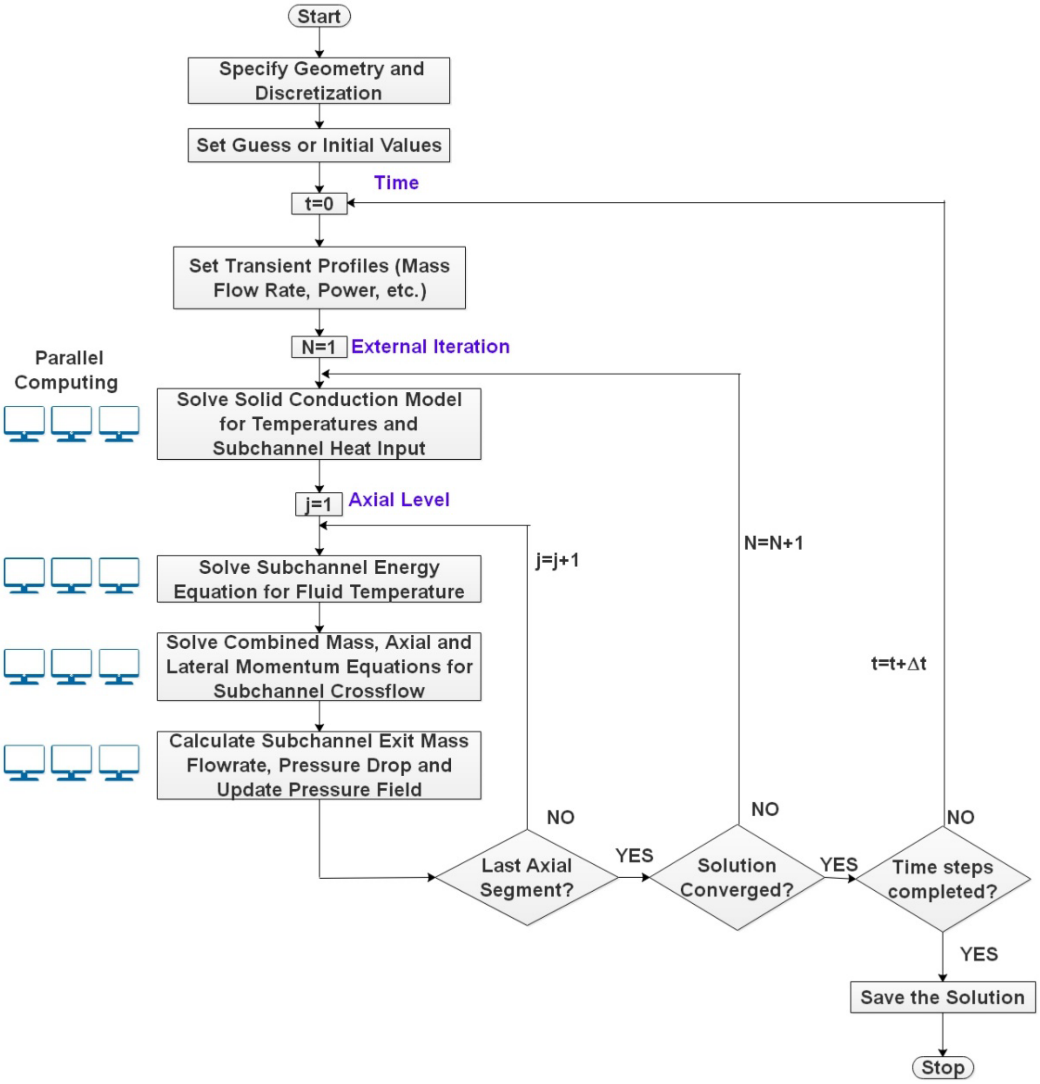

Figure 2.7: Overall core model structure

Following the solid region computations, the model enters a marching scheme in which computations start from the bottom of the core and march axially upwards. At each fluid axial segment or control volume, the energy equation for the subchannels is first solved to determine the fluid temperatures. Following this, quantities such as friction factor, heat transfer coefficient, etc., are also calculated using the updated fluid temperatures. The combined continuity, axial and lateral momentum equations are then solved to obtain the crossflows between the subchannels, and following this, the axial mass flow rate and pressure drop of the subchannels at the axial location are also determined, and the pressure field at this location is updated. The model then marches to the next upward axial segment and continues until reaching the top of the core. All the fluid region computations are also parallelized such that simultaneous computations can be carried out on all the fuel assemblies. At the end of fluid region computations, the solution is checked against the specified convergence criteria to determine convergence. The convergence criterion for subchannel axial mass flow rate is provided in Equation 2.33.

$$\left|\frac{\tilde{m} - m}{m}\right| \leq \epsilon_m \tag{2.33}$$

The mass flow rate with the tilde superscript in Equation 2.33 indicates the value from current iteration. The ϵ_m value is typically set to 10^{-6} for steady-state simulations. For transient simulations, a relatively looser tolerance of 10^{-4} is imposed, which is still considered as a good tolerance value for single-phase fluids in the COBRA-IV manual (Stewart et al., 1977). A similar convergence criterion is also applied for subchannel enthalpy. The crossflow convergence criterion for the present model is shown in Equation 2.34.

$$\left|\frac{\widetilde{w} - w}{w^*}\right| \leq \epsilon_w \tag{2.34}$$

The crossflow convergence criterion in the present model is similar to that of COBRA-IV model, in which the convergence criterion is adapted to the magnitude of crossflow. The starred variable in the denominator in Equation 2.34 indicates the magnitude adapting term, and the definition of this adapting term is provided in Equation 2.35.

$$w^* = 10^{-3} \cdot \left(\frac{\overline{w}}{w_g}\right)^2 + w_g \tag{2.35}$$

The variable with an overbar in Equation 2.35 ($\overline{w}$) represents the arithmetic mean of the crossflows (w_g) across all the gaps in the fuel assembly at a given axial location, and is shown in Equation 2.36.

$$\overline{w} = \frac{1}{N_{gap}} \sum_{g=1}^{N_{gap}} w_g \tag{2.36}$$

It can be seen that for smaller crossflows, the first term in Equation 2.35 becomes larger, leading to a looser convergence requirement compared to only using the value from the previous iteration in the denominator of Equation 2.35. While a convergence condition for the subchannel crossflow can also be imposed with typical tolerances (ϵ_w) such as 0.01 for steady-state cases, using a crossflow constraint has been shown to increase the number of external number iterations per time step during transient simulations. This leads to a substantial increase in the code runtime, although including the crossflow constraint has very little impact on quantities of interest such as temperature, pressure and mass flow rate profiles for the predominantly axial flow cases investigated in the present study. Therefore, a crossflow constraint is not imposed for the accident simulations presented in this study. The relative insensitivity of the model results to the value of crossflow tolerance is also demonstrated for a steady-state case in Section 4.2 of this thesis. In addition to these convergence criteria, the model continues to run until the pressure drops across all the pin bundles in the core are less than 1 *Pa*, if the inlet flow distribution is determined using the equal pressure drop option discussed in Section 2.2.2.6.

If a transient simulation is being performed, after the solution is deemed to be converged at the current time step, the model proceeds to the next time step until the total time step or the total simulation time requirements are satisfied. For a steady-state simulation, the model exits and saves the solution after one time step.

CHAPTER 3. SUBCHANNEL MODEL VERIFICATION AND CODE-TO-CODE COMPARISON

The verification studies for the subchannel-based thermal hydraulic model developed in the previous chapter are discussed in this chapter. The key sub-models in the thermal hydraulic model, such as the conduction model for fuel and non-fuel solid regions, and the mass, momentum, and energy transport models for the fluid region, are first verified individually by comparing the results with the pertinent analytical, numerical, or experimental benchmark data. This is followed by a more comprehensive code-to-code comparison study in which the results from the subchannel-based model are compared with a CFD-based model for 1/12th of a single fuel assembly in the core.

3.1 Sub-model verification

3.1.1 Solid region

For select solid regions in the core, the solution from the finite volume conduction model in the present study is compared with the finite element solution using COMSOL Multiphysics (2018). For the verification of the conduction model employed for the cylindrical regions in the core (such as fuel and moderator pins), a single interior fuel pin with a uniform axial power generation is considered. For both the conduction model in the present study as well as the finite element model in COMSOL, different heat transfer coefficients are applied to the pin at six azimuthal segments to model the variations in the subchannel heat transfer coefficients around the pin periphery. The mean temperature along the axial length is increased from the bottom to the top of the pin to simulate the increase in coolant temperature due to heating from the pin. Figure 3.1a and Figure 3.1b show the boundary conditions applied at the outer surface of the cladding.

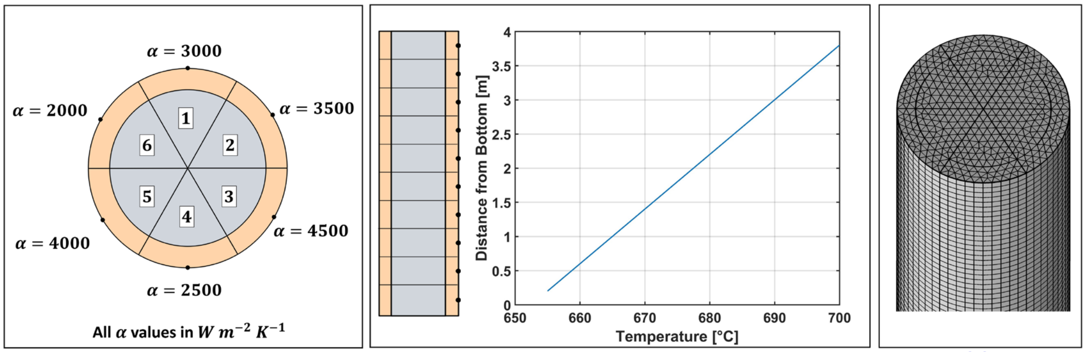

(a) (b) (c)

Figure 3.1: Fuel pin model verification (a) azimuthal boundary condition, (b) axial boundary condition, and (c) COMSOL mesh

The temperature dependent thermal conductivities of the TRISO fuel and cladding regions are provided to COMSOL in the form of a polynomial profile. Grid refinement is performed for the COMSOL solution until the peak temperature change between successive grid refinements is less than 0.1°C. Figure 3.1c shows a representative grid for the COMSOL model. The grid independent mesh employs ~2.2 million triangular prismatic elements with a prescribed element size of 1.5 mm. The pin centerline temperatures at different axial locations from the grid independent COMSOL solution and the predictions of the conduction model in the present study (Figure 3.2) show good agreement. The number of radial segments for the present model shown in Figure 3.2 correspond to the number radial segments in the active fuel region. The cladding region has three radial segments (in addition to the active fuel radial segments) for both the cases shown in the figure.

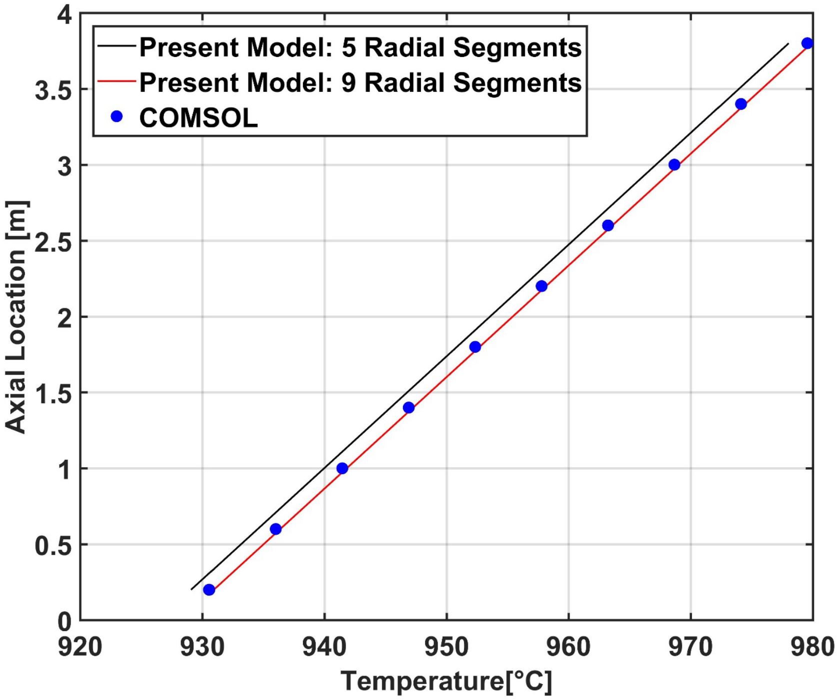

Figure 3.2: Comparison of pin centerline temperatures between the COMSOL and present models

The largest difference in the temperature predictions between the COMSOL model and the present model with fine radial gridding is ~4°C, which occurs at the azimuthal location with the lowest heat transfer coefficient marked as segment "6" in Figure 3.1a. This indicates that good agreement can be achieved with the relatively coarse azimuthal discretization employed in the present model, even for cases with boundary conditions that have extreme azimuthal asymmetry.

In addition to the verification of the conduction model employed for the cylindrical regions in the core (such as fuel and moderator pins), the conduction model employed for non-cylindrical regions such as the hexagonal fuel reflector region is also verified with a COMSOL model. In this case, a single hexagonal reflector with different values for heat transfer coefficient are applied to each inner face is considered, as shown in Figure 3.3a. Additionally, all the inner faces at each 0.8 m length of the 4 m long hexagonal reflector are provided with a constant coolant mean temperature, with values linearly increasing from the bottom to the top of the hexagonal reflector, to simulate the increase in coolant temperature (from 650°C to 700°C) as it flows through the fuel assembly. The outer surface of the hexagonal reflector is maintained at a constant temperature of 600°C throughout the entire length of the hexagonal reflector.

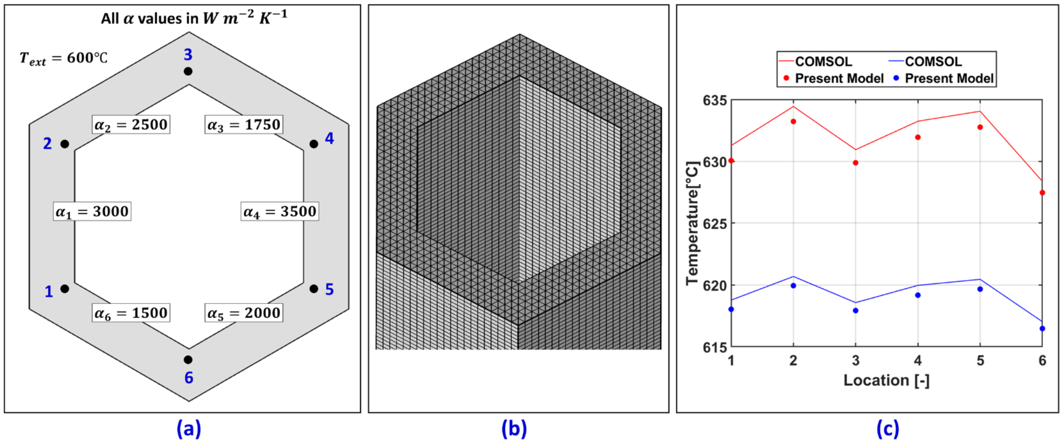

Figure 3.3: Hexagonal reflector: (a) boundary conditions and temperature comparison locations, (b) COMSOL mesh, and (c) temperature comparison between COMSOL and present models

Grid refinement is performed for the hexagonal reflector until the maximum temperature difference between two successive refinements is less than 0.1°C. A representative mesh for the COMSOL hexagonal reflector model is shown in Figure 3.3b. The grid independent mesh employs ~400,000 triangular prismatic elements with a prescribed element size of 12.5 mm. Temperature values are determined at two axial locations (0.2 m and 3.8 m from the bottom of the hexagonal reflector) for the six corner locations shown in Figure 3.3a. The comparison between the COMSOL solution and the present model shown in Figure 3.3c for the temperatures at the corner locations (the blue line and blue circles correspond to 0.2 m axial location, and the red line and red circles correspond to 3.8 m axial location). It can be observed that the present model with a relatively coarse grid provides reasonably good agreement with the high mesh density COMSOL model even for large variations in heat transfer coefficient around the inner faces of the hexagonal reflector.

3.1.2 Fluid region

For the subchannel-based fluid region model, there are two different mechanisms for lateral transport between adjacent subchannels – pressure-driven crossflow and turbulent mixing. To ensure that these two mechanisms are modeled correctly, two different verification tests are performed. The ability of the present subchannel model to predict mass flow distribution is pin bundle geometries is then validated using the single-phase, isothermal datasets from GE 3×3 rod bundle experiments (Lahey Jr. et al., 1970).

The first test is performed to verify the pressure-driven crossflow behavior (the turbulent mixing between adjacent subchannels is turned off in this test). A pair of channels (marked as ‘Channel 1’ and ‘Channel 2’ in Figure 3.4) connected by a gap is considered in this test. The dimensions of Channel 1 are set to values close to that of a typical PWR pin-lattice geometry (Todreas and Kazimi, 2001). Channel 2 has a flow area that is twice that of Channel 1. The wetted perimeter for Channel 1 and Channel 2 are the same; therefore, the hydraulic diameter of Channel 2 is twice that of Channel 1. The coolant used in this test is water, with the outlet pressure set to a value of 155 bar, while the inlet mass flux and temperature are set to 3500 kg m^{-2} s^{-1} and 200°C, respectively. No heat addition is considered in this case (the water remains subcooled throughout the channel length). The geometry and operating conditions for this problem are similar to the one considered in the CTF validation study (Salko et al., 2015).

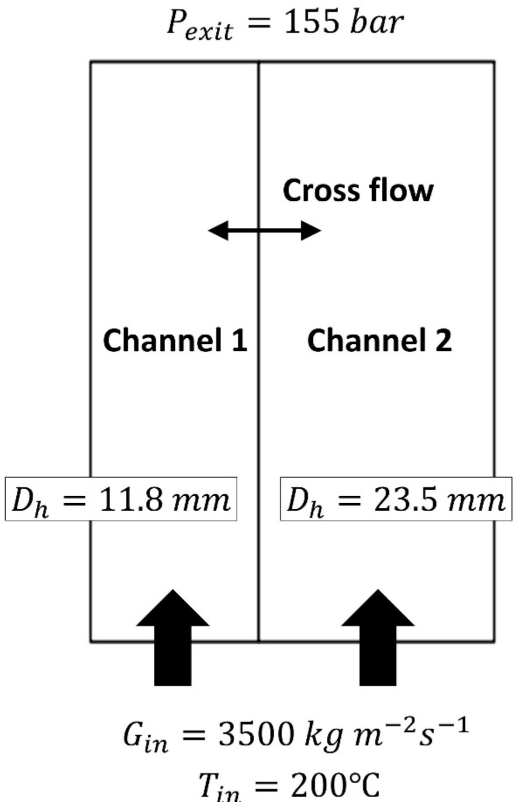

Figure 3.4: Two-channel system for crossflow verification

The velocity at the inlet of both channels is uniform. Due to the isothermal flow, the gravitational pressure drops in both the channels are the same, and acceleration pressure losses are zero. However, due to the difference in the geometry between the two channels, the frictional pressure drop in both the channels is different, which leads to a lateral pressure gradient that causes crossflow between the two channels. As a consequence of this crossflow, the flow velocity increases in the channel with lower hydraulic resistance, while the flow velocity decreases in the channel with higher hydraulic resistance as the flow moves up through the channel. The crossflow continues until the frictional pressure drop is equal in both the channels (as a result of flow redistribution), the point at which the channels are said to have achieved mechanical equilibrium. The channel mass flow rates that would achieve mechanical equilibrium can be analytically estimated by simply equating the channel pressure drops as outlined in the CTF validation study (Salko et al., 2015). The mass flow rate of Channel 2 can be expressed as shown in Equation 3.1.

$$m_2 = \frac{m_{in}}{\left\{1 + \left(\frac{D_{h2}}{D_{h1}}\right)^{\left(\frac{CN-1}{CN+2}\right)} \cdot \frac{A_1}{A_2}\right\}} \tag{3.1}$$

Where D_{h1} and D_{h2} are the hydraulic diameters of Channels 1 and 2, and A_1 and A_2 are the flow areas of Channels 1 and 2 respectively. m_{in} is the total mass flow rate into Channels 1 and 2. The variable CN is the exponent in the friction factor correlation used in this test. The value is set to -0.2, based on the correlation considered in the CTF code (Salko et al., 2015).

The mass flow rate of Channel 1 can then be computed using the mass balance shown in Equation 3.2.

$$m_1 = m_{in} - m_2 \tag{3.2}$$

The mass flux distribution predicted by the present subchannel model for both the channels is shown in Figure 3.5a. The results from the CTF model (Salko et al., 2015) are shown in Figure 3.5b. It should be noted that the mass fluxes plotted in Figure 3.5 are the normalized values shown in Equation 3.3.

$$G_{i,norm} = \frac{G_i - \bar{G}}{\bar{G}} \cdot 100 \tag{3.3}$$

Where G_i is the mass flux of the specific channel i, and $\bar{G}$ is the average mass flux of both channels.

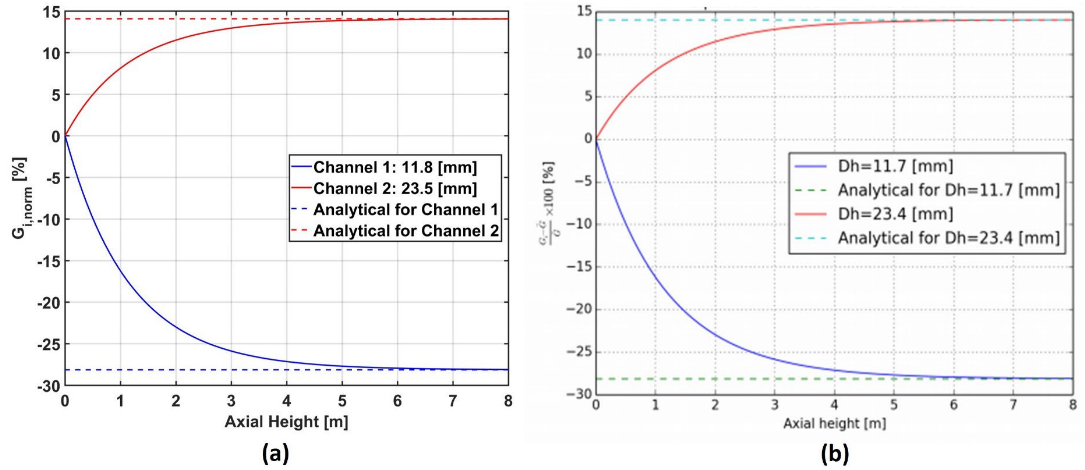

Figure 3.5: Normalized mass flux profile (a) present model, and (b) CTF model (Salko et al., 2015)

It can be seen from Figure 3.5 that the hydraulic diameters of the channels in the present model are slightly different from the one considered in the CTF model. The reason for this small difference is not clear (although both models use the same PWR-lattice geometry.) However, the difference is very small and a comparison between the two models is still valid. From Figure 3.5a, it can be seen that the present model redistributes the flow until the channels reach mechanical equilibrium, after which the mass fluxes approach the analytical values calculated using Equations 3.1 and 3.2. In addition to correctly approaching these analytical values, the axial mass flux profile leading up to the point of mechanical equilibrium predicted by the present model agrees well with the profile predicted by the CTF model. This indicates that the pressure-driven crossflow is correctly modeled in the present subchannel model.

Following the verification of crossflow modeling, the turbulence mixing behavior between adjacent subchannels is verified. For this test, a pair of channels connected by a gap as shown in Figure 3.6 is considered. Channels 1 and 2 have identical geometry, and the area, perimeter, and hydraulic diameter considered are similar to the interior subchannels in the SmAHTR pin bundle geometry.

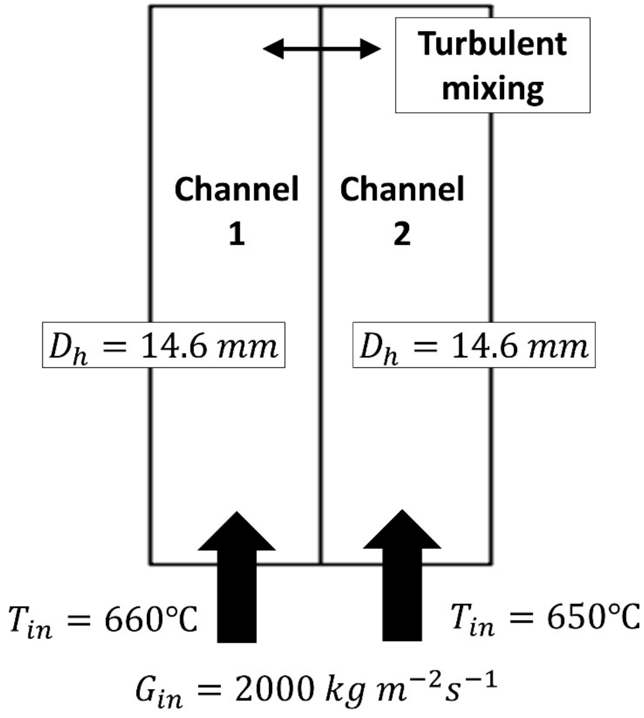

Figure 3.6: Two-channel system for turbulent mixing verification

The inlet mass flux for both channels is set to 2000 kg m^{-2} s^{-1}, while the inlet temperature of Channel 1 is set to 660°C and inlet temperature of Channel 2 is set to 650°C. It must be noted that the temperature-dependent coolant property variations are intentionally not included in this test, and the coolant properties are set to constant values (evaluated at 650°C.) Not including temperature-dependent properties leads to the same frictional pressure drop in each channel (as both the channels have the mass flux and geometry), which in turn effectively turns off lateral pressure-driven crossflow. This now allows turbulent mixing to be the only lateral transport mechanism between the adjacent subchannels. The energy equation for Channels 1 and 2 are shown in Equations 3.4 and 3.5 respectively.

$$m_1 \cdot \frac{d}{dz}(h_1) + W_{12}'^{H} \cdot (h_1 - h_2) = 0 \tag{3.4}$$

$$m_2 \cdot \frac{d}{dz}(h_2) - W_{12}'^{H} \cdot (h_1 - h_2) = 0 \tag{3.5}$$

Where m_1 and m_2 are the mass flow rates for Channels 1 and 2 respectively. The values of m_1 and m_2 are identical in this test. The terms h_1 and h_2 are the enthalpies of Channels 1 and 2 respectively. The term z is the axial coordinate. The term $W_{12}'^{H}$ is the mixing rate of energy per unit length between Channels 1 and 2. A relatively simple form of expressing $W_{12}'^{H}$ is shown in Equation 3.6.

$$W_{12}'^{H} = \beta \cdot s \cdot \bar{G} \tag{3.6}$$

Where β is the mixing coefficient, and s and $\bar{G}$ are the gap width between Channels 1 and 2 and area-weighted average mass flux, respectively. A nominal value of 0.0035 is used for β. The actual value of β depends on multiple factors such as geometry of the bundle, coolant properties, operating conditions, etc. However, the actual value of β and hence $W_{12}'^{H}$ are not important for this test as long as the same values are used in both the subchannel model and the analytical solutions to the linear, first-order ordinary differential energy equations (Equations 3.4 and 3.5) for Channels 1 and 2. These solutions are shown in Equations 3.7 and 3.8.

$$h_1 = \frac{\left(h_{1,in} + h_{2,in}\right)}{2} - \frac{\left(h_{2,in} - h_{1,in}\right)}{2} \cdot \exp\left(\frac{-2 \cdot W_{12}'^{H}}{m} \cdot z\right) \tag{3.7}$$

$$h_2 = \frac{\left(h_{1,in} + h_{2,in}\right)}{2} + \frac{\left(h_{2,in} - h_{1,in}\right)}{2} \cdot \exp\left(\frac{-2 \cdot W_{12}'^{H}}{m} \cdot z\right) \tag{3.8}$$

The temperature profiles for Channels 1 and 2 that correspond to the enthalpy predictions from the subchannel model as well as the analytical solution are shown in Figure 3.7.

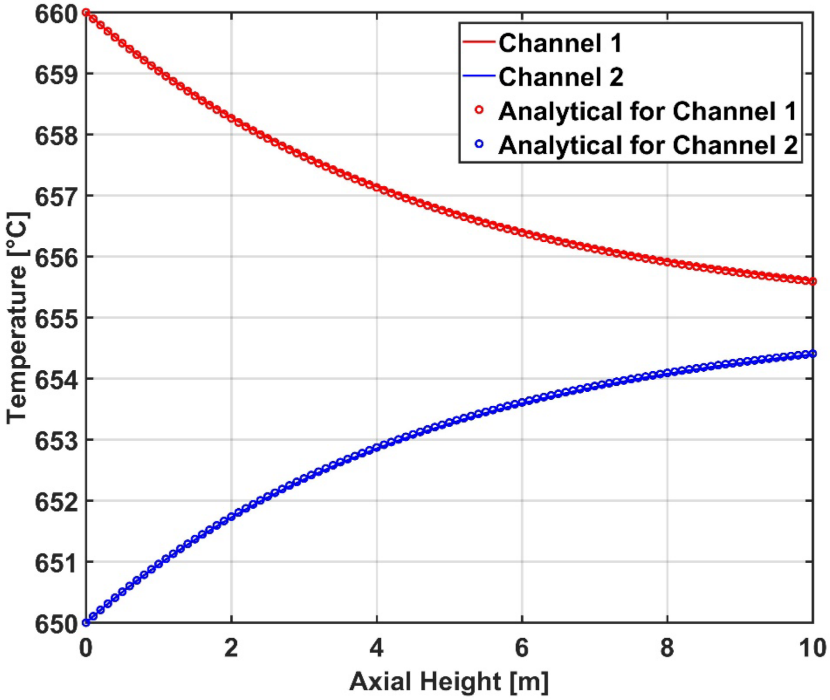

Figure 3.7: Axial temperature profile for the two channels predicted by the present subchannel model and analytical solution

From the figure, it can be seen that the subchannel model predictions are in very good agreement with the analytical predictions, thus indicating that the turbulent mixing behavior is correctly modeled in the subchannel model.

Following the crossflow and turbulent mixing verification studies, the mass flux distribution for the edge, corner and interior subchannels for single-phase, isothermal flow of water in the GE 3×3 rod bundle experiments (Lahey Jr. et al., 1970) is compared with the predictions from the subchannel model developed in the present study. The GE 3×3 rod bundle is shown in Figure 3.8. The pin diameter is ~15 mm, while the total length of the bundle is ~1.8 m. The rod bundle uses cylindrical pin spacers fusion welded between the pins and to the walls at six axial locations to maintain the gap between the pins. The closure models for friction factor and turbulent mixing employed in this verification study are based on the values provided in the CTF verification and validation studies (Salko et al., 2016). Properties of water at 25°C are used. A nominal value of 0.5 is used for the form loss coefficient for the cylindrical pin spacers.

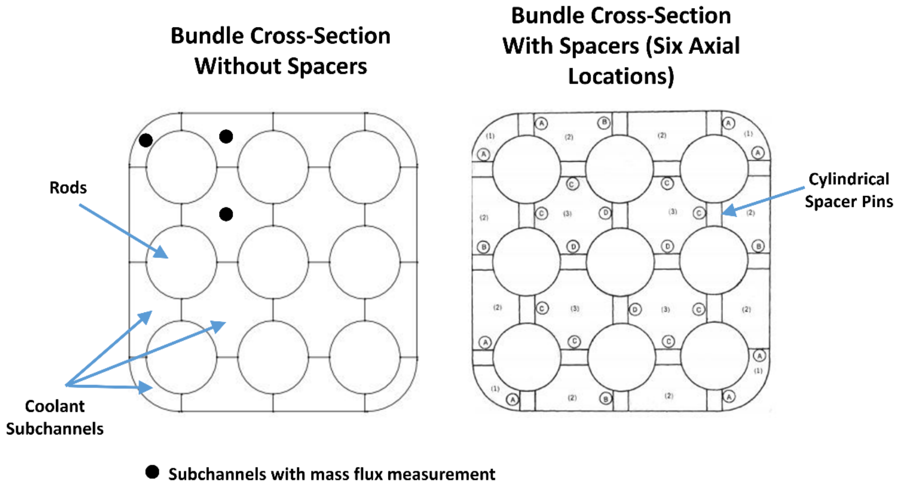

Figure 3.8: GE 3×3 rod bundle and spacer geometry

The measured and predicted values of exit mass fluxes for edge, corner and interior subchannels are shown for four different bundle mass flux values (test points 1B, 1C, 1D, and 1E from the GE 3X3 rod bundle test data) in Figure 3.9a. The predictions from the

CTF model are shown in Figure 3.9b. Figure 3.9a shows that the subchannel mass fluxes predicted by the present model agree well with the measured mass flux values, especially for the edge and interior subchannels. For the corner subchannels, the prediction accuracy of the present model at low mass fluxes is comparable to the CTF model, while some deviation is observed at higher mass flux values. It must be noted that the form loss coefficients employed by the CTF model could be different from the nominal value of 0.5 used in the present model, which could be responsible for the deviations observed between the two models. The use of more accurate form loss factors in the present model might provide better characterization of the crossflows along the length of the bundle, which could also further improve the agreement between the measured and experimental values.

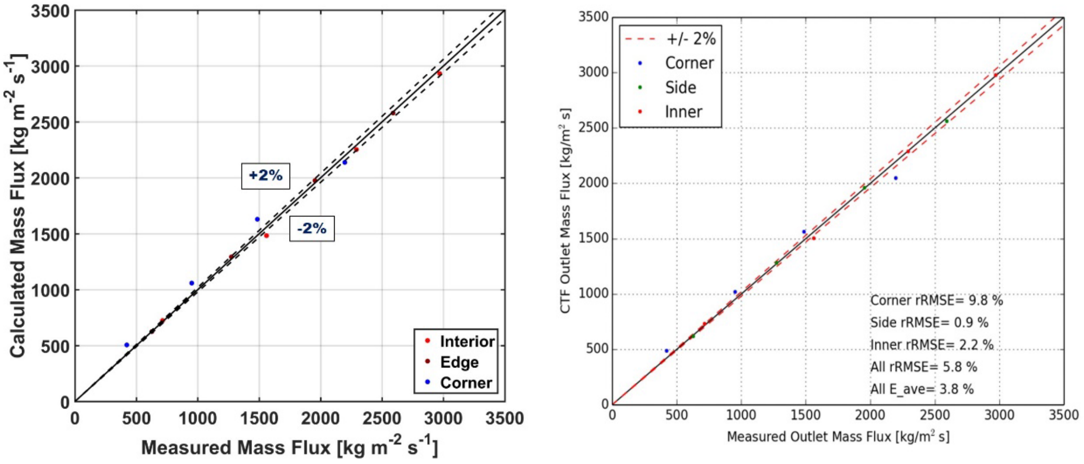

(a) (b)

Figure 3.9: (a) Comparison between measured and predicted mass fluxes for the GE 3×3 rod bundle, and (b) CTF model predictions from Salko et al. (2016)

3.2 Comprehensive code-to-code comparison

Following the verification of the key sub-models in the subchannel-based thermal hydraulic model, a CFD model is developed for a 1/12th symmetry of a single fuel assembly in the core to aid a more comprehensive code-do-code comparison between the subchannel-based and the CFD-based thermal hydraulic models. Before performing the code-to-code comparison, the effects of grid refinement, inlet turbulence specification, and the choice of turbulence modeling on the temperature and pressure drop predictions from the CFD model are first investigated and quantified. The CFD model, sensitivity studies, and the results from the code-to-code comparison are discussed in the subsequent sections.

3.2.1 CFD Model

The CFD model domain is shown in Figure 3.10.

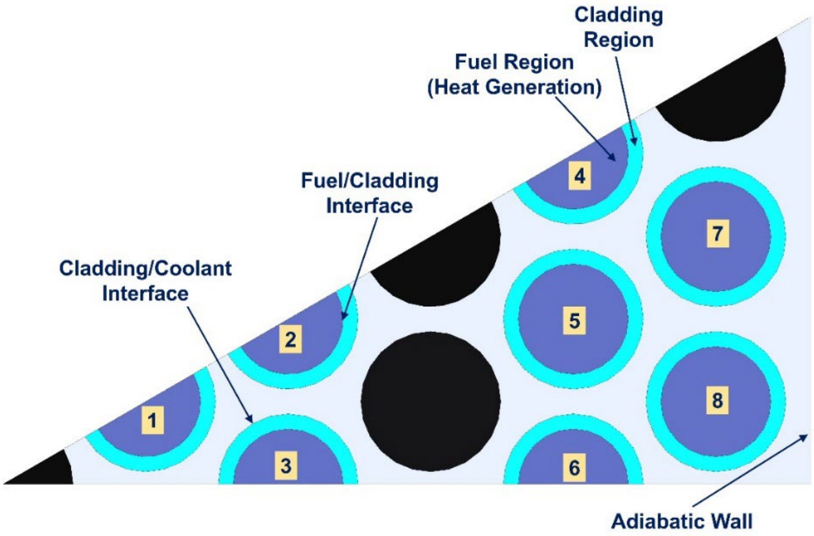

Figure 3.10: CFD model domain

This domain represents a 1/12th section of the bare fuel assembly shown in Figure 2.1d. The fuel pins, numbered 1 through 8 in the figure, have an active fuel region surrounded by a graphite matrix coating. Similar to the subchannel-based model, the active fuel regions in the CFD model domain are treated as a homogenous media. Volumetric heat generation is assigned to these active fuel regions in the model domain. The black-colored pins shown in Figure 3.10 represent non-fuel pins. All the non-fuel pins in the model domain are assumed to be graphite H-451. It must be noted that the control rod assembly (control rod, coolant in the annulus region and the guide tube) shown in Figure 2.1d is modeled as a single solid pin in this CFD study. This simplification is not expected to significantly change the flow behavior as the coolant flow through the narrow region between the guide tube and annulus represents a very small fraction (~0.1%) of total flow into the pin bundle. This control rod assembly simplification also avoids the complexity of meshing the narrow coolant region between the guide tube and control rod. All the non-fuel pins in the model domain are assumed to have zero heat generation. Symmetry boundary conditions are assigned to the appropriate boundaries, and an adiabatic wall boundary condition is assigned at the coolant/inner hexagonal wall interface (Figure 2.1d). The coolant temperature and mass flow rate are specified at the inlet of the bundle and a constant pressure is specified at the bundle exit. The thermophysical properties of the TRISO fuel, graphite matrix, graphite H-451, and the FLiBe coolant presented in the previous chapter for the subchannel-based model are also used in the CFD model.

Figure 3.11 shows the baseline grid used in this study. The solid region and the freestream of the bulk fluid flow (referred to as freestream region) in the model domain employ triangular prism elements. The axial grid size in both the solid and fluid regions is

5 mm. The grid size in the cross-section of the solid region is 1.50 mm, while the grid size for the freestream fluid cross-section is 1.25 mm. A wall grid is implemented in the fluid region near the walls to resolve the viscous sublayer. The baseline wall grid has a total of 13 layers and a growth rate of 1.2. The total thickness of the wall grid is ~1 mm. The thickness of the first cell closest to the wall is chosen such that $y^+ < 1$.

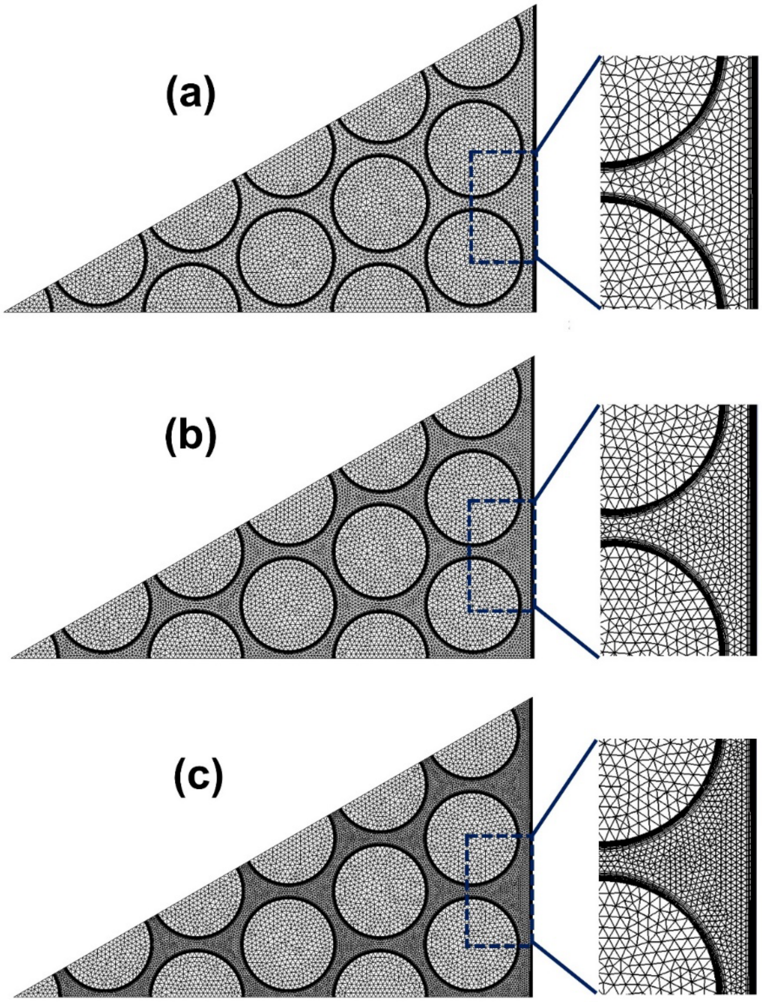

Figure 3.11: Freestream grid refinement (a) baseline grid, (b) freestream grid 2 (FSG 2), and (c) freestream grid 3 (FSG 3)

Two different grid sensitivity analyses are performed in this CFD study. The axial grid spacing is held constant in both these analyses. The solid region cross-sectional grid is also maintained the same in the grid sensitivity analyses, similar to the conjugate heat transfer study by Palomino and El-Genk (2019a). In the first analysis, the effect of freestream grid (FSG) spacing for the fluid region is investigated by successively reducing the grid size from the baseline case by a factor of 1.3, while the wall grid remains unchanged. Figure 3.11b and Figure 3.11c show the grids referred to as FSG 2 and 3, which have a freestream grid size of 0.96 mm and 0.74 mm respectively.

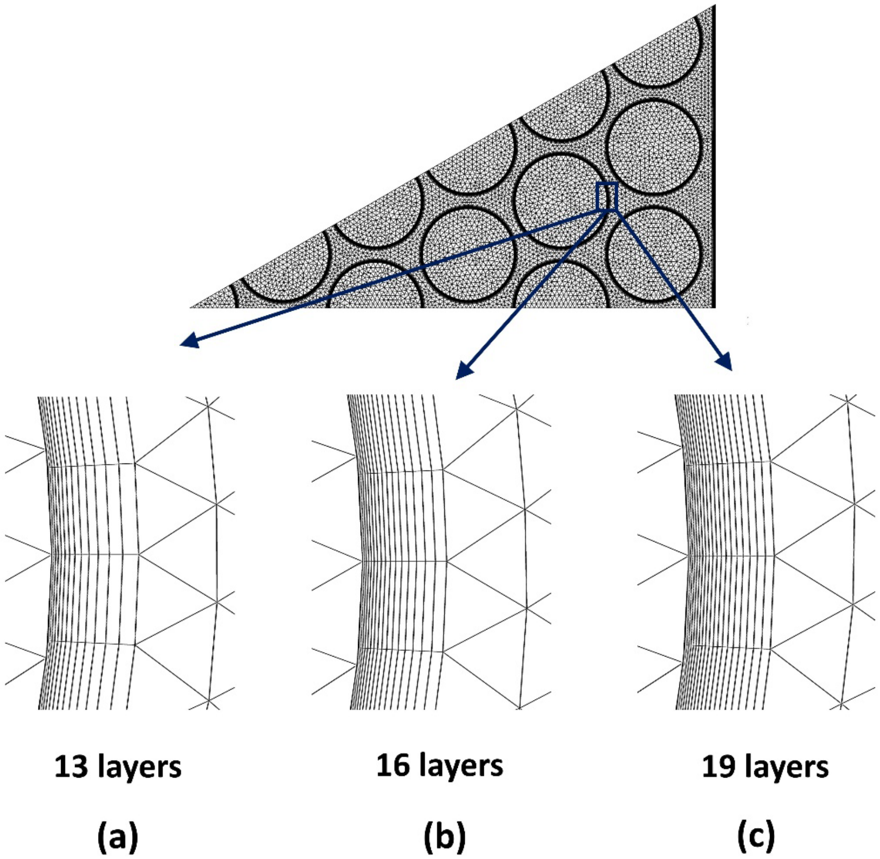

Figure 3.12: Wall grid refinement (a) baseline grid, (b) wall grid 2 (WG 2), and (c) wall grid 3 (WG 3)

In the second analysis, the effect of number of layers in the wall grid (WG) is investigated while the freestream fluid grid remains unchanged (at baseline conditions). The number of layers in the WG is increased by decreasing the growth rate, while the first cell thickness (which has a $y^+ < 1$) is held constant. Figure 3.12a, Figure 3.12b, Figure 3.12c show the three different wall grids used in this CFD study. Figure 3.12a represents the baseline wall grid described earlier (13 layers), while Figure 3.12b and Figure 3.12c, referred to as WG 2 and WG 3, have reduced growth rates to accommodate 16 layers and 19 layers respectively. It must be noted that the total thickness of wall grids shown in Figure 3.12b and Figure 3.12c are similar to the baseline wall grid (~1 mm).

Table 3.1 summarizes the parameters of the different grids used in this CFD study.

Table 3.1: Summary of grid refinements

Parameter	Baseline (FSG 1 /WG 1)	Freestream grid 2 (FSG 2)	Freestream grid 3 (FSG 3)	Wall grid 2 (WG 2)	Wall grid 3 (WG 3)
Axial grid spacing (mm)	5.00	5.00	5.00	5.00	5.00
Solid region grid size (mm)	1.50	1.50	1.50	1.50	1.50
Freestream grid size (mm)	1.25	0.96	0.74	1.25	1.25
Wall grid layers (-)	13	13	13	16	19
Approx. number of elements (-)	12.9 M	16.4 M	21.4 M	14.4 M	16 M

The three dimensional continuity, momentum and energy equations for the fluid region, and the three dimensional energy equation for the solid regions are solved in the present study. The RANS modeling approach is used to account for the turbulence in the fluid region of the model domain. The *k-ω* SST model (Menter, 1994) is chosen as the baseline turbulence model in the present study. As mentioned in the introduction chapter, there is no single turbulence model recommended for flow through rod bundle geometries, and therefore, it is important to investigate the effect of the turbulence model on the temperatures and the pressure drop in the model domain. To accomplish this, the results from the baseline *k-ω* SST model are compared with the other turbulence models shown in Table 3.2. These turbulence models include the *k-ω* 'baseline' or BSL model (Menter, 1994), which is similar to the *k-ω* SST model but does not account for the transport of turbulence shear stress in the definition of turbulent viscosity, the *k-ε* realizable model (Shih et al., 1995), a widely used model from the *k-ε* family, and two different Reynolds stress models (RSM). The RSM are different from the two-equation *k-ε* and *k-ω* family of models in that they abandon the isotropic eddy viscosity hypothesis and model the transport equations for Reynolds stresses along with an equation for dissipation rate (ANSYS, 2021). The two RSM considered here are the linear pressure-strain and stress-BSL models. The linear pressure-strain model uses an *ε*-based scale equation, whereas the blending approach outlined in Menter (1994) for the *k-ω* BSL model is used for the scale equation in the stress-BSL model. The approach for modeling turbulent diffusion, pressure-strain and other terms that appear in the Reynolds stress transport equations are outlined in the ANSYS theory guide (ANSYS, 2021) for both the Reynolds stress models used in this study. A constant turbulent Prandtl number of 0.85 is used in all the turbulence models. Table 3.2 also includes the near-wall treatment for the different turbulence models in the present study. The *ω*-based near-wall models – *k-ω* SST, *k-ω* BSL and RSM stress-BSL directly resolve all the way up to the viscous sublayer and do not require a separate near-wall treatment. The *k-ε* realizable and RSM linear pressure-strain models use the two-layer wall treatment approach. In the two-layer approach, the flow domain is divided into the viscosity-affected region and the fully-turbulent region based on the turbulent Reynolds number (ANSYS, 2021). The k-ε realizable and RSM linear pressure-strain models are used in the fully-turbulent region, while the one-equation model of Wolfshtein (1969) is used in the viscosity-affected region. The ε field in the viscosity-affected region is calculated using the length scale from Chen and Patel (1988).

Table 3.2: Turbulence models

Turbulence Model	Near-Wall Treatment
k-ω SST	Directly resolved up to the wall
k-ω BSL	Directly resolved up to the wall
k-ε realizable (RZL)	Two-layer model
RSM Linear Pressure-Strain (Lin P-Stn)	Two-layer model
RSM Stress-BSL (Str-BSL)	Directly resolved up to the wall

The pressure-velocity coupling is achieved using the SIMPLE algorithm. The convective terms in the governing equations are discretized using a second-order upwind scheme. Convergence is deemed to be achieved when the normalized residuals for flow and turbulence quantities are less than 10^{-5} and the normalized residual for the energy equation is less than 10^{-6}. The achievement of convergence is also verified by two other methods, which are described in Section 3.2.2.1. The computations were performed on a single node from the partnership for an advanced computing environment (PACE, 2017) computing cluster, using 12-24 cores of the Dual Intel® Xeon Gold 6226 CPU. The runtime ranged ~1-4 hours for the different cases considered in this study.

3.2.2 CFD model results

The results from CFD model described in the previous section are presented and discussed in this section. Table 3.3 shows the key baseline parameters used in the CFD studies.

Table 3.3: **Baseline parameters**

Parameter	Value
Grid	Baseline Grid (1.25 mm freestream grid size; 13 wall grid layers)
Turbulence Model	k-ω SST
Power Profile	Uniform
Volumetric Heat Generation	6.6×10^{7} W m^{-3}
Coolant Inlet Mass Flow Rate	4.5 kg s^{-1}
Coolant Inlet Temperature	650°C
Inlet Turbulence Specification	Turbulence Intensity (5%) and Hydraulic Diameter (0.015 m)

The hydraulic diameter listed in Table 3.3 is calculated using the conventional definition, as shown in Equation 3.9.

$$D_h = \frac{4 \cdot A_c}{PE_w} \tag{3.9}$$

Where A_c is the fluid flow cross-sectional area and PE_w is the wetted perimeter. For the coolant inlet conditions listed in Table 3.3, the Reynolds number and Prandtl number at the bundle inlet are ~3460 and 14.7 respectively.

3.2.2.1 Convergence

As mentioned earlier in Section 3.2.1, the model is deemed to be converged when the residuals for flow, turbulence and energy quantities are less than the prescribed tolerance values. Convergence is also verified by two other methods – monitoring the stabilization of key temperatures and the bundle inlet pressure, and ensuring that global mass and energy balances are satisfied. Figure 3.13a shows the maximum fuel and cladding temperatures, and the mean coolant temperature at the exit for all the iterations.

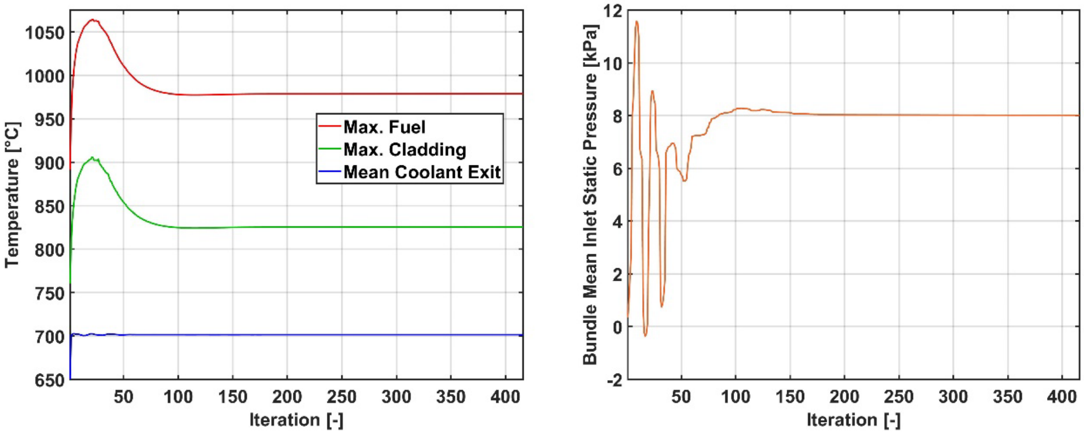

(a) (b)

Figure 3.13: Convergence profiles for (a) key temperatures, and (b) bundle mean inlet static pressure

It can been seen from this figure that these temperatures stay constant and do not have large fluctuations after ~100 iterations. Figure 3.13b shows the bundle-averaged static pressure at the inlet. Again, as with the temperatures, the pressure stabilizes after ~160 iterations.

The second method used for convergence verification is checking the global mass and energy balances. The % error for global mass balance for fluid flow is calculated using Equation 3.10.

$$\%\ Mass\ balance\ error = \left|\frac{m_{in} - m_{out}}{m_{in}}\right| \cdot 100 \qquad (3.10)$$

Where m_{in} and m_{out} are the bundle inlet and outlet mass flow rates, respectively.

The % error for global energy balance is calculated using Equation 3.11.

$$\%\ Energy\ balance\ error = \left|\frac{(m_{in} \cdot c \cdot T_{in}) - (m_{out} \cdot c \cdot T_{out}) + \sum q_{gen}}{\sum q_{gen}}\right| \cdot 100 \ (3.11)$$

Where c is the coolant specific heat, T_{in} and T_{out} are the bulk temperatures of the coolant entering and leaving the bundle. The numerator in Equation 3.11 has the total enthalpy of the coolant entering and leaving the bundle, as well as the total energy added to the coolant while flowing through the bundle, which is just the sum of heat generated by all the fuel pins ($\sum q_{gen}$) in the bundle. For all the CFD calculations performed in this study, the % errors for global mass and energy balances were well below 0.01%.

3.2.2.2 Effect of grid refinement

Figure 3.14a shows the effect of reducing the size of the fluid freestream grid spacing on the peak temperatures for fuel pins in the model domain.

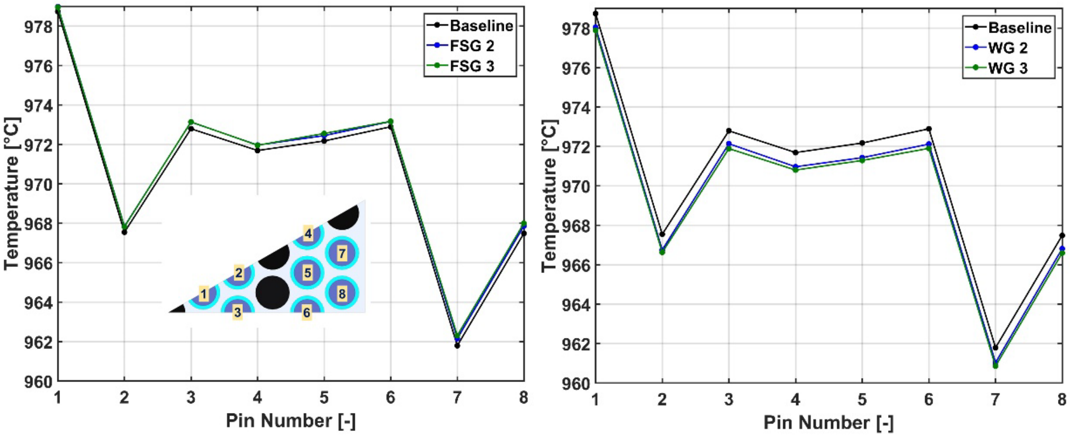

(a)

(b)

Figure 3.14: Fuel pin peak temperatures for (a) freestream grid refinements, and (b) wall grid refinements

While a small change in peak temperatures is observed as the grid spacing is refined from the baseline value of 1.25 mm to 0.96 mm (FSG 2), further decreasing the grid size from

0.96 mm (FSG 2) to 0.74 mm (FSG 3) has a very little effect on the peak temperatures. It should also be noted that the change in temperature from the coarsest (baseline) to the finest (FSG 3) grid changes the peak fuel temperature for all the pins by <1°C. The effect of refining the wall grid is shown in Figure 3.14b. Compared to the freestream grid refinement, the wall grid refinement has a slightly larger effect on the peak fuel pin temperatures. Nevertheless, the change in peak fuel pin temperatures going from the baseline grid with 13 layers to WG 3 with 19 layers is again <1°C. Table 4 lists the bundle pressure drop for all the five grids – baseline, FSG 2, FSG 3, WG 2 and WG 3. All the pressure drops reported here exclude the gravitational pressure change in the bundle. It can be observed from the table that the change in pressure drop from the baseline case, for both freestream and wall grid refinements, is <1%. Based on these results, the baseline grid is deemed to exhibit sufficient grid independence.

Table 3.4: Pressure drop for different grid refinements

Grid	Bundle Pressure Drop (kPa)	% Difference from Baseline
Baseline	8.01	0.0
FSG 2	8.03	0.3
FSG 3	8.06	0.6
WG 2	8.04	0.4
WG 3	8.04	0.4

3.2.2.3 Non-dimensional velocity and temperature profiles

For the baseline parameters listed in Table 3.3, Figure 3.15a and Figure 3.15b show the non-dimensional axial velocity, u^+ (Kays et al., 2004) as a function of non-dimensional distance from the wall, y^+ (Kays et al., 2004) for two different locations at the core exit.

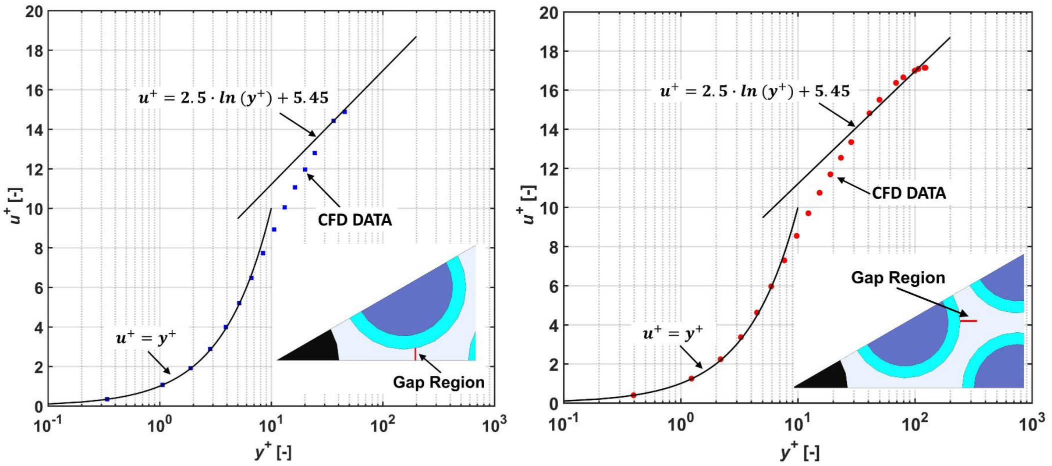

(a) (b)

Figure 3.15: Non-dimensional axial velocity vs. non-dimensional wall distance for (a) narrow gap region, and (b) wide gap region

Figure 3.15a is for the narrow gap region (from the cell near the wall to the center of the narrow gap), while Figure 3.15b is for the wide gap region (from the cell near the wall to the center of wide gap).

From these figures, it can be seen that the viscous sublayer and log-law regions are distinctly present in these non-dimensional velocity profiles. The CFD results also agree well with the linear law for up to y^+ values of ~6, and the log-law of the wall for y^+ values greater than ~30. The slope and intercept for the log-law of the wall are from the FLUENT theory guide (ANSYS, 2021). Figure 3.15a and Figure 3.15b also show that a very large part of the narrow gap and a substantial part of the wide gap are both in the viscosity-affected sub-layer and buffer-layer regions.

Figure 3.16a and Figure 3.16b show the non-dimensional temperature profile, T^+ (Kays et al., 2004) as a function of y^+ for the narrow and wide gap regions.

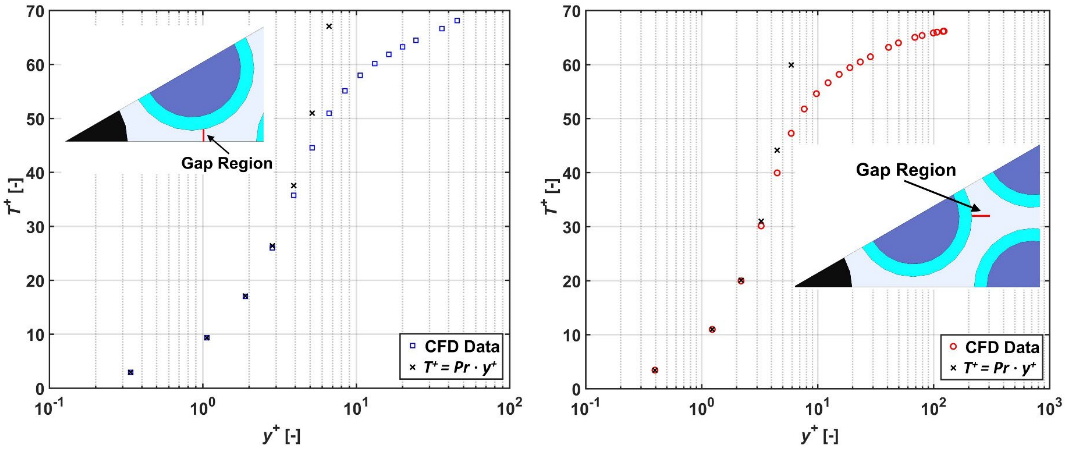

(a) **(b)**

Figure 3.16: Non-dimensional temperature vs. non-dimensional wall distance for (a) narrow gap region, and (b) wide gap region

From these figures, it can again be seen that the viscous sub-layer and log-law regions are distinctly present in the non-dimensional temperature profiles. Figure 3.16a and Figure 3.16b also show the expected non-dimensional temperature profile for the sublayer region, which is just the product of the y^+ and the Prandtl number (molecular) of the fluid in the cell. From these figures it can be seen that the CFD results for up to y^+ values of ~2 are in good agreement with the expected non-dimensional temperature profile for the sublayer region.

3.2.2.4 Effect of inlet turbulence specification

For the coolant entering the rod bundle, the transported turbulence quantities must also be specified, in addition to the inlet mass flow rate and temperature. The quantities that must be specified depend on the turbulence model used. For instance, if a model from the k-ω family is used to account for turbulence, then the appropriate profiles for k and ω

must be specified at the inlet. These profiles are typically determined from experimental data or empirical formulas. If accurate profiles for the inlet turbulence quantities are unknown, a uniform value for the turbulence quantities can be specified instead of experimentally or empirically determined profiles. The specification of these uniform turbulence quantities is accomplished by providing two inputs – turbulence intensity and either viscosity ratio, hydraulic diameter, or a length scale. The turbulence intensity is the ratio of the root mean square (RMS) of the mean velocity fluctuations to the mean flow velocity. A turbulence intensity of 1% is generally considered low, while a value of 5% is considered as medium intensity (ANSYS, 2021). The viscosity ratio is the ratio of turbulent viscosity to the dynamic viscosity of the fluid.

It is important to understand the effect of the different turbulence inlet specifications on the temperatures and pressure drop in the rod bundle. The table in Figure 3.17 shows the four cases considered in the present study. The value of turbulence intensity is similar between cases 1 and 2; however, the other quantity specified is different. Case 1 has the hydraulic diameter of the rod bundle specified as the other input, whereas Case 2 has a viscosity ratio of 10 (which is the default value in FLUENT) as the other input. Cases 1, 3 and 4 all have turbulence intensity and hydraulic diameter as the inlet specifications, but the value of turbulence intensity is different for the three cases.

Case	Specification
1	Turbulent intensity = 5%; Hydraulic diameter = 0.015 m
2	Turbulent intensity = 5%; Viscosity ratio = 10
3	Turbulent intensity = 3%; Hydraulic diameter = 0.015 m
4	Turbulent intensity = 1%; Hydraulic diameter = 0.015 m

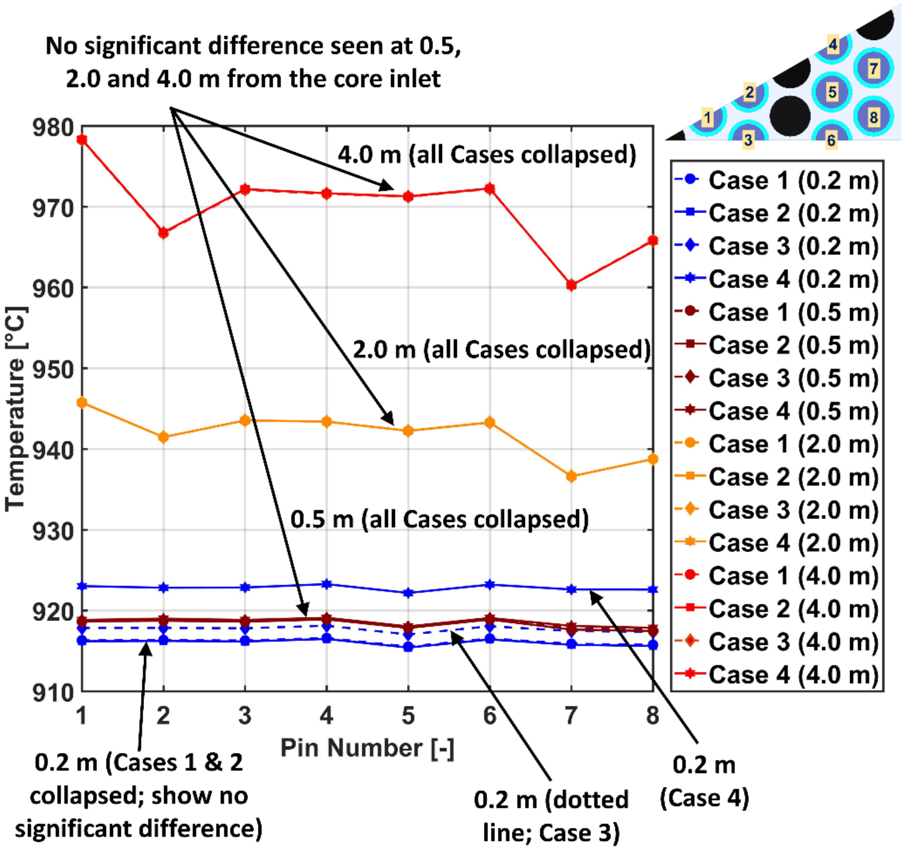

Figure 3.17: Fuel pin centerline temperatures at four axial locations (0.2, 0.5, 2.0 and 4.0 m) from the core inlet for different inlet turbulence specifications

For all the four cases, the plot in Figure 3.17 shows the centerline temperatures for the fuel pins in the model domain at four different axial locations from the core inlet. The baseline *k-ω* SST model is used in these analyses. It can be seen that the pin temperatures predicted by Cases 1 and 2 are almost identical at all the four axial locations. A similar behavior is also observed for the bundle pressure drop. This means changing the second input for inlet turbulence specification from bundle hydraulic diameter to viscosity ratio (with a value of 10) has no substantial impact on bundle pressure drop and temperatures considered in this study. It should be noted that that the inlet turbulent kinetic energy for both cases 1 and 2 is the same, as the value of turbulence intensity value is the same. For case 1, the specified hydraulic diameter yields an inlet specific dissipation rate (ω) of 85.3 s^{-1}, while the viscosity ratio of 10 specified in case 2 yields an ω value of 68.6 s^{-1}. These relatively close ω values could explain the similar pin temperatures and bundle pressure drop from the inlet for cases 1 and 2.

Comparing cases 1, 3, and 4, it can be seen that the pin temperatures at 0.5 m, 2.0 m and 4.0 m from the inlet are almost identical, indicating that the value of turbulence intensity does not have a significant impact on the pin temperatures relatively far from the core inlet. However, the pin temperatures at a location of 0.2 m show a different trend. The pin temperatures predicted from Case 4, with an inlet turbulent intensity of 1%, are noticeably higher (~7°C) than the pin temperatures predicted from Case 1 with a turbulent intensity of 5%. The pin temperatures predicted by Case 3 with 3% turbulence intensity (shown by the dotted blue line) also show a small difference from Case 1 (5% intensity). These results indicate that the value of turbulence intensity has a noticeable impact, but only on the pin temperatures closer to the core inlet. For the conditions investigated in the present study, increasing the inlet turbulence intensity may lead to enhanced heat transport, which results in higher heat transfer coefficients at axial locations closer to the inlet where the impact of inlet boundary conditions is felt more strongly. These higher heat transfer coefficients in turn lead to lower pin centerline temperatures. Similar trends have been observed in other studies (Lin and Ebadian, 1999; Gorman et al., 2016) for Nusselt numbers. The differences in the bundle pressure drop predictions between Cases 1, 3 and 4 are not significant.

3.2.2.5 <u>Effect of turbulence model</u>

Following the inlet turbulence specification sensitivity study, the effect of the turbulence models (Table 3.2) on the temperatures and pressure drop in the rod bundle is investigated. Figure 3.18 shows the peak fuel pin temperatures (for pins 1-8) for the different turbulence models considered.

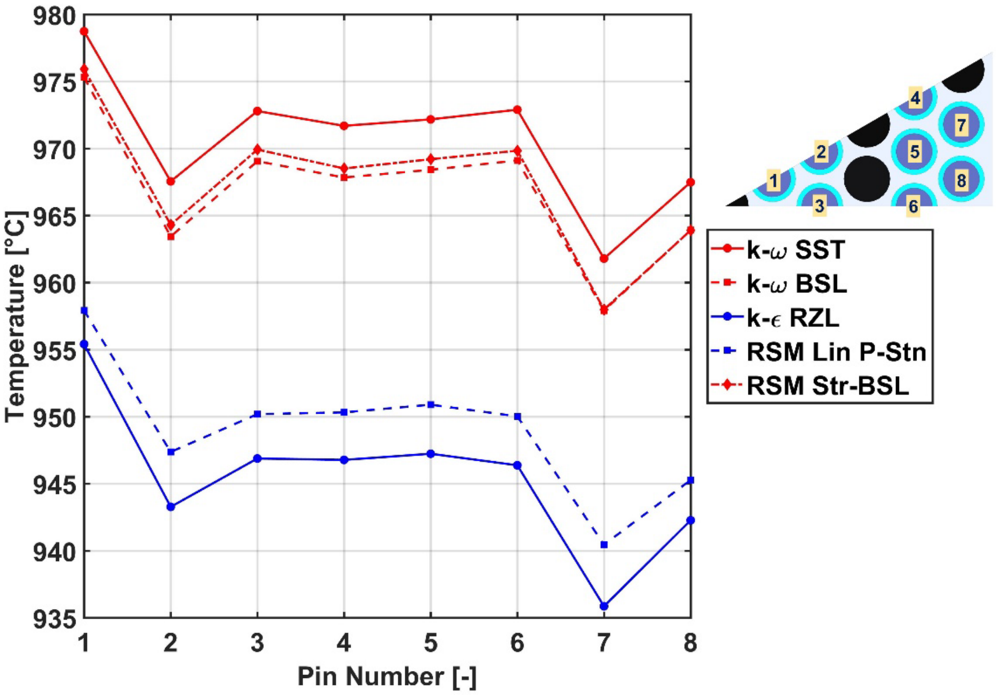

Figure 3.18: Fuel pin peak temperatures for different turbulence models

It can be seen from the figure that the choice of turbulence model can have a significant impact on the peak fuel temperatures, with the highest difference of ~26°C observed between the *k-ω* SST and *k-ε* realizable models. The peak temperature predictions from the *k-ω* BSL model are relatively close to those of the *k-ω* SST model. This is reasonable, as both the models use the same approach that blends the *k-ω* model in the near wall region and the *k-ε* model in the bulk fluid flow region, while the SST model also accounts for the transport of the turbulence shear stress in the definition of turbulent viscosity. It interesting to note that the results from the RSM linear pressure-strain model, which uses an *ε*-based scale equation, are somewhat closer to the results from the *k-ε* realizable model, whereas the results from the RSM stress-BSL model, which uses a BSL (the blending approach)-based scale equation, are closer to the *k-ω* BSL model. It is possible that for the conditions investigated in the present study, coolant mixing due to the secondary flows caused by anisotropy of the Reynolds stresses is not significant. This could explain the relatively close peak pin temperatures predicted by the eddy viscosity model such as the *k-ω* BSL model, and the anisotropic RSM model (RSM stress-BSL) that uses a BSL scale equation. Further modeling and experimental studies are needed to verify and understand this phenomenon. The invariant analyses by Busco et al. (2019), Merzari and Ninokata (2011), and Kraus et al. (2021) for different rod bundle geometries, pitch-to-diameter ratios, and Reynolds numbers reveal that the turbulence behavior between the wide-gap and the narrow-gap regions in the rod bundles can be significantly different. Characterization of these turbulence behaviors for the pitch-to-diameter ratio and the Reynolds number range in the present study will provide insights into the anisotropy behavior and the associated secondary flows in the rod bundle. This could lead to an understanding of the coolant mixing and heat transfer behavior due to the secondary flows for FHR bundle geometries and operating conditions.

Figure 3.19 shows the Pin 1 (Figure 3.18) centerline temperature along the core axial length predicted by the different turbulence models. The trends discussed above for the peak pin temperature can also be seen for the axial temperature profile. The pin centerline temperature for most of the core length (except close to the core inlet) is linearly increasing, which is due to the axially uniform heat generation in the fuel pins.

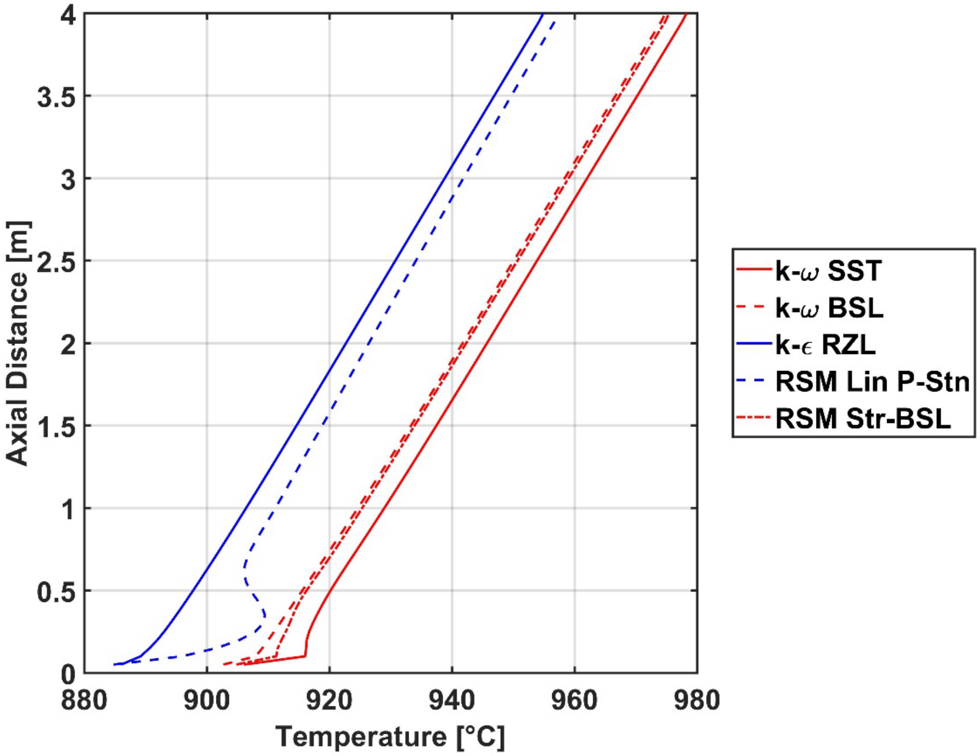

Figure 3.19: Fuel pin 1 centerline temperature along the core length for different turbulence models

Figure 3.20 shows the solid and fluid temperatures along the diagonal line of symmetry at the core exit.

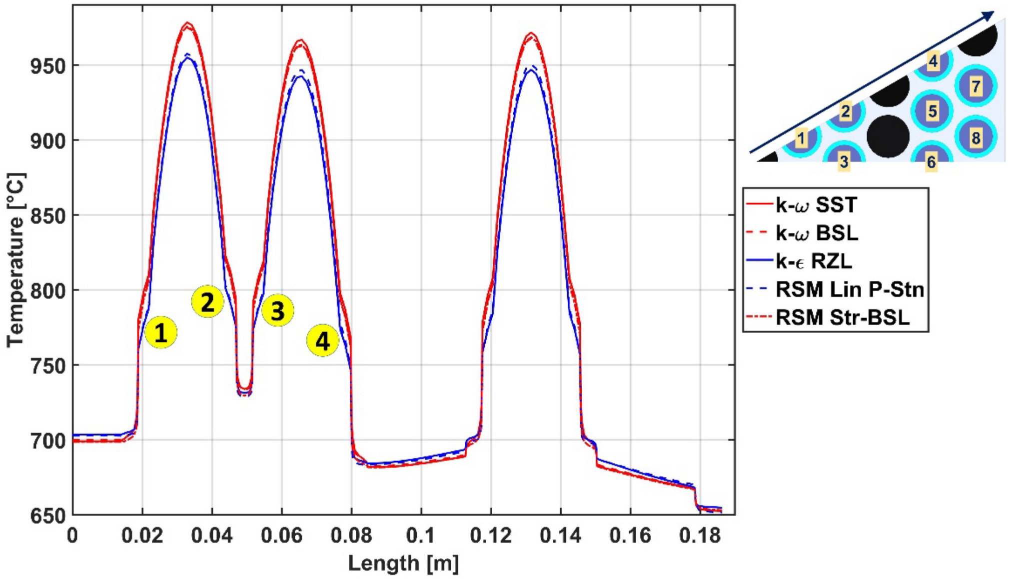

Figure 3.20: Temperatures (at the core exit) along the diagonal symmetry for different turbulence models

The fuel pin temperature profiles in Figure 3.20 roughly resemble the temperature profile for one dimensional radial conduction in a cylindrical system with heat generation in the active fuel region, which has a parabolic profile, surrounded by a cladding region, which has a logarithmic temperature profile. The sharp decrease in temperature marks the transition from the cladding region to the coolant region. Comparing the temperature profiles at points marked 1&2 and 3&4, it can be seen that fuel pins 1 and 2 clearly have an azimuthal asymmetry (temperature profiles to the left and right of the pin center are not the same for both the pins.) The non-fuel pins have relatively low temperatures, which is expected for non-heat generating solid elements in the bundle. It can also be seen that the non-fuel pin at the center of the bundle has a flat temperature profile, which is attributed to bundle symmetry. The similar trends seen in Figure 3.18 and Figure 3.19 for the different turbulence models can also be seen in Figure 3.20, again with the largest temperature difference observed between the *k-ω* SST and *k-ε* realizable models.

Table 3.5 shows the bundle pressure drop for the different turbulence models. The largest difference again is between the *k-ω* SST and the *k-ε* realizable models, with the latter model predicting a pressure drop ~17% higher than the former model. The pressure drop predicted by the anisotropic RSM stress-BSL model is also close to the prediction from the isotropic eddy viscosity-based *k-ω* BSL model. However, there is a significant difference between the RSM linear pressure-strain model and the *k-ε* realizable models.

Table 3.5: Pressure drop for different turbulence models

Turbulence Model	Bundle Pressure Drop (kPa)	% Difference from Baseline (k-ω SST)
k-ω SST	8.01	0.0
k-ω BSL	8.58	7.1
k-ε Realizable (RZL)	9.34	16.6
RSM Linear Pressure-Strain (Lin P-Stn)	8.33	4.0
RSM Stress-BSL (Str-BSL)	8.49	6.0

In addition to the uniform power profile, turbulence model sensitivity studies were also conducted with a center-peaked power profile for all the fuel pins in the model domain. The center-peaked axial power profile is shown in Figure 3.21. The relative power in the figure is the ratio of the local pin power density to the average pin power density.

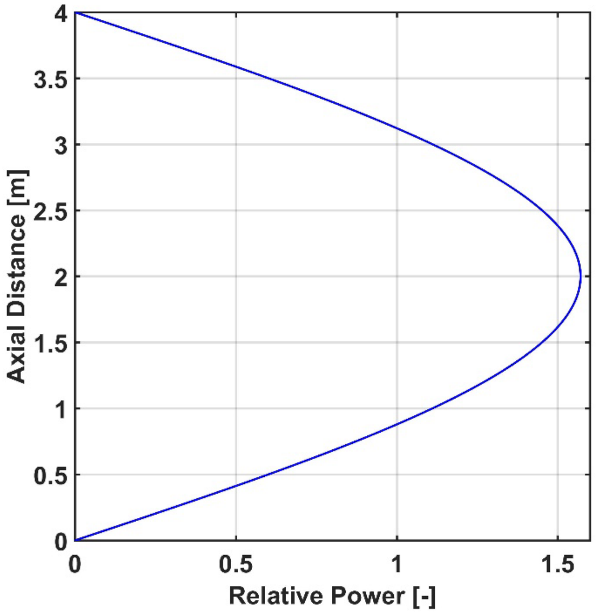

Figure 3.21: Center peaked power profile for CFD model

Figure 3.22 shows the peak fuel pin temperatures for the center-peaked power profile. The trends observed for the uniform power profile (Figure 3.18) can also be observed in Figure 3.22. However, the differences in the temperatures predicted by the different turbulence models for the center-peaked power profile are larger than those of the uniform power profile. For instance, the largest difference between the peak pin temperatures predicted by the *k-ω* SST model and the *k-ε* realizable model is ~26°C for the uniform profile, whereas it is ~40°C for the center-peaked profile. The differences in pin centerline temperatures predicted by different turbulence models is also proportional to the local power density, and therefore, the center-peaked power profile with higher local power densities has a larger temperature difference compared to the uniform power profile.

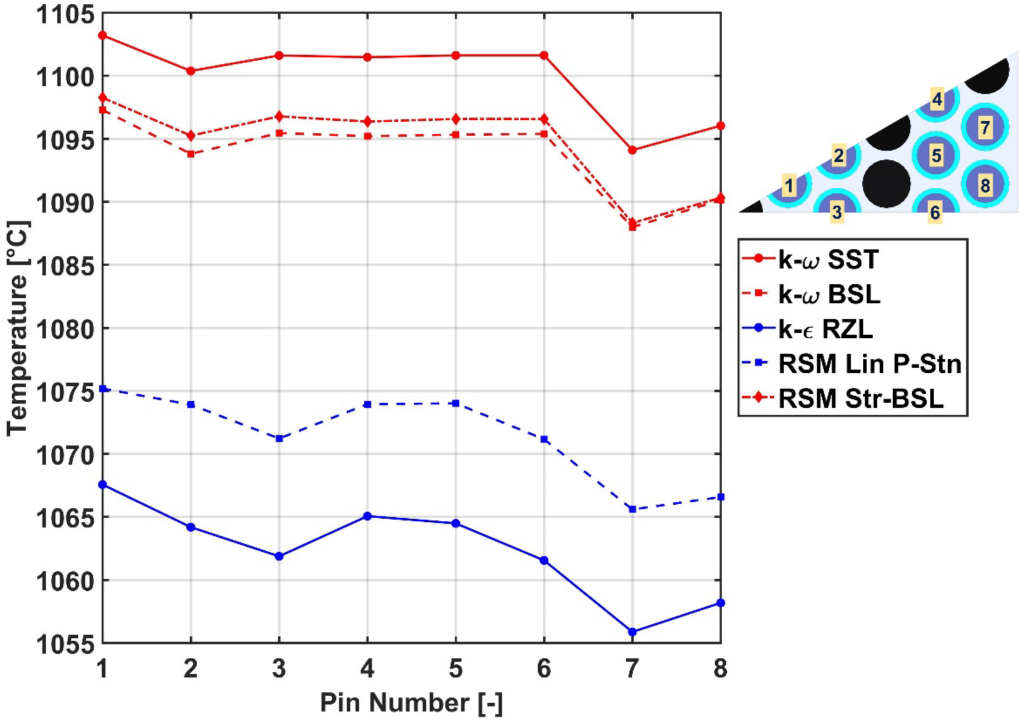

Figure 3.22: Fuel pin peak temperatures for different turbulence models

Figure 3.23 shows the centerline temperature for fuel pin 1 along the axial length of the core. It can be seen that despite the symmetry in power profile, the centerline temperatures for the top half of the core are higher than the bottom half, due to the higher coolant temperature. Similar to the peak temperatures, the *k-ω* SST model predicts the highest temperatures while the *k-ε* realizable model predicts the lowest temperatures. The bundle pressure drop values for the center-peaked profile are similar to that of the uniform power profile.

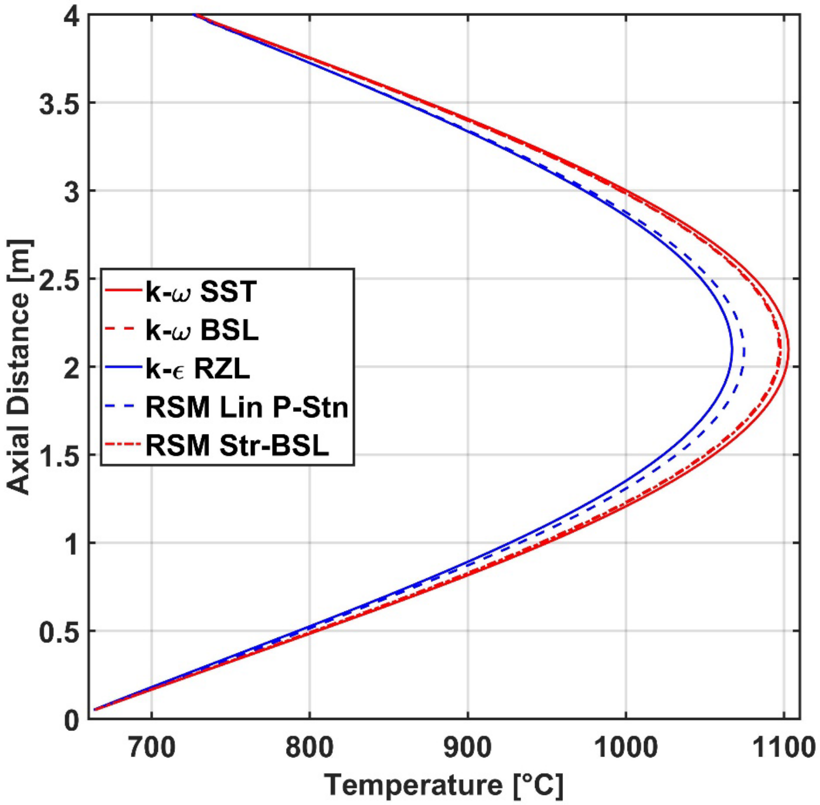

Figure 3.23: Fuel pin 1 centerline temperature along the core length for different turbulence models

It should be noted that the recommended viscosity and thermal conductivity correlations for the FLiBe salt referenced from the work of Romatoski (2017) have relatively large uncertainty values, with ± 20% uncertainty for viscosity and ± 10% for thermal conductivity. The density and specific heat capacity correlations have relatively small uncertainties of ± 2% and ± 3%, respectively. These large uncertainties for viscosity and thermal conductivity in turn result in large uncertainties in the Reynolds and Prandtl numbers, the two key dimensionless groups that characterize the heat transfer and pressure drop in single-phase flow. Therefore, the thermophysical property correlations for the molten salts used in reactor applications must be improved to obtain more accurate characterization of the thermal-hydraulic behavior of FHR core geometries. In addition to the uncertainties in the FLiBe thermophysical properties, other aspects such as TRISO and cladding (graphite matrix) properties, and boundary conditions, including the coolant mass flow rate and temperature, also influence conduction and convection heat transfer in the rod bundle. Therefore, the uncertainties in solid region material properties and boundary conditions must also be accounted in the future studies to understand and establish the uncertainties in the temperature field (including peak fuel temperatures) predicted by the CFD models for FHR pin bundles.

3.2.3 Comparison between CFD and subchannel models

Following the CFD analyses, the results from the baseline *k-ω* SST CFD model are compared with a subchannel-based model. The results from subchannel models that use two different heat transfer correlations (Gnielinski and Hausen) are compared with the CFD results. Figure 3.24 shows the peak fuel pin temperatures predicted by the CFD model as well as the two subchannel model correlations for a uniform power profile.

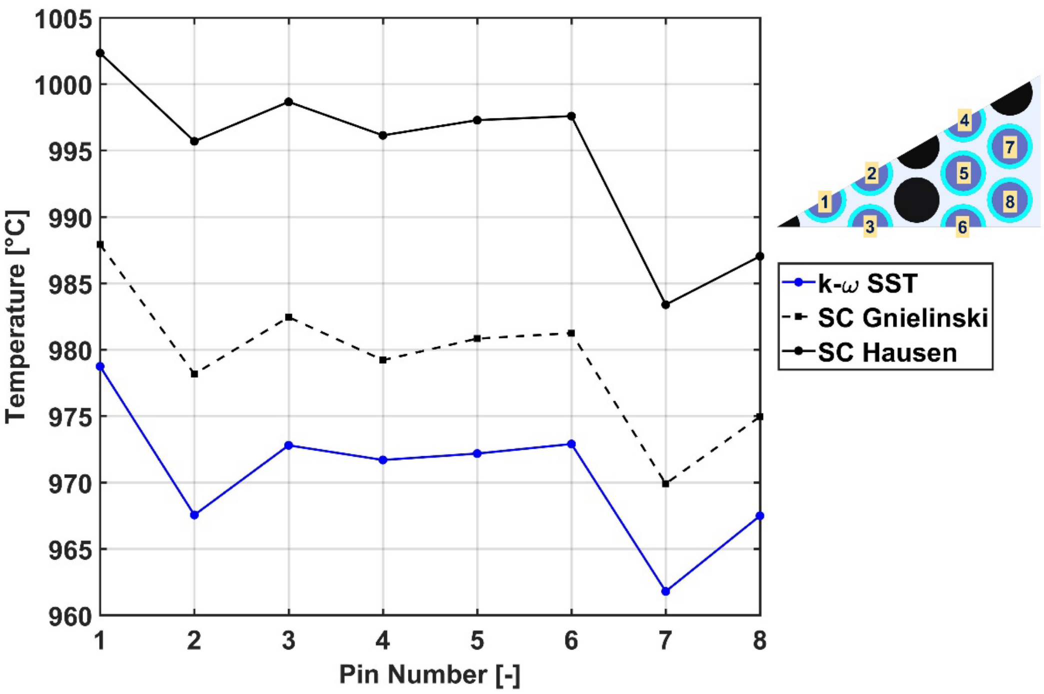

Figure 3.24: Fuel pin peak temperatures for CFD model and subchannel (SC) models

From the figure, it can be seen that agreement between the CFD model and the subchannel model that uses the Gnielinski correlation is better compared to the model that uses the Hausen correlation. The largest temperature difference between the CFD and the Gnielinski models is ~11°C (with the Gnielinski model predicting higher temperatures), whereas the difference between CFD and Hausen models is ~28°C (with the Hausen model predicting higher temperatures). A similar trend is also seen in Figure 3.25, which shows the centerline temperatures for pin 1 along the axial length of the core. It must be noted that rod bundle is discretized into ten axial segments in the subchannel model, whereas the bundle is discretized into ~800 axial segments in the CFD model.

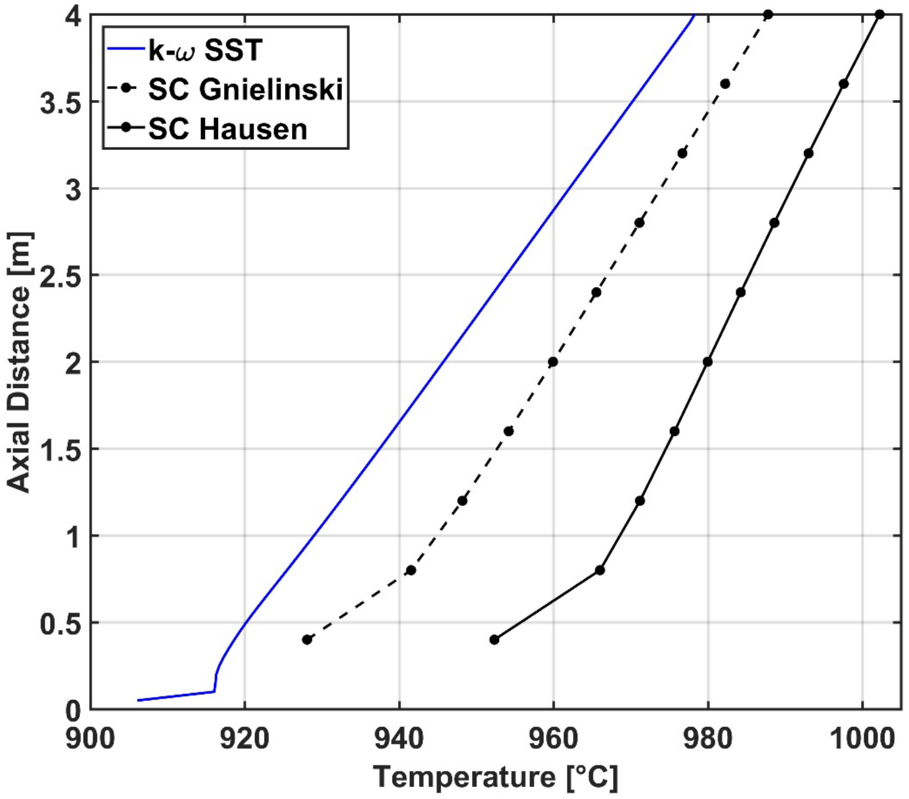

Figure 3.25: Fuel pin 1 centerline temperature along the core length for the CFD model and subchannel (SC) models

It can also be seen from Figure 3.25 that the two subchannel curves have a noticeably different slope close to the inlet of the core. This difference close to the inlet is attributed to the thermal entrance effect. As the fluid moves upward through the core, the thermal entrance effect decreases, which in turn leads to a decrease in the subchannel heat transfer coefficients. However, as the coolant fluid moves upward through the core, the increase in temperature effectively increases the subchannel heat transfer coefficients due to temperature-dependent fluid properties. The increase in heat transfer coefficient due to temperature-dependent properties is more than the decrease in heat transfer coefficient due to the diminishing thermal entrance effect, which leads to relatively steeper slopes for the axial segments far away from the core inlet. It must also be noted that as the temperature shown in Figure 3.25 is the fuel centerline temperature, other factors such as temperature dependent thermal conductivities of the fuel and cladding regions also play a role in determining the axial slope of the temperature curves. The region close to the core inlet of the CFD temperature curve also shows a different slope behavior, which could be a result of the uniform turbulence specification at the inlet. Figure 3.25 shows that there is generally good agreement between the CFD and Gnielinski models.

Figure 3.26 shows the temperatures along the diagonal line of symmetry at the core exit. From Figure 3.26, it can be noted that there are discontinuities in the temperature profiles for the two subchannel models. These discontinuities are associated with the fluid region, and are because the fluid temperatures calculated by the subchannel model are mean temperatures in the different subchannels in the bundle region, and do not correspond to physical spatial locations. The CFD model, on the other hand, calculates the fluid temperatures that correspond to physical spatial locations as shown in Figure 3.26. The trends observed for the peak and axial pin temperatures can also be observed in Figure 3.26, which shows good agreement between the Gnielinski model and the CFD model.

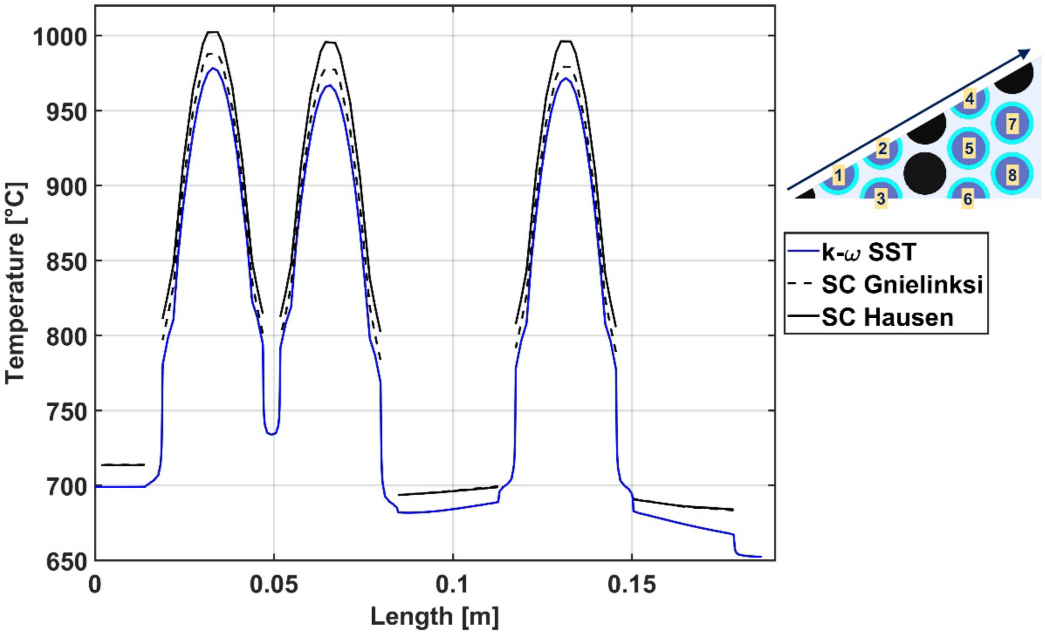

Figure 3.26: Temperatures (at the core exit) along the diagonal symmetry for the CFD model and subchannel (SC) models

Table 3.6 shows the bundle pressure drop for the CFD and two subchannel models. The bundle pressure drop predicted by the Gnielinski and Hausen models are ~11% and ~12%, respectively, within the prediction of the CFD pressure drop, which indicates good agreement. The small difference in the pressure drop predicted between the Gnielinski and Hausen models can be attributed to the fluid property correction term applied to the friction factor, which is dependent on the wall temperature of the cladding, which in turn depends on the heat transfer coefficient correlation employed in the subchannel model.

Table 3.6: Pressure drop for the CFD and subchannel models

Model	Bundle Pressure Drop (kPa)	% Difference from CFD Model
k-ω SST CFD	8.01	0.0
Subchannel (SC) Gnielinski	7.16	10.6
Subchannel (SC) Hausen	7.05	12.0

Figure 3.27a and Figure 3.27b show the contour temperature profile at the exit of the core for the CFD and Gnielinski subchannel models.

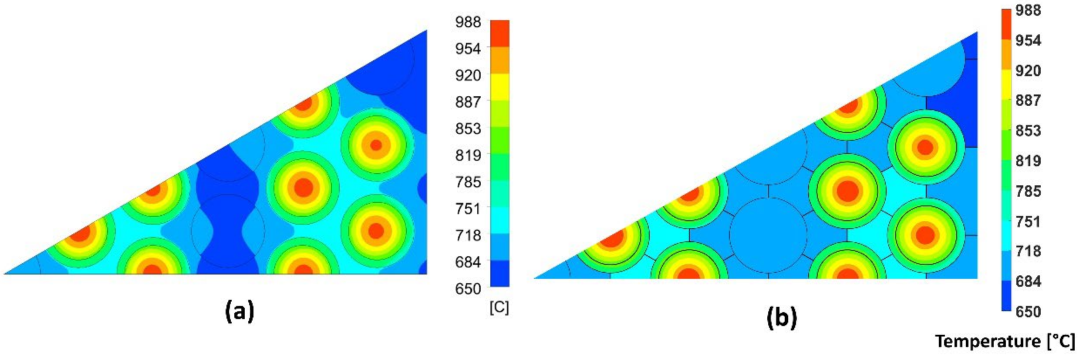

Figure 3.27: Core exit temperature contours: (a) k-ω SST CFD model, and (b) Gnielinski subchannel model

From these figures, it can be seen that the temperature values and distribution for the fuel pins are consistent and agree well with each other. It must be also noted that similar to the CFD model, the subchannel model is also able to predict the large azimuthal temperatures variations in the fuel pins close to the bundle periphery. This is because the three dimensional conduction model for the fuel pin accounts for the temperature and heat transfer coefficient variations in the subchannels surrounding the pin. The fluid temperatures reported in Figure 3.27b are the mean subchannel temperatures. While it is not possible to directly compare the coolant temperatures between the CFD and subchannel models, it can be seen that the temperature distribution in general is consistent between the two models.

Figure 3.28a and Figure 3.28b show the velocity contours at the core exit for the CFD and Gnielinski subchannel models.

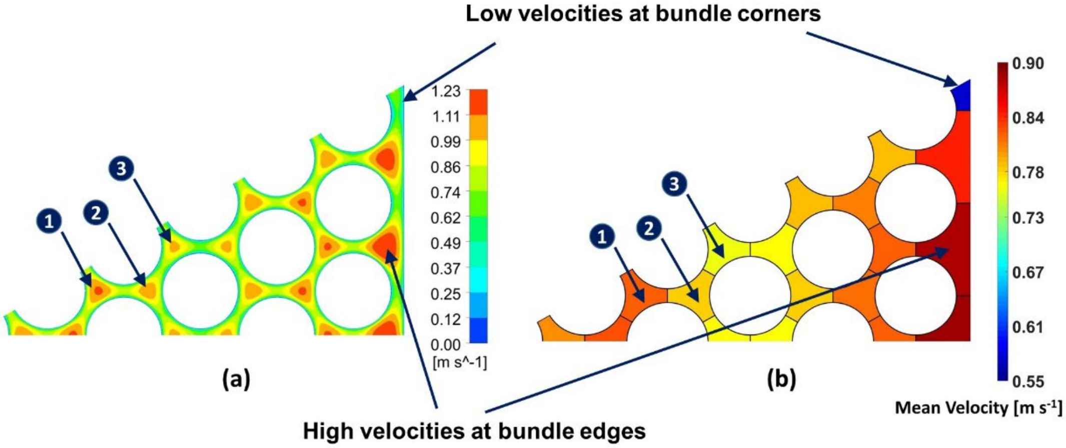

Figure 3.28: Core exit velocity contours: (a) *k-ω* SST CFD model, and (b) Gnielinski subchannel model

As with the case of temperatures, the fluid velocities reported in Figure 3.28b are the mean subchannel velocities. While a direct comparison between the velocity profiles is not possible, it can still be seen from Figure 3.28a and Figure 3.28b that the velocity distributions from the CFD model are consistent with the mean subchannel velocities predicted by the subchannel model. The CFD model predicts low fluid velocities in the corner region of the bundle, which is consistent with the low corner subchannel mean velocity predicted by the subchannel model. Similarly, the CFD model predicts high velocities in the edge region of the pin bundle, which is again consistent with the high mean edge subchannel velocities predicted by the subchannel model. It can also be seen from Figure 3.28 that the CFD model has different velocity profiles at locations marked ‘1’, ‘2’ and ‘3’, which are also consistently captured by the mean velocity predictions from the subchannel model (with mean velocity for subchannel marked ‘1’ being the highest and subchannel marked ‘3’ being the lowest).

Following the uniform power profile case, a comparison between the CFD and subchannel models is also performed for a center-peaked power profile. The CFD model uses the power profile shown in Figure 3.21, whereas the subchannel model uses a ‘chopped cosine’ power profile shown in Figure 3.29. The relative power in the figure again is the ratio of the local pin power density to the average pin power density.

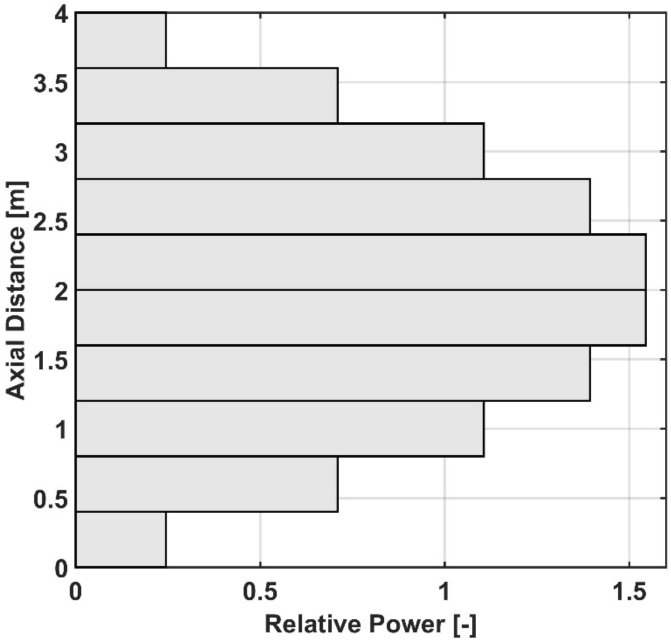

Figure 3.29: Center-peaked power profile for subchannel model

Figure 3.30 shows the peak fuel pin temperatures for the CFD model as well as the Gnielinski and Hausen subchannel models. Similar to the uniform power profile, the Gnielinski model shows better agreement with the CFD model compared to the Hausen model. The maximum difference between the peak fuel pin temperatures predicted by the CFD and Gnielinski models is ~23°C, whereas the maximum difference between the CFD and Hausen models is ~52°C.

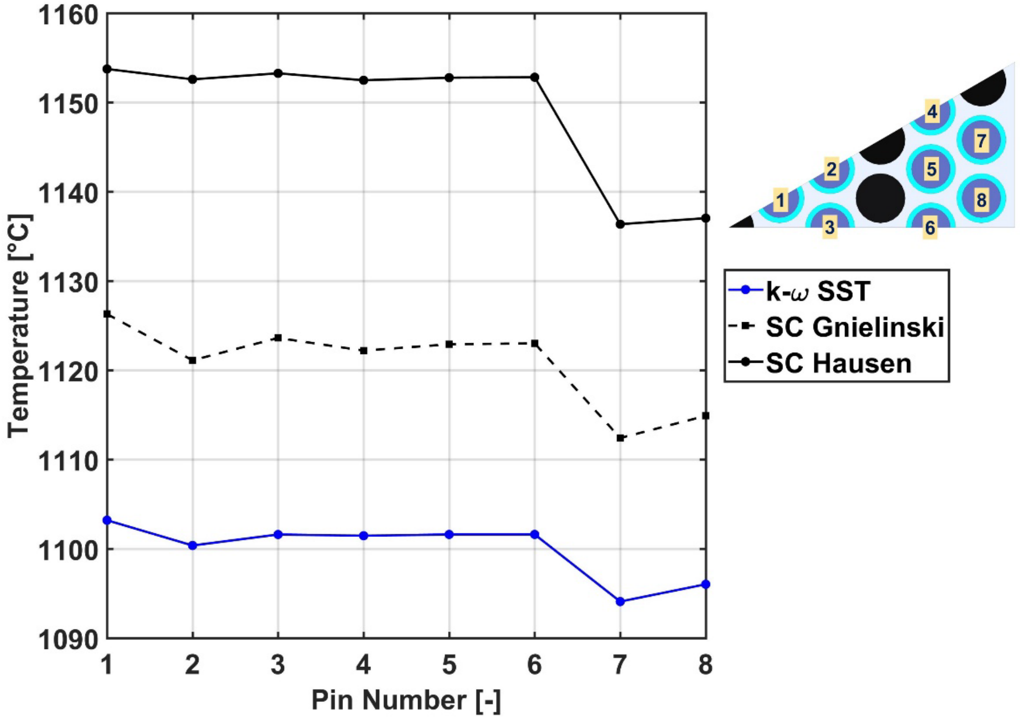

Figure 3.30: Fuel pin peak temperatures for CFD model and subchannel (SC) models

Figure 3.31a shows the centerline temperatures for pin 1 along the axial length of the core.

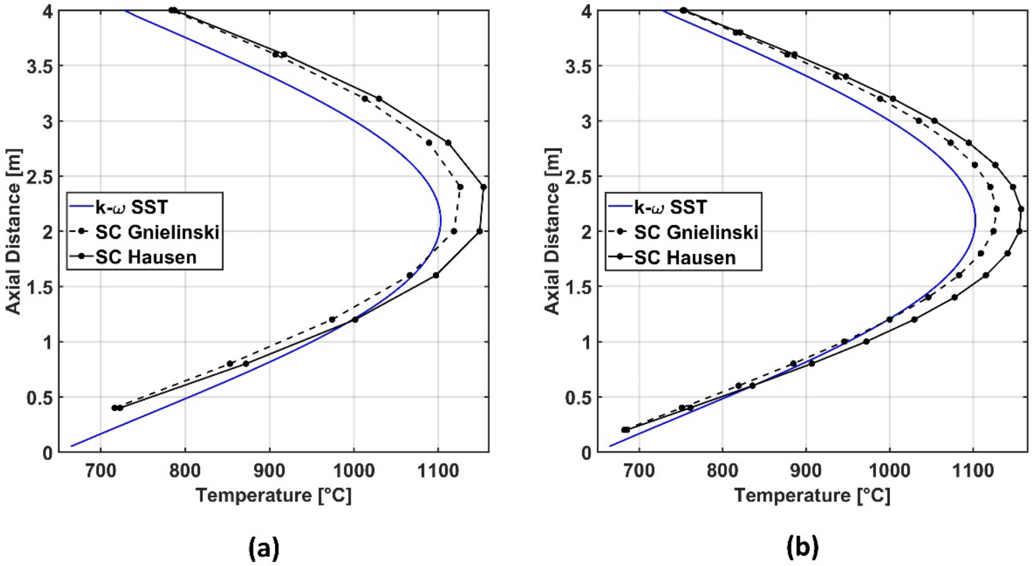

Figure 3.31: Fuel pin 1 centerline temperature along the core length for the CFD model and subchannel (SC) models (a) 10 axial segments, and (b) 20 axial segments for the subchannel model

From the figure, it can be seen that the axial temperature profile for the CFD model is different compared to the two subchannel models. This is attributed to the fact that the CFD model has a much finer axial discretization (~800 elements) and power profile (Figure 3.21) compared to the subchannel models in Figure 3.31a that have ten axial segments and a relatively coarse power profile (Figure 3.29). This is also verified by comparing the CFD model with subchannel models that have twice the number of axial segments (20 instead of 10) in Figure 3.31b. Comparing Figure 3.31a and Figure 3.31b, it can be readily seen that increasing the number of axial segments for the subchannel model improves the agreement with the CFD model. It should be noted that increasing the number of axial segments for the subchannel model will only aid in reducing the temperature discrepancies due to the coarse power profile, and there will still be differences between CFD and subchannel models even if they both have the same axial discretization. These differences are due to the differences in the way solid-to-fluid heat transfer is characterized by the two models. Subchannel models also typically employ much coarser axial discretization compared to the CFD models. This relatively coarse axial discretization aids in maintaining reasonable computational overheads and runtimes, especially when performing whole-core calculations. From Figure 3.31, it can also be seen at the axial locations closer to the core center where the fuel temperatures are the highest, that the predictions from the Gnielinski model are generally in good agreement with the CFD model. The bundle pressure drop values for the center-peaked profile are similar to that of the uniform power profile.

From these results, it can be seen that the results from the *k-ω* SST CFD model are consistent and agree well with the Gnielinski subchannel model. However, as observed in Section 3.2.2.5, the choice of turbulence model can have a large impact on the temperature and pressure drop predictions in the model domain. In addition, some of the quantities such as the fluid temperature and velocity from the well-resolved CFD model cannot be directly compared with the average values from the subchannel model. Therefore, the comparison between CFD and subchannel models should be treated as an initial code-to-code comparison study and not as verification for either of these models. Experimental and subsequent modeling studies are needed to determine the accuracy of both the *k-ω* SST CFD and subchannel model correlations for the bundle geometry and conditions investigated in this study. It is also important to note that unlike circular tubes that have a well-established critical Reynolds number for the laminar-to-transition as well as transition-to-fully turbulent flows, precise critical Reynolds numbers are not available for rod bundle geometries. For the pitch-to-diameter ratio of 1.175 in the present study, the

Cheng and Todreas (1986) correlation that is typically used in subchannel modeling yields a critical bundle Reynolds number of ~13,200 for transition to fully turbulent flow. However, as pointed out by the same authors, this critical Reynolds number correlation has been developed to enable the use of a constant Reynolds number exponent in the friction factor correlations (Cheng, 1984; Cheng and Todreas, 1986), and fully turbulent flow may be achieved much earlier in rod bundles. This is evident from the criterion provided by for infinite bare triangular bundle arrays, which yields a critical bundle Reynolds number of ~3,000 for transition to fully turbulent flow for the same pitch-to-diameter ratio. Determination of accurate critical Reynolds numbers is an important issue for rod bundles in molten salt reactors, as they typically operate at Reynolds numbers much lower than 10,000. Therefore, future studies must also characterize the transition criteria to enable the use of accurate, regime-specific closure relations in the subchannel model. Also, as mentioned in Section 2.2.2.3, due to the lack of subchannel geometry-specific correlations, the heat transfer correlations that were originally developed for the circular tube geometry are used in the present subchannel model. For FHR pin bundles, it is possible that the use of these circular tube correlations could be resulting in a considerable under prediction of heat transfer in the subchannels. This could explain the consistently higher fuel temperatures predicted by the subchannel model compared to the CFD model. In future studies, an experimentally validated CFD model could be used either to modify the existing circular tube correlations (with a correction factor or term) or develop new subchannel geometry-specific heat transfer correlations, which could improve the temperature predictions for the subchannel model. The CFD model with the well-resolved coolant domain could also provide the temperature and flow profiles for the development of other closure relations needed for the thermomechanical and corrosion analyses of any metallic structures within the core region of the FHRs.

CHAPTER 4. STEADY-STATE RESULTS FOR SOLID PIN-FUELED SMAHTR

Following the verification and code-to-code comparison studies, whole-core simulations have been performed for the solid pin-fueled SmAHTR using the subchannel-based model. Based on the code-to-code comparison between the CFD and subchannel models, the Gnielinski (1976) correlation is used to quantify the subchannel heat transfer in the transition flow regime. The results for simulations with different power profiles, core inlet mass flow rates, and inlet flow boundary conditions are presented and discussed. The results from sensitivity analyses that quantify the effect of crossflow tolerance, gap resistance modeling approach, and the radial reflector coolant channel mass flow rate on the key quantities of interest (peak temperatures, core pressure drop, etc.,) are also discussed in this chapter.

4.1 Whole-core results

Table 4.1 shows the baseline parameters using for the whole-core model.

Table 4.1: Baseline parameters

Parameter	Value
Core power	125 MW(t)
Axial power profile	Uniform
Coolant inlet flow rate (active core)	1018 kg s^{-1}
Coolant inlet flow rate (radial reflector coolant channels)	20 kg s^{-1}
Coolant inlet temperature	650°C

The core power in the table is from the pre-conceptual design report (Greene et al., 2011). As mentioned in Section 2.2.1, all the energy generated due to fission is assumed to be deposited on the fuel pins for all the cases presented here. A radially flat power profile is considered in the baseline case, which implies that all the fuel pins in all the fuel assemblies across the core have the same amount of power generation. Furthermore, the baseline case also assumes an axially uniform power profile for the fuel pins in the core. The uniform power profile is shown in Figure 4.1.

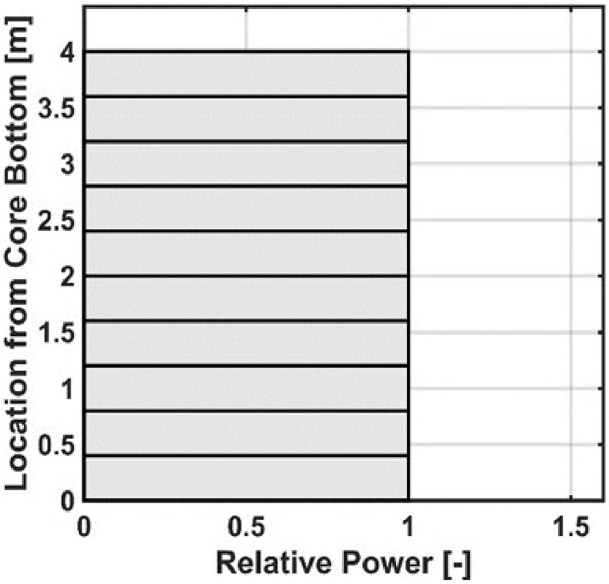

Figure 4.1: Uniform power profile

The relative power in Figure 4.1 is the ratio of local power density to the average power density of the core. For the uniform power profile, the relative power is equal to one at all axial locations, which means that the local power density for any fuel pin in the core at any axial location is equal to the average core power density. The primary FLiBe coolant inlet flow rate to the active core region (the 19 fuel assemblies in the core) is set to a value of 1018 kg s^{-1}, based on the value from the pre-conceptual SmAHTR design report. For the coolant channels in the radial reflector region, a nominal value of 20 kg s^{-1} is set to be total inlet flow rate (the pre-conceptual design report does not provide the coolant flow rate values to be used for the radial reflector coolant channels), which is ~2% of the coolant flow rate into the active core region for the baseline case shown in Table 4.1. The primary coolant inlet temperature is set to 650°C (pre-conceptual design report value). The core is divided into 10 axial segments, and the number of radial segments in the active fuel region of the fuel pin is set to five (the cladding region has three additional radial segments) for all the cases presented in this chapter. The whole core steady-state simulations reported here were performed within a code runtime of ~15 minutes.

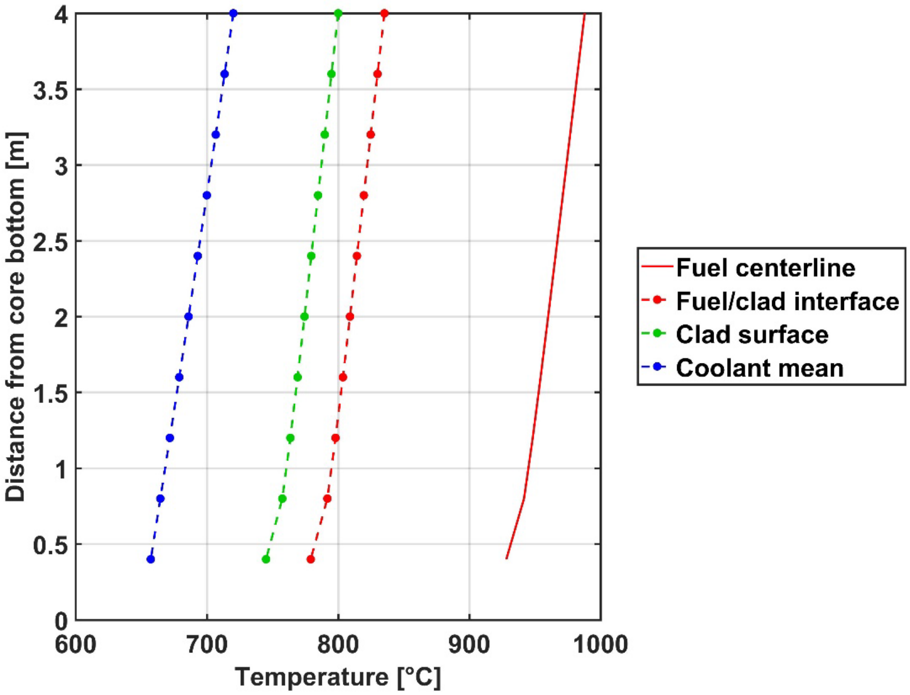

Figure 4.2: Temperature profile for the hottest pin in the core for uniform power profile

For the radially flat and axially uniform power profile, Figure 4.2 shows the azimuthally-averaged temperatures at different axial and radial locations for the hottest pin in the core.

The peak fuel centerline temperature, ~988°C, is at the top of the core. The temperature profiles for other regions (cladding inner and outer surface, and coolant) follow a similar profile.

The whole-core, 3-D temperature profile for the fuel pins is shown in Figure 4.3. The temperature values shown are volumetrically weighted averages at each axial segment of the fuel pins. The white colored pins in the figure represent the non-fuel pins in the fuel assemblies. The combination of uniform axial power profile and upward coolant flow leads to a monotonic increase in the average fuel pin temperatures from the bottom to the top of the core. Despite equal heat generation for the fuel pins across the fuel assembly, there are considerable differences in average pin temperatures within each fuel assembly due to variations in mean temperature and heat transfer coefficient in the coolant subchannels surrounding each fuel pin. The average and peak pin temperature values, and the temperature distribution are essentially the same for all the fuel assemblies at an axial level, which is attributed to the flat radial power profile, and the relatively low heat transfer from the outer fuel assemblies to the surrounding graphite regions.

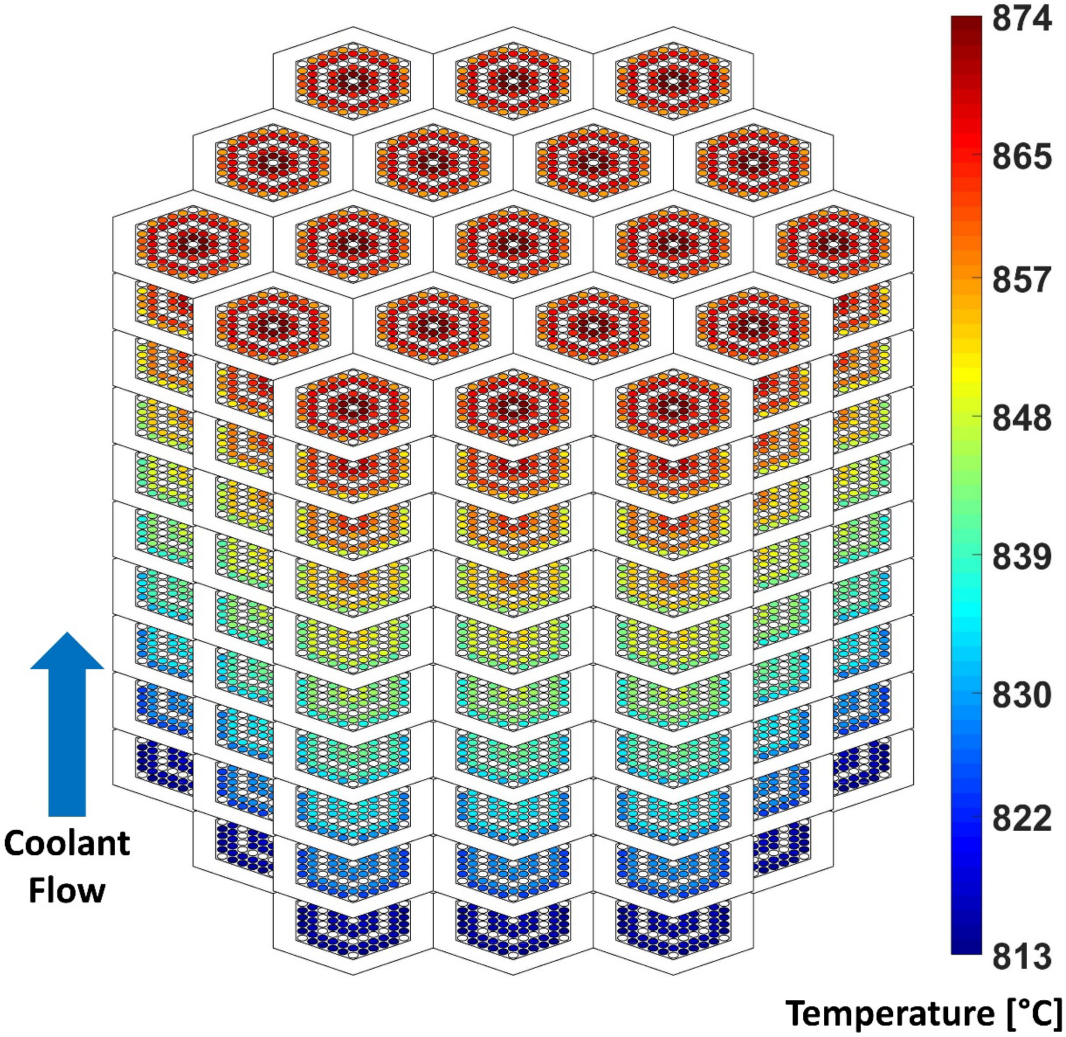

Figure 4.3: 3-D, whole-core fuel pin temperature distribution for uniform power profile

Figure 4.4 shows the temperature profile for the key non-fuel solid regions in the core (moderator pins and graphite reflectors). The temperature of the coolant channels in the radial reflector region is also shown in the figure. The moderator pin temperatures shown in the figure are the volumetrically weighted-average values. As there is no heat generation in the non-fuel regions, the temperatures at a given axial location are generally close to the coolant temperatures (which monotonically increases from the bottom to the top of the core.)

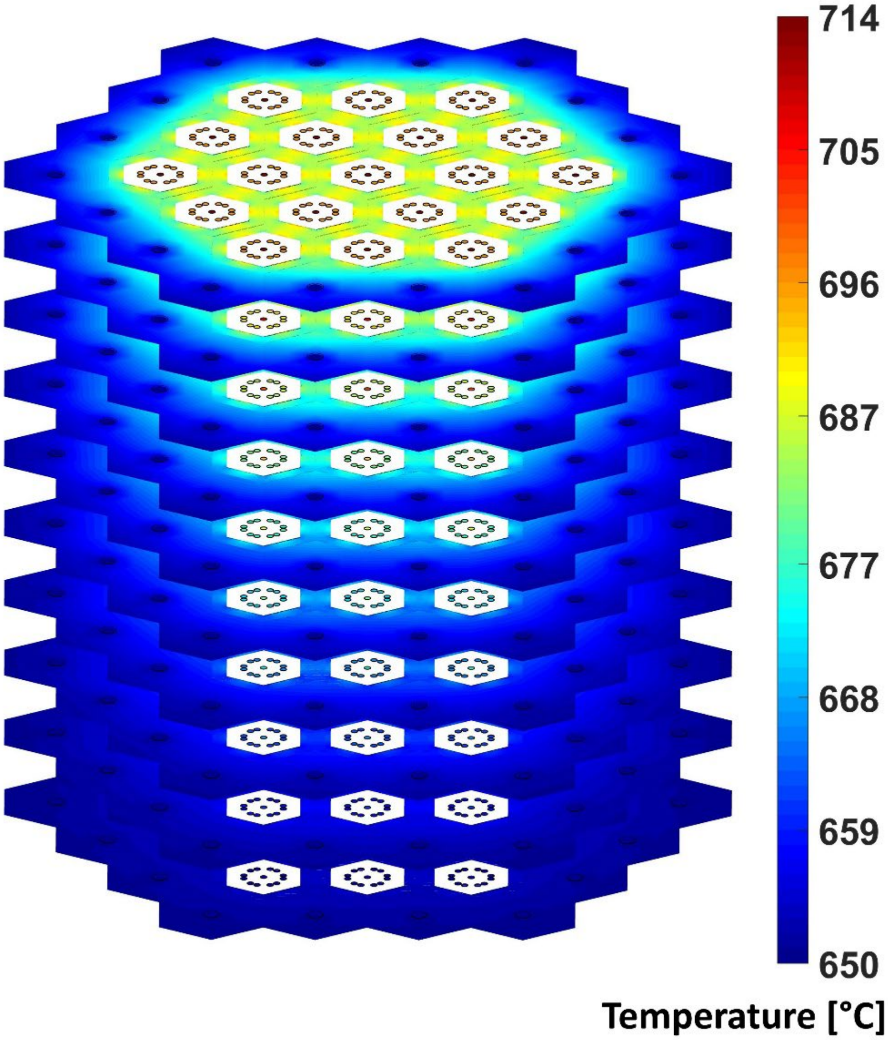

Figure 4.4: 3-D, whole-core temperature profile for moderator and reflector regions (including reflector coolant channels)

The whole-core, 3-D coolant mean temperature profile is shown in Figure 4.5, along with a magnified view for one of the fuel assemblies at two different axial locations (one near the middle of the core and the other at core exit.)

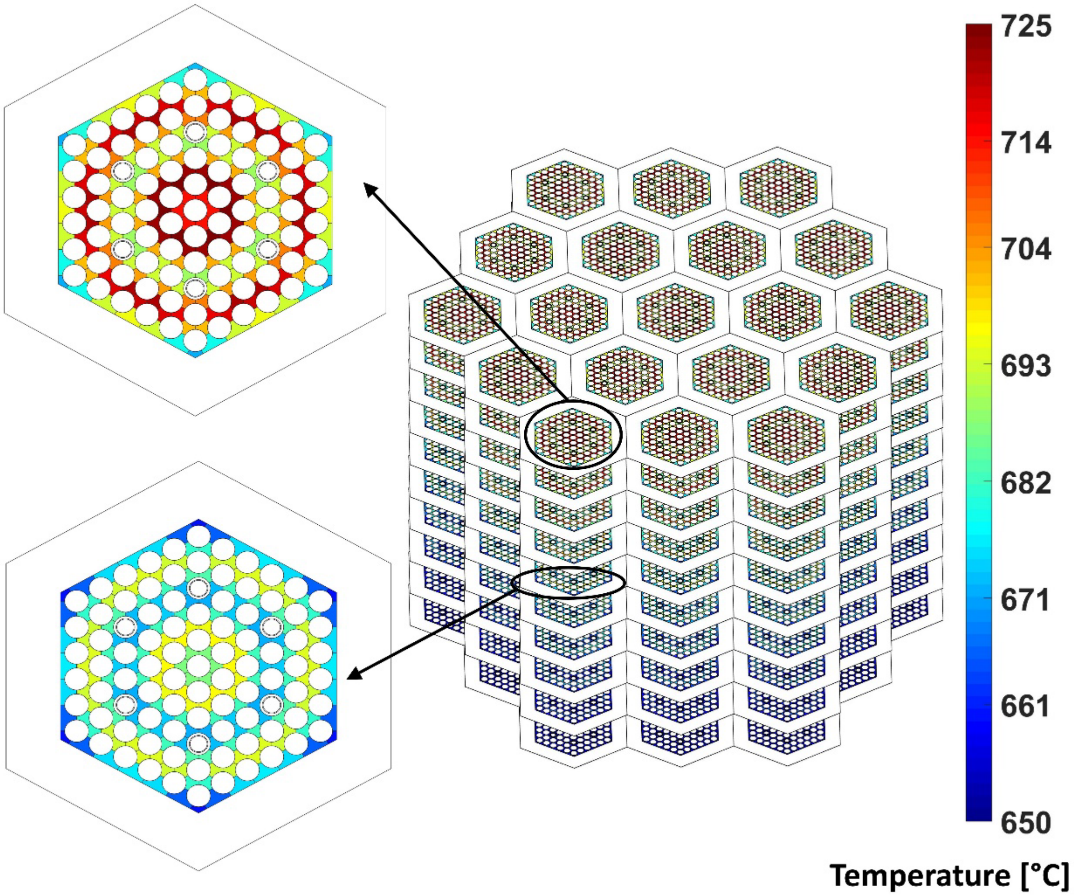

Figure 4.5: 3-D, whole-core temperature profile for the coolant subchannels

In addition to the axial coolant temperature variation caused by heat addition from the fuel pins, large variations in coolant temperatures are also observed within each fuel assembly. From the figure, it can be seen that the corner subchannels have the lowest mean temperature, as they do not directly receive heat from any fuel pins in the assembly. However, the corner subchannels at the core exit still have a mean temperature of ~672°C, which is ~22°C higher than the core inlet temperature. This elevated temperature in corner subchannels is primarily attributed to the inter-channel transport between the corner and the adjacent edge subchannels. The azimuthal conduction in the corner pin also plays a minor role, as heat from hotter subchannels surrounding the corner pin is transferred through the pin, and into the relatively cold corner subchannel. Temperature variations also exist among the edge and interior subchannels, primarily due the differences in the number of fuel pins connected to the subchannel and subchannel mass flow rate. As with the case of fuel pin temperatures, all the core fuel assemblies at an axial level have very similar temperature profiles due to the radially flat power profile. The maximum temperature of the coolant in the pin bundle is ~725°C.

The subchannel mean velocity profile at the exit of the core is shown in Figure 4.6, along with an enlarged image for a single fuel block. While there are no significant variations in velocity distribution from one fuel block to another, the mean velocities of the different subchannels in each fuel assembly show considerable differences. It can be observed from the magnified fuel assembly shown in the figure that the corner subchannels have the lowest mean velocity, followed by the interior subchannels, while the edge subchannels have the highest mean velocity. At the exit of the core where the radial pressure gradients are small and the subchannel flows are approaching mechanical equilibrium, it can be demonstrated that the variations in mean velocities among different subchannel geometries are primarily due to the differences in the hydraulic diameter between the edge, corner and interior subchannels. Differences also exist among the subchannels of same geometry, which is attributed to the density and viscosity changes due to temperature. The average core pressure drop excluding gravity is ~7.2 kPa. The core pressure drop including consideration of the effect of gravity is ~83.7 kPa. It must be noted that the all the pressure drop values reported in this chapter are for the pin bundles in the active core region, and other regions with a very small fraction of coolant flow (such as the guide tube annulus in the control rod assemblies) and the regions outside the active core region (such as the radial reflector coolant channels) are not included in the pressure drop calculation.

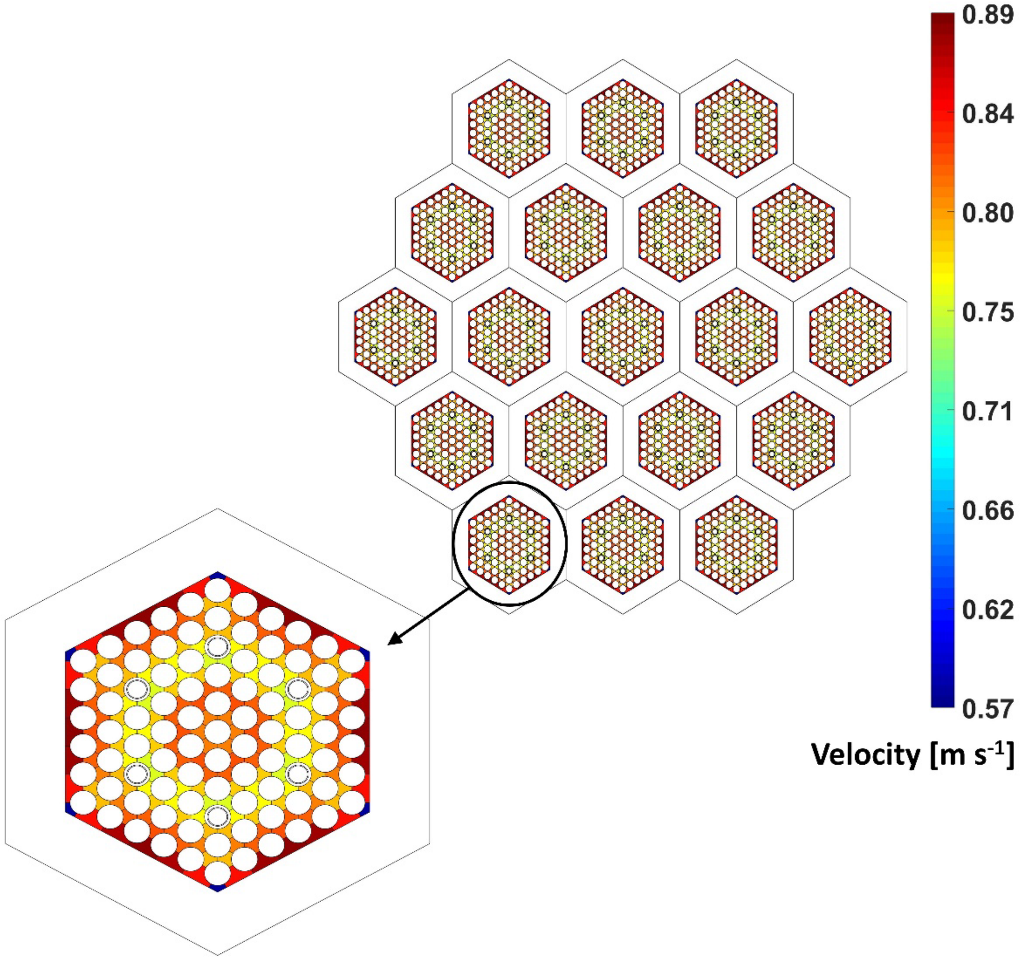

Figure 4.6: Mean coolant velocity distribution at the exit of the core

Following the uniform axial power profile, a radially flat and axially center-peaked power distribution is performed using the same parameters in Table 4.1. This center-peaked power profile is the 'chopped cosine' profile (Figure 3.21) used in the code-to-code comparison between subchannel and CFD models discussed in Chapter 3.

The azimuthally-averaged temperature profiles for the hottest pin in the core are shown in Figure 4.7. Along the length of coolant flow, the slope of the coolant temperature curve initially increases, and then decreases to reflect the axial change in local power density. The axial temperature profiles of the fuel and cladding follow the power profile. The peak centerline temperature for this case, ~1126°C, is ~14% higher than the baseline case with uniform axial power profile. This increase in peak temperature is attributed to the higher local power density for the center-peaked power profile.

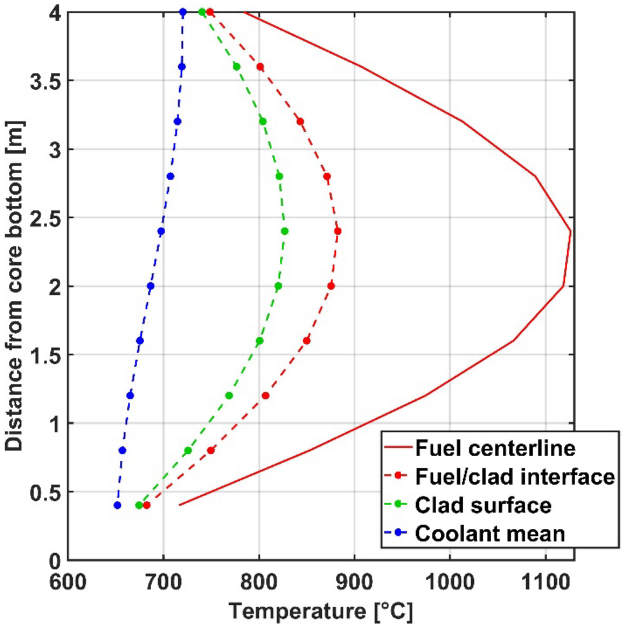

Figure 4.7: Temperature profile for the hottest pin in the core for center-peaked power profile

The whole-core, 3-D temperature profile for the fuel pins for the center-peaked axial power profile is shown in Figure 4.8.

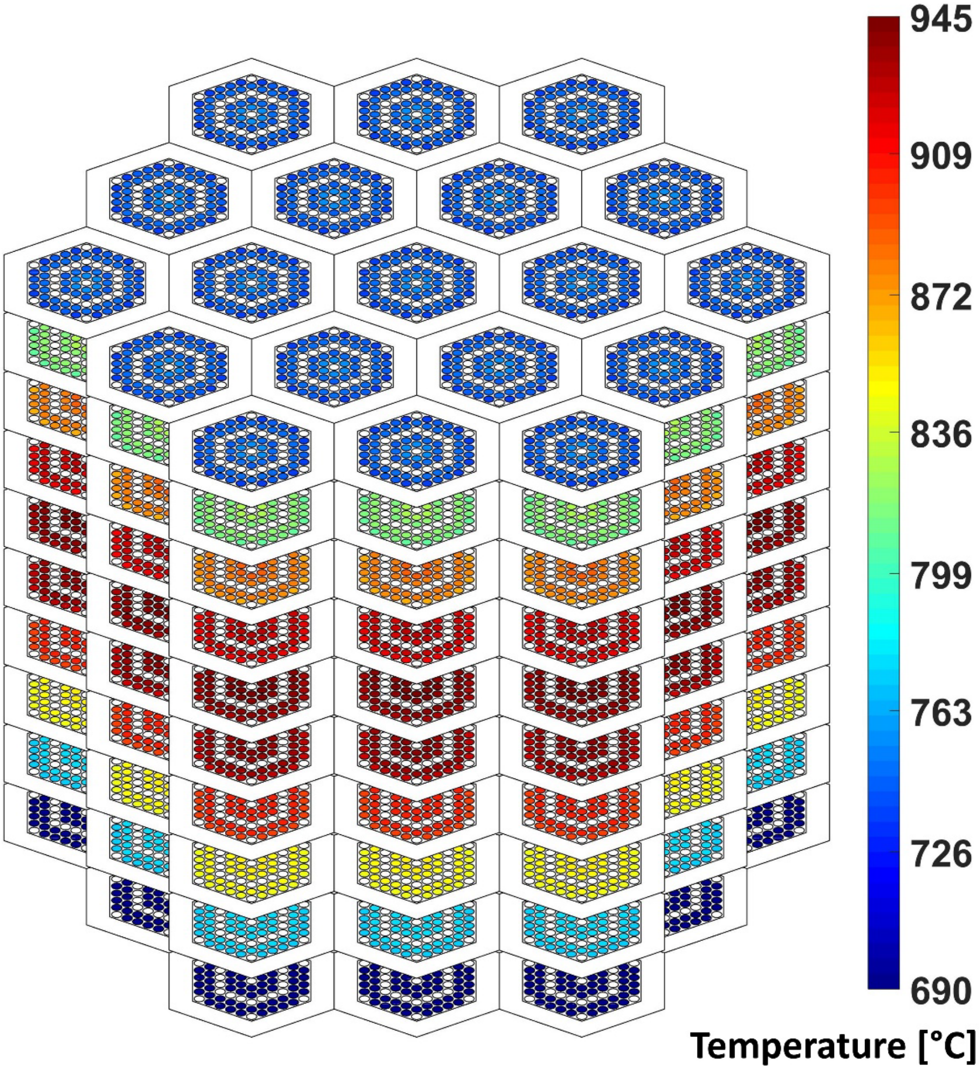

Figure 4.8: 3-D, whole-core fuel pin temperature distribution for center-peaked power profile

It can once again be seen that there are no observable temperature differences between the fuel assemblies in the core, which can be attributed to the radially flat power profile considered here. The 3-D, axial temperature profile follows the same trend as that of the fuel region in Figure 4.7, with the center region of the core being the hottest, while the top and bottom regions of the core are relatively colder. Although the center-peaked power profile has an axial symmetry, it can be still seen that the fuel pin temperatures in the top half of the core are noticeably higher than in the bottom half of the core, which can be attributed to the increase in coolant temperature. The pressure drop for the center-peaked power profile is similar to that of the uniform axial power profile discussed earlier.

Following the analyses with assumed core power profiles, steady-state thermal hydraulic computations are performed using the preliminary pin power distributions from the COMET neutron transport model (Zhang and Rahnema, 2018). The axially integrated pin power distribution is shown in Figure 4.9a, while the 3-D core-level pin power distribution is shown in Figure 4.9b.

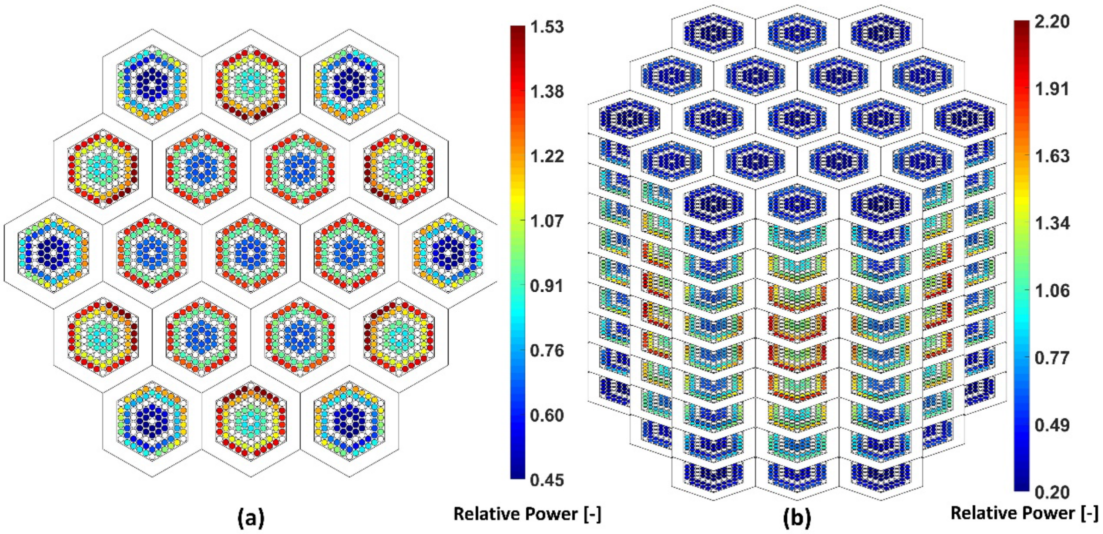

Figure 4.9: COMET power profile (a) axially integrated power profile, and (b) 3-D pin power profile

Once again, the relative power shown in Figure 4.9 is the ratio of local power density to the average power density of the core. These pin power distributions correspond to a near-critical case. The white colored pins shown in Figure 4.9 correspond to non-fuel pins. Additional details about the near-critical case and the COMET model for this

SmAHTR configuration can be found in Rahnema and Zhang (2021). Further information about the neutronics benchmark model and control rod positions for the near-critical case can be found in the work of Reed (2021).

Table 4.2 shows the peak fuel temperature for different core inlet mass flow rates. The pre-conceptual design report for the SmAHTR prescribes a maximum steady-state operating temperature for the fuel to be less than 1250°C, to ensure that there is no unacceptable release of radioactive fission products from the SmAHTR fuel during normal operation.

Table 4.2: Steady-state peak fuel temperatures for different flow rates

Active core region inlet mass flow rate (kg s^{-1})	**Peak fuel temperature (°C)**	**Total core pressure drop (kPa)**
1018	1297.3	83.7
1200	1265.0	86.0
1350	1244.3	88.1
1500	1227.3	90.3
1650	1213.1	92.7
1750	1204.9	94.4

Table 4.2 shows that for the pin power distribution considered in the present study, using the baseline 1018 kg s^{-1} flow rate suggested in the pre-conceptual design report results in a peak fuel temperature that exceeds the safe normal operation limit. The total inlet flow rate to the active core region (the active core region excludes the coolant holes in the radial reflector) is increased to reduce the peak fuel temperature. The coolant inlet temperature is fixed at 650°C while increasing the core inlet flow rate. It can be seen that a coolant flow rate of 1350 kg s^{-1} results in a fuel temperature that is marginally below the safe normal operation limit. For a coolant flow rate of 1750 kg s^{-1}, the peak fuel temperature

~45°C below the safe operating limit, and therefore this case is chosen for further studies. While a coolant flow rate of 1750 kg s^{-1} is substantially above the 1018 kg s^{-1} flow rate prescribed for this configuration in the pre-conceptual design report, it must be noted that a subsequent design variant of the SmAHTR, referred to as SmAHTR-CTC (Ilas et al., 2014) that uses a plate/plank type fuel design and a carbonate thermochemical cycle (CTC) for power conversion, considered core inlet mass flow rates that were ~1750 kg s^{-1}. Therefore, the high core inlet flow rates considered in the present study are still within the operating flow rates being considered for other small modular FHRs. While a further increase in flow rate would result in even lower peak fuel temperatures, the associated pressure drop penalty also increases with increasing flow rate. In addition, the issues related to erosion and wear of tubing in components such as heat exchangers could also be exacerbated at these very high flow rates. Therefore, it is important to ensure that the pumping power for these integral FHRs and other considerations such as erosion and wear are also evaluated when the core mass flow rate is increased. It should also be noted that the peak fuel temperatures in the core could be decreased by flattening the radial and axial power distributions. Another approach to reduce the peak temperatures without a significant increase in core flow rate would be to employ an orifice plate at the inlet of the core that provides more flow to the hotter fuel assemblies in the core.

The detailed steady-state results for the highest flow rate case are discussed next.

Figure 4.10 shows the azimuthally averaged, radial and axial temperature profiles for the hottest fuel pin in the core. As mentioned earlier, the peak fuel temperature for this case is ~1205°C.

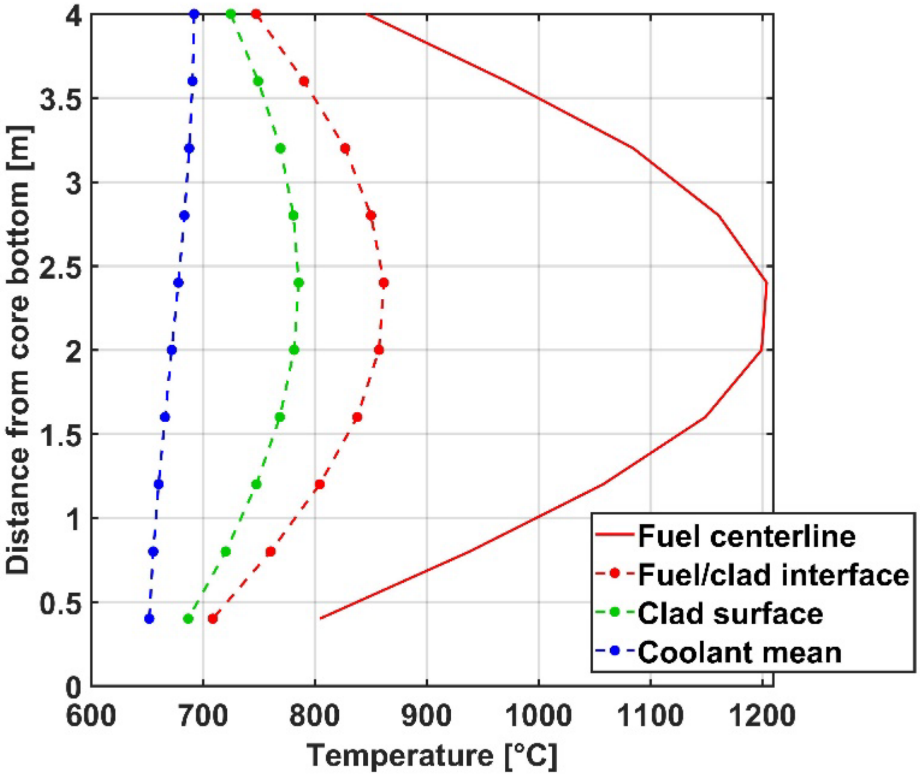

Figure 4.10: Temperature profile for the hottest pin in the core for COMET power profile

The axial temperature profiles for all the regions (fuel, clad, and coolant) correspond to a center-peaked axial pin power profile discussed earlier.

Figure 4.11 shows the shows the 3-D, volumetrically weighted average temperature at each axial location for all the fuel pins in the core.

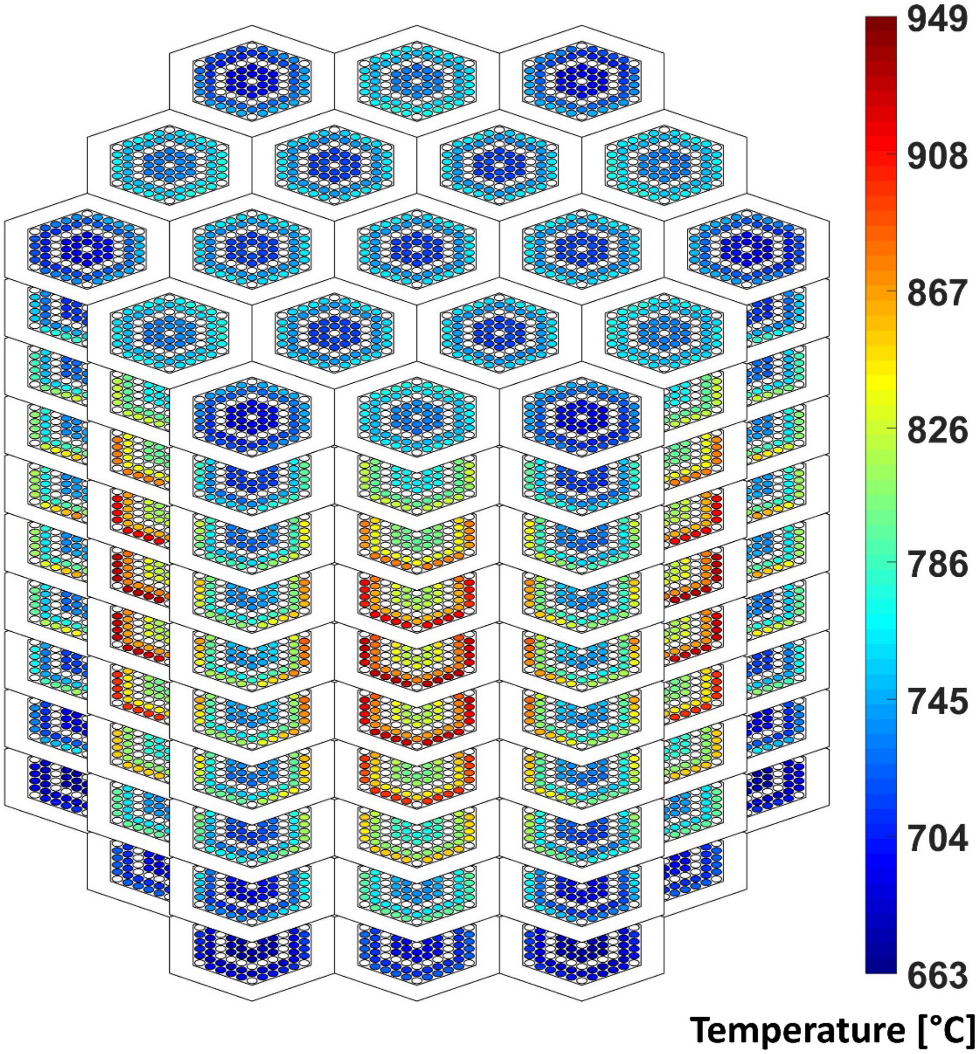

Figure 4.11: 3-D, whole-core fuel pin temperature distribution for COMET power profile

Temperature differences are observed axially, between the fuel assemblies, and within fuel assemblies, corresponding to the 3-D local pin power densities shown in Figure 4.9b.

Figure 4.12a shows the 3-D temperature profile for the moderator pins, hexagonal reflectors, radial reflector, and the coolant channels in the radial reflector in the core. The temperatures of the moderator pins are the volumetrically weighted average temperatures at each axial location.

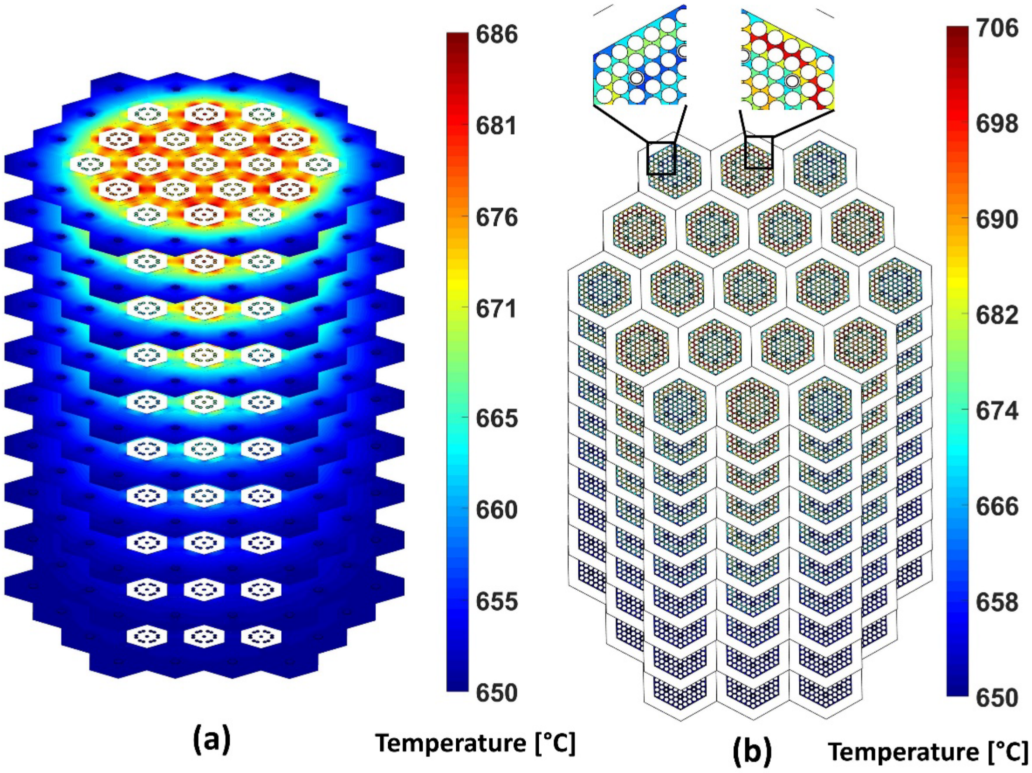

Figure 4.12: COMET power profile results: (a) 3-D moderator and reflector region temperature profile, and (b) 3-D bundle coolant temperature profile

The 3-D, core-level, coolant subchannel temperature distribution in the pin bundle region is shown in Figure 4.12b. The coolant temperature increases from the bottom to the top of the core due to heat addition from the fuel pins. Coolant temperature variations within each fuel assembly (shown by the two magnified images), as well as among the different fuel assemblies, are observed due to the power profile considered in this study.

So far, all the results discussed in this chapter have a prescribed inlet flow rate boundary condition, with the inlet core flow rate equally split among all the 19 fuel assemblies in the core. As discussed previously in Section 2.2.2.6, the present thermal hydraulic model also has the ability to determine the coolant inlet flow rates for each fuel assembly that would provide equal coolant pressure drop across all the fuels assemblies in the core. The inlet flow rates determined by enforcing equal pressure drops across the fuel assemblies could provide a more accurate flow distribution if the differences in power densities across the fuel assemblies in the core are large, such as the case with the COMET power profile investigated in this chapter (Figure 4.9.)

Table 4.3 shows the key results from the equal pressure drop case compared with the uniform flow split case.

Table 4.3: Key results from equal pressure drop and uniform flow split cases

Case	Coolant mass flow rate (kg s^{-1})		Peak fuel temperature (°C)	Peak coolant temperature (°C)	Total core pressure drop (kPa)
	Hot assembly	Cold assembly			
Equal pressure drop	92.8	91.1	1203.8	705.3	94.4
Uniform flow split	92.0	92.0	1204.9	705.8	94.4

The table shows that for the equal pressure drop case, the hot fuel assemblies (the fuel assemblies with the highest power density) in the core receive slightly higher flow rate compares to the cold fuel assemblies (fuel assemblies with lowest power density). However, these inlet flow rate differences are less than 1% from the equal flow split case. From the results shown in the table, it can be seen that for the power profile and flow rate conditions investigated here, the fuel assembly inlet mass flow rates determined using equal pressure drop case are not significantly different from those for the case in which the fuel assembly inlet mass flow rates are assumed to be equal.

4.2 Sensitivity studies

Following the steady-state simulations, studies are performed (using the 1750 kg s^{-1} core flow rate case) to demonstrate the relative insensitivity of the crossflow resistance model and the crossflow tolerance criterion on key results from the core model. These results are summarized in Table 4.4.

Table 4.4 shows that key results such as peak fuel pin temperature, peak coolant subchannel temperature, and core pressure drop (average value for the pin bundle regions in the active region of the core) are insensitive to whether the crossflow resistance is modeled using the Gunter and Shaw (1945) correlation, or a constant value of 0.5 is used. Table 4.4 also shows results in which the subchannel crossflow convergence criterion is included in the overall core model in addition to the subchannel axial mass flow and enthalpy criteria. The crossflow criterion is shown in Equation 2.34 in Section 2.2.3.

Table 4.4: Crossflow resistance and tolerance sensitivity

Crossflow resistance correlation (-)	Crossflow tolerance (-)	Peak fuel temperature (°C)	Peak coolant subchannel temperature (°C)	Core pressure drop (kPa)
Gunter and Shaw (1945)	0.01	1204.9	705.8	94.4
Constant (0.5)		1204.9	705.8	94.4
Constant (0.5)	1	1204.9	705.8	94.4
	100	1204.9	705.8	94.4

It is also seen that changing the crossflow convergence tolerance from 0.01 to 100 has no impact on the results shown in Table 4.4. These sensitivity studies provide the justification for the use of a constant crossflow resistance in steady-state and transient analyses, as well as not including the crossflow convergence criterion (especially for transient cases with predominantly axial flows that are investigated in the present study.)

As outlined in Table 4.1, a nominal value of 20 kg s^{-1} is used as the total inlet flow rate for the radial reflector coolant channels in the core. To understand the impact of the radial reflector coolant channel flow rate on the peak fuel and coolant temperatures, the total coolant flow rate in the radial reflector coolant channels is increased from 20 kg s^{-1} to 50 kg s^{-1}. Table 4.5 shows the results from both these cases. These simulations have been performed for the COMET power profile case with the active core region (the 19 fuel assemblies) inlet flow rate of 1750 kg s^{-1}.

Table 4.5: Radial reflector coolant channel flow rate sensitivity

Radial reflector coolant channel flow rate (kg s^{-1})	Peak fuel temperature (°C)	Peak coolant subchannel temperature (°C)
20	1204.9	705.8
50	1204.9	705.8

It is seen from the table that the coolant flow rate in the radial reflector coolant channels does not have a significant impact on the peak fuel and coolant temperatures. Figure 4.13 shows the heat transfer path from the pin bundle region to the radial reflector coolant channel. The heat transfer from the pin bundle to the radial reflector coolant channels involves multiple resistances including the convection resistance between the pin bundle coolant and the hexagonal reflector, conduction resistance through the hexagonal and radial reflectors, interface resistance between the hexagonal and radial reflectors, and convection resistance between the radial reflector and the coolant in the radial reflector coolant channels. The high heat transfer resistance due to the combination of these conduction, convection, and contact resistances leads to a very low fraction of heat generated in the core being transferred from the pin bundles to the outer graphite reflector regions in the core. This low heat transfer rate therefore explains the insensitivity of peak fuel and coolant temperatures in the core to the increase in the flow rate through the radial reflector coolant channels.

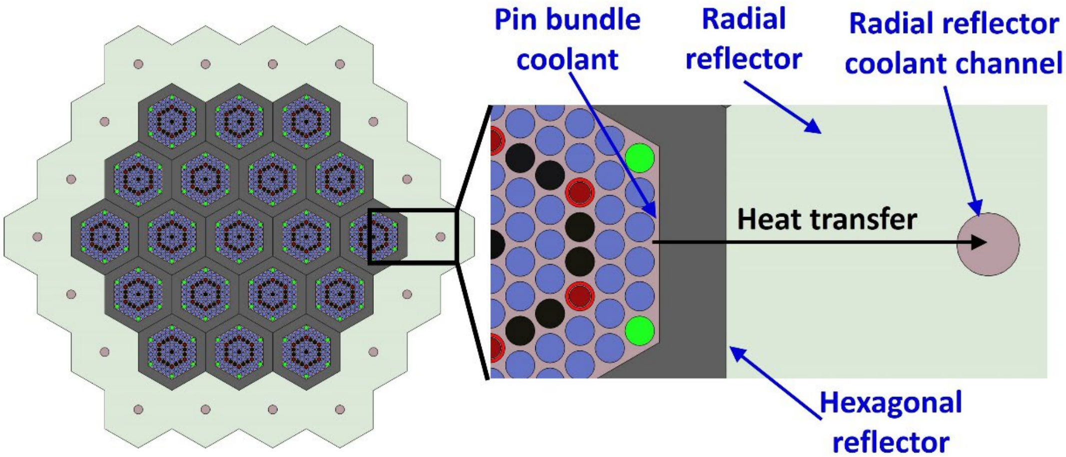

Figure 4.13: Heat transfer path from pin bundle region to the radial reflector coolant channel

CHAPTER 5. STEADY-STATE THERMAL HYDRAULIC MODELING AND ANALYSIS OF ANNULAR PIN-FUELED SMAHTR

Following the steady-state analyses of the solid pin-fueled SmAHTR, the other proposed pin bundle design with annular fuel pins is investigated in this chapter. The objective here is to demonstrate that the subchannel-based thermal hydraulic modeling framework developed in this study can be extended to analyze annular pin-fueled FHR configurations. The extension of the subchannel model, code-to-code verification between CFD and subchannel models, and whole-core analyses for the annular pin-fueled SmAHTR are discussed in this chapter.

5.1 Annular pin-fueled SmAHTR geometry

The reactor system and the core cross-section for the annular fuel configuration are similar to the solid pin fuel configuration (Figure 2.1b). The core consists of a total of 19 fuel assemblies. Five layers of fuel assemblies, each 0.8 m in height, are stacked to a total core height of 4 m. Each fuel assembly has 15 fuel pins and four moderator pins. Each fuel pin has an active fuel region sandwiched between two graphite sleeves. TRISO UCO fuel kernels 500 μm in diameter are loaded into this active fuel region with a volumetric packing density of 50%. Similar to the solid pin-fueled SmAHTR design, the cylindrical inner housing for the fuel assembly in the pre-conceptual design resulted in a substantial amount of coolant flowing through the large, unobstructed gap between the cylindrical housing and the bundle periphery. To ensure sufficient coolant flow rates through the interior of the bundle, this study considers a hexagonal inner housing instead of a cylindrical housing. The fuel assemblies from the pre-conceptual design and the present study are shown in Figure 5.1a and Figure 5.1b. The tie rods shown in the figure provide mounting for the shorter annular fuel segments to create a 4-m-long annular fuel pin (Greene et al., 2011). Table 5.1 shows the key dimensions of the fuel and moderator pins.

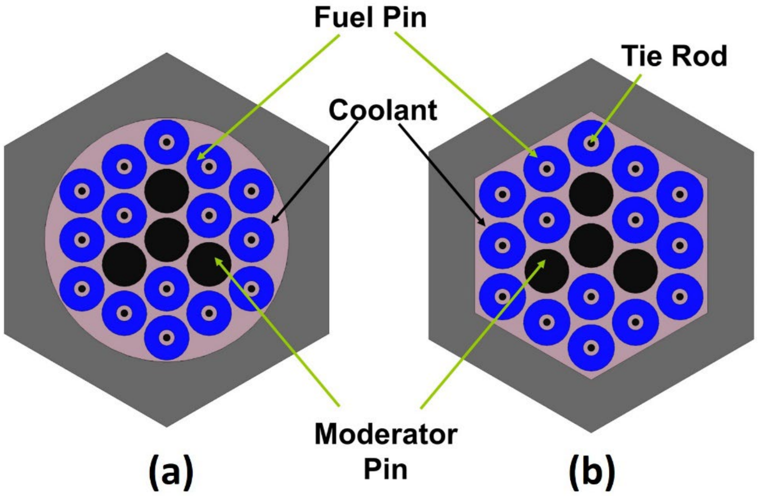

Figure 5.1: Annular pin-fueled SmAHTR (a) pre-conceptual design (Greene et al., 2011), and (b) present study

Table 5.1: Fuel and moderator pin key dimensions

Parameter	Value
Original pitch (mm)	67.8
Modified pitch (mm)	70.9
Radius of tie rod (mm)	5.0
Inner radius of inner sleeve (mm)	11.0
Inner radius of active fuel region (mm)	14.0
Outer radius of active fuel region (mm)	29.5
Outer radius of outer sleeve (mm)	32.5
Radius of moderator pin (mm)	30.8

5.2 Steady-state thermal hydraulic modeling

5.2.1 Solid region

The representative discretization for the annular fuel pin is shown in Figure 5.2. The active fuel, graphite sleeve/cladding, tie rod, and annulus channel (the region between fuel pin and the tie rod through which the coolant flows in addition to the pin bundle region) are also shown in the figure.

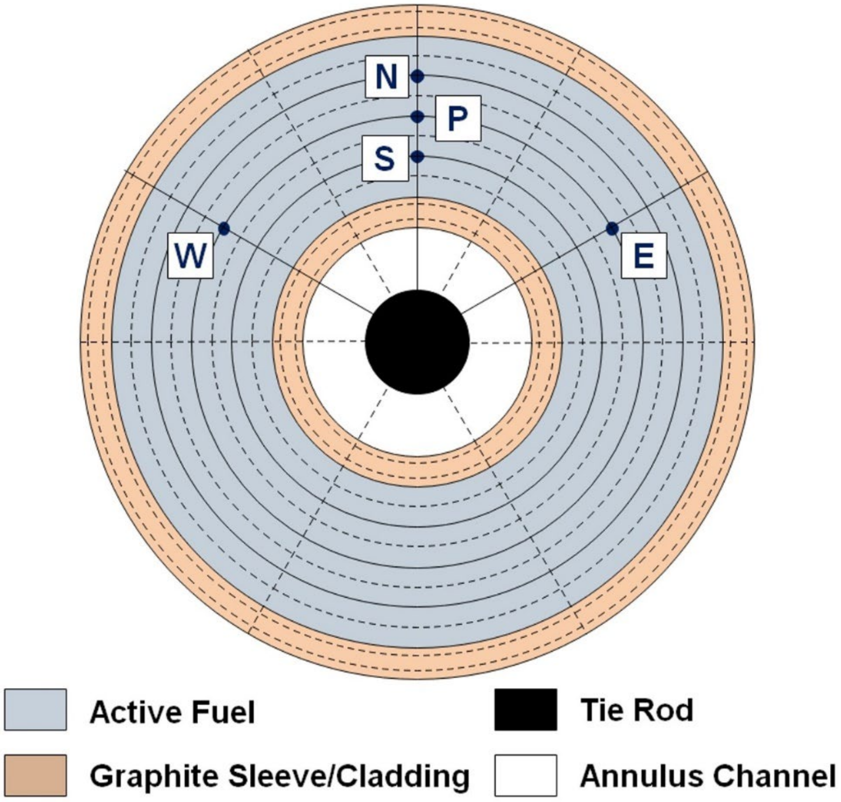

Figure 5.2: Representative annular fuel pin discretization

The fuel pin is divided into finite volumes and the temperatures are determined by performing an energy balance over each finite control volume. For the volume with the center node *P* shown in Figure 5.2, the energy balance is written using the using the east, west, north, south, top and bottom convention. The resulting equation is similar to that of the equation for the solid fuel pin (Equation 2.1) shown in Chapter 2. The conduction modeling for the moderator pins, as well as the hexagonal and radial graphite regions for the annular pin-fueled SmAHTR is similar to that used for the solid pin design discussed in Chapter 2.

5.2.2 Fluid region

The fluid region for this fuel configuration has the FLiBe coolant flowing through the hexagonal pin bundle as well as the annulus region between the fuel pin and the tie rod (the annulus channel region). Figure 5.3 shows the fluid region discretization for a fuel assembly.

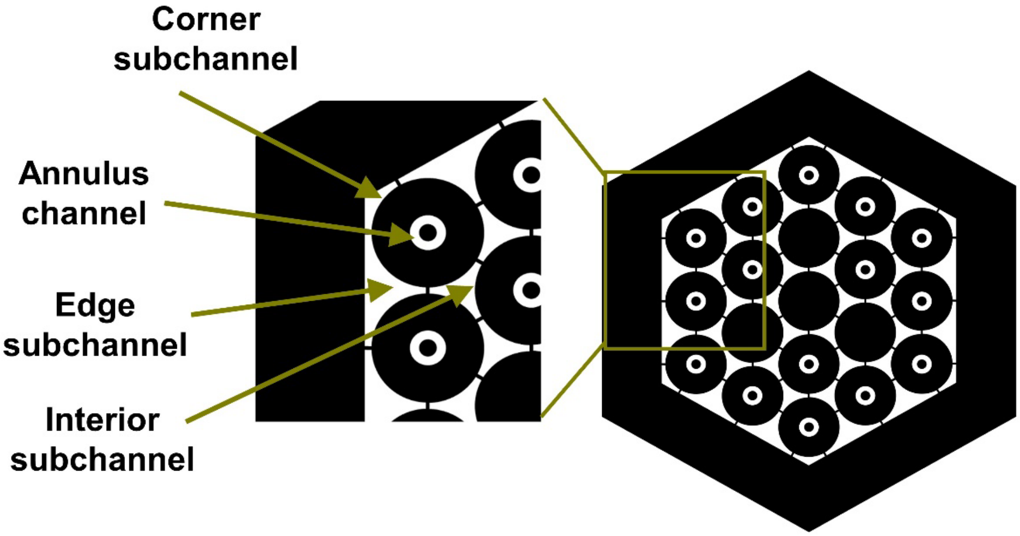

Figure 5.3: Fluid region discretization for the annular pin-fueled SmAHTR

The coolant in the pin bundle region is discretized into corner, edge and interior subchannels and the resulting mass, momentum and energy equations are systematically solved. The subchannel solution methodology for the annular pin-fueled configuration is similar to the one for the solid pin-fueled configuration discussed in Chapter 2. The subchannel closure models for the axial friction factor, heat transfer coefficient, lateral resistance and turbulent mixing are summarized in Table 5.2.

Table 5.2: Subchannel model closure relations

Closure Relation	Description
Friction factor	Cheng and Todreas (1986) (all flow regimes)
Heat transfer coefficient	Sieder and Tate (1936) (laminar regime) Gnielinski (1976) (transition and turbulent regimes)
Lateral resistance	Gunter and Shaw (1945) (option 1) 0.5 (option 2)
Turbulent mixing	Petrunik (1973)

For the annulus channels, the 1-D forms for mass, momentum and energy equations (Equations 2.6-2.8) shown in Chapter 2 are solved. For the annulus channels, the appropriate closure relations for heat transfer coefficient and friction factor in the laminar, transition and turbulent flow regimes are identified and employed in the thermal-hydraulic model. These are listed in Table 5.3.

Table 5.3: Annulus channel closure relations

Closure Relation	Description
Friction factor	Shah (1978) (laminar regime) logarithmic interpolation (transition regime Re < 5000) Kakac et al. (1987) (transition; Re > 5000 and turbulent regimes)
Heat transfer coefficient	Lundberg et al. (1963) (laminar regime) Gnielinski (1976) (transition and turbulent regimes)

The laminar friction factor correlation for the annulus channels shown in Table 5.3 includes the effect of the hydrodynamic development. The local laminar Nusselt number as a function of the non-dimensional channel length from the inlet is first determined using the calculation procedure outlined in the work of Lundberg et al. (1963). It must be noted that the work by Lundberg et al. (1963) provides the local Nusselt numbers for thermally developing flow in annular ducts, while the laminar heat transfer in annulus channels in the present case might be affected by both hydrodynamic and thermal (simultaneous) development effects. However, as pointed out in Kays et al. (2004), for fluids with relatively higher Prandtl numbers (>5) such as the FLiBe coolant considered here (with a Prandtl number of ~15 at core inlet), the thermal-entry solutions provide a good approximation even if the velocity profile is developing simultaneously. A curve fit for the local Nusselt number obtained from the work of Lundberg et al. (1963) as a function of non-dimensional channel length is then developed, and numerically integrated (up to the appropriate channel length) to determine the average Nusselt number.

The boundary conditions for the subchannel equations include specified mass flow rate and enthalpy at the inlet, zero inlet crossflow, and zero radial pressure gradient at the exit. The individual subchannel inlet mass flow rates are estimated from the total mass flow rate entering the hexagonal pin bundle by using a uniform mass flux assumption. For the annulus channels, the inlet flow rate and enthalpy are specified, along with zero radial pressure gradient at the exit. Similar to the solid pin-fueled model, the annular pin-fueled thermal hydraulic model employs a procedure that iteratively adjusts the fraction of the inlet-flow split between hexagonal pin bundles and annulus channels in the core to achieve equal pressure drop across all channels in the core.

The entire pin bundle region in each fuel assembly is treated as a single channel in this procedure. The total inlet mass flow rate through the bundle is the sum of the individual subchannel mass flow rates. This leads to a total of 16 channels (1 pin bundle channel + 15 annulus channels) in each fuel assembly in the core. Figure 5.4 shows a simple illustration of the inlet mass flow rate estimation procedures used for the annular pin-fueled model.

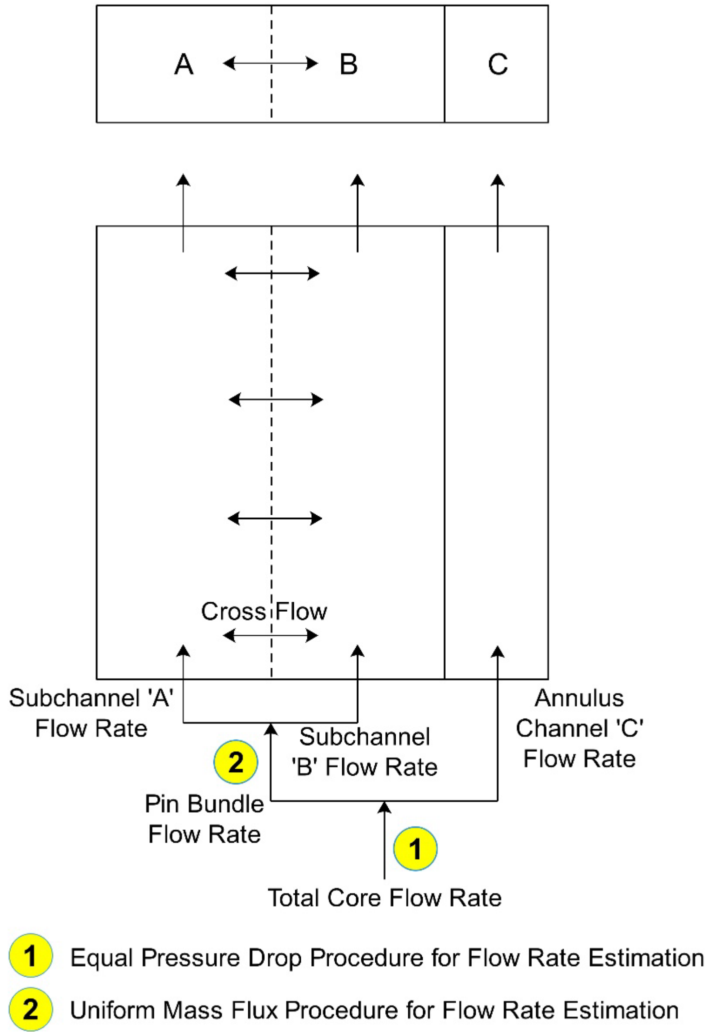

Figure 5.4: Mass flow rate estimation procedure

The core in this illustration has a pin bundle that consists of two subchannels (‘A’ and ‘B’), and an annulus channel (‘C’). The equal pressure drop procedure is used to estimate the inlet-flow split between the pin bundle and the annulus channel. Once the pin bundle inlet flow rate is determined, the inlet mass flow rates for the individual subchannels (‘A’ and ‘B’) are then determined using the uniform mass flux procedure.

The overall model structure for the annular pin-fueled model is similar to one for the solid pin-fueled model discussed in Section 2.2.3.

5.3 Code-to-code comparison

The subchannel-based model developed in the present study is compared with a CFD model for a preliminary verification. The CFD model domain is shown in Figure 5.5.

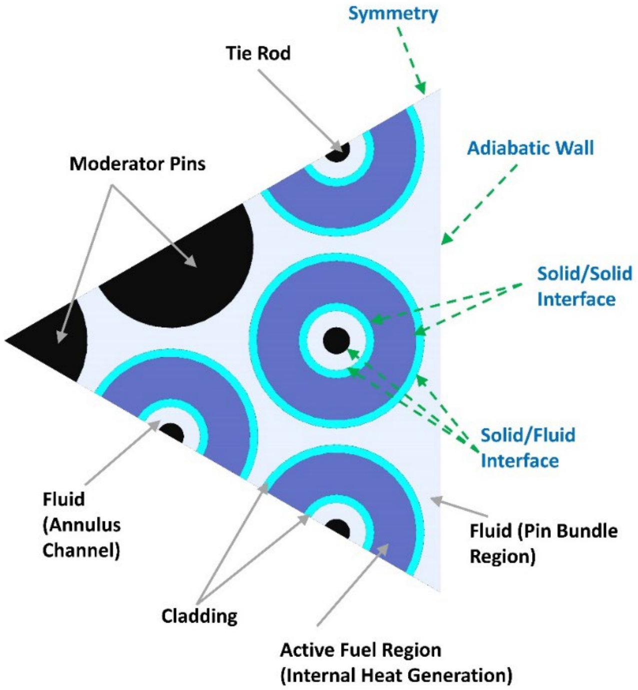

Figure 5.5: CFD model domain

This domain represents a 1/6th section of the fuel assembly shown in Figure 5.1b. The fuel pins have an active fuel region surrounded by a graphite matrix coating. Volumetric heat generation is assigned to these active fuel regions in the model domain. The moderator pins and tie rods are represented in black color in the figure, and these regions have zero heat generation. Symmetry boundary conditions are assigned to the appropriate boundaries, and an adiabatic wall boundary condition is assigned at the coolant/inner hexagonal wall interface (Figure 5.1b). The coolant temperature and mass flow rate are specified at the inlet of the bundle and a constant pressure is specified at the bundle exit. It is to be noted that for this code-to-code comparison study, a uniform mass flux boundary condition is used to determine the inlet mass flow rates for both the pin bundle and annulus channel regions (the equal pressure drop procedure is not used for the subchannel-based model.) This is done to enable a consistent comparison between the CFD and subchannel models.

Figure 5.6 shows the grids used in this study. For all three grids, the solid region and the freestream of the bulk fluid flow (referred to as freestream region) in the model domain employ triangular prism elements.

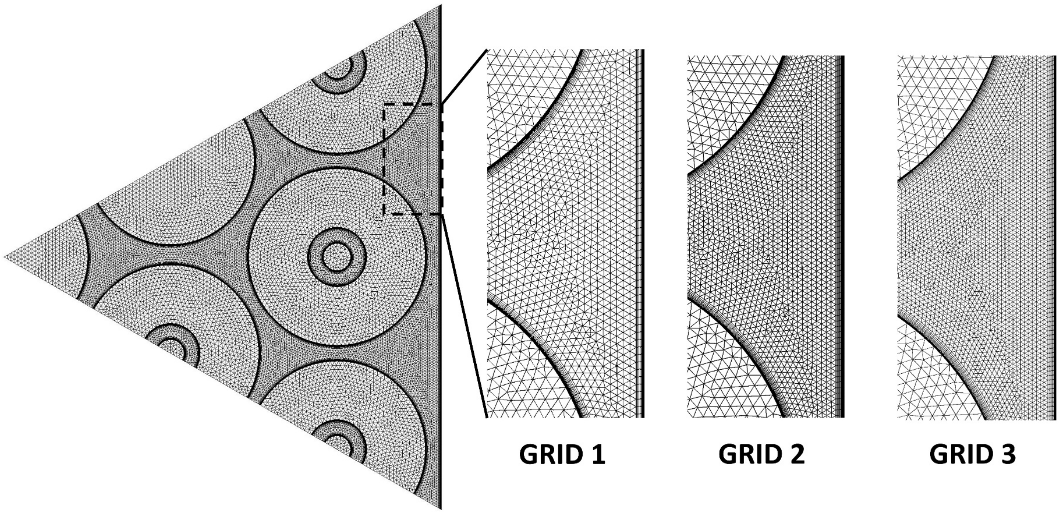

Figure 5.6: CFD model grids

The axial grid size in both the solid and fluid regions is 5 mm. The maximum grid size in the cross-section of the solid region is 1.50 mm. Grid independence studies are conducted by successively reducing the maximum grid size of the freestream fluid cross-section from the baseline case by a factor of 1.3, while the axial grid spacing and solid region grid are held constant, similar to the study by Palomino and El-Genk (2019a). The grids labeled as ‘GRID 1’, ‘GRID 2’, and ‘GRID 3’ in Figure 5.6 have a fluid cross-section freestream grid spacing of 0.96 mm, 0.74 mm, and 0.57 mm, respectively. A wall grid is implemented in the fluid region near the walls to resolve the viscous sublayer. The baseline wall grid has a total of 13 layers and a growth rate of 1.2. The total thickness of the wall grid is ~1 mm. The thickness of the first cell closest to the wall is chosen such that $y^+ < 1$. Table 5.4 shows a summary of the different grids used in this study.

Table 5.4: Summary of CFD model grids

Parameter	GRID 1	GRID 2	GRID 3
Axial grid spacing (mm)	5.00	5.00	5.00
Solid region grid size (mm)	1.50	1.50	1.50
Freestream grid size (mm)	0.96	0.74	0.57
Number of elements (-)	~28.5 M	~37.7 M	~51.5 M

The three-dimensional continuity, momentum and energy equations for the fluid region, and the three-dimensional energy equation for the solid regions are solved. The RANS modeling approach is used to account for the turbulence in the fluid region of the model domain. The *k-ω* SST model is chosen as the turbulence model. The simulations are performed using the commercial CFD code, FLUENT (ANSYS, 2021). The pressure-velocity coupling is achieved using the SIMPLE algorithm. The convective terms in the governing equations are discretized using a second-order upwind scheme. Convergence is deemed to be achieved when the normalized residuals for flow and turbulence quantities are less than 10^{-5}, and the normalized residual for the energy equation is less than 10^{-6}.

The peak temperature for all the fuel pins in the model domain is compared for the three grids employed in this study. From the results, 'GRID 2' is deemed to have sufficient grid independence, as the maximum difference in peak fuel pin temperature is < 1°C when compared to the values from 'GRID 3'. The CFD model results reported in this study are therefore from 'GRID 2'. Figure 5.7a shows the peak temperatures for the fuel pins in the model domain from both subchannel and CFD models.

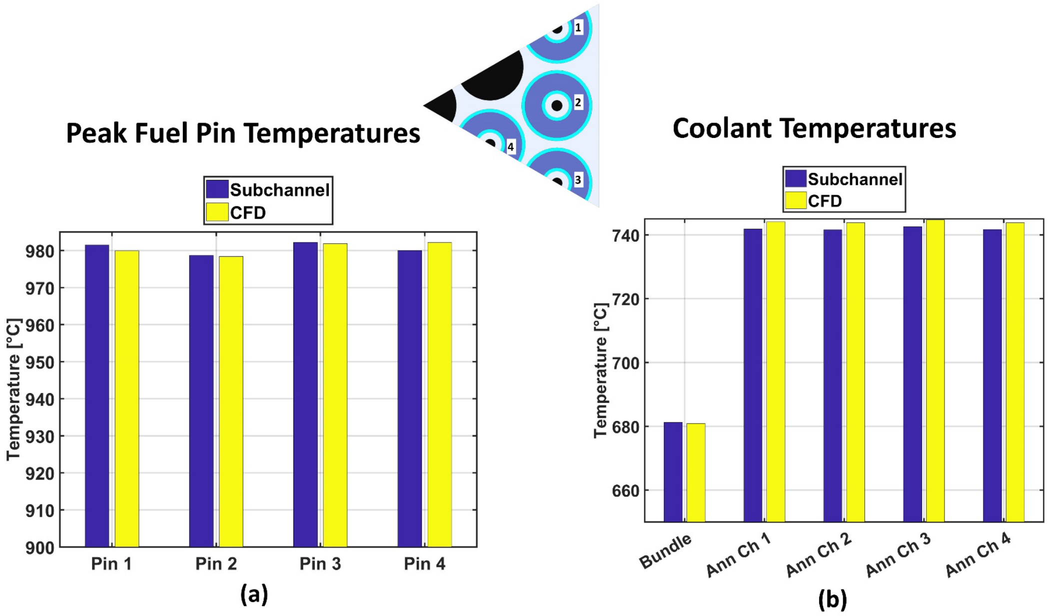

Figure 5.7: Comparison between CFD and annular fuel pin subchannel models (a) fuel pin peak temperatures, and (b) coolant temperatures

From the figure, it can be seen that the results predicted by the subchannel and CFD models have excellent agreement, with a maximum difference of ~2°C (for fuel pin 4). For the subchannel and CFD models, Figure 5.7b shows the mean coolant temperature at the core exit for the pin bundle and annulus channels. The annulus channel numbers (1-4) shown in Figure 5.7b correspond to the fuel pin numbers indicated in Figure 5.7. From the figure, it can be seen that both the subchannel and CFD models predict a larger coolant mean temperature at the core exit for the annulus channels compared to the pin bundle. The mean temperature values predicted by the subchannel and CFD models are also in good agreement.

Figure 5.8a and b show the temperature profiles at the core exit from the CFD and subchannel models, respectively.

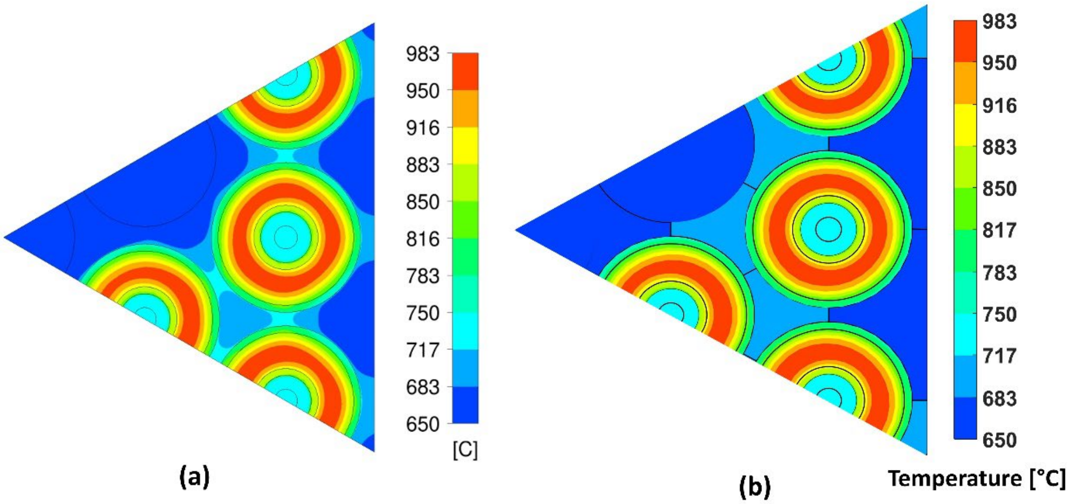

Figure 5.8: Core exit temperature profile for the annular pin-fueled configuration (a) CFD model, and (b) subchannel model

From these figures, it can be seen that the temperature values and distribution for the fuel pins are consistent and agree well with each other. From Figure 5.8b, it can be seen that the subchannel model is also able to predict azimuthal fuel pin temperature variations that exist due to the differences in mean fluid temperatures and heat transfer coefficients in the subchannels surrounding each fuel pin. The fluid temperatures shown in Figure 5.8b are the mean subchannel and annulus channel temperatures. While it is not possible to directly compare the coolant temperatures between the CFD and subchannel models, it can be seen that the temperature distribution, in general, is consistent between the two models.

Figure 5.9 shows the static pressure (excluding gravity) in the core predicted by the CFD and subchannel models.

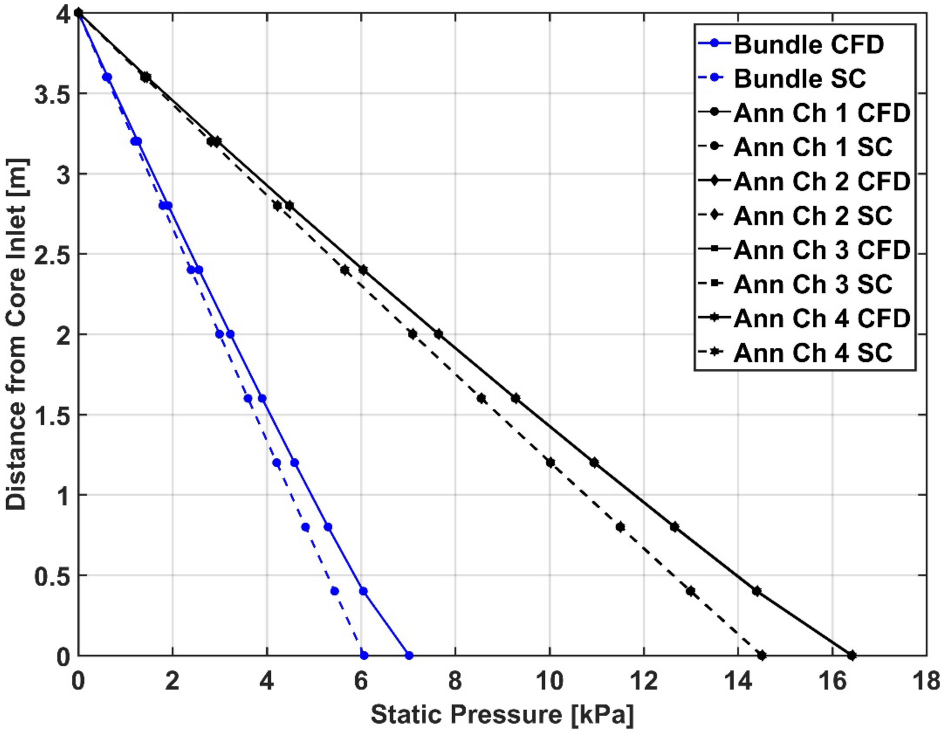

Figure 5.9: Pressure drop profile for CFD and subchannel models

The static pressure at the core exit is set to zero in both the CFD and subchannel models. The static pressure at the core inlet represents the total pressure drop (excluding gravity) for the pin bundle and annulus channels regions in the model domain. It can be seen that the pin bundle and annulus channels have significantly different pressure drops, which is a result of the uniform mass flux boundary condition prescribed at the core inlet. The total bundle pressure drop predicted by the CFD model is ~14% higher than the subchannel model prediction. For the annulus channel region, the pressure drop predicted by the CFD model is ~12% higher than the subchannel model prediction. These results indicate good agreement between the CFD and subchannel models.

5.4 Whole-core results

The thermal-hydraulic model developed in the previous section is employed in investigating the temperature, flow rate and pressure profiles for the SmAHTR with annular fuel pin configuration. The key input parameters used in the analysis are shown in Table 5.5.

Table 5.5: Annular fuel pin model key input parameters

Parameter	Value
Total power	125 MW(t)
Coolant inlet flow rate (active core)	1325 kg s^{-1}
Coolant inlet flow rate (radial reflector coolant channels)	50 kg s^{-1}
Coolant inlet temperature	650°C

The mass flow rate for the active core region shown in the table is from the pre-conceptual design document (Greene et al., 2011). The core power and coolant inlet temperature are similar to the values employed for the solid pin-fueled SmAHTR analysis. A nominal value of 50 kg s^{-1} is used as the total flow rate into the radial reflector channels in the core. The core is axially divided into 10 segments, while each fuel pin in the core has 11 radial segments (5 in the active fuel region, and 3 segments each in the inner and outer graphite sleeve/cladding regions). The Gunter and Shaw (1945) correlation (option 1 in Table 5.2) is used for calculating the lateral resistance for the pin bundle geometry. The equal pressure drop procedure is used to determine the inlet flow distribution between the pin bundles and annulus channels in the core.

An arbitrary radial power variation among the different fuel assemblies is considered in this study (Figure 5.10a). The power factor shown in Figure 5.10a is the ratio of total power generated within a fuel assembly to the average fuel assembly power. All the fuel pins within a given fuel assembly are assumed to have the same power generation. A center-peaked power profile, as shown in Figure 5.10b, is used for all the fuel pins in the core to model the axial variation in pin power density.

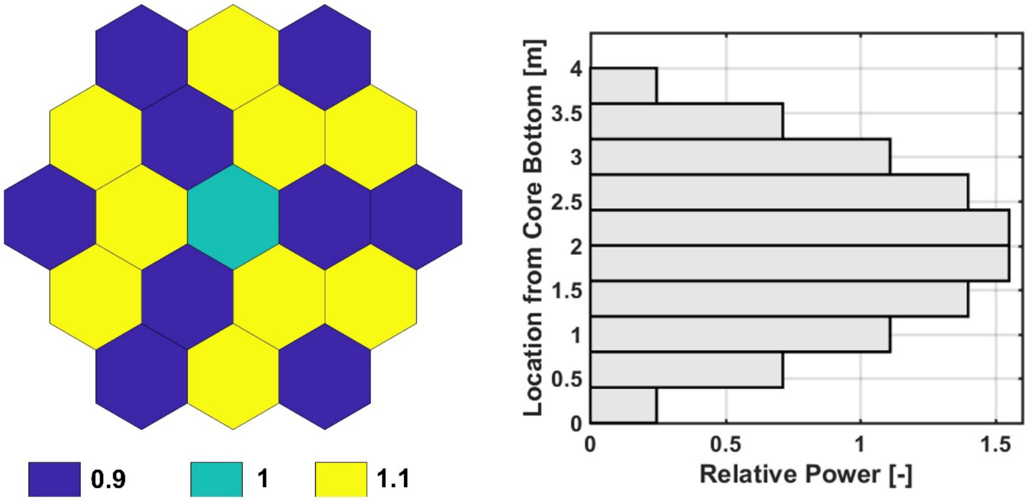

(a) (b)

Figure 5.10: (a) Radial power distribution, and (b) axial power distribution

The radial and axial temperature profiles of the hottest fuel pin in the core are shown in Figure 5.11. The local peak fuel pin temperature for the case investigated in this study is ~1202°C, which is located in the active fuel region at an axial location immediately above the core center.

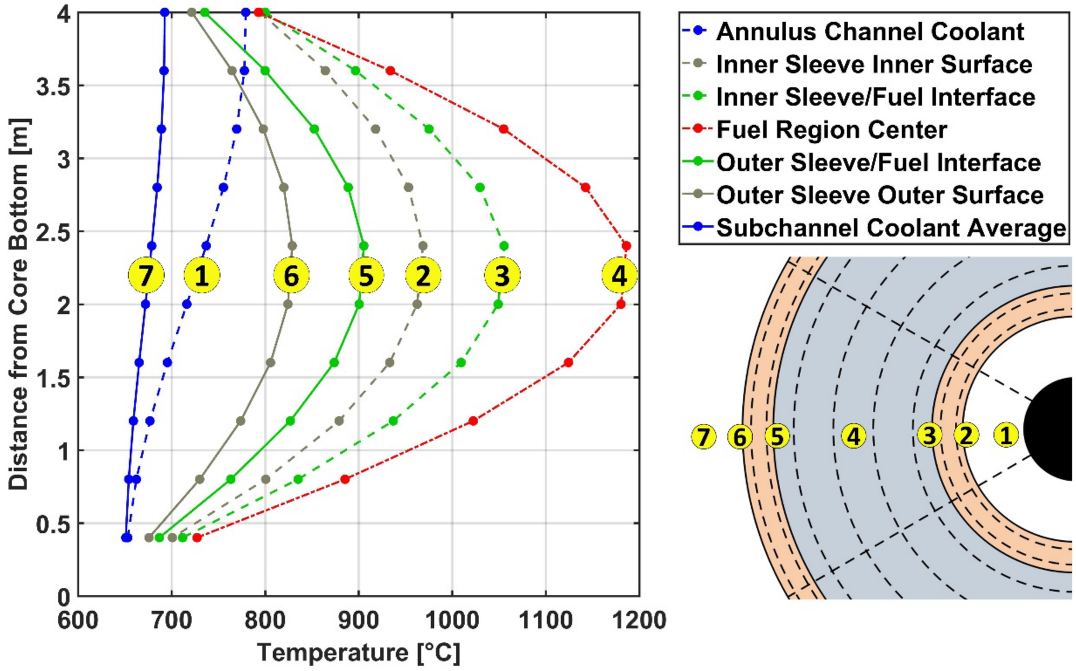

Figure 5.11: Axial and radial temperature profile for the hottest annular fuel pin in the core

In Figure 5.11, the numbered items on the different curves in the temperature plot indicate a radial location on the fuel pin. From the figure, it can be seen that the coolant temperature in the annulus channel (Curve #1) is significantly higher than the average temperature in the subchannels (Curve #7) surrounding the outer surface of the pin. The slope of the coolant temperature in both the subchannel as well the annulus channel regions has an axial increase followed by an axial decrease, which corresponds to the axial variation in the pin power density. The surface temperature of the inner sleeve (Curve #2) is also significantly higher than the outer sleeve surface temperature (Curve #6). The conduction resistance through the inner sleeve region results in the temperature difference between the inner sleeve inner surface (Curve #2) and the inner sleeve/fuel interface (Curve #3). Similarly, the conduction resistance in the outer sleeve region results in the temperature difference between Curves #5 and #6. Curve #4 in the figure corresponds to the center of the active fuel region.

Figure 5.12 shows the 3-D, volumetrically weighted average temperature at each axial location for all the fuel pins in the core.

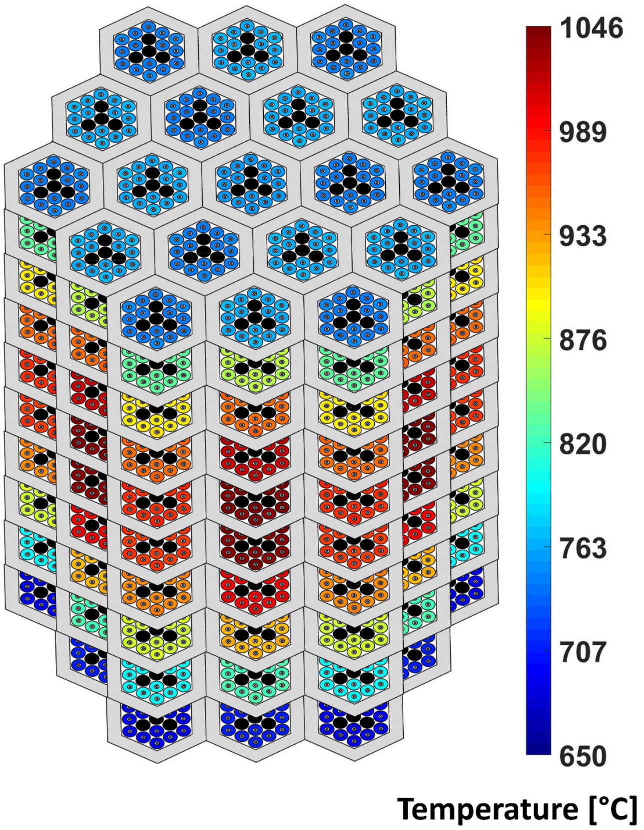

Figure 5.12: Whole-core, 3-D average fuel pin temperature profile for annular fuel pin configuration

Temperature differences are observed both axially as well as among the different fuel assemblies, which is expected for the radial and axial power profiles applied in this study. The black colored pins correspond to the moderator pins in the fuel assembly. The pin temperature variations within a fuel assembly are not significant, which is due to the radially flat power profile assumed within each fuel assembly.

Figure 5.13 shows the 3-D temperature profile for the key non-fuel elements (moderator pins, hexagonal reflectors, radial reflector, and the coolant channels in the radial reflector) in the core.

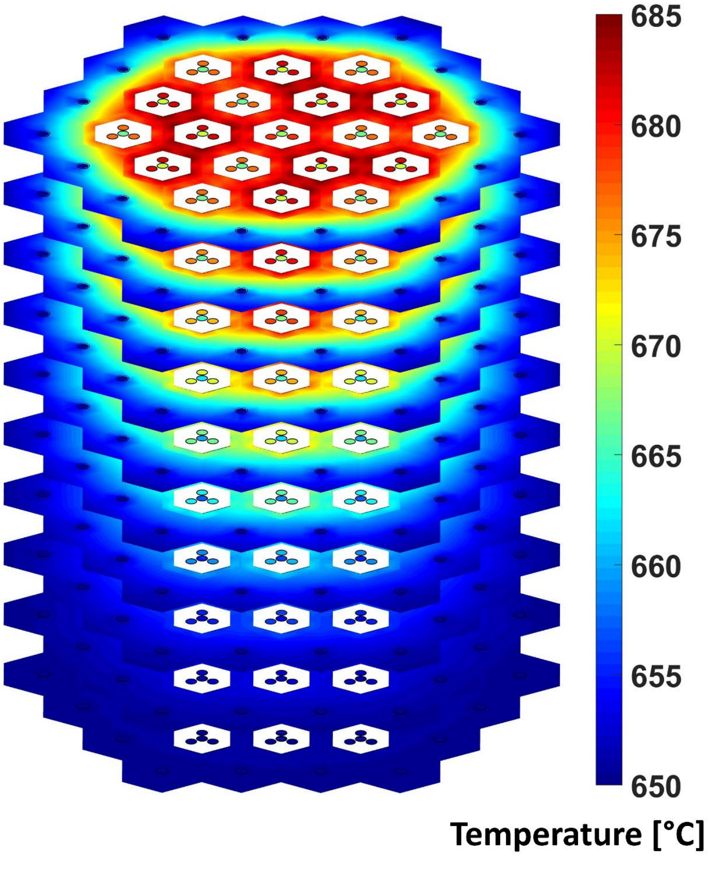

Figure 5.13: Whole-core, 3-D non-fuel region temperature profile for annular fuel pin configuration

The temperature of the moderator pins is the volumetrically weighted average temperature at each axial location. As with the case of Figure 5.12, moderator pin temperature differences are observed both axially as well as among the different fuel assemblies in the core. Axial temperature differences are also seen in the hexagonal reflectors and the radial reflector.

Figure 5.14 shows the mean temperature distribution at the exit of the core. One of the fuel assemblies and a magnified view of that assembly is also shown in the figure.

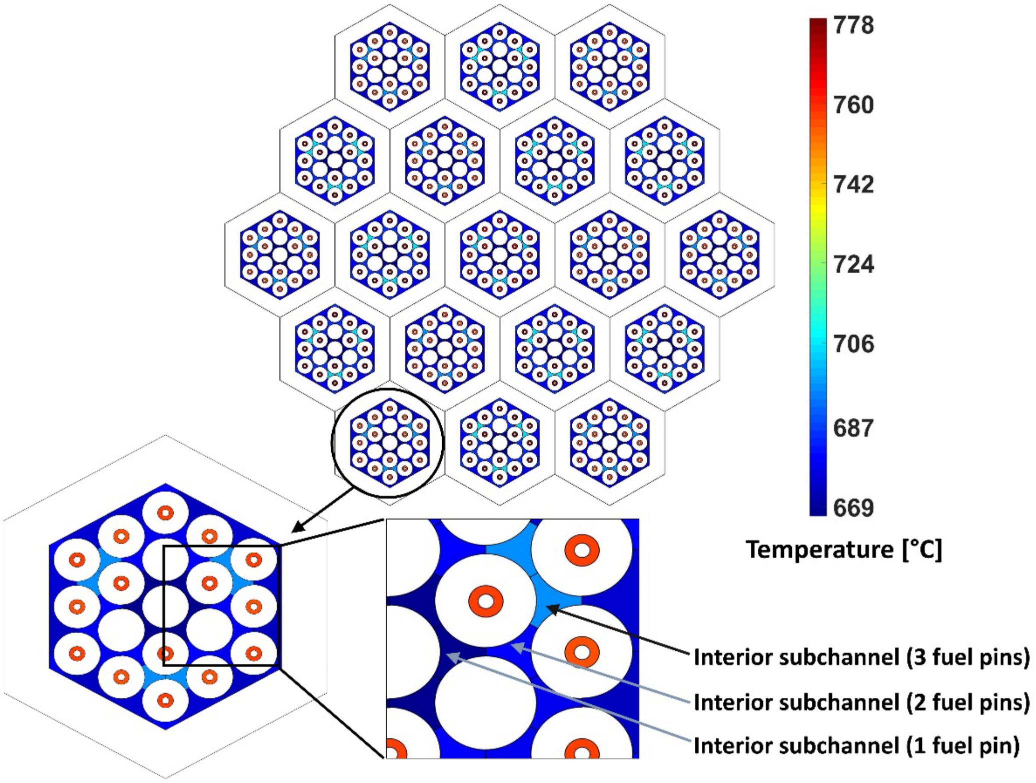

Figure 5.14: Core exit coolant temperature profile for annular fuel pin configuration

From the figure, it can be seen that the mean temperatures of the annulus channels are higher than the subchannel temperatures in the pin bundle region. Within the pin bundle region, the interior subchannels connected to three fuel pins have the highest mean temperature, while the interior subchannels connected to only one fuel pin have the lowest mean temperature. For the single fuel assembly shown in Figure 5.14, the coolant flowing through the annulus channels accounts for ~9% of the total mass flow rate, while transporting ~28% of heat generated in the fuel assembly.

The 3-D, core-level coolant temperature distribution in the pin bundle region is shown in Figure 5.15.

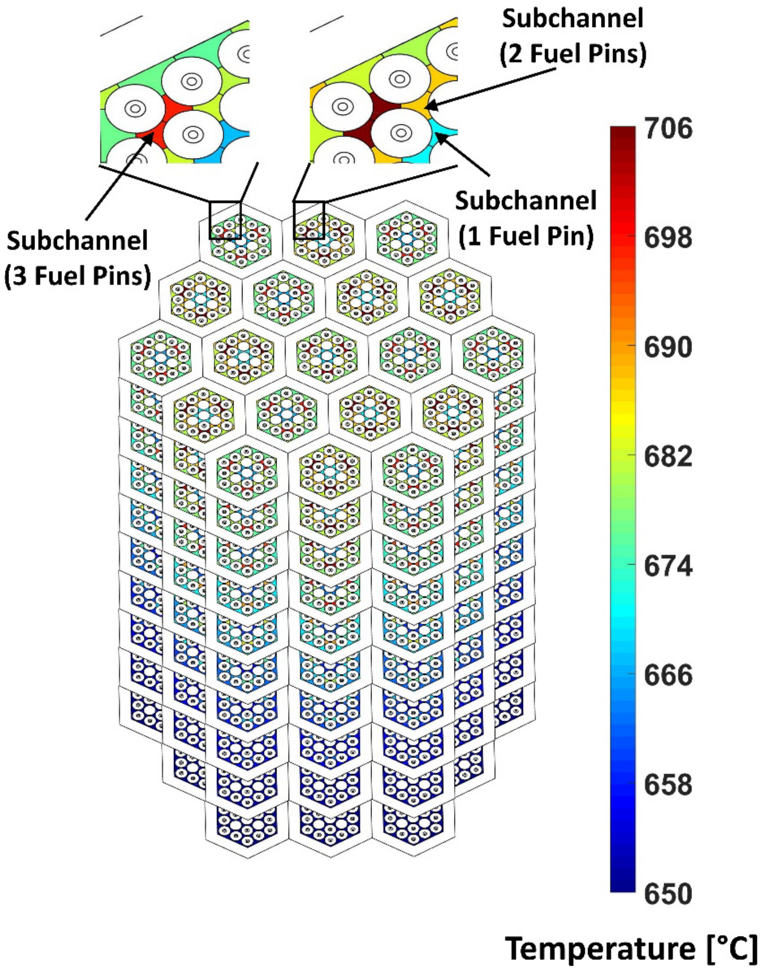

Figure 5.15: Whole-core, 3-D pin bundle coolant temperature profile for annular fuel pin configuration

The coolant temperature increases from the bottom to the top of the core due to heat addition from the fuel pins. In addition to the coolant temperature variations within each fuel assembly, temperature variations are also observed among the different fuel assemblies (shown by the two magnified images) due to the radial power profile applied in this study. The interior subchannels connected to 3, 2 and 1 fuel pins are also shown in Figure 5.15.

Figure 5.16 shows the mean velocity distribution at the exit of the core. One of the fuel assemblies and its magnified view are also shown.

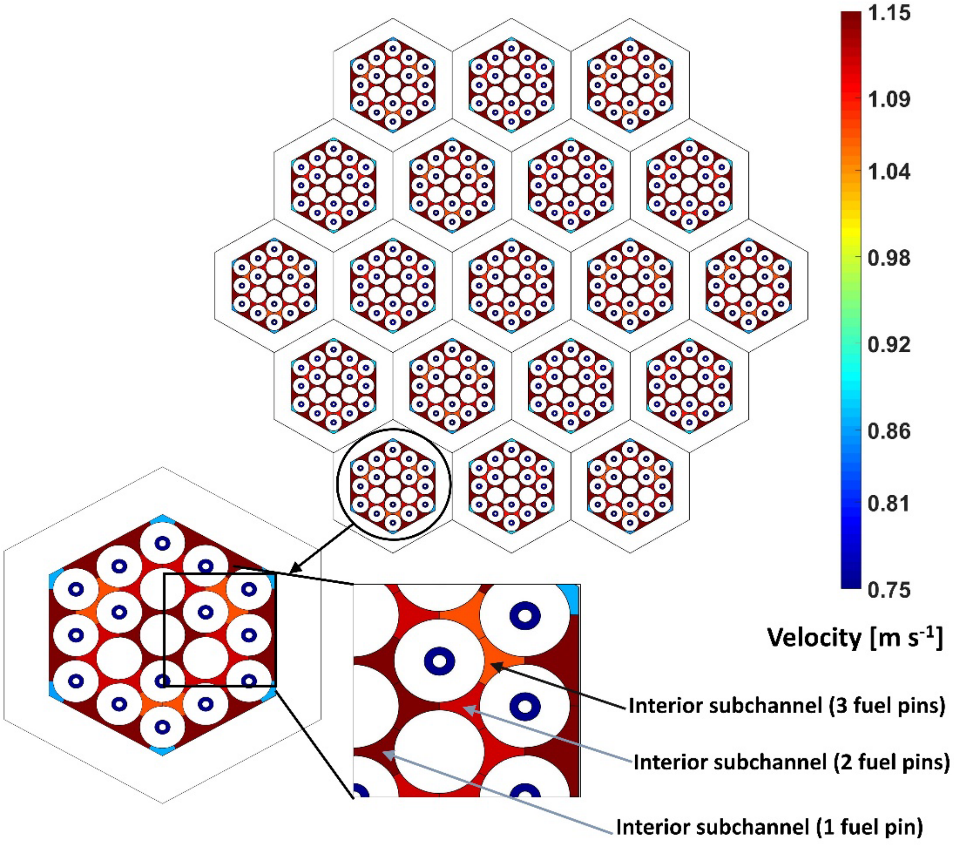

Figure 5.16: Core exit velocity profile for annular fuel pin configuration

From the figure, it can be seen that the annulus channels have a lower mean velocity compared to the subchannels in the pin bundle region. This variation in mean velocities can be attributed to the differences in the hydraulic resistance between the annulus channels and the pin bundle. Within the pin bundle, the corner subchannels have the lowest mean velocity, followed by the interior subchannels, and the edge subchannels have the highest mean velocity. It must be noted that while radial pressure gradients can exist between the different subchannels in a fuel assembly, the actual magnitude of these radial gradients is typically small, especially close to the exit of the core. For these negligible radial pressure gradients, it can be demonstrated that the variations in mean velocities among different subchannel geometries are primarily due to the differences in the hydraulic diameters. The outer diameter of the moderator pin (61.6 mm) is slightly smaller than the outer diameter of the fuel pin (65 mm) for this fuel configuration. The difference in moderator and fuel pin diameters results in hydraulic diameter variations among the different interior subchannels in the fuel assembly. These variations in hydraulic diameters in addition to temperature-dependent fluid properties cause the mean velocity differences between the interior subchannels as shown in magnified fuel assembly in Figure 5.16. For the magnified fuel assembly, the total pressure drop, including gravity, is ~83 kPa (for both pin bundle and annulus channels). The pressure drop excluding gravity is ~6.5 kPa for the pin bundle and ~7.4 kPa for the annulus channels. These pressure drop differences are attributed to the temperature-dependent density variations that result in different gravitational pressure drops for the pin bundle and the annulus channels. It must be noted that the present model does not account for the inlet and exit pressure losses. The SmAHTR pre-conceptual design report does not include any information on the core support structures near inlet and outlet, and flow distributors near the inlet of the core for this annular fuel configuration. When the information becomes available, the entrance and exit pressure drops can be readily included in the flow distribution procedure developed in this study.

Figure 5.17 shows the effect of varying the core inlet mass flow rate on the maximum fuel pin temperature in the core. The normal operation temperature limit for the fuel (1250°C) is also shown in the figure.

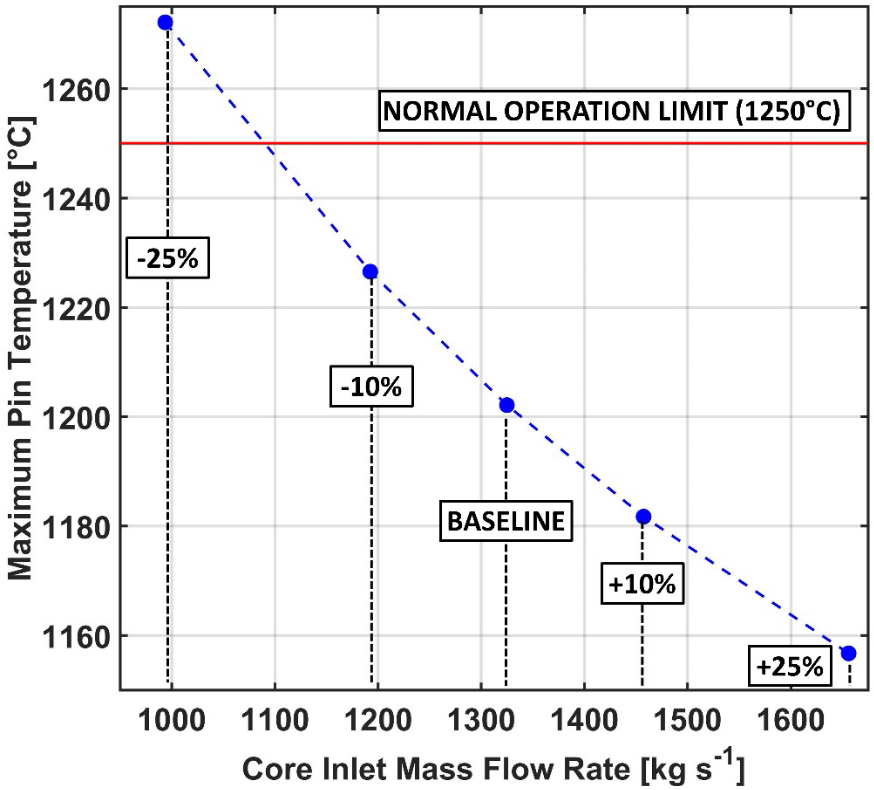

Figure 5.17: Effect of core inlet flow rate on maximum fuel pin temperature for annular fuel configuration

It can be seen from the figure that increasing the core inlet flow rate from the baseline value by 10% and 25% results in lower maximum fuel temperatures. This reduction in maximum fuel temperature is due to (1) the increase in heat transfer coefficient (2) decrease in mean coolant temperature that result from a higher mass flow rate. Similarly, decreasing the coolant flow rate by 10% and 25% from the baseline value results in higher maximum fuel pin temperatures. For the lowest core flow rate investigated, the maximum fuel pin temperature is above the normal operation limit for this reactor configuration.

Table 5.6 shows the total inlet core mass flow rate, bundle and annulus channel inlet velocities, bundle and annulus channel Reynolds numbers (Re), and core-level pressure drop for the different mass flow rates investigated. From the Re values listed in Table 5.6, it can be seen that the flow through the bundle is in the fully-turbulent flow regime according to the transition criterion by Johannsen (1983) (~4200 for a pitch-to-diameter ratio of ~1.1), while the flow through the annulus channels is in the laminar or transition flow regime.

Table 5.6: Mass flow rate parametric study for the annular fuel pin configuration

Total mass flow rate (kg s^{-1})	Bundle velocity (m s^{-1})	Annulus channel velocity (m s^{-1})	Bundle Reynolds number (-)	Annulus channel Reynolds number (-)	Pressure drop (kPa)
993.8	0.84	0.61	5582.5	2119.6	80.4
1192.5	1.01	0.69	6748.1	2381.7	82.1
1325.0	1.13	0.74	7517.5	2584.3	83.2
1475.5	1.25	0.80	8283.5	2793.8	84.5
1656.3	1.42	0.90	9430.3	3118.0	86.6

It can also be seen from Table 5.6 that the pressure drop through the core increases with increasing mass flow rates. The increase in pressure drop is predominantly due to the increase in the frictional losses, which in turn are directly proportional to the fluid velocity (or mass flow rate) through the core. The pressure drop considered here also includes the gravitational pressure drop incurred in moving the coolant upwards through the core. From the table, it can be seen that increasing the core flow rate from 993.8 kg s^{-1} to 1656.3 kg s^{-1} (an increase of ~67%), increases the core-level pumping power by ~80%. In addition to the pumping power through the core, an increase in core inlet mass flow rate will also increase the pumping power through other reactor elements (primary heat exchangers, plenum regions, etc.). Therefore, the total pumping power could be significantly larger for the entire reactor system.

CHAPTER 6. TRANSIENT THERMAL HYDRAULIC MODELING AND ANALYSIS OF SOLID PIN-FUELED SMAHTR

The application of the subchannel-based whole-core thermal hydraulic model for normal operation of solid- and annular-pin fueled SmAHTR configurations was discussed in the previous chapters. As mentioned in Section 2.2, the thermal hydraulic model can also be used for transient analysis that involve various postulated accident scenarios for the SmAHTR. The details of the time stepping scheme, transient code-to-code verification, system-level coupling, and the results for two different postulated accident scenarios – protected loss of heat sink (P-LOHS) and unprotected transient overpower (U-TOP) accident, are discussed in this chapter.

6.1 Adaptive time stepping scheme

Both the solid and fluid region models discussed in Section 2.2 employ a fully implicit scheme for temporal discretization, and therefore, the overall thermal hydraulic model does not have stability-based time step size restriction. While the choice of time step is not limited by stability constraints, it must still be judiciously chosen to accurately capture the transient variations during accident simulation. Many accident scenarios have the characteristic of rapid transients for some duration of the accident, and much slower transients during other time periods. Therefore, using a constant time step for the entire duration of the accident might either penalize the ability to capture fast transient changes (if a large constant time step is used) or computational runtime (if a small constant time step is used). The present model includes an adaptive time stepping scheme that uses small time steps in regions with large variations and large time steps in regions with slow changes. The model uses a resolution control time stepping scheme, which is based on the basic time step controller implemented in the work by Akakpo (2016) for simulating hydrocarbon reservoirs. In this scheme, the largest temperature change between the current and previous time steps is first determined for all the solid and fluid regions in the core. The size of the next time step is then determined based on this largest temperature change, ΔT_{max}, the set temperature resolution, ΔT_{set}, and the current time step size, Δt_t, using Equation 6.1.

$$\Delta t_{t+1} = \alpha \cdot \left(\frac{\Delta T_{set}}{\Delta T_{max}}\right) \cdot \Delta t_t \tag{6.1}$$

The set temperature resolution can be set to any value (such as 5°C.) The adaptive time stepping scheme then adjusts the next time step size such that the maximum temperature difference between the current and next time steps is close to 5°C. The present scheme rejects the results from the current time step if the largest temperature change (ΔT_{max}) is greater than the set resolution (ΔT_{set}). In this case, the current time step size is then halved (after the rejection) and the results are recomputed. A time step reduction factor, α (with typical values of ~0.8-0.9) is also added to Equation 6.1 to reduce the number of rejected time steps. To ensure that the size of the time step does not get too small or too large, a user-defined maximum and minimum limit is also placed on the time step size predicted from Equation 6.1, similar to that implemented in the work of Akakpo (2016). In some cases, it is possible that the minimum user defined time step size is still unable achieve the set temperature resolution. At this point, the user needs to either increase the set resolution, the time step reduction factor, or reduce the minimum time step size to enable the use of the adaptive time stepping scheme.

6.2 Transient code-to-code comparison

The transient version of the subchannel model developed in Section 2.2 is compared to a transient CFD model to perform preliminary code-to-code comparison. The model domain (Figure 3.10) and the baseline mesh (Figure 3.11a) from the steady state CFD analysis are used in this transient study. The Fluent (ANSYS, 2021) CFD code is used for the computations. Pressure-velocity coupling is achieved using the SIMPLE algorithm. The convective terms in the governing equations are discretized using a second-order upwind scheme. Computations are performed on a single node from the partnership for an advanced computing environment (PACE, 2017) computing cluster, using 16 cores of the Dual Intel® Xeon Gold 6226 CPU. Convergence is deemed to be achieved for this transient CFD model when the normalized residuals for flow and turbulence quantities are less than 10^{-4} and the normalized residual for the energy equation is less than 10^{-6}.

The total flow rate into the core at steady-state is taken to be 1018 kg s^{-1} in these simulations, based on the value provided in the SmAHTR pre-conceptual design report (Greene et al., 2011). Transient simulations are performed using both the CFD and subchannel models for a scenario in which the inlet core flow rate varies with time. Initially, the core is operating at steady-state at 100% flow rate value (1018 kg s^{-1} for the total core). The core flow rate is then linearly decreased for the next 30 seconds to ~67% ($2/3^{rd}$) of the initial flow rate. Finally, the core flow rate is linearly ramped-up back to the initial (100%) flow rate in the next 60 seconds. The transient simulations are continued until the core approaches a steady state. The transient mass flow rate profile is shown in Figure 6.1a. The core power and the coolant inlet temperature are held constant throughout the entire duration of these simulations.

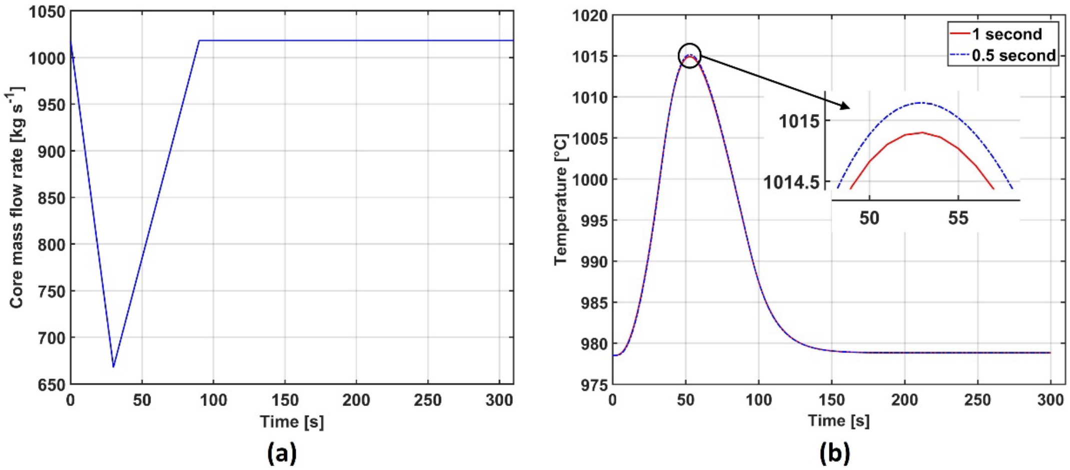

Figure 6.1: Code-to-code comparison (a) transient mass flow rate profile, and (b) CFD time step independence

The coolant flow rate used in the CFD model corresponds to the transient mass flow rate profile shown for the core in Figure 8a, but scaled down appropriately for 1/12th of a single fuel assembly. Similarly, the coolant flow rate is scaled down appropriately for the subchannel model domain, which in this case is a whole single fuel assembly.

CFD simulations with two different time step sizes, 0.5 s and 1 s, were performed to establish time step independence. The peak fuel pin temperatures from the two simulations are shown in Figure 6.1b. The figure shows that the temperature difference between the two simulations is very small, thus demonstrating that the 1 s time step is sufficient.

For the adaptive time stepping scheme in the subchannel model, the set temperature resolution (ΔT_{set}) is 0.5°C, with the option to reject the time step if the maximum temperature (ΔT_{max}) is greater than the set resolution. A time step reduction factor (α) value of 0.8 is used in Equation 6.1 to ensure that too many time steps are not rejected. The time step size is bound to a minimum value of 0.01 s and a maximum value of 10 s.

Figure 6.2a shows the maximum temperatures for the fuel and cladding regions, as well as the coolant mean temperatures at the inlet and outlet of the fuel pin bundle, predicted by the CFD and subchannel models (the subchannel model is labeled as ‘SC’ in the figures).

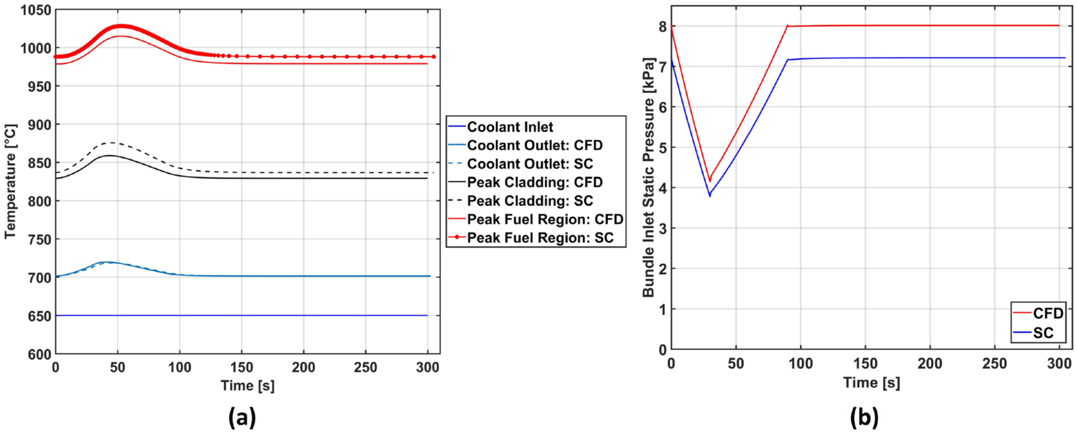

Figure 6.2: Code-to-code comparison (a) fuel, cladding, and coolant temperatures, and (b) pressure drop

The figure shows good agreement between the two models. The highest fuel temperature value (for the entire transient) predicted by the CFD model is ~1015°C, while the value predicted by the subchannel model is ~1028°C. For the subchannel model, the distance between the red dots in the peak fuel region curve (Figure 6.2a) show the time step size. The adaptive time stepping algorithm employs very fine time steps in the first half of the simulation, when the temperatures are changing rapidly, and uses larger time steps for the next half of simulation in which the changes are slow. Figure 6.2b shows the bundle pressure drop (excluding gravity) predicted by the CFD and subchannel models as a function of time. Good agreement is seen between both models, with ~10% difference in the pressure drop predicted between the CFD and subchannel models at 30 seconds where the core flow rate is the lowest, and ~11% difference at 300 seconds as the model approaches steady state.

The temperature profiles for the solid and fluid regions at the exit of core are shown in Figure 6.3 for three different times (~0 s, 25 s, and 50 s). The slightly different time instants between the CFD and subchannel models is a consequence of using the adaptive time stepping scheme for the subchannel model. These figures show good agreement between the CFD and subchannel model predictions of the transient increase in solid fuel pin temperatures.

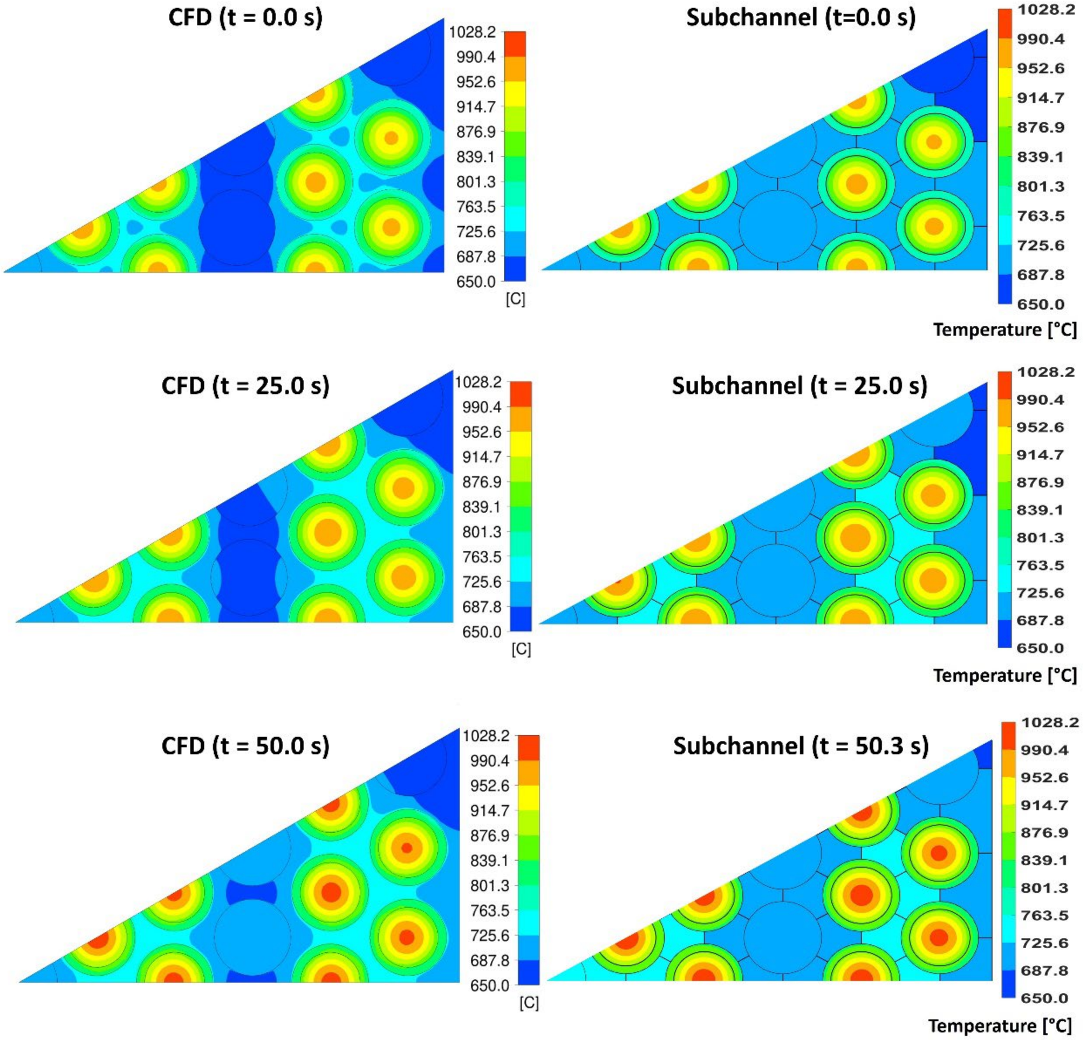

Figure 6.3: Code-to-code comparison: temperature contours at core exit for ~0, 25, and 50 s

Figure 6.4 shows the transient evolution of solid and fluid temperatures at the core exit for three different later times (~75 s, 100 s, and 300 s). Again, the transient decrease in solid fuel pin temperatures predicted by the CFD and subchannel models show good agreement.

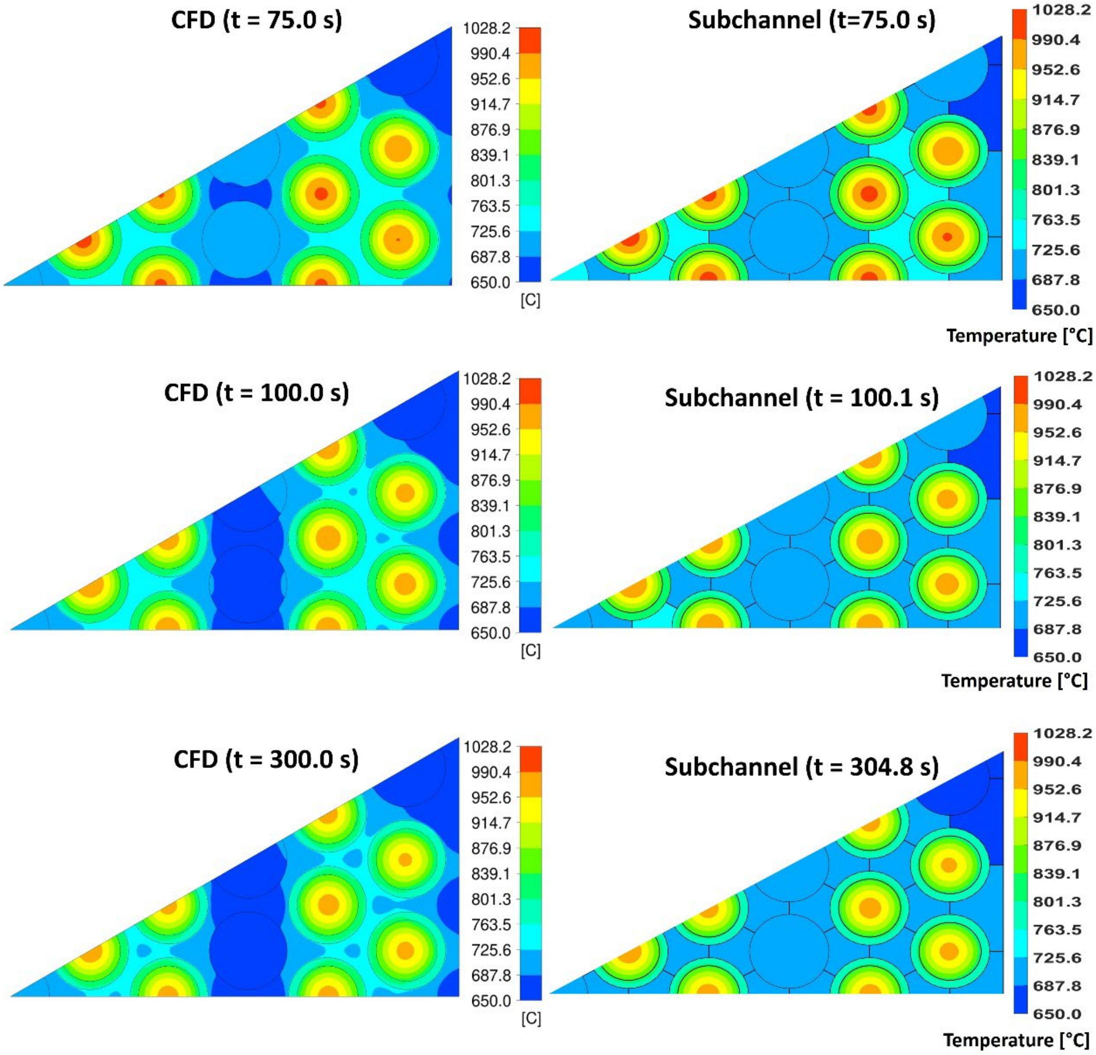

Figure 6.4: Code-to-code comparison: temperature contours at core exit for ~75, 100, and 300 s

Figure 6.5 shows good agreement for the centerline temperatures of the fuel pins predicted by the CFD and subchannel models at the exit of the core for six different times.

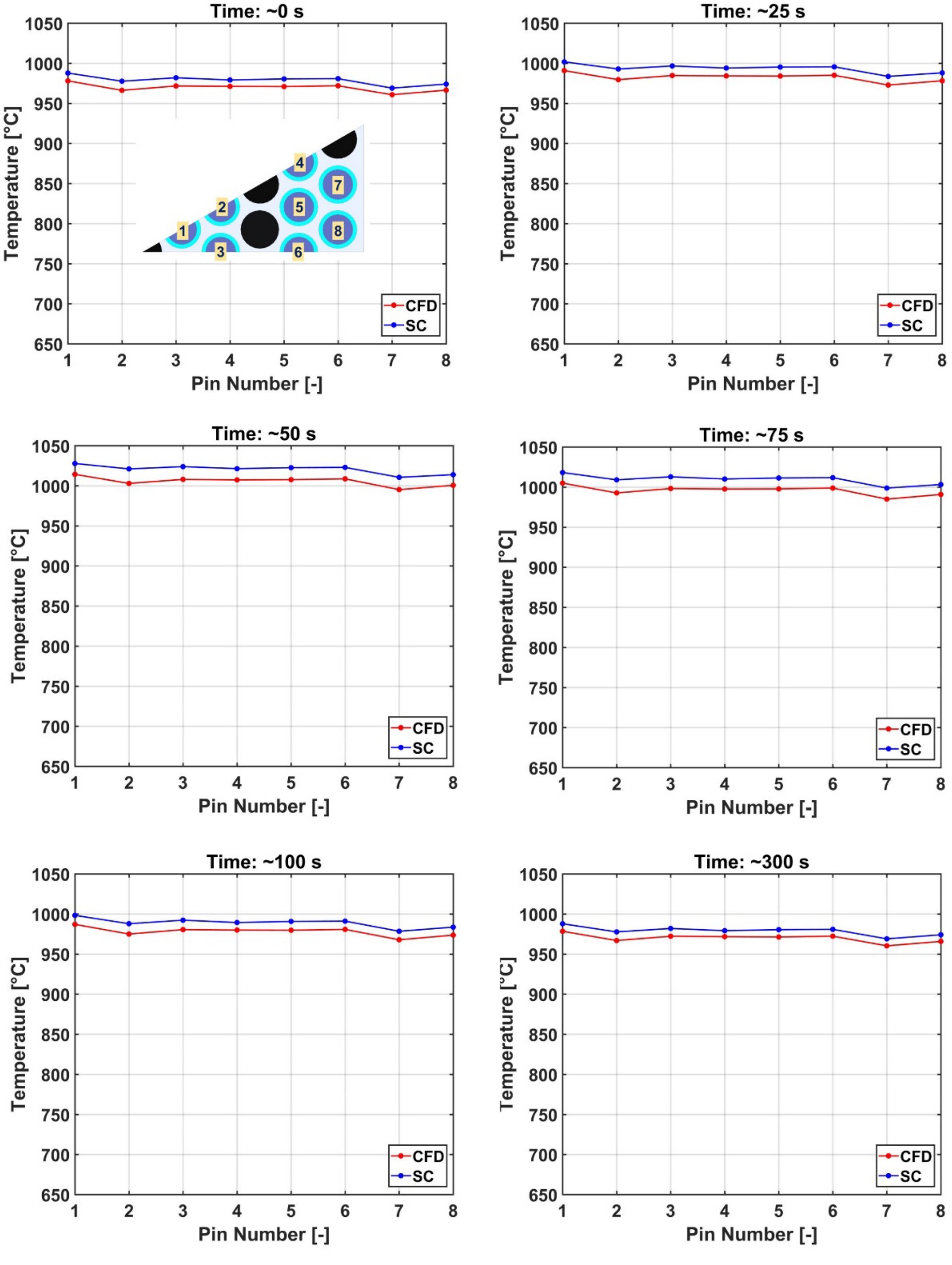

Figure 6.5: Code-to-code comparison: pin centerline temperatures at core exit for different times

Thus, transient results such as peak fuel and cladding temperatures, core pressure drop, fuel pin temperature distribution at the core exit, and pin centerline temperatures predicted by the subchannel-based model agree well with the CFD model predictions. While this provides initial confidence in the subchannel model developed in the present study, this exercise is a preliminary code-to-code comparison, not code verification. To ensure that the present subchannel model behaves in an expected manner and produces physically correct and accurate results, an extensive verification and validation (V&V) must be conducted in the future.

6.3 Simplified system-level coupling

The primary focus of the present study is the development of a thermal hydraulic model for the core region of the SmAHTR. However, due to the high volumetric heat capacity ($\rho \cdot c$) of the molten salt coolant, the thermal storage of the molten salt in the rest of the reactor system (plenum regions, downcomer, etc.,) outside the core can be critical in determining accident behavior. A simplified model for the molten salt in the rest of the reactor system (Figure 6.6) is developed and coupled to the core model to provide a preliminary understanding of the reactor response during postulated accident scenarios. The system model shown in Figure 6.6 has one volume upstream of the core that represents the molten salt in the lower plenum and downcomer regions, and another volume downstream of the core that represents the salt in the upper and top plenum regions (the volume occupied by control rod drives and any other structural elements in the plenum regions is neglected, and only salt is considered to occupy these regions.)

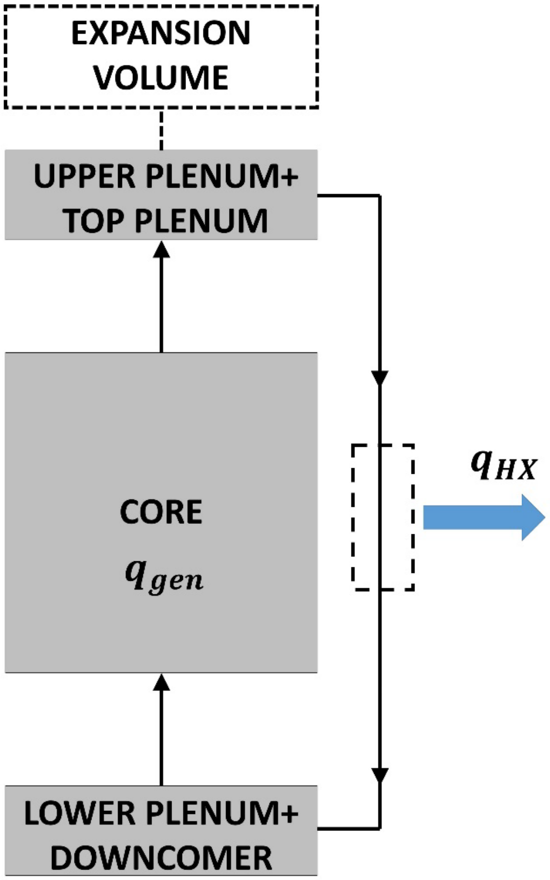

Figure 6.6: Simplified system-level modeling

In the SmAHTR, the actual pump flow rate is higher than the total flow rate into the core. This is because some of the flow from the pump bypasses the core, and flows into the three DHXs even during normal operation. The amount of flow bypass depends on the diodicity of the vortex diode installed at the bottom of the DHX. This bypass coolant flows through the DHXs, cools down, and then flows into the top plenum, where it mixes with the hot coolant from the upper plenum, leading to the temperature of the top plenum being slightly lower than the temperature of the upper plenum (Greene et al., 2011). This temperature difference between the top and upper plenum regions is neglected in this model. The thermal masses of the salt and metallic structures in the PHX and DHX systems are also not considered in this simplified model. Heat from the fluid leaving the downstream (top and upper plenum) volume is removed at the rate of q_{HX} before it enters the upstream (lower plenum and downcomer) volume. Both the downstream and upstream volumes are treated as rigid volumes. In reality, the thermal expansion/contraction of the salt during transient scenarios can cause the level of coolant to change in the reactor vessel (the expansion of salt compresses the cover gas and contraction of the salt expands the cover gas.) In the present model, the pressure and volume variations of the coolant salt are not considered, and the salt that cannot be held by the rigid system without increasing in pressure/volume is assumed to enter a notional 'expansion volume' (this is similar to a fluid accumulator) connected to the top volume that represents the upper and top plenums. The salt stored this 'expansion volume' is not considered to provide any thermal storage during the transient. Coolant salt can also flow from the 'expansion volume' to the top volume, when the reactor vessel is cooling down (for example, when the heat removal capacity exceeds the decay heat generation in the core during an accident). The 'expansion volume' is assumed to have no salt storage at normal operating conditions. While this simplified 'expansion volume' along with rigid volume representation for the top and upper plenums cannot be applied for certain transient cases (such as overcooling) in which the coolant is thermally contracting and the coolant level in the reactor vessel decreases below the steady-state value. A more accurate plenum model that tracks the coolant level is needed for these simulations.

Both the downstream and upstream volumes are modeled as well-mixed 0-D control volumes, and the mass and energy equations for a representative volume are shown in Equations 6.2 and 6.3.

$$\frac{d}{dt}(\rho \cdot V) = m_{in} - m_{out} \tag{6.2}$$

$$\frac{d}{dt}(I) = (m \cdot h)_{in} - (m \cdot h)_{out} \tag{6.3}$$

where $I = \rho \cdot V \cdot i$, the total internal energy of the control volume.

When the core model is coupled to this simplified system-level model, iterations are also performed at the overall system level. The overall system model is deemed to be converged when the change in core inlet temperature between two successive iterations is less than 0.1°C. This convergence tolerance value is chosen to keep the number of system-level iterations at each time step (the whole-core model has to be solved multiple times until convergence within each system-level iteration) within a reasonable limit.

As mentioned earlier, the objective of this simplified model is to simulate the response from the rest of the reactor system during accident scenarios in the present study. A more detailed system-level response can be obtained by coupling the present model with system-level codes such as SAM (INL, 2017) or TRANSFORM (Greenwood et al., 2020).

6.4 Simulation of postulated forced flow accident scenarios

6.4.1 Protected loss of heat sink (P-LOHS) accident

The simulation of the P-LOHS accident is performed with the following assumptions and considerations.

The reactor is initially operating at full power (125 MWt). In the system-level model, the initial temperature of the volume upstream (lower plenum and downcomer) of the core is set to the core inlet temperature (650°C), and the total coolant flow rate into this volume is set to 1770 kg s^{-1} (1750 kg s^{-1} for the active core and 20 kg s^{-1} for the radial reflector coolant channels). The initial temperature of the volume downstream (upper plenum and top plenum) of the core is set to the core outlet temperature (~680°C). The profiles for temperature, pressure, and mass flow rate for the solid and fluid regions in the core obtained from the steady-state model with the COMET power profile are set as initial values.

Of the 125 MW generated by the reactor at steady state, the three PHXs are assumed to remove 124 MW, while the three DHXs are assumed to remove the remaining 1 MW of power. This assumption is made because there is a parasitic loss of power (due to flow bypass) through the DHXs during normal operation. The actual value of the parasitic loss during normal operation is dependent on the diodicity of the vortex diode (which controls the amount of flow bypass), but a nominal value of 1 MW is chosen in the present study as it is closer to the typical heat loss values provided in the pre-conceptual design report (Greene et al., 2011).

At time t = 0 s, the loss of heat sink is initiated, and the heat removal capability of the entire PHX system (all three individual PHXs) is subjected to an exponential decay similar to the one used in the study by Guo et al. (2013) for a liquid fueled molten salt reactor. The exponential decay constant is chosen such that the PHX system heat removal capability approaches zero within 30 seconds of the accident initiation. While the PHX system heat removal is exponentially decreasing, the heat removed by the DHX system (the three DHXs) is kept at the constant rate of 1 MW throughout the entire duration of the accident. With the loss of the PHX system, the heat loss through the DHX system, which was a parasitic loss during normal operation, now provides emergency cooling to the reactor. The total heat removal from the combined PHX and DHX systems is referred to as q_{HX} (Figure 6.6). The coolant flow rate into the upstream volume (lower plenum and downcomer) is kept at the steady-state value throughout the entire duration of the accident.

At time t = 0 s, the reactor control system scrams the reactor, and the reactor power is quickly reduced to decay heat levels. The correlation from El-Wakil (1978) is used to calculate the total decay heat power over time. This simplified correlation is applicable for shut down times greater than 200 seconds, and is considered conservative compared to the ANS-5.1 standard for times less than 200 seconds (Henry, 1992). It must also be noted that this simplified decay heat correlation was developed for standard light water reactors (LWRs), but is still used in this study as specific decay heat curves for solid-fueled FHRs are not currently available.

The thermal hydraulic simulation was performed for a total of ~20,000 seconds (~5.6 hours.) The total runtime for this simulation was ~17 hours. Figure 6.7 shows the thermal power generated and removed by the coolant in the core throughout the duration of the accident.

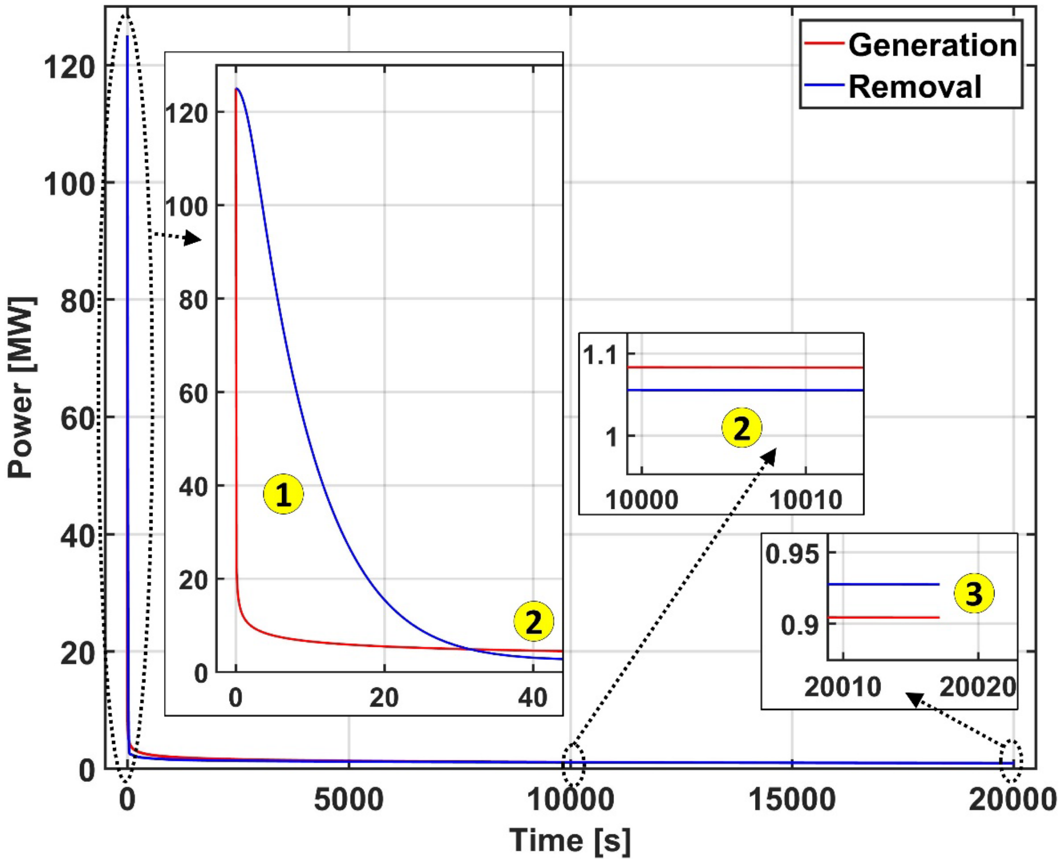

Figure 6.7: P-LOHS accident thermal power transient profile

Figure 6.7 illustrates three distinct phases in the P-LOHS accident. The first phase (highlighted by the yellow circle as ‘1’) is a brief cool-down phase that occurs due to the reactor power decreasing at a faster rate (due to initiation of scram) than the decreasing coolant removal rate (due to PHX system failure.) This initial cool-down phase lasts only for a relatively short time (~30 seconds) compared to the total simulated duration of the accident. This first cool-down phase is then followed by a heat-up phase (highlighted by the yellow circle as ‘2’), as the coolant heat removal capacity decreases below the decay heat generation rate in the core. This heat-up phase lasts for ~4 hours after the end of the previous cool-down phase. When the coolant heat removal rate is finally greater than the core heat generation rate, the final cool-down phase is initiated (highlighted by the yellow circle as ‘3’).

Figure 6.8a shows the transient temperature profile for the coolant entering and leaving the core, as well as for the total heat exchanger system (including both PHX and DHX systems) for times up to ~30 seconds after the initiation of the accident. Figure 6.8b shows the same temperature profiles but for the entire duration of the accident.

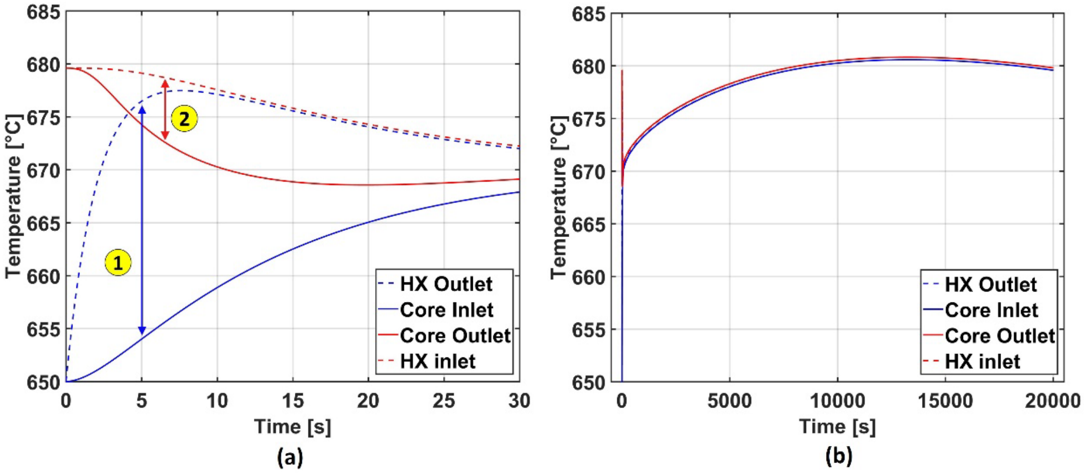

Figure 6.8: P-LOHS accident (a) inlet and outlet temperatures for the core and heat exchanger for times up to ~30 seconds after accident initiation, and (b) core and heat exchanger coolant temperatures for the entire accident duration

From Figure 6.8a, it is seen that the heat exchanger system (referred hereafter as HX) coolant outlet temperature starts to quickly increase after the initiation of the LOHS accident, due to the drastic decrease in the PHX system heat removal capability. However, the increase in the core inlet temperature is slower than the HX coolant outlet temperature (difference denoted in Figure 6.8 by yellow circle marked ‘1’), and this lag is attributed to the storage of thermal energy in the fluid volume upstream of the core shown in Figure 6.6 (the lower plenum and the downcomer), which initially was at 650°C during steady-state operation. Similarly, it can also be seen from Figure 6.8a that the coolant outlet temperature from the core starts rapidly decreasing due to the initiation of the scram. However, the decrease in the HX coolant inlet temperature is slower than the decrease in core outlet temperature (difference denoted in Figure 6.8 by yellow circle marked ‘2’) due to the thermal storage in the fluid volume downstream of the core (upper plenum and top plenum) shown in Figure 6.6, which was initially at a temperature of ~680°C during steady-state operation. After ~30 seconds, the difference between the core inlet and outlet temperatures is much smaller compared to the steady-state condition. The difference between core coolant inlet and outlet temperatures remains relatively small throughout the entire duration of the accident, which is attributed to the fact that there is still forced flow (close to the same steady-state mass flow rate) into the core, while the decay power generation is now only a very small fraction of the normal operating power (the ΔT of the coolant required for this small fraction of power generation is therefore also smaller.) Figure 6.8b shows that both the heat exchanger and the core inlet and outlet temperatures slowly continue to increase over time as long as the heat generation in the core exceeds the heat removal capability. When the reactor heat generation finally becomes lower than the heat removal capability, the coolant temperatures begin to slowly decrease over time.

The total mass of the coolant salt entering the notional ‘expansion volume’ is <1% of the initial salt stored in the downstream volume (upper plenum and top plenum) during the reactor heat-up phase. This relatively small amount of mass therefore does not significantly affect the overall thermal response of the system (as mentioned previously, the mass stored in the expansion volume does not provide thermal storage during the transient.) The total mass of the coolant leaving the 'expansion volume' is ~0.03% during the reactor cool-down phase.

The peak temperatures for different solid regions (active fuel, cladding, moderator pins, and graphite reflectors) and the fluid regions (coolant subchannels and coolant channels in radial reflector) in the core are shown in Figure 6.9.

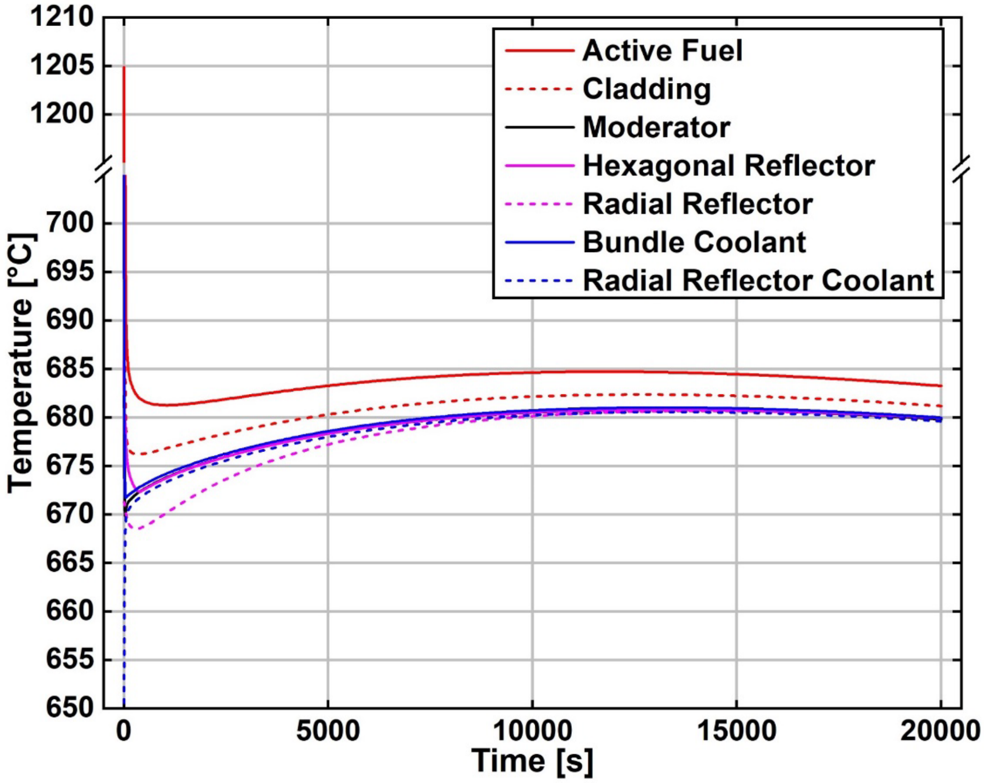

Figure 6.9: P-LOHS accident peak temperature transient profile

The peak temperature for the active fuel region is the highest at the normal operating condition. After the reactor is scrammed, the peak fuel temperatures quickly decreases during the initial cool-down phase. The peak fuel temperature only increases by a few degrees during the following heat-up phase, and then decreases back again during the final cool-down phase. The temperature profiles for all the other solid and fluid regions follow a similar trend. Overall, the temperatures for all the regions in the core remain within safe limits for the duration of the simulated accident. At steady-state, the peak temperature of the coolant in radial reflector coolant channels is close to 650°C (which is the steady-state coolant inlet temperature.) However, after the initiation of the accident, the temperatures in the radial reflector coolant channels increase due to the increasing core coolant inlet temperatures.

Figure 6.10 shows the 3-D, volumetrically weighted average temperature at each axial location for all the fuel pins in the core at four different times. The temperatures at 0 s correspond to the steady-state temperature profile. The pin temperatures at ~10 s are significantly lower than the steady-state profile, due to the initiation of scram. By ~20 s, the temperatures are now significantly lower, and the axial and radial temperature differences across the core (between different fuel assemblies as well as within each fuel assembly) are also substantially lower than the previous two times due to the low core power generation. A similar trend is seen at the end of the simulation (~20,000 s), in which the temperature magnitudes are substantially lower and the radial and axial temperature differences across the core are also very small.

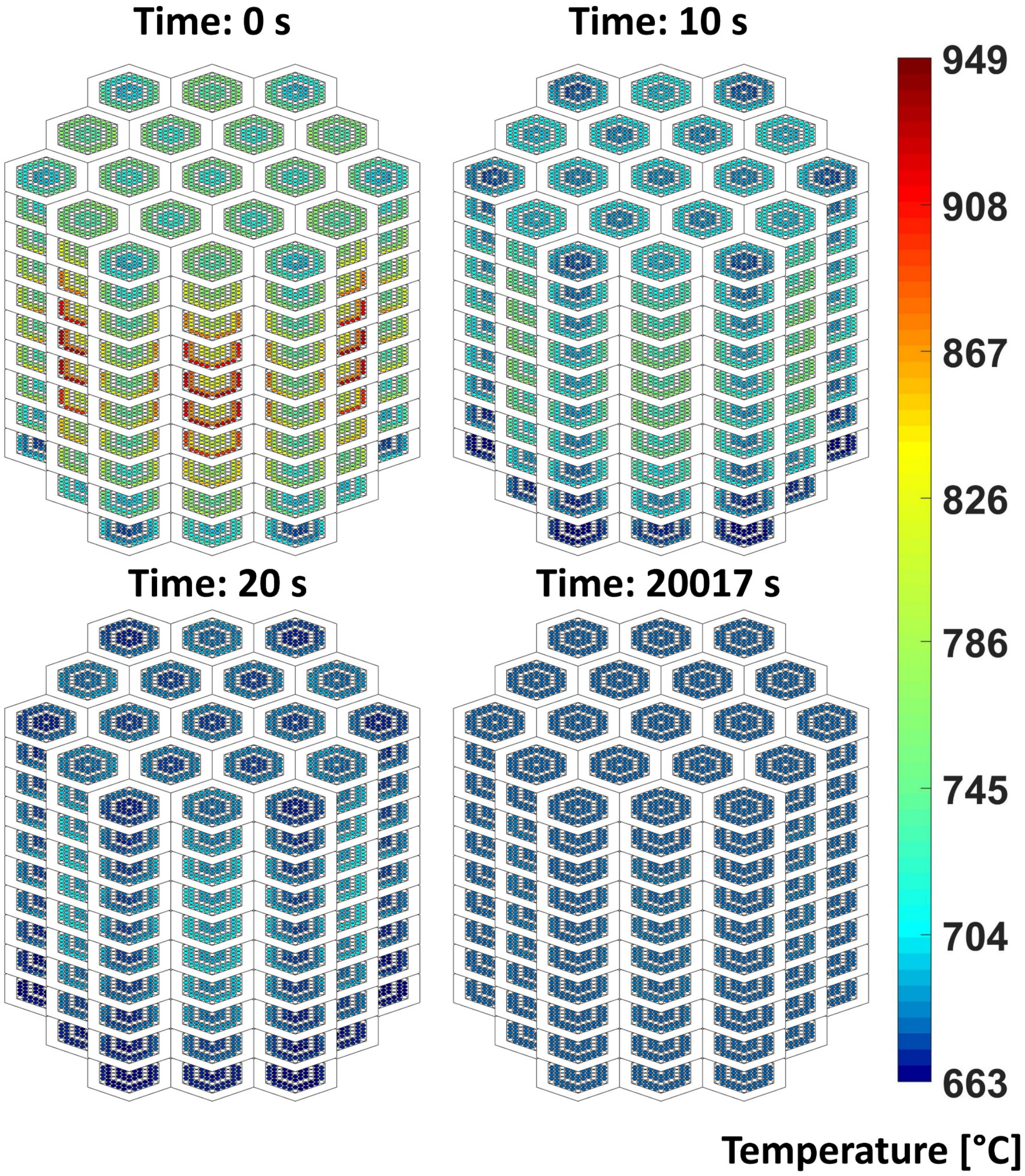

Figure 6.10: 3-D fuel pin temperature distribution for four different times after the P-LOHS accident initiation

Figure 6.11 shows the composite temperature profile for the fuel, moderator, and coolant regions at an axial location near the core center for one of the fuel assemblies with relative pin high power densities for four different times.

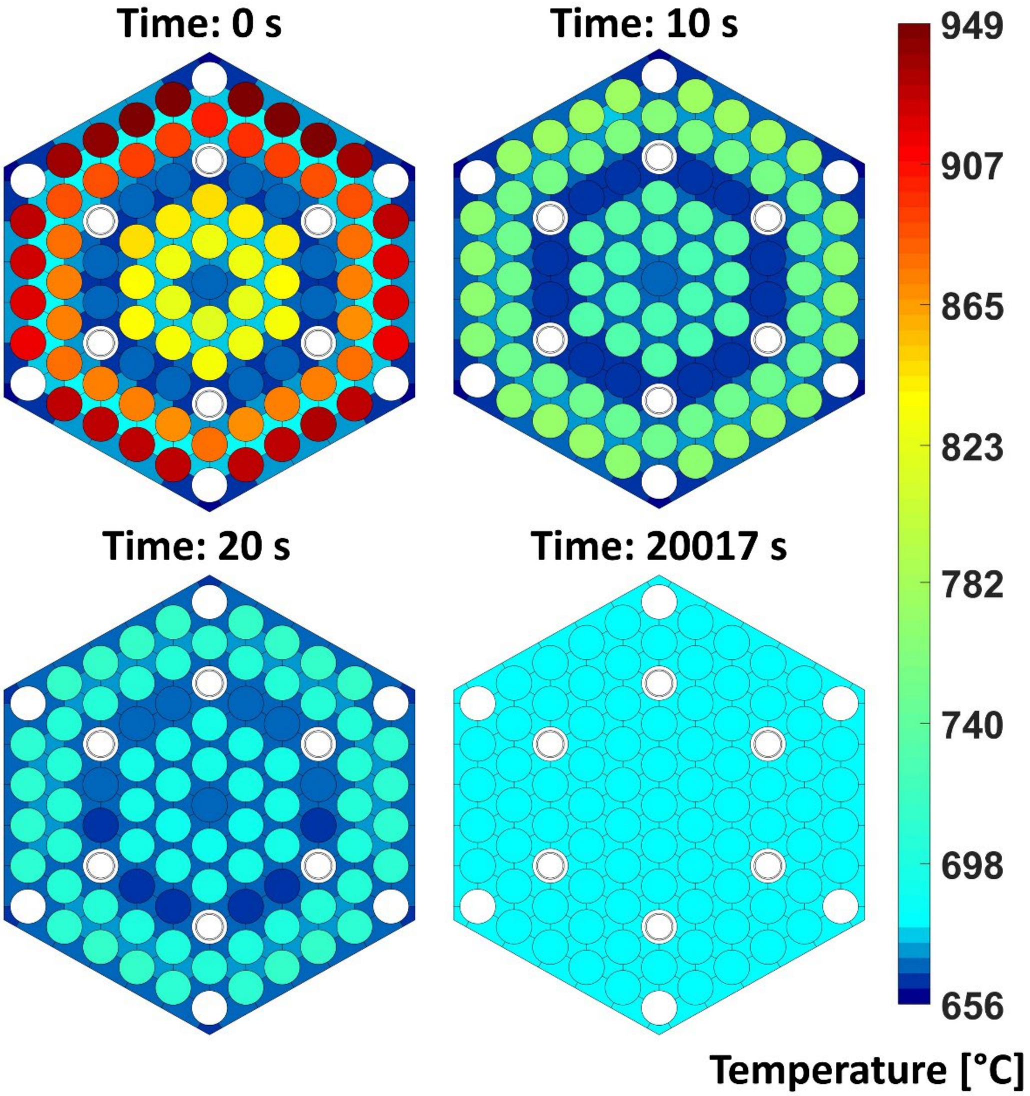

Figure 6.11: P-LOHS fuel assembly temperature distribution for four different times after accident initiation

The temperatures shown for the fuel and moderator pins correspond to the volumetrically weighted average temperatures. Similar to Figure 6.10, the temperature at t = 0 corresponds to the steady-state temperature profile. At time t = 0, the edge fuel pins with higher power densities are substantially hotter than the interior fuel pins in the bundle. The interior coolant subchannels near the bundle periphery receive a higher heat input (due to the connection with hotter fuel pins) and therefore have a higher mean temperature compared to the interior subchannels closer to the center of the bundle. At t ~ 10.0 s, the reactor power is lower due to scram, and therefore the temperatures of the different regions in the bundle are also significantly lower than the initial temperatures. At t ~ 20 s, the temperatures are even lower, and finally at the end of simulation (~20,000 s), the temperature magnitudes as well as the temperature gradients across the fuel assembly are very low (the temperature gradients still exist at t ~ 20,000 s, but are too small to be shown in Figure 6.11.)

Figure 6.12 shows the maximum temperature difference between current and previous time steps (ΔT_{max}) and the time step size variation throughout the duration of the accident. The x-axis of this plot shows both the time step as well as the total time simulated at the end of few different time steps. The settings for the adaptive time stepping scheme used in the simulation are somewhat different from the one used for the code-to-code comparison study discussed in Section 6.2. These changes were made to enable reasonable simulation runtimes for the whole-core model. A higher set temperature resolution (ΔT_{set}) of 5°C was used for the adaptive time stepping scheme in the P-LOHS accident simulation, with the option to reject the time step if the maximum temperature (ΔT_{max}) was greater than the set resolution. A time step reduction factor (α) value of 0.8 was used in Equation 6.1 to ensure that too many time steps were not rejected. The time step size was bound to a minimum value of 0.001 s and a maximum value of 60 s.

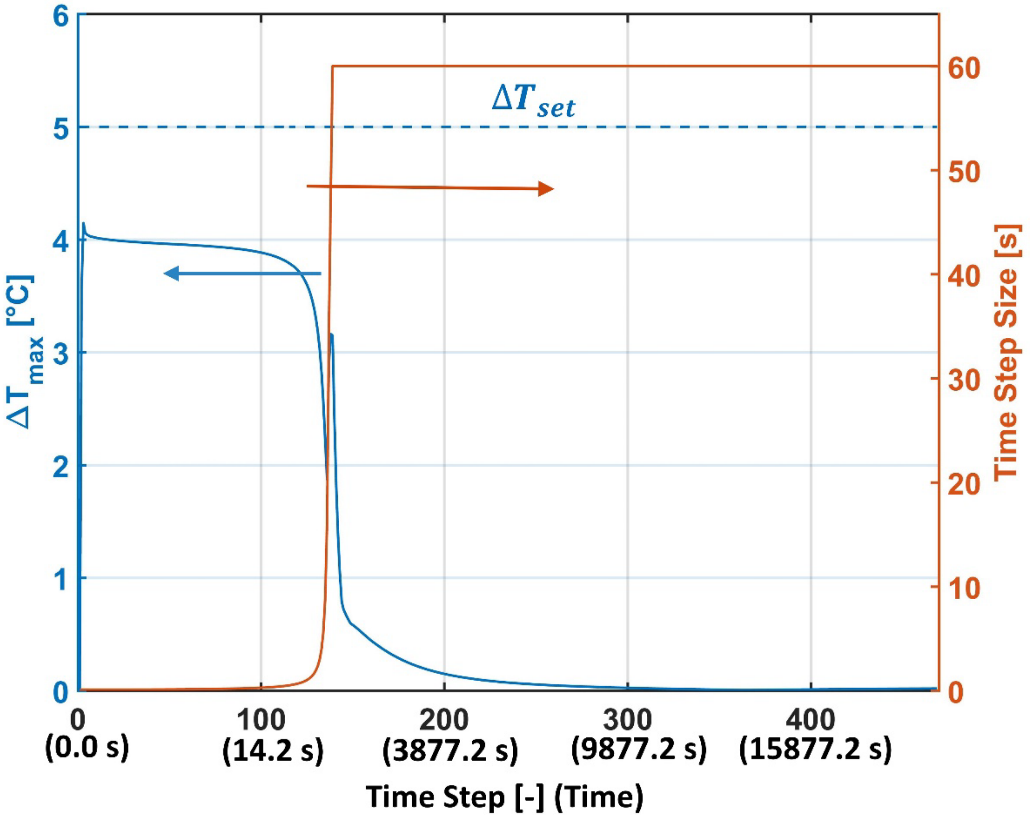

Figure 6.12: P-LOHS accident maximum temperature difference between successive time steps and time step size

Figure 6.12 shows that the ΔT_{max} values during the initial stages of the accident are close to 4°C, instead of the ΔT_{set} value of 5°C. This is attributed to the time step reduction factor of 0.8 used in Equation 6.1, which not only prevents too many times steps from being rejected (no time steps were rejected in this case), but also effectively makes the set resolution as 4°C (80% of 5°C) instead of the actual ΔT_{set} (5°C). This indicates that a higher time step reduction factor value (0.9 or 0.95) that would result in ΔT_{max} being closer to the actual ΔT_{set} (5°C) and also reduce the number of rejected time steps could be used in the adaptive time stepping scheme. The value of ΔT_{max} approaches zero at the end of the accident because the temperature changes in the core are very small even when a time step size as big as 60 s is used. The figure also shows that at the initial stages of the accident when there are fast changes in the core temperatures, very small time step sizes as low as ~0.1 s are employed by the adaptive time stepping scheme. After this initial phase, the temperature changes in the core become slower, and therefore, the time step starts to increase to a point where the time stepping scheme starts to use the specified maximum time step value (60 s in this case).

Overall, the results for the P-LOHS accident for the conditions/assumptions used in this study show that the temperatures of the fuel, graphite, and coolant regions in the core are within safe limits for the entire duration of the accident.

6.4.2 Unprotected transient overpower (U-TOP) accident

Following the U-LOHS simulation, another postulated accident scenario is investigated using the transient subchannel-based model. A transient overpower accident occurs when reactor control elements are partially or fully removed from the core, causing rapid power increase in the fuel elements. The amount and rate of power increase depend on the amount of reactivity insertion as well as the rate of insertion. If the reactor is not scrammed following this power surge (which would be an unprotected-TOP or U-TOP), the increase in the fuel (as well as moderator and coolant, depending on the feedback coefficients) temperatures will cause a drop in the core reactivity due to negative feedback, which in turn decreases the temperature of the core elements. The fuel, coolant, and moderator temperatures in the core then stabilize at values that provide a negative temperature feedback that compensates for the external reactivity (which is the result of partial/total removal of control elements.)

The capability of the present model to simulate postulated U-TOP scenarios is demonstrated using an assumed power transient. A simple linear power profile is considered in this accident. A more realistic power profile can be obtained by coupling the present thermal hydraulic model with system-level codes such as RELAP (INL, 2012) or TRANSFORM (Greenwood et al., 2020) that include point kinetics neutronics modeling, or codes such as COMET (Rahnema and Zhang, 2021) that could provide detailed spatial and temporal profiles of the core power evolution during the U-TOP transient. The key considerations and assumptions in the present simulation are outlined next.

The reactor is initially operating at full power (125 MW). The upstream and downstream volumes in the system-level model are set to the same conditions as in the P-LOHS accident. The profiles for temperature, pressure, and mass flow rate for the solid and fluid regions in the core from the steady-state model are set as initial values. The reactor power is linearly increased by 100% (from 125 MW to 250 MW) in the first 10 seconds, and then linearly decreased from 250 MW to a power value of 137.5 MW (which is 110% of the 125 MW initial steady-state value). The reactor power remains at 137.5 MW for the rest of the accident duration. The transient power generation profile is shown in Figure 6.13.

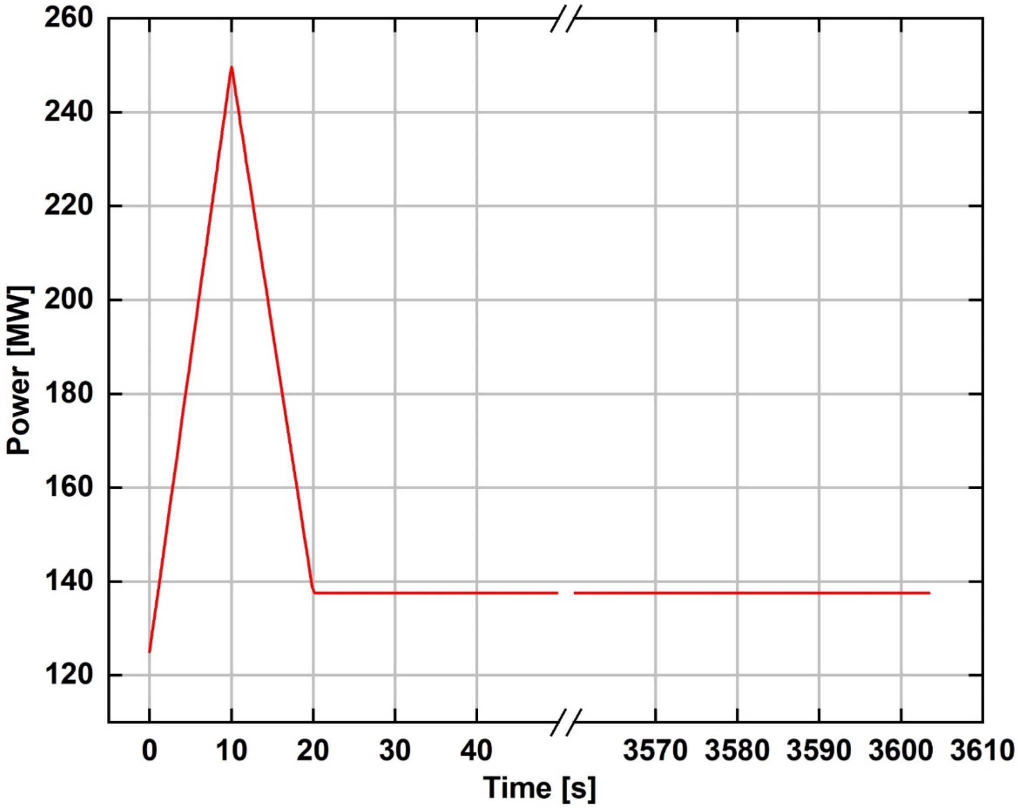

Figure 6.13: U-TOP core transient power profile

The coolant flow rate into the upstream volume (lower plenum and downcomer) is kept at the steady-state value (1770 kg s^{-1}) throughout the entire duration of the accident. The transient evolution of the heat removal capability of the heat exchanger system (q_{HX}) is modeled using a constant heat exchanger effectiveness (ε) approach. In this approach, all the heat from the reactor is assumed to be removed through the PHX system (the DHX heat removal is set to zero.) It is also assumed that thermal storage effects in the PHX system can be neglected in this simplified model, which allows for the application of the heat exchanger effectiveness concept throughout the duration of the U-TOP accident. As mentioned in the discussion of the U-LOHS simulation, the objective in the present study is to model the core behavior during transients with reasonable system-level inputs, and some of the assumptions made in relation to modeling the system-level response can be eliminated by coupling the present core model with a system-level code such as RELAP, SAM, or TRANSFORM.

The effectiveness of the PHX system at the initial steady state (t = 0) is computed using the following equation.

$$\varepsilon = \frac{q_{HX}}{q_{ideal}} \tag{6.4}$$

where

$$q_{ideal} = (m \cdot c)_{min} \cdot \left(T_{pr,in} - T_{sec,in}\right) \tag{6.5}$$

The minimum thermal capacity rate fluid in this case is the secondary coolant (FLiNaK). The mass flow rate of FLiNaK (m_{min}) is set to 740 kg s^{-1}, based on the value considered in the pre-conceptual design report (Greene et al., 2011). The specific heat of FLiNaK (c_{min}) is set to 1884 J kg^{-1} K^{-1}, based on the work of Romatoski (2017). The primary coolant inlet temperature is set to a value of ~680°C (this is based on the core power, primary coolant mass flow rate, and FLiBe specific heat capacity), while the secondary coolant inlet temperature is set to a value of 580°C. The PHX system parameters from the present study and the pre-conceptual design document are summarized in Table 6.1.

Table 6.1: PHX system parameters

Parameter	Present study	Pre-conceptual design
Heat exchanger capacity (MW)	125	
Primary coolant flow rate (kg s^{-1})	1770	~1050
Primary coolant specific heat capacity (J kg^{-1} K^{-1})	2386	
Primary coolant inlet temperature (°C)	~680	~700
Primary coolant outlet temperature (°C)	650	
Secondary coolant flow rate (kg s^{-1})	740	
Secondary coolant specific heat capacity (J kg^{-1} K^{-1})	1884	
Secondary coolant inlet temperature (°C)	580	600
Secondary coolant outlet temperature (°C)	~670	~690
CAT between primary inlet and secondary outlet (K)	~10	

It can be seen from the above table that the SmAHTR pre-conceptual design document specifies a PHX secondary coolant inlet temperature of 600°C. However, the PHX design in the pre-conceptual design considers a lower primary coolant mass flow rate (~1050 kg s^{-1}) compared to the 1770 kg s^{-1} considered in the present study (as mentioned earlier, this high mass flow rate value is needed to maintain the peak steady-state temperature of the core sufficiently below the normal operation limit). As a result of this lower flow rate, the primary coolant inlet temperature for the PHX in the pre-conceptual design document is ~700°C, while it is ~680°C in the present study. The secondary coolant inlet temperature of 580°C is chosen in the present study to maintain the same closest approach temperature (CAT) value between the primary inlet and secondary outlet (~10 K) as that of the pre-conceptual design.

Using the q_{HX} value of 125 MW, and the q_{ideal} value from Equation 6.5 using the values listed in Table 6.1, the effectiveness of the PHX system is calculated from Equation 6.4 to be ~0.9. In the present model, it assumed that the effectiveness of the PHX system remains constant throughout the entire duration of the accident. The heat exchanger effectiveness in general is a function of the variables shown in Equation 6.6.

$$\varepsilon = f\left(C_{pr}, C_{sec}, R_{pr}, R_{sec}, R_{wall}\right) \tag{6.6}$$

where, $C_{pr} = m_{pr} \cdot c_{pr}$ and $C_{sec} = m_{sec} \cdot c_{sec}$ are heat capacity rates for the primary and secondary fluid. The terms R_{pr}, R_{sec}, and R_{wall} represent the heat transfer resistances of the primary fluid, secondary fluid, and heat exchanger wall respectively. The primary and secondary coolant flow rates as well as the specific heat capacities of the FLiBe and FLiNaK fluids remain constant (the specific heat capacities for both these fluids are largely independent of temperature) throughout the U-TOP accident, and therefore the values of C_{pr} and C_{sec} in Equation 6.6 remain constant as well. The wall resistance is not expected to change significantly during the accident. The change in heat transfer resistances of the primary and secondary fluids during the accident are determined by the change in the heat transfer coefficients. The heat transfer coefficients are not expected to change substantially during the accident, as the primary and secondary coolant flow rates still remain the same, and the heat transfer coefficient variations due to temperature-dependent fluid properties are expected to be relatively lower due to the large volumetric heat capacity of both the primary and secondary coolants. The assumption that the heat exchanger effectiveness remains constant during the accident is therefore reasonable. For a given primary coolant inlet temperature, the PHX primary coolant outlet temperature at any given point in time is then determined by first determining the PHX heat duty as shown in Equation 6.7.

$$q_{HX}(t) = \varepsilon \cdot q_{ideal}(t) = \varepsilon \cdot m_{sec} \cdot c_{sec} \cdot \left\{T_{pr,in}(t) - T_{sec,in}\right\} \tag{6.7}$$

The primary coolant outlet temperature is then calculated using Equation 6.8.

$$T_{pr,out}(t) = T_{pr,in}(t) - \left\{\frac{q_{HX}(t)}{m_{pr} \cdot c_{pr}}\right\} \tag{6.8}$$

The thermal hydraulic simulation was performed for a total of ~3,600 seconds (~1 hour.) The total runtime for this simulation was ~7 hours.

Figure 6.14 shows the thermal power generation and removal by the coolant in the core after the initiation of the U-TOP accident. The core power follows the linear profile outlined earlier. The heat removal by the coolant follows a similar transient profile. Figure 6.14 shows that the thermal power removed by the coolant is lower than the thermal power generated in the core for ~16 seconds after the UTOP accident, and the difference between the generation and coolant removal is stored in the solid and fluid elements in the core, resulting in temperature increases across the fuel, non-fuel and coolant regions in the core. After this heat-up phase, the coolant heat removal rate exceeds core power generation, which leads to a cool-down phase in which the temperatures of all the solid and fluid regions in the core decrease over time. The coolant heat removal then approaches thermal power generation until a new steady state is reached.

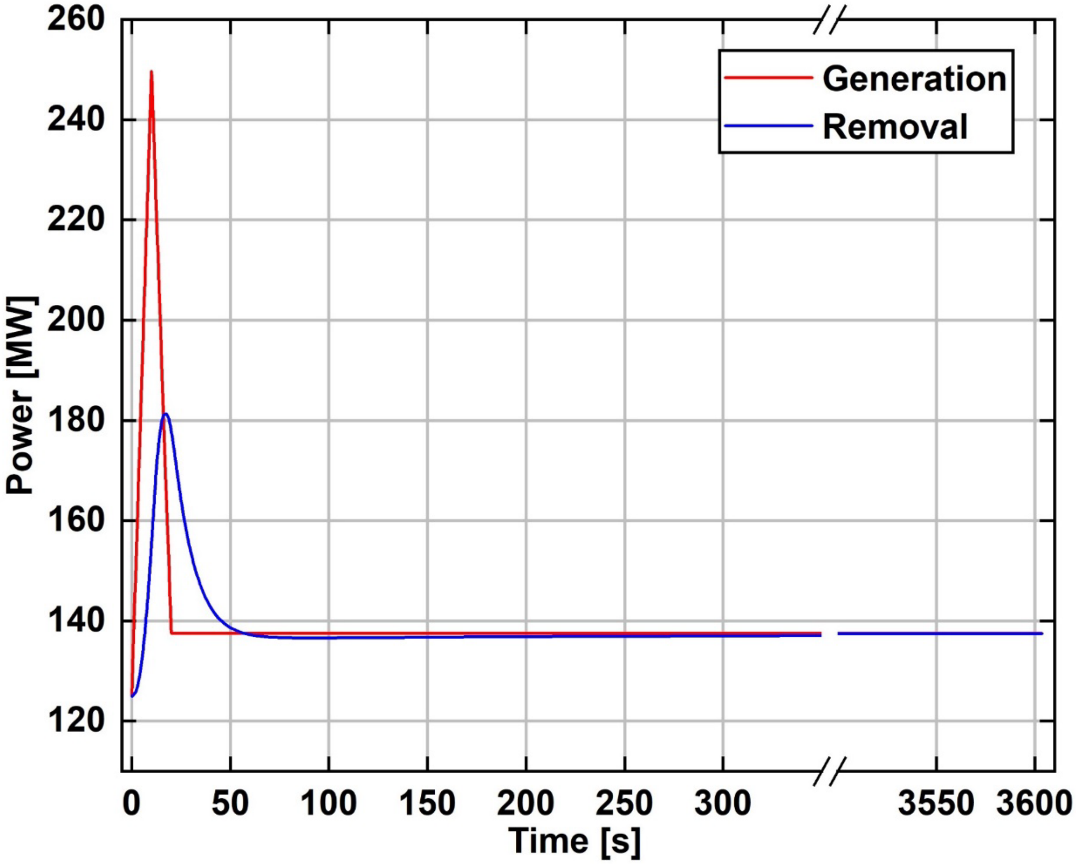

Figure 6.14: U-TOP accident core transient thermal power generation and removal profile

Figure 6.15a shows the transient temperature profile for the coolant entering and leaving the core, as well as for the HX system for times up to ~50 s after the initiation of the accident. Figure 6.15b shows the same temperature profiles but for the entire duration of the accident. From Figure 6.15a, it is seen that the core outlet temperature starts increasing after the initiation of the U-TOP accident due to the increasing heat generation in the core. However, the increase in the temperature of the HX inlet is slower than the increase in core outlet temperature (difference denoted by the yellow circle marked ‘1’) due to the thermal storage associated with the fluid volume downstream of the core (upper plenum and top plenum). Similarly, the increase in the core inlet temperature is slower than the increase in HX outlet temperature due to the thermal storage in the fluid volume upstream of the core (difference denoted by yellow circle marked ‘2’). After the initial transient, the inlet and outlet temperatures of the core as well as the HX start to stabilize as the system approaches a new steady state, as shown in Figure 6.15b.

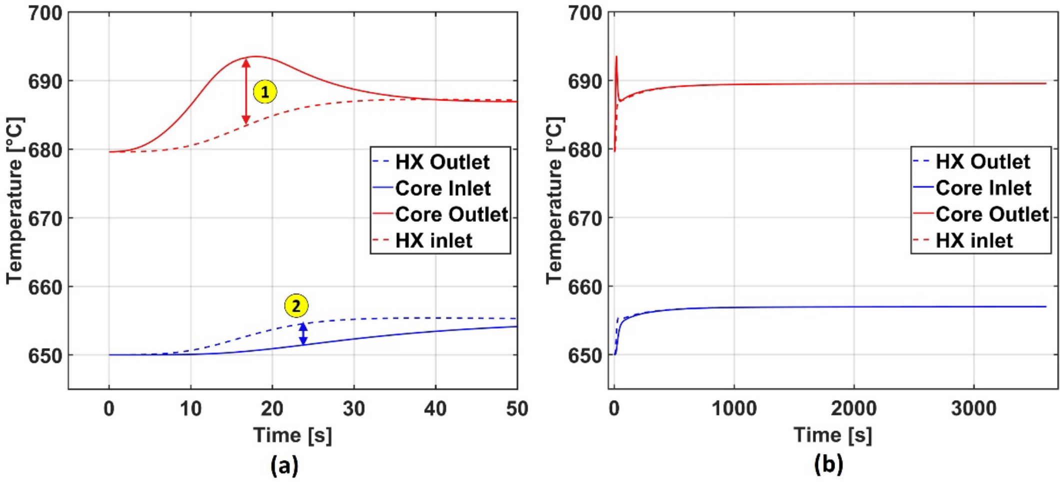

Figure 6.15: U-TOP accident (a) inlet and outlet temperatures for the core and heat exchanger for times up to ~50 seconds after accident initiation, and (b) core and heat exchanger coolant temperatures for the entire accident duration

Overall, the maximum coolant temperature from the core outlet is ~694°C, which is ~14°C higher than the initial steady state temperature. The core outlet temperature as the system approaches a new steady state is ~690°C, which is ~10°C than the initial steady state temperature. The maximum core outlet temperature throughout the U-TOP accident stays below 700°C, therefore indicating that the metallic structures in the reactor system will be safe for the conditions investigated in the present simulation.

Similar to the P-LOHS case, the total mass of the coolant salt entering the notional ‘expansion volume’ is a relatively small value (~0.2%) of the initial salt stored in the downstream volume (upper plenum and top plenum) during the U-TOP accident. This small amount of mass therefore does not significantly affect the overall thermal response of the system (as mentioned previously, the mass stored in the expansion volume does not provide thermal storage during the transient.)

The peak temperatures for different solid regions (active fuel, cladding, moderator pins, and graphite reflectors) and the fluid regions (coolant subchannels and coolant channels in radial reflector) in the core are shown in Figure 6.16.

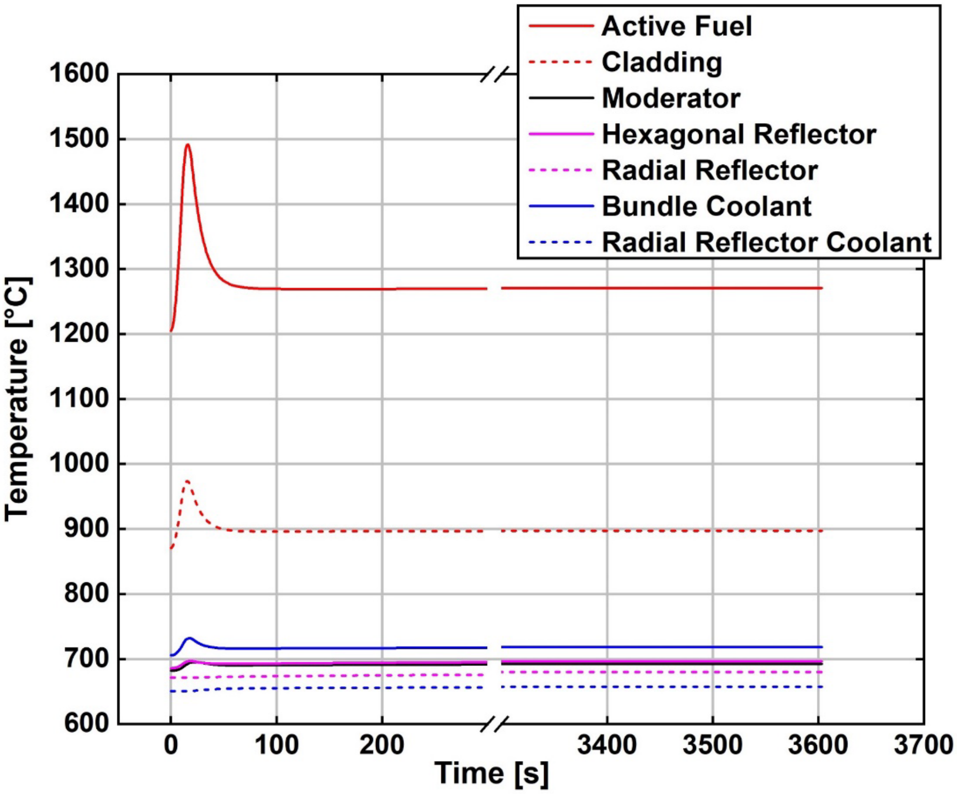

Figure 6.16: U-TOP accident peak temperature transient profile

The peak temperature for the active fuel region is ~1205°C at the initial steady-state condition. The peak fuel temperature reaches a maximum value of ~1492°C at a time ~16 s into the U-TOP accident. Such steep increases in fuel temperatures immediately following the initiation of reactivity insertion accidents have also been observed by Wang et al. (2016b) for a pebble bed FHR design and Wang et al. (2017) for a prismatic FHR design. The maximum allowable temperature for the coated-particle TRISO fuel is 1600°C, which indicates that for accidents with larger power excursions (which could occur if the amount of reactivity insertion or the ramp rate of the reactivity insertion is higher), the peak fuel region temperature might exceed 1600°C. Therefore, it might be necessary to optimize the core design to achieve flatter radial and axial power profiles across the core to reduce the peak fuel temperatures at steady-state, and also to provide sufficient thermal safety margins against more severe U-TOP accidents. The temperature profiles for all the other solid and fluid regions follow a similar trend. Overall, for the settings considered in this simulation, the temperatures for all the regions in the core remain within safe limits. Figure 6.16 also shows that all the peak temperatures are almost constant near the end of the simulated accident duration, as the system approaches a new steady state.

Figure 6.17 shows the 3-D, volumetrically weighted average temperature at each axial location for all the fuel pins in the core at four different times. The temperatures at 0 s correspond to the steady-state temperature profile. The pin temperatures at ~15 s are significantly higher than the steady-state profile, due to the increase in core heat generation. By ~25 s, the temperatures are now somewhat lower, as the core is now in the cool-down phase. At the end of the simulated accident duration (~3,600 s), the fuel pin temperatures are relatively lower than the temperatures at time ~25 s. It must be noted that the fuel temperatures at time ~3,600 s are higher than the initial steady state (t=0), as the core power is now 10% higher.

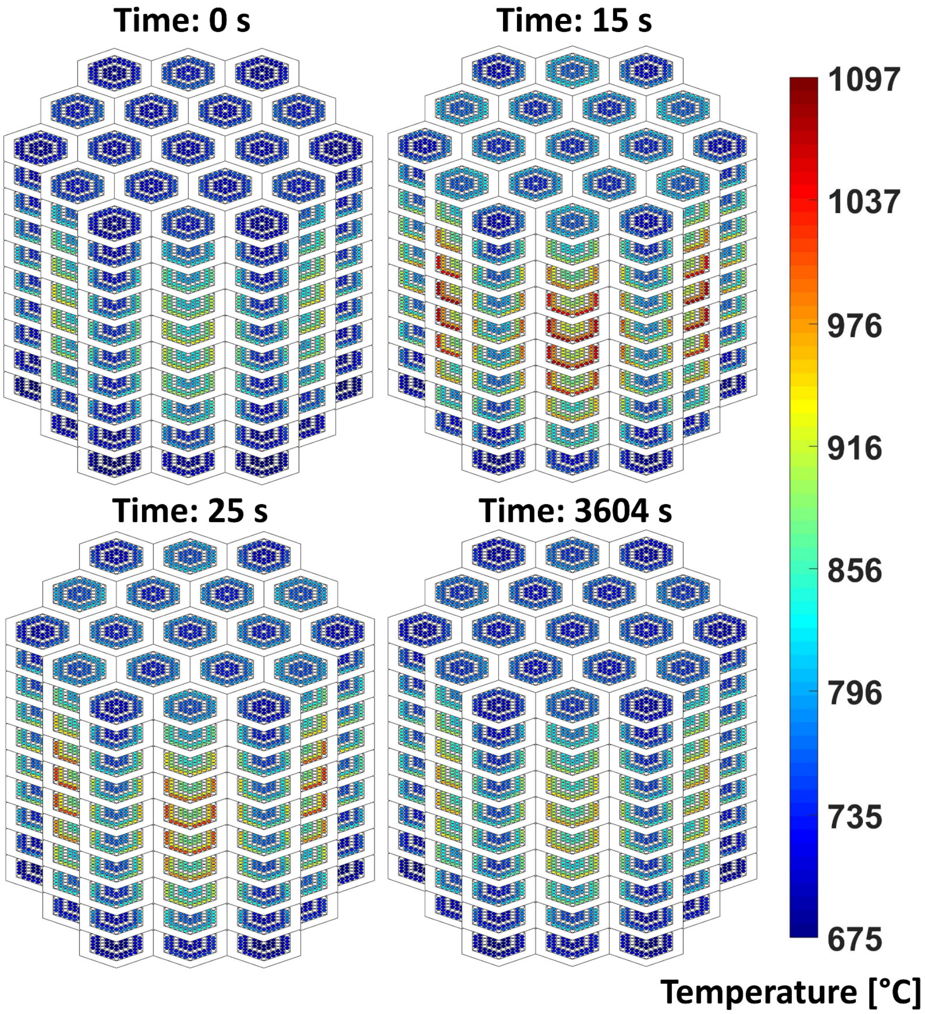

Figure 6.17: U-TOP accident 3-D fuel pin temperature distribution for four different times after accident initiation

Figure 6.18 shows the composite temperature profile at an axial location near the core center for one of the fuel assemblies with relatively high pin power densities for four different times. The transient evolution of fuel, coolant, and moderator temperatures is similar to the one shown in Figure 6.17.

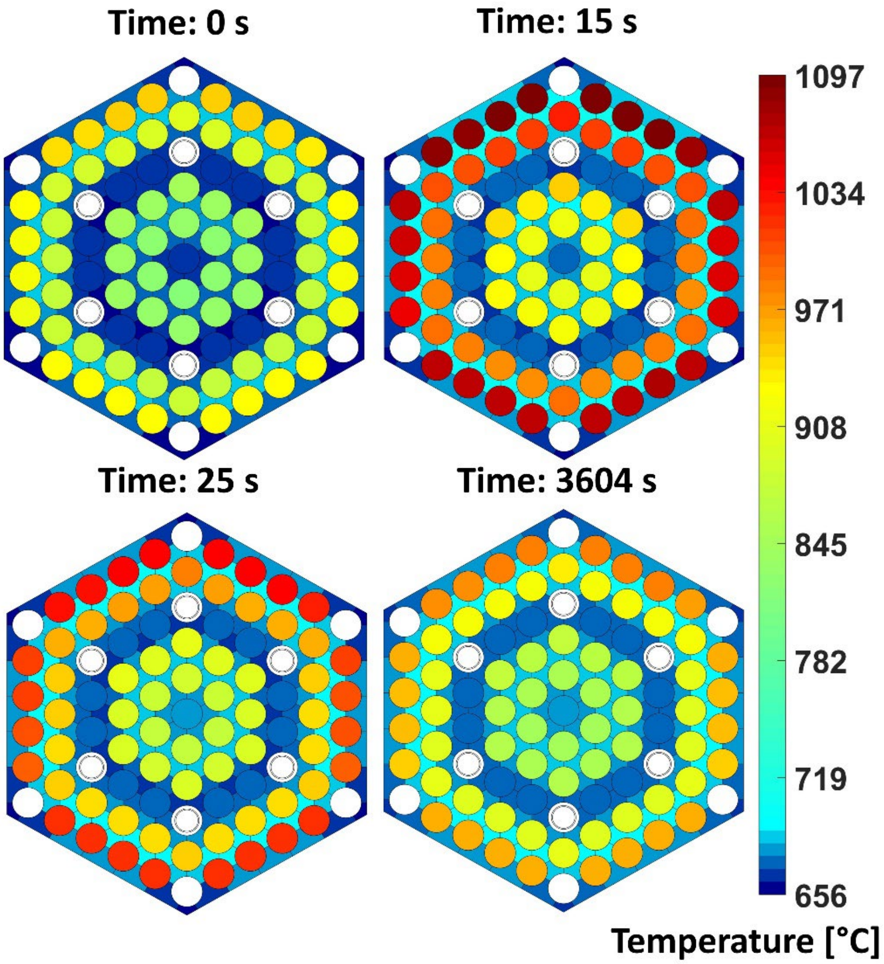

Figure 6.18: U-TOP accident fuel assembly temperature distribution for four different times after accident initiation

Figure 6.19 shows the maximum temperature difference between current and previous time steps (ΔT_{max}) and the time step size variation throughout the duration of the accident.

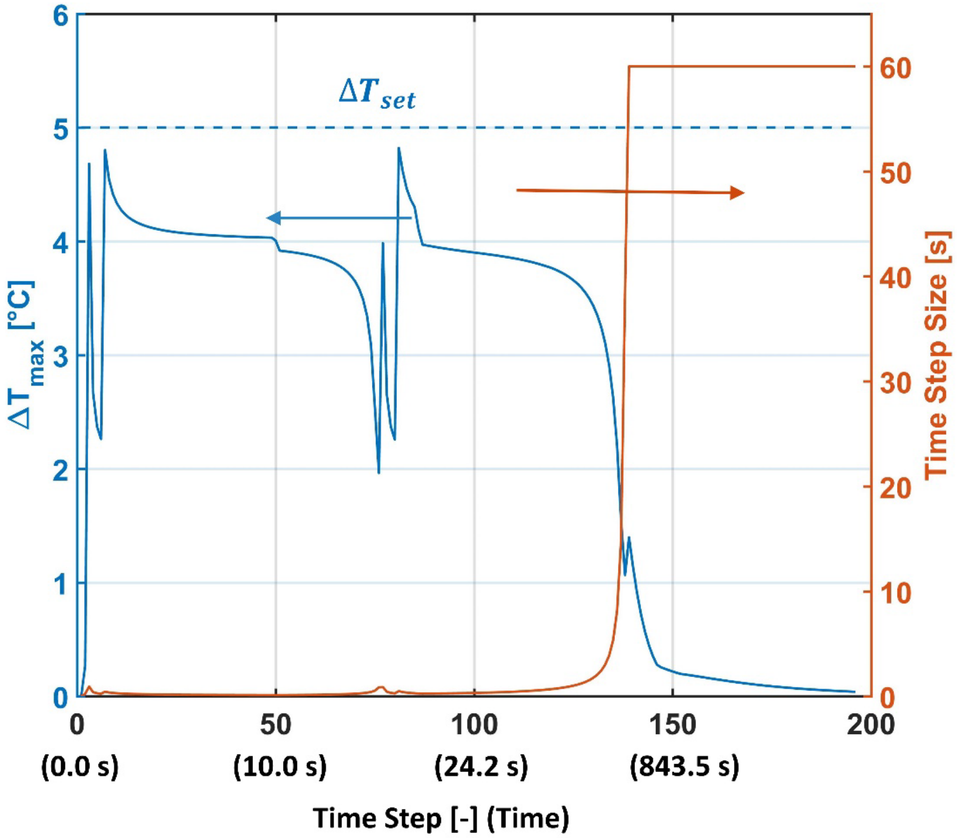

Figure 6.19: U-TOP accident maximum temperature difference between successive time steps and time step size

The x-axis of this plot shows both the time step as well as the total time simulated at the end of a few different time steps. The settings for the adaptive time stepping scheme used in the simulation are similar to the one employed in the U-LOHS simulation. The value of ΔT_{max} approaches zero at the end of the accident because the temperature changes in the core are very small even when a time step size as big as 60 s is used. It can also be seen from the figure that at the initial stages of the accident when there are fast changes in the core temperatures, very small time step sizes as low as ~ 0.1 s are employed by the adaptive time stepping scheme. After this initial phase, the temperature changes in the core become slower, and therefore, the size of the time step starts to increase until a point where the time stepping scheme starts to use the specified maximum time step value (60 s in this case).

Overall, the results for the U-TOP accident for the conditions/assumptions used in this study show that the temperatures of the fuel, graphite, and coolant regions in the core are within safe limits for the entire duration of the accident. However, as pointed out earlier, it is possible for the fuel temperatures to exceed the maximum allowable temperature for the TRISO fuel for more severe power excursions, and therefore, the core design might have to be optimized to provide better thermal margins against these accidents. A coupled analysis with a point kinetics neutronics model or a spatially resolved model such as COMET will provide a more accurate reactivity feedback, and can thus aid the determination of whether the core design needs to be optimized to provide better thermal margins for transient over power accidents with different ramp rates and reactivity insertion values.

CHAPTER 7. TRANSIENT ANALYSIS OF SOLID PIN-FUELED SMAHTR DURING LOW-FLOW ACCIDENT SCENARIOS

The application of the subchannel-based thermal hydraulic model for postulated forced-flow accidents involving high core inlet flow rates was investigated in the previous chapter. In this chapter, the application of the subchannel model for postulated accident scenarios that involve low core inlet flow rates is investigated. These low flow rates are encountered in situations such as unprotected or protected loss of forced flow (LOFF) into the core. After the loss of pump-induced forced flow, the flow into the core is provided by the buoyancy-induced natural circulation flows that are setup due to the heat addition from the core and the heat removal through the emergency decay heat removal system, such as the DRACS heat exchangers in the SmAHTR.

7.1 Thermal hydraulic modeling of special flow cases for pin bundle geometries

The thermal hydraulic model developed in the present work can be used for modeling steady-state and transient scenarios that cover a wide range of postulated accidents. However, for some cases that involve flow reversals, recirculating flows, or situations in which the magnitude of crossflows are comparable to the axial flows, the solution methodology of the fluid region (the subchannel mass, momentum, and energy equations) needs to be modified to provide converging, physically consistent solutions. The modification of the solution methodology to the subchannel conservation equations is necessary as the present methodology assumes unidirectional axial flow and also that the magnitude of the axial flows is significantly larger than that of the lateral crossflows. In fact, subchannel based codes such as COBRA-IV (Stewart et al., 1977) and COBRA-WC (George et al., 1980) offer two different solution methodologies, one for solving predominantly axial flows (similar to the one developed in the present work) and the other for solving special flow situations. The solution methodology for predominantly axial flows is from now on referred to as the ‘axial flow solver’, while the methodology for special flow cases is referred to as ‘general flow solver’. The solution methodology that solves special flow cases (recirculating flows, large magnitude crossflows, etc.,) is referred to as the ‘general flow solver’ because it can also solve the cases that involve predominantly axial flows. However, the application of the general flow solver for predominantly axial flows is not usually recommended as the general solver tends to be more computationally expensive compared to the axial flow solver. Therefore, the general solver is used only when the accident simulation under consideration warrants its application.

The general solver for subchannels in the pin bundle has discretization and formulation and conservation equations to allow flow in both positive and negative axial directions. The model has the ability to accept both pressure and flow inlet boundary conditions in contrast to the axial flow solver that can accept the flow inlet boundary condition. The control volumes for scalar and vector quantities are usually staggered to avoid the pressure checkerboarding issue (Patankar, 2018). Special schemes such as SIMPLE (Patankar, 2018), ACE (Stewart et al., 1977), or RECIRC (George et al., 1980) are used to achieve coupling of the conservation equations for the subchannel system under consideration.

The general solver is typically employed to analyze scenarios that have very low inlet flows, and natural circulation accident scenarios that have complex flow patterns inside the pin bundle (reversed flows in some subchannels and flow recirculation.) It must be noted that the reversed and recirculating flows have the net effect of reducing the transverse temperature gradient in the fuel assembly pin bundle regions, thus possibly reducing the fuel and coolant temperatures encountered during the natural circulation accident (Khan et al., 1979). Therefore, neglecting these complex flow patterns in the pin bundle is expected to provide conservative estimates for the core-level temperatures during LOFF scenarios. Neglecting reversed flows leads to a simplified unidirectional axial flow profile for the pin bundle which can be modeled using the subchannel model (with the axial flow subchannel solver) developed in the present study. The objective of the analyses presented in this chapter is to understand the general behavior of the SmAHTR solid pin-fueled core during a postulated LOFF accident scenario with scram, and get conservative predictions of the temporal evolution of the solid and fluid temperatures during the accident. Several simplifying assumptions have been made to enable the subchannel model developed in the present study to analyze LOFF scenarios. These assumptions are outlined in the subsequent sections. It must be noted that for the core-level thermal hydraulic model, the simplifying assumptions that have been made provide conservative estimates for the fuel and coolant regions in the core. However, some of the assumptions made in relation to the system-level response, such as the heat exchanger performance during the accident, are not necessarily conservative. For these system-level assumptions, sensitivity analyses have been performed to understand the impact of the fuel and coolant temperatures in the core during the transient.

7.2 Low-flow model simplifications/assumptions for LOFF analysis

7.2.1 Transient flow rate

During the LOFF, the primary coolant pumps in the reactor system initially operating at normal conditions lose power, which results in the coolant flow rate from the primary pumps decreasing until it reaches a value of zero. Figure 7.1 shows the transient coolant flow rate profile for the entire simulated LOFF accident (with scram) duration from the RELAP model. This RELAP modeling study was performed for the solid-pin fueled configuration and presented in the pre-conceptual design document (Greene et al., 2011).

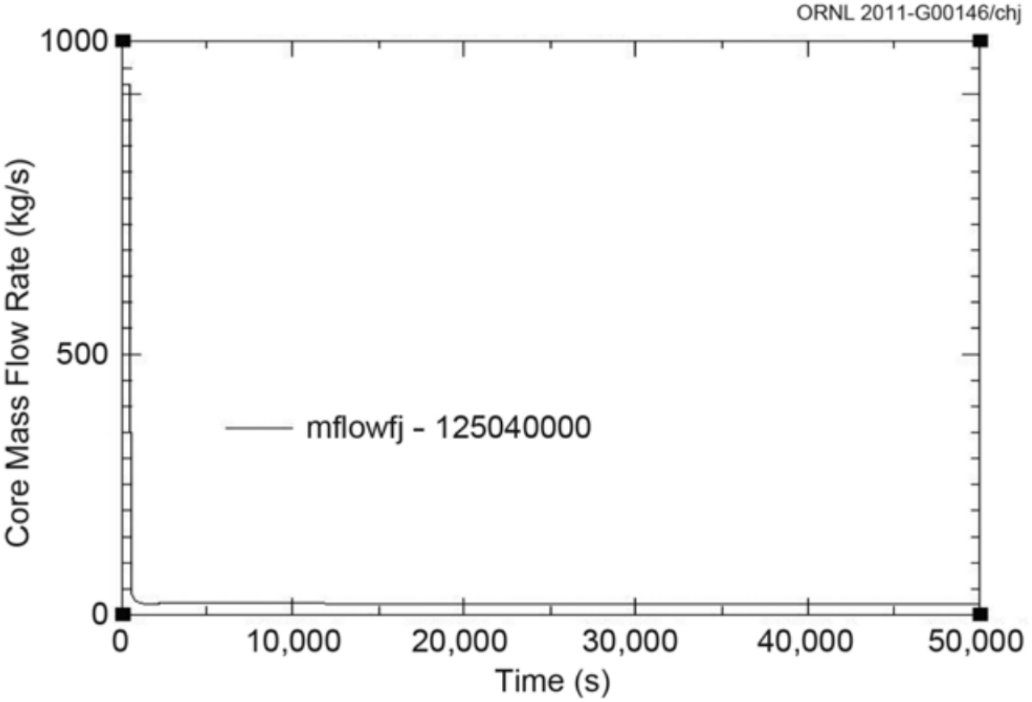

Figure 7.1: Core inlet flow rate for the RELAP LOFF model (Greene et al., 2011)

The reduction in the coolant flow rate from the pumps, referred to as the pump coastdown, is assumed to be linear in the RELAP model. The pump coastdown from normal operating conditions to zero flow is assumed to occur within 30 seconds after the accident initiation. It is to be noted that for the RELAP model, the reactor system is assumed to operate normally for the first 500 seconds of the simulated duration. The LOFF accident is initiated at t = 500 s.

From Figure 7.1, it can be seen that the coolant flow rate drops to a small fraction of the flow rate during normal operating conditions quickly after the LOFF. As the pump head, and hence the flow rate from the pumps, keeps decreasing during the coastdown period, the buoyancy effects slowly start increasing, and at the end of the pump coastdown, the coolant flow is solely due to the buoyancy effect. After the end of pump coastdown, the hot FLiBe fluid exiting the core then enters the DHX system, wherein it transfers the heat to the secondary FLiNaK coolant which is also driven by natural circulation. The heat from this secondary FLiNaK coolant is then ultimately rejected to the ambient through an air cooling tower (the flow of air is also driven by natural circulation.) The available buoyancy pressure head during natural circulation cooling depends on the difference in the average densities between the hot and cold legs, and the difference in elevation between the thermal centers of the heat source (core) and the heat sink (the DHXs). The primary coolant flow rate in the reactor system during natural circulation conditions is the flow rate that can be supported by the available buoyancy head, while overcoming the friction, form, spatial and temporal acceleration pressure losses in the reactor system (core, plenums, downcomer, heat exchangers, etc.) Therefore, the determination of the accurate coolant flow rate needs detailed modeling of the DHX system as well as the modeling of pressure losses in several reactor components outside the core, which is outside the scope of the present work.

Referring back to Figure 7.1, it can be seen that the coolant inlet flow rate during natural circulation cooling of the core remains approximately constant for the accident duration simulated in the RELAP model. The coolant flow rate will continue to decrease slowly over time for the protected LOFF accident, as the decay heat produced by the core will continue to decrease over time. While the coolant flow rates will be significantly different for very long durations after the onset of natural circulation, for the simulation durations considered in the RELAP model and in the present study, it is reasonable, based on Figure 7.1, to assume that the coolant flow rate during natural circulation remains approximately constant.

7.2.2 Core flow distribution

The discussion in the previous section pertained to the total flow rates during the LOFF transient. This section relates to the determination of the coolant flow distribution in the core once the total core flow rate has been specified. For the LOFF simulation in this chapter, the mass, momentum, and energy transport due to lateral pressure-driven crossflow are turned off, as the combination of low flow rates, steep radial power gradients, and small values of the subchannel geometry parameter ($A/\Delta z^2$) that determines convergence lead to unstable solutions for flow conditions that represent natural circulation cooling. It is possible to mitigate the convergence issues related to the geometry parameter by increasing the number axial segments in the core. However, this would significantly increase the computational cost of the simulations. The other two sources of convergence issues are related to boundary conditions and pin power distribution, which cannot be mitigated in this analysis. As mentioned earlier, the lateral flows between adjacent subchannels have the net effect of reducing the lateral temperature gradients in the rod bundle. This is due to the cooler fluid from the regions with higher fluid density (near the non-fuel pins or pins with low power densities) drifting towards the hotter fluid (with lower density) near pins with relatively higher power densities. This density gradient induced lateral flow thus provides an additional mechanism to mix the coolant in the pin bundle region, thus reducing the peak fuel and coolant temperatures during the LOFF. The assumption to model the coolant to be in a unidirectional axial flow with no lateral transport is therefore expected to provide conservative estimates for the fuel and coolant temperatures during the LOFF transient.

As a consequence of neglecting the lateral crossflows, the radial pressure gradients among the different subchannels in the fuel assembly are zero, and the mass flow rate distribution of the coolant in the fuel assembly needs to be determined by enforcing equal pressure drop among the subchannels in the fuel assembly. However, enforcing equal pressure drop at every time step in the LOFF simulation is computationally expensive. One simple option would be to assume that the coolant mass flow rate distribution during the LOFF remains the same as that of the steady-state, normal operating condition. However, this is not a realistic assumption as the flow distribution in the fuel assembly pin bundle is markedly different for low flow rate conditions compared to the flow distribution for normal operating conditions. This is due to the pin bundle flow regime shifting from transition flow (Cheng and Todreas, 1986) during normal operation to laminar flow during natural circulation cooling of the core. To provide a more realistic mass flow rate distribution for the core without incurring additional computational cost, the 'cold flow split' approach is used in the subchannel model for LOFF simulations.

In the cold flow split approach, the inlet mass flow rate into each individual subchannel in the core is determined by first calculating the subchannel flow split parameter for the given bundle inlet Reynolds number. The subchannel flow split parameter is defined in Equation 2.14. For laminar and fully turbulent flow regimes, the equations to calculate the flow split parameters for the three different types of subchannels in hexagonal pin bundle geometries is provided in the work of Cheng and Todreas (1986). For the transitional flow regime, the flow split parameter cannot be calculated directly, as the subchannel friction factors for this regime are calculated using an interpolation scheme. To determine the flow split parameters for the transitional flow regime for the specific pin bundle geometry considered here, isothermal simulations are performed using the present subchannel model for a range of bundle Reynolds numbers that are of interest to the LOFF analyses. Lateral crossflows between adjacent subchannels are not included, and the flow distribution is determined by enforcing equal pressure drop across all the subchannels in the pin bundle. The procedure for enforcing equal pressure drops across all the subchannels is similar to the one discussed in Chapter 2 for enforcing equal pressure drop across all fuel assemblies in the core. The flow split parameters from the isothermal model for different types of subchannels as a function of bundle inlet Reynolds number are shown in Figure 7.2.

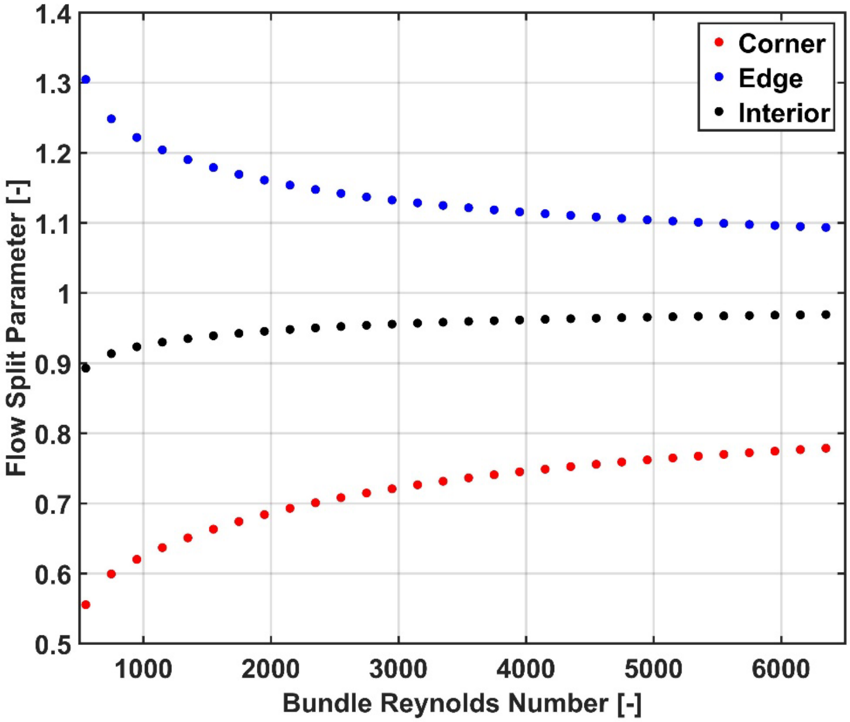

Figure 7.2: Subchannel flow split parameters

The bundle inlet Reynolds number for the normal operating condition is ~5,950. This Reynolds number value represents the highest value encountered during the LOFF accident. The critical Reynolds number for laminar-to-transition flow for this bundle geometry is ~595, while the critical Reynolds number for transition to fully turbulent flow is ~13,260 (Cheng and Todreas, 1986). All the data points shown in Figure 7.2 correspond to the transition flow regime for the bundle, except for the data point that corresponds to the lowest bundle Reynolds number, which is in the laminar flow regime.

For the corner and edge subchannels, a polynomial curve fit is developed for the flow split parameters in the transition flow regime. For a given bundle Reynolds number, the flow split parameter for the interior subchannels in the pin bundle is determined by first calculating the flow split values for the edge and corner subchannels, and then applying mass continuity. If the bundle Reynolds number is less than the critical Reynolds number, the equations from the work of Cheng and Todreas (1986) are used for calculating the flow split values. Table 7.1 summarizes the flow split parameter computations for the LOFF model.

Table 7.1: Flow split parameter estimation for subchannels

Subchannel type	Flow split parameter	Range
Corner	$4.7541 \cdot 10^{-1} + 1.9606 \cdot 10^{-4} \cdot Re_b - 6.1796 \cdot 10^{-8} \cdot Re_b^2 + 9.6861 \cdot 10^{-12} \cdot Re_b^3 - 5.7377 \cdot 10^{-16} \cdot Re_b^4$	$Re_{b,norm} \geq Re_b \geq Re_{crit,lam}$
	Cheng and Todreas (1986)	$Re_b < Re_{crit,lam}$
Edge	$1.4025 - 2.5338 \cdot 10^{-4} \cdot Re_b + 9.1421 \cdot 10^{-8} \cdot Re_b^2 - 1.5141 \cdot 10^{-11} \cdot Re_b^3 + 9.1949 \cdot 10^{-16} \cdot Re_b^4$	$Re_{b,norm} \geq Re_b \geq Re_{crit,lam}$
	Cheng and Todreas (1986)	$Re_b < Re_{crit,lam}$
Interior	Mass continuity	$Re_{b,norm} \geq Re_b \geq Re_{crit,lam}$
	Mass continuity	$Re_b < Re_{crit,lam}$

The $Re_{b,norm}$ shown in the table refers to the pin bundle Reynolds number during the normal operating conditions, which represents the highest Reynolds number encountered during LOFF scenarios. The polynomial curve fits for corner and edge subchannels shown in the table have a coefficient of determination (R^2) value of ~1, indicating a very good fit. As these flow split values are determined for an isothermal case without accounting for the temperature-dependent fluid property variations, this flow split is referred to as the 'cold' flow split. This cold flow split approach only accounts for the variations in the frictional pressure drops among the different types of subchannels (corner, edge, and interior) to determine the flow distribution in the pin bundle. During the LOFF transients, the fluid properties (density and viscosity) that influence pressure drop could markedly vary along the length of the subchannel, among the different types of (corner, edge, and interior) subchannels, and also among the subchannels of the same type (the fluid properties for an interior subchannel connected to three fuel pins will be different from an interior subchannel connected to two fuel pins). These temperature-dependent fluid property variations will influence the pressure drops in subchannels and therefore in turn influence the flow distribution in the pin bundle. To understand the impact of the temperature-dependent fluid properties, steady-state simulations are performed for a pair of fuel assemblies in the SmAHTR core for different axial core temperature rise (ΔT) values of the primary coolant. As the ΔT value increases, the temperature-dependent property variations play a larger role in influencing subchannel pressure drops and flow distribution in the pin bundle. One of the fuel assemblies considered in these simulations has the highest power density in the core, while the other fuel assembly has the lowest power density. The axially integrated relative power densities for the two fuel assemblies are shown in Figure 7.3.

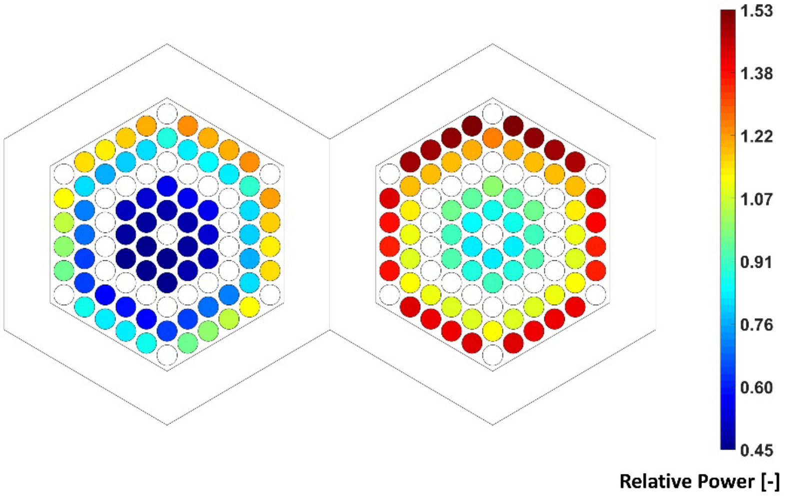

Figure 7.3: Fuel assemblies for temperature-dependent property variations

In one set of steady-state simulations, the flow distribution is determined by including the effects of the temperature-dependent fluid properties. In the other set of steady-state simulations, the cold flow split parameters outlined Table 7.1 are used for determining the flow distribution. The key results from these steady-state simulations are outlined in Table 7.2.

Table 7.2: Temperature-dependent fluid property effects for the two-fuel assembly system

Case	Power (MW)	Total pin bundle flow rate (kg s^{-1})	Axial coolant ΔT (K)	Peak fuel temperature (°C)	Peak clad temperature (°C)	Peak coolant subchannel temperature (°C)
ΔP	13.0	107.0	50.8	1293.4	954.0	758.0
CFS				1303.4	968.7	766.8
ΔP	13.0	137.8	39.5	1247.6	912.3	736.4
CFS				1253.1	920.2	741.0
ΔP	13.0	184.0	29.6	1204.3	872.0	716.1
CFS				1207.1	876.0	718.3
ΔP	8.7	184.0	19.8	1011.7	800.5	694.5
CFS				1013.7	802.4	695.5
ΔP	4.3	184.0	9.9	826.0	726.6	672.4
CFS				826.4	727.2	672.7

ΔP: Equal pressure drop across all subchannels including temperature-dependent fluid properties
CFS: Cold assembly flow split parameters

Two important conclusions about the effect of temperature-dependent fluid property effects on the flow distribution, and hence the key temperatures in the fuel assembly can be derived from the table. First, it can be observed that the peak temperatures of the fuel, cladding, and the coolant regions predicted by the equal pressure drop (ΔP) case are always lower than the cold flow split (CFS) case. This implies that using the cold flow split for determining the flow distribution should provide conservative estimates for the peak temperatures for the key solid and fluid regions in the core. The other key conclusion is that the effects of temperature-dependent fluid properties decrease with decreasing ΔT. This is evident from the differences in the peak temperatures predicted by the ΔP and CFS cases for the highest ΔT (50.8°C), which are noticeably larger compared to the difference between both the cases for the lowest ΔT (9.9°C) investigated here.

Figure 7.4 shows the subchannel mass flow rates predicted by the equal pressure drop and cold flow split cases for the highest (50.8°C) and lowest (9.9°C) ΔT values investigated here. These mass flow rates are for one of the hottest fuel pins in the two-fuel assembly system considered here.

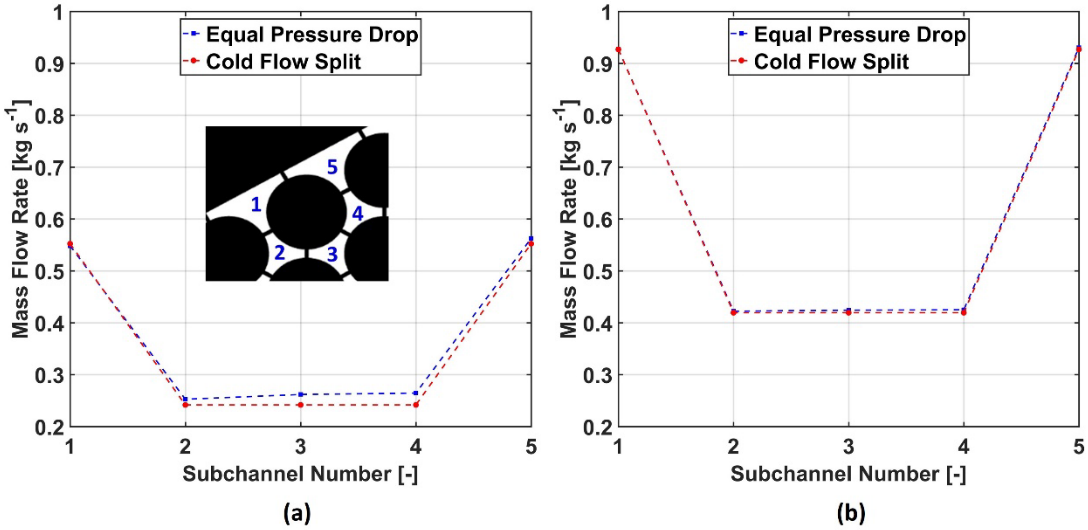

Figure 7.4: Subchannel mass flow rates for the hot fuel pin (a) ΔT=50.8°C, and (b) ΔT=9.9°C

Figure 7.4a shows that the subchannel mass flow rates surrounding the hot pin predicted by the equal pressure drop case are markedly higher than the flow rates from the cold flow split case, with the highest difference being ~8.6%. The difference between these two cases is attributed to the temperature-dependent fluid properties, which affect the subchannel hydraulic resistances and hence the flow distribution in the fuel assembly system. The inclusion of temperature-dependent properties effectively lead to more coolant flowing through the hotter regions of the pin bundle for the conditions investigated here. These higher flow rates result in lower peak fuel, cladding, and coolant subchannel temperatures for the equal pressure drop case compared to the cold flow split case (Table 7.2). Figure 7.4b shows the subchannel flow rates for the lowest (9.9°C) ΔT investigated. The differences between the two cases (equal pressure drop and cold flow split) are much smaller for this ΔT, which is expected as the impact of the temperature-dependent fluid properties on the flow distribution should be lower. However, the subchannel mass flow rates for the hotter pin bundle regions predicted by the equal pressure drop case are still slightly higher than the cold flow split case.

In summary, the studies for quantifying the impact of temperature-dependent fluid properties on flow distribution indicate that the cold flow split approach is generally more conservative than the equal pressure drop approach that includes temperature dependent fluid property variations. During transient scenarios, the subchannels will also have an additional pressure drop due to temporal acceleration/deceleration of the coolant. However, the temporal acceleration for a single-phase coolant such has FLiBe which also has a very high volumetric heat capacity is expected to be negligible, especially for accidents with scram such as P-LOFF. Therefore, the cold flow split approach is used in the LOFF simulations.

7.2.3 Heat exchanger system transient heat duty profile

As previously discussed in the P-LOHS simulation in Section 6.4.1, both the PHX system which comprises three individual heat exchangers, as well as DHX system, which comprises three additional heat exchangers could all be operational at normal operating conditions. The heat generated from the core that leaves through the PHX system is transferred to the secondary FLiNaK coolant for process heating or electricity generation, while the heat transferred into the secondary FLiNaK coolant in the DRACS system is rejected to the ambient, thus being a parasitic loss for the system. While this parasitic loss is aimed to be minimized, the SmAHTR design still requires a small fraction of heat to be transferred to the DRACS during normal operation, to prevent the secondary FLiNaK from freezing. When the LOFF accident is initiated, several different complex, interconnected phenomena occur in the PHX and DHX systems before the system transitions from being at forced flow conditions to natural circulation cooling conditions. The heat duty of the PHX system starts decreasing after the onset of LOFF due to pump coast down and decreasing primary coolant (FLiBe) flow rate into the PHXs. At the same time, the flow of primary coolant through the DHXs, which was initially from the bottom to top during normal operation, starts reversing, until the FLiBe coolant flows from the top to bottom of the DHXs. The flow remains from the top to bottom direction for the DHXs throughout the rest of the transient. The simulation of these complex phenomena including the transient heat duty reduction of the PHX system and the transient heat duty variations in the DHX system require detailed models for several different components outside the core, which as mentioned earlier, is outside the scope of the present analysis. To understand the core behavior during the LOFF accident for some reasonable system-level inputs, a simplified transient heat duty modeling approach is considered. Sensitivity studies on some of the heat duty modeling assumptions are also performed to understand the impact on the key temperatures in the core during the LOFF accident. In the baseline case, it is assumed that the PHX system heat duty undergoes an exponential decay, similar to the profile considered in the P-LOHS accident discussed in Section 6.4.1. It is also assumed that the DHX system heat duty remains a constant value throughout the accident, and this value is set to 1.25 MW (1% of the normal core power). A sensitivity analysis is also performed in which the effect of PHX heat duty decay profile is investigated by comparing the results from the baseline exponential decay profile with a linear decay profile. The linear profile is chosen for comparison as it is similar to the linear pump coast down profile considered in this study. Figure 7.5 shows the two PHX decay profiles investigated in this study. Both the profiles are set such that the PHX heat duty is effectively zero at 30 s after the onset of the LOFF accident.

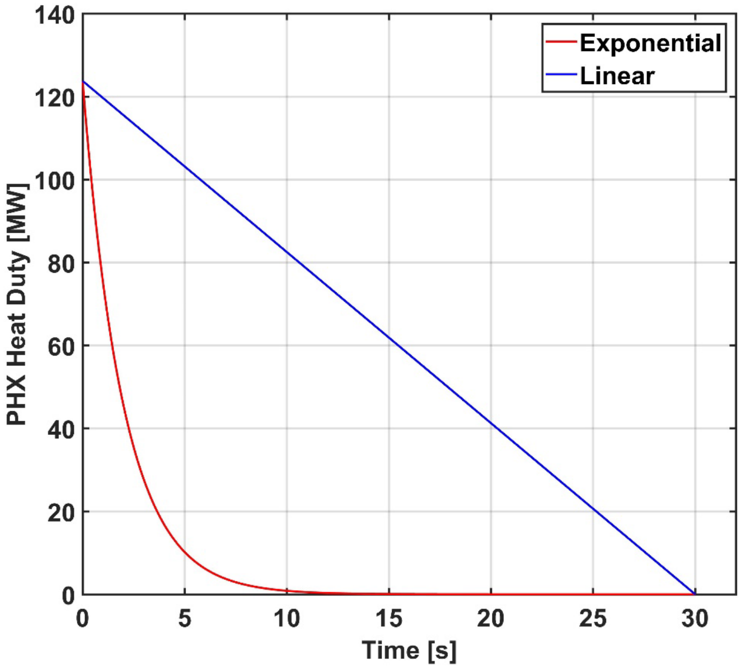

Figure 7.5: PHX heat duty decay profiles

7.3 LOFF simulations

7.3.1 Accident settings

For the LOFF simulations, the reactor is initially operating at full power (125 MW). In the system-level model, the initial temperature of the upstream volume (lower plenum and downcomer) is set to the core inlet temperature of 650°C, while the initial temperature of the downstream volume (upper plenum and top plenum) is set to the core outlet temperature of ~680°C. The total coolant flow rate into the upstream volume is set to 1770 kg s^{-1} (1750 kg s^{-1} for active core region and 20 kg s^{-1} for the radial reflector coolant channels.) As the present subchannel modeling methodology is somewhat different from the modeling presented in the previous chapters, a new steady-state simulation with no lateral crossflow is performed to initialize the LOFF accident. The cold flow split approach discussed earlier is used for determining the flow distribution for this steady-state model. The transport between adjacent subchannels due to turbulent and molecular effects is still included. The power profile from the COMET neutronics model is used in the steady-state simulation. The profiles for temperature, pressure, and mass flow rate for the solid and fluid regions in the core obtained from this steady-state simulation are set as initial values for the LOFF model. Table 7.3 compares the key results from the new steady-state simulations with cold flow split inlet boundary condition with the steady-state results presented in Section 4.1 (which includes lateral crossflow).

Table 7.3: Steady-state results comparison

Case	Crossflow	Inlet flow boundary condition	Peak fuel temperature (°C)	Peak coolant subchannel temperature (°C)	Total core pressure drop (kPa)
1	No	Cold flow split	1206.1	706.8	94.3
2*	Yes	Uniform mass flux	1204.9	705.8	94.4

From the table, it can be seen that the key steady-state results corresponding to the new simulation (Case 1) are only slightly different from the results presented in Section 4.1 (Case 2 in this table).

At t = 0, the primary coolant flow rate is subjected to a linear coast down. Within 30 s, the primary coolant flow rate is reduced from the initial value of 1770 kg s^{-1} to a value of 27 kg s^{-1}. The flow rate of 27 kg s^{-1} at the end of 30 s represents the three DHXs operating at the nominal rated capacity, each with a flow rate of 9 kg s^{-1}, which is the DHX design value provided in the pre-conceptual design report (Greene et al., 2011). The exponential PHX heat duty decay profile is used in the baseline study.

At t = 0, the reactor system scrammed, and the core power levels quickly decrease to decay heat levels. Similar to the P-LOHS simulation, the decay heat profile from El-Wakil (1978) is used in the LOFF simulations. The baseline simulation was performed for a total of ~12,000 s (~3.3 hours). The total runtime for this simulation was ~25 hours. The results from this simulation are discussed next.

7.3.2 Results and discussion

Figure 7.6 shows the thermal power generation and removal by the coolant in the core after the initiation of the P-LOFF accident.

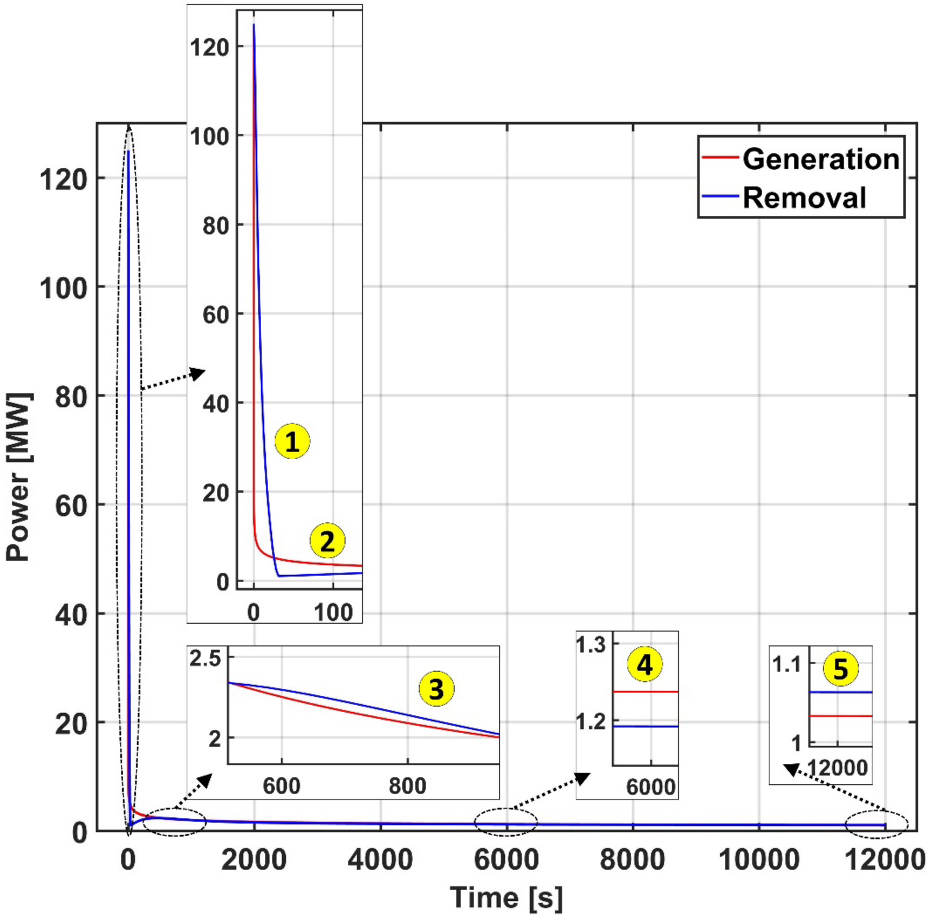

Figure 7.6: P-LOFF accident core transient thermal power generation and removal profile

The core power generation starts decreasing due to the scram and quickly reduces to a small fraction of the initial power value. The thermal power removed by the coolant also starts rapidly reducing due to the combination of decreasing flow rate through the core as well as the decreasing heat removal capacity of the PHX system. The first phase where the coolant heat removal is above the core heat generation is marked as ‘1’ in Figure 7.6. During this phase, the temperatures of the core elements, especially the fuel and coolant regions decrease. This is followed by the phase marked as ‘2’ in Figure 7.6, in which the coolant heat removal falls below core heat generation, leading to an increase in thermal storage in the solid and fluid regions in the core. The coolant heat removal then starts to slowly increase until it briefly surpasses the thermal energy generation in the core (marked as ‘3’ in Figure 7.6, until it once again decreases to a value below the core heat generation (marked as ‘4’ in Figure 7.6). This heat-up phase (marked as ‘4’) continues for a relatively long time (~8,190 s), after which the coolant heat removal finally surpasses thermal generation, leading to the final cool-down phase (marked as ‘5’ in Figure 7.6). This cool-down phase begins after ~9,220 s of the onset of the P-LOFF accident and continues for the rest of the simulated accident duration. The complex behavior of the coolant heat removal curve is influenced by several factors such as the temperature difference between the fuel and coolant regions in the core (which provides the driving temperature difference for heat transfer to the coolant), heat transfer between the coolant and other non-fuel graphite regions (moderator pin, poison pin, graphite reflectors, etc.,) and thermal storage in the fuel, coolant, and graphite regions in the core. These factors influence how the thermal energy is stored, redistributed, and removed by the coolant flowing through the core.

Figure 7.7a shows the transient temperature profile for the coolant entering and leaving the core, as well as for the HX system for times up to ~60 s after the initiation of the accident. Figure 7.7b shows the same temperature profiles but for the entire duration of the accident.

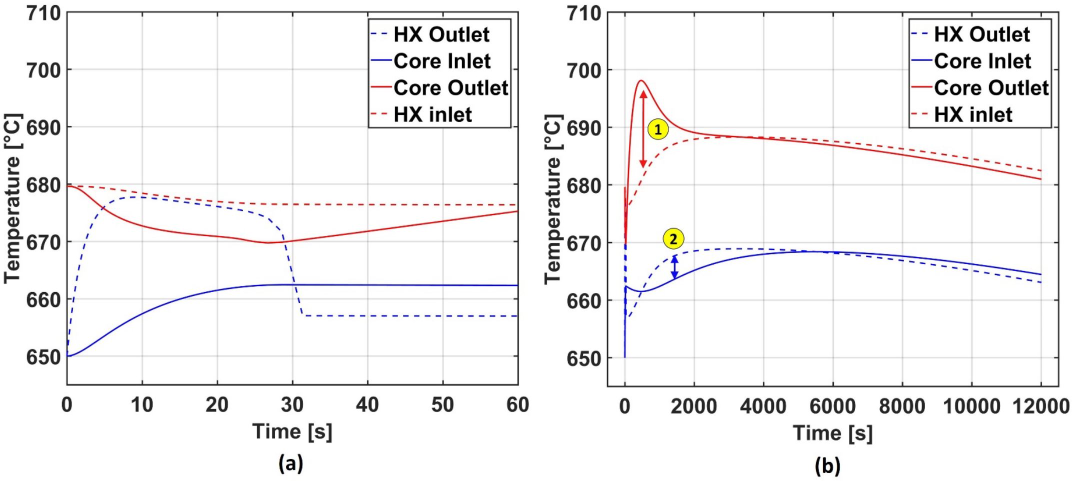

(a) (b)

Figure 7.7: P-LOFF accident (a) inlet and outlet temperatures for the core and heat exchanger for times up to ~60 seconds after accident initiation, and (b) core and heat exchanger coolant temperatures for the entire accident duration

From Figure 7.7a, it is seen that the core outlet temperature starts decreasing immediately after the initiation of the LOFF accident due to initiation of the scram. However, after ~30 s of the initiation of the accident, the core outlet temperature starts increasing until it reaches a maximum value of ~698°C ~460 s into the accident. The core outlet temperature then continues to decrease for the remainder of the simulated accident duration. The heat exchanger outlet temperature shown in Figure 7.7a initially has a sharp increase. This sharp increase is due to the PHX heat duty decaying faster (exponentially), while the primary coolant flow rate decaying relatively more slowly (linearly). At the end of the pump coastdown period (~30 s), the HX outlet temperature reaches a relatively lower value. The HX outlet temperature then slowly increases over time to a peak value of ~678°C, after which it decreases for the rest of the simulated accident duration. Similarly, the core inlet temperature increases up to a maximum value of ~668°C (which is 18°C higher than the initial normal operation value), after which it continues to decrease over time. Overall, the coolant temperatures outside the reactor core remain within the safe limits to not cause any structural damage to the metallic components in the reactor. Figure 7.7b also shows the lag between the core outlet temperature and the HX inlet temperature (marked by ‘1’), which is attributed to the thermal storage in the volume downstream of the core that represents upper and top plenum regions. Similarly, the lag between the HX outlet temperature and core inlet temperature (marked by ‘2’) is attributed to the thermal storage in the volume corresponding to lower plenum and downcomer regions.

The total mass of the coolant salt entering the notional ‘expansion volume’ is <1% of the initial salt stored in the downstream volume (upper plenum and top plenum) during the reactor heat-up phase. This relatively small amount of mass therefore does not significantly affect the overall thermal response of the system (as mentioned previously, the mass stored in the expansion volume does not provide thermal storage during the transient.) The total mass of the coolant leaving the ‘expansion volume’ is ~0.25% during the reactor cool-down phase.

The peak temperatures for different solid regions (active fuel, cladding, moderator pins, and graphite reflectors) and the fluid regions (coolant subchannels and coolant channels in radial reflector) in the core are shown in Figure 7.8. The peak temperature for the active fuel region is the highest at the normal operating condition. After the reactor is scrammed, the peak fuel temperatures quickly decrease during the initial cool-down phase. The peak fuel temperature only increases by a few degrees during the heat-up phase, to the highest value of ~756°C at ~188 s after the onset of the LOFF accident, and then continues decrease for the rest of simulated accident duration. The temperature profiles for cladding, moderator, and coolant regions follow a similar trend. The highest coolant subchannel temperature within the core is ~ 723°C, at ~ 370°C after the LOFF accident onset. The temperatures of the graphite reflectors and the coolant channels in the radial reflector also remain within relatively low values. Overall, the temperatures for all the regions in the core remain within safe limits for the duration of the simulated accident.

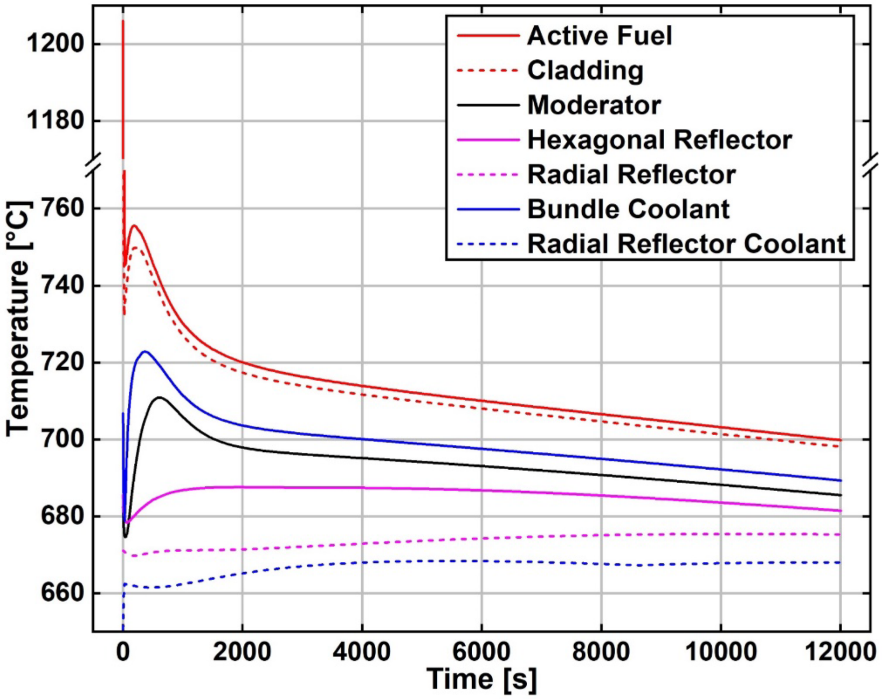

Figure 7.8: P-LOFF accident peak temperature transient profile

Figure 7.9 shows the 3-D, volumetrically weighted average temperature at each axial location for all the fuel pins in the core at four different times.

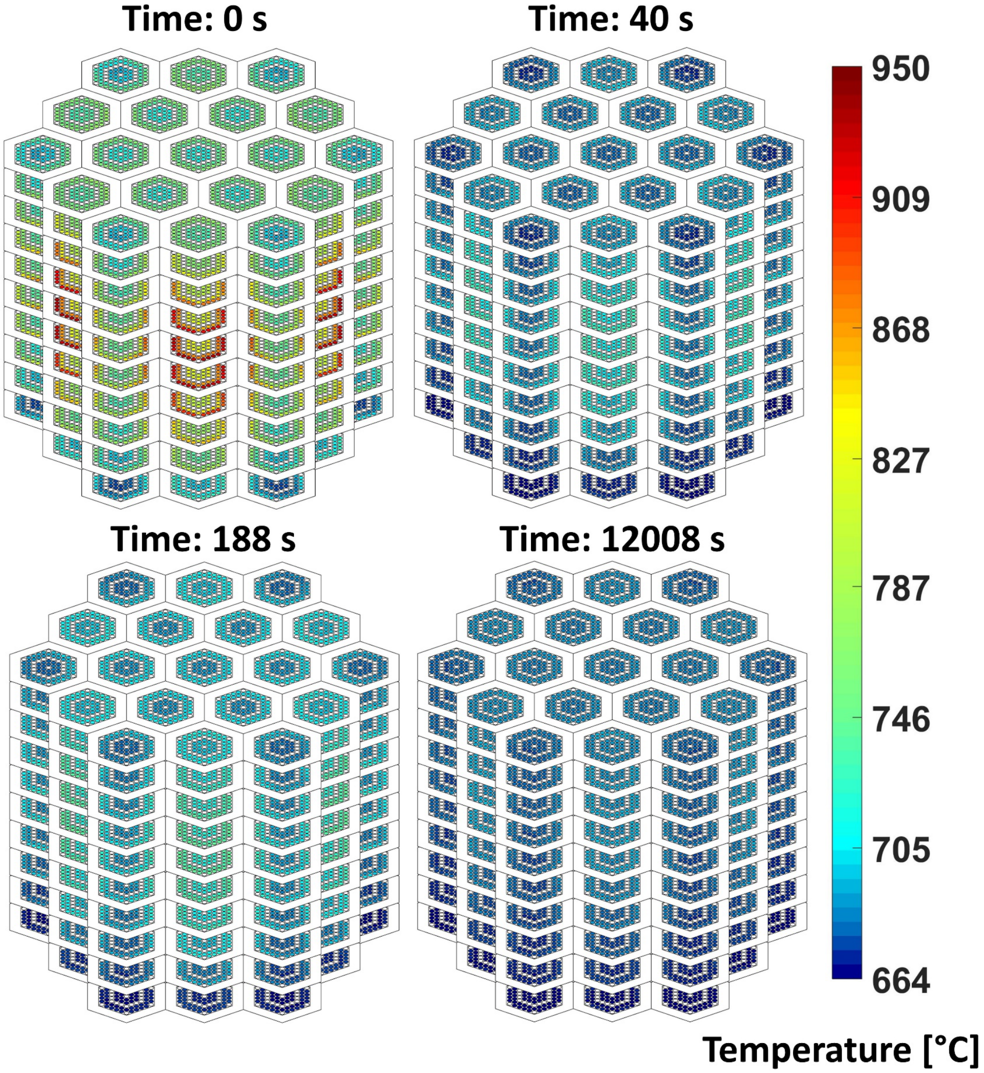

Figure 7.9: P-LOFF accident 3-D fuel pin temperature distribution for four different times after accident initiation

The temperatures at 0 s correspond to the steady-state temperature profile. The pin temperatures at ~40 s are significantly lower than the steady-state profile, due to the initiation of scram. By ~188 s, the temperatures are slightly higher that the temperatures corresponding to t ~40 s, which is due to the core being in the heat-up phase (this also follows the peak fuel temperature trend shown in Figure 7.8.) At the end of the simulated time, the fuel temperatures are now much lower, and the radial and axial temperature differences across the core are also very small.

Figure 7.10 shows the composite temperature profile for the fuel, moderator, and coolant regions at an axial location near the core center for one of the fuel assemblies with relative pin high power densities for four different times.

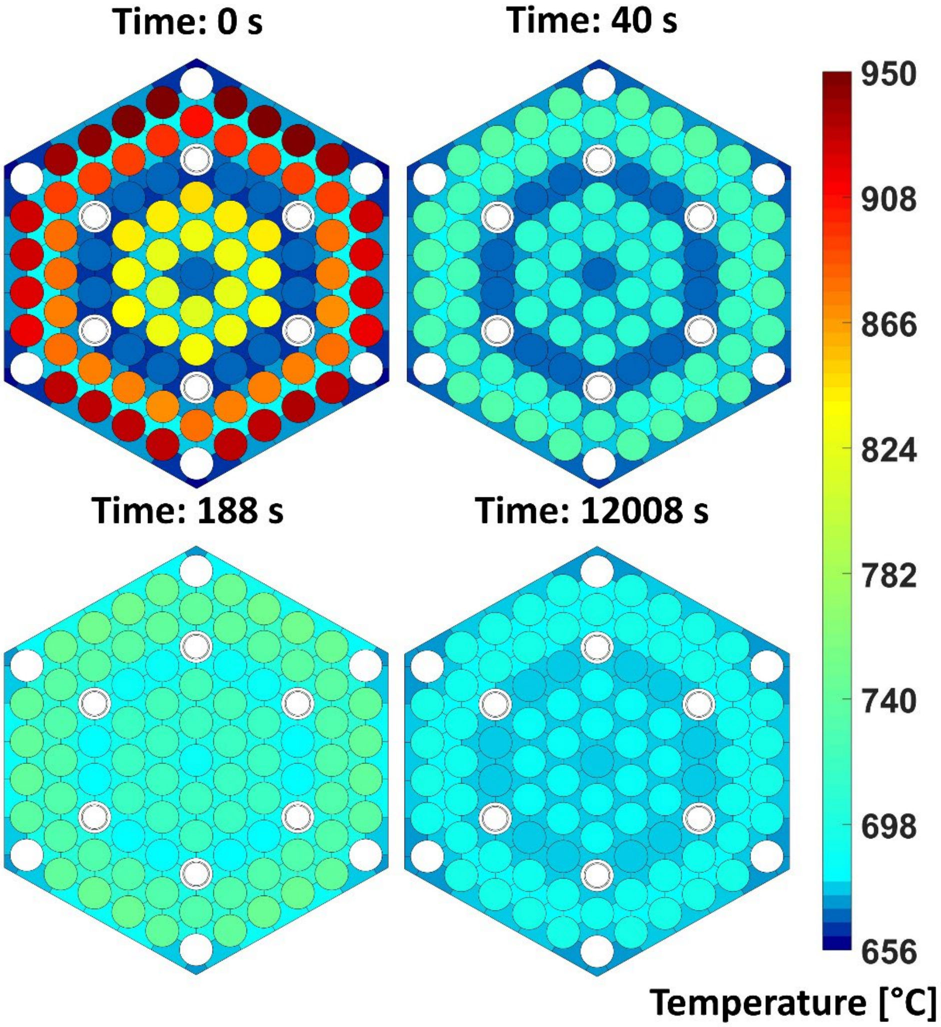

Figure 7.10: P-LOFF accident fuel assembly temperature distribution for four different times after accident initiation

The fuel temperature trends in Figure 7.10 are similar to the 3-D fuel temperature profiles shown in Figure 7.9. The temperature gradient of the subchannels across the core are flatter at the end of simulated time (t=12008 s) compared to the initial, steady-state (t~0 s) condition. It can also be seen from the figure that the temperatures of the moderator pins, especially at times 188s and 12008s after the onset of LOFF, are higher than the steady-state values, which is attributed to the increase in the coolant subchannel temperatures, which in turn heat the moderator pins.

Figure 7.11 shows the maximum temperature difference between current and previous time steps (ΔT_{max}) and the time step size variation throughout the duration of the accident. The adaptive time stepping settings used for the LOFF simulation are similar to the ones employed in the previous chapter for the P-LOHS and the U-TOP accident simulations, except that the maximum time step size is now limited to 30 s instead of 60 s. This maximum time step size was chosen to improve the convergence performance (and reduce the number of internal iterations) for this simulation. Once again, the value of ΔT_{max} is ~4°C (instead of the ΔT_{set} value of 5°C) because of the time step reduction factor value of 0.8 used in this simulation. As with the previous accident simulations, the adaptive time stepping scheme employs relatively small time steps (~0.1 s) during the initial stages, while the largest time step size (30 s) is used in the later stages of the P-LOFF accident simulation.

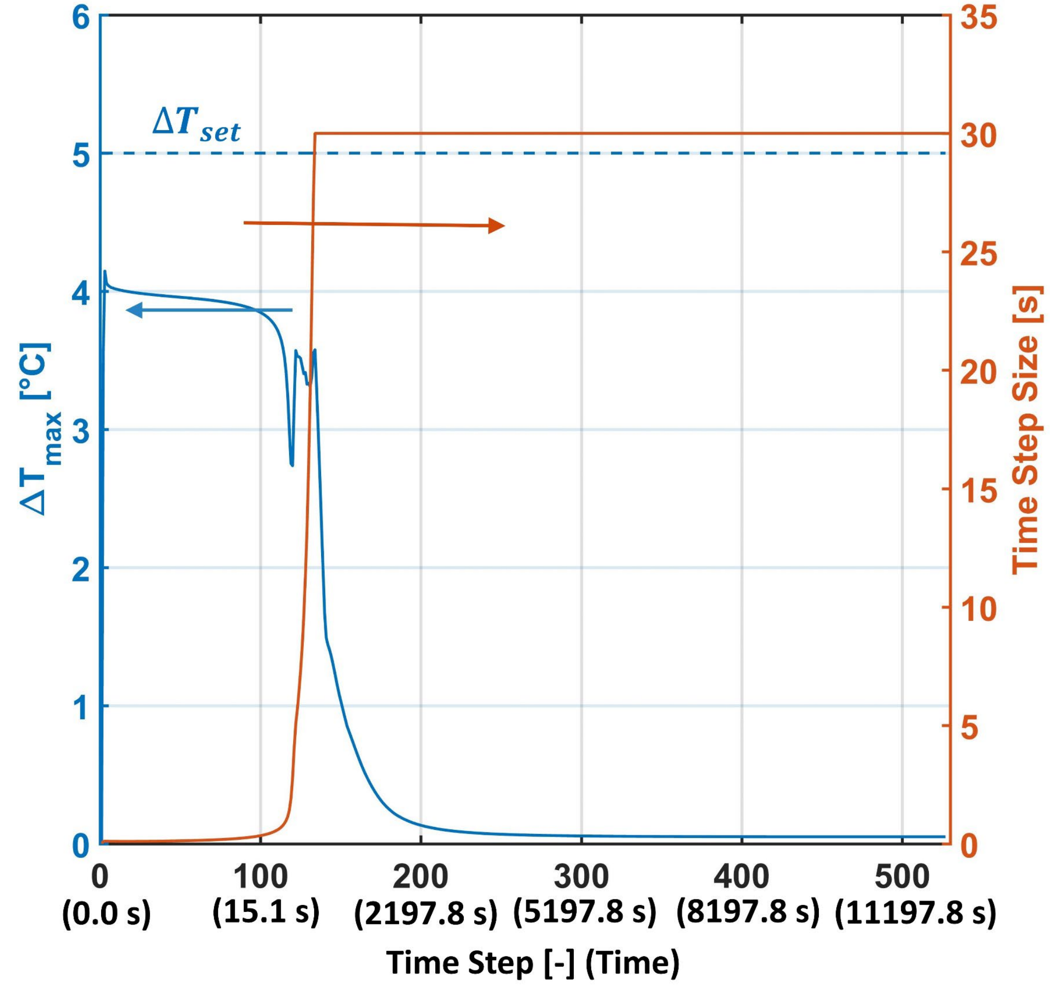

Figure 7.11: P-LOFF accident maximum temperature difference between successive time steps and time step size

7.3.3 PHX transient heat duty profile sensitivity analysis

As mentioned earlier, the baseline study considers an exponential profile for the PHX heat duty decay during the LOFF transient. To assess the sensitivity of this PHX profile on the key results from the LOFF accident, the results from a simulation with exponential PHX heat duty profile are compared with the result from a simulation with a linear PHX profile (Figure 7.5). Table 7.4 shows the key results from both the simulations.

Table 7.4: PHX heat duty profile sensitivity

PHX profile	Active fuel region		Coolant subchannel	
	Peak temperature* (°C)	Time (s)	Peak temperature (°C)	Time (s)
Exponential	755.6	~188	722.9	~370
Linear	744.6	~177	714.0	~357

* Peak temperature during the LOFF transient after the initial cool-down phase

From the table, it can be seen that a linear profile results in lower fuel and coolant temperatures compared to the exponential profile. This is expected, as the linear PHX decay provides more heat removal from the reactor system (including the core) compared to the exponential profile (Figure 7.5). Also, the table shows that the difference in temperatures, as well as the time at which the peak fuel and coolant temperatures are reached are not significantly different between the exponential and linear profiles, thus demonstrating the relative insensitivity of on the results from the model to the PHX transient decay profile.

Overall, the results from the LOFF simulations indicate that for the accident settings considered in this study, the temperatures of the fuel, coolant, and other regions in the core, as well as the coolant temperatures outside the core remain within safe limits during the accident.

CHAPTER 8. SUMMARY AND CONCLUSIONS

A whole-core thermal hydraulic model with fast turnaround times was developed for pin-fueled FHRs. The modeling methodology for the different solid and fluid regions in the core was outlined, and the overall modeling architecture was discussed. Code verification was performed to first verify the key sub-models (solid conduction, lateral crossflow, and turbulent mixing.) The present thermal hydraulic model was also able to predict the flow split results from the GE 3×3 rod bundle data with excellent agreement. To enable a more comprehensive code-to-code comparison, a CFD model with conjugate heat transfer was developed for 1/12th of a single fuel assembly in the solid pin-fueled FHR.

Before comparing with the subchannel model, the effects of grid refinement, inlet turbulence specification and turbulence model for the CFD model were investigated. The results indicated that the value of turbulence intensity has a noticeable impact on the fuel pin temperatures, but only at axial locations close to the core inlet. For the bundle geometry and conditions investigated in this study, replacing the bundle hydraulic diameter with viscosity ratio as the second turbulence specification parameter has no noticeable impact on fuel pin temperatures.

The choice of turbulence model has a significant impact on the temperatures and pressure drop in the model domain. For the conditions investigated in this study, the k-ε realizable model predicts the lowest fuel pin temperatures, while the k-ω SST model predicts the highest temperatures. The temperatures predicted by the anisotropic RSM linear pressure-strain model that uses an ε-based scale equation is somewhat closer to the eddy viscosity-based *k-ε* realizable model, while the predictions from the anisotropic RSM stress-BSL that uses a BSL-based scale equation are closer to the eddy viscosity-based *k-ω* BSL model. It is possible that the secondary flows induced by anisotropy in Reynolds stresses are not important to coolant mixing for the conditions investigated in this study, which could explain the agreement especially between the anisotropic RSM stress-BSL and isotropic eddy viscosity-based *k-ω* BSL models.

The differences in temperature predictions between the different turbulence models is larger for the center-peaked power profile compared to the uniform profile. The largest difference between peak fuel pin temperatures predicted by the *k-ω* SST and *k-ε* realizable models is ~26°C for the uniform power profile, whereas it is ~40°C for the center-peaked power profile. The larger difference in pin centerline temperature for the center-peaked power profile is primarily attributed to the higher local power densities.

The subchannel models that use Gnielinski and Hausen correlations show temperature predictions higher than the *k-ω* SST CFD model. However, the agreement between the CFD and Gnielinski models is better compared to the agreement between the CFD and Hausen models. The largest difference in the peak fuel pin temperatures predicted between the CFD and Gnielinski models is ~11°C for the uniform power profile and ~23°C for the center-peaked power profile. The pressure drop, as well as the coolant temperature and velocity distribution between the CFD and subchannel models, also show good agreement, thus providing preliminary verification for the subchannel model.

The thermal hydraulic model was then applied to analyze the SmAHTR reactor. Two different simple power profiles – uniform and center-peaked - were first considered. The whole-core fuel, non-fuel, and coolant temperature profiles, as well as coolant velocity profile and pressure drop were presented and discussed. Whole-core results with pin power distribution from the COMET neutronics model were then discussed. The core mass flow rate that results in safe normal operation temperature was determined using the whole-core model. The analysis of the fuel pin temperatures in the solid pin-fueled SmAHTR design indicates that a substantial reduction in peak fuel temperatures is possible by reducing the maximum distance between the heat generation and coolant heat removal locations, as the active fuel region has the highest radial temperature gradient. The distance between the heat generation and removal locations could be either reduced by decreasing the size of the fuel pins, or by replacing the solid fuel pins with annular fuel pins that can provide cooling from both inner and outer surfaces of the pin. For each of these design modifications, the fuel pin and pin bundle geometries will need to be evaluated against neutronic, thermal hydraulic, and other considerations (such as structural support for the pins) to determine the optimal geometry. To enable the analysis of multiple FHR geometries, the modeling approach initially developed for solid pin-fueled FHRs was then extended to analyze annular pin-fueled FHRs. A code-to-code comparison study with a CFD model was also performed for this fuel configuration, which showed excellent agreement between the CFD and subchannel models. The subchannel-based model was then used in the analysis of the annular pin-fueled pre-conceptual SmAHTR design for a test case with representative power distribution. The effect of varying the core inlet mass flow rate on the maximum fuel pin temperature was also investigated.

The transient analysis of solid-pin fueled FHRs was performed next. An adaptive time stepping scheme was developed for the transient model to automatically adjust the time step sizes during the course of simulated accidents. Before performing accident simulations, the subchannel-based code was also compared with a transient CFD model and excellent agreement was demonstrated. A simplified model was also developed to simulate the system-level response during postulated accidents. Two different postulated accidents involving protected loss of heat sink and unprotected transient overpower were performed and the transient profiles for the key solid and fluid regions in the core were discussed.

The subchannel-based model was then modified to perform accidents that involve low flow rates into the core, such as the loss of forced flow scenario. The pertinent model assumptions/simplifications were discussed and the results from a postulated loss of forced flow accident were presented and discussed.

Overall, the model developed in the present study can perform steady-state and transient simulations for pin-fueled FHRs. The fully parallelized solid-pin fueled FHR model can provide steady-state, whole-core results within a runtime of ~15 minutes. This model can aid core design optimization, and further development of pin-fueled FHR designs.

8.1 Recommendations for future work

The thermal hydraulic model developed in the present work can be used for analyzing steady-state and a variety of transient scenarios for pin-fueled FHRs. However, several avenues for further research and areas in need of improvement for FHR modeling were revealed during the course of this study.

The thermophysical property correlations of the FLiBe coolant, especially the viscosity and thermal conductivity correlations have relatively high uncertainties of ± 20% and ± 10%, respectively. As the two properties have a large impact on the two key non-dimensional groups, Reynolds and Prandtl numbers, for quantifying single-phase fluid flow and heat transfer, more accurate property correlations must be developed to provide better thermal hydraulic estimates for the FHR designs. Similarly, standardized calculation procedures must also be developed for the key thermophysical properties (density, specific heat, and thermal conductivity) for the TRISO fuel and graphite matrix regions in the FHR core.

The transition criteria for pin bundle geometries must be studied further to develop more accurate critical Reynolds number correlations for laminar-to-transition and transition-to-turbulent flows. The accurate determination of these critical Reynolds numbers is important for FHR pin bundle geometries, as FHRs typically operate at significantly lower Reynolds numbers compared to water and sodium-cooled reactors due to the high viscosity of the molten salt coolant. These critical Reynolds numbers will determine applicable ranges for heat transfer, fluid flow, and other closure relations in the subchannel model.

The development of experimental benchmark data for pin-bundle geometries with FHR operating conditions will be important for validating the CFD and subchannel models. Heat transfer oils such as Dowtherm-A or Dowtherm-RP could be used to simulate the FLiBe coolant at much lower temperatures, by matching the pertinent non-dimensional groups (Reynolds number, Prandtl number, Grashof number, etc.) These benchmark data could be used to validate the closure models for heat transfer, pressure drop, turbulent mixing, etc., in the subchannel model.

The development of a subchannel model that can model flow reversals and recirculating flows, with the ability to include either a flow or pressure boundary condition at the inlet would provide better, more accurate estimates for the certain accident scenarios such as loss of forced flow, flow blockage in a pin bundle, etc. For simulating accidents such as loss of forced flow, the subchannel model will need to employ solution algorithms such as SIMPLE, ACE, or RECIRC to achieve tight coupling between mass, momentum, and energy equations for the fluid region. This tight coupling is necessary to accurately simulate the thermal and flow behavior of the fluid during buoyancy-driven natural circulation cooling of the core. In addition, coupling these subchannel codes with system-level codes such as SAM, TRANSFORM, and RELAP would also provide a more accurate system-level response during the simulated accidents.

REFERENCES

Akakpo, D. E. (2016). *A Control Perspective to Adaptive Time Stepping in Reservoir Simulation*. MS Thesis, Texas A&M University.

Andreades, C., A. T. Cisneros, J. K. Choi, A. Y. K. Chong, M. Fratoni, S. Hong, L. R. Huddar, K. D. Huff, J. Kendrick, D. L. Krumwiede, M. R. Laufer, M. Munk, R. O. Scarlat and N. Zweibau (2016), "Design Summary of the Mark-I Pebble-Bed, Fluoride Salt–Cooled, High-Temperature Reactor Commercial Power Plant," *Nuclear Technology*. Vol. 195(3), pp. 223-238 DOI: 10.13182/NT16-2.

ANSYS (2021). *ANSYS Fluent Theory Guide*, Version 2021 R1. ANSYS, Inc., Canonsburg, Pennsylvania.

Avigni, P. and B. Petrovic (2014), "Fuel Element and Full Core Thermal–Hydraulic Analysis of the AHTR for the Evaluation of the LOFC Transient," *Annals of Nuclear Energy*. Vol. 64, pp. 499-510 DOI: https://doi.org/10.1016/j.anucene.2013.05.029.

Avigni, P. and B. Petrovic (2020), "Thermal Hydraulics Modeling of On-line Refueling for the Advanced High Temperature Reactor (AHTR)," *Nuclear Engineering and Design*. Vol. 358, p. 110440 DOI: https://doi.org/10.1016/j.nucengdes.2019.110440.

Basehore, K. and N. E. Todreas (1980). "SUPERENERGY-2: A Multiassembly, Steady-State Computer Code for LMFBR Core Thermal-Hydraulic Analysis," Battelle Pacific Northwest Labs., Richland, WA (USA), PNL-3379.

Bergman, T. L., A. S. Lavine, F. P. Incropera and D. P. DeWitt (2011). *Fundamentals of Heat and Mass Transfer*. 7th Ed. John Wiley & Sons.

Blandford, E., K. Brumback, L. Fick, C. Gerardi, B. Haugh, E. Hillstrom, K. Johnson, P. F. Peterson, F. Rubio, F. S. Sarikurt, S. Sen, H. Zhao and N. Zweibaum (2020), "Kairos Power Thermal Hydraulics Research and Development," *Nuclear Engineering and Design*. Vol. 364, p. 110636 DOI: https://doi.org/10.1016/j.nucengdes.2020.110636.

Boldon, L., P. Sabharwall, C. Painter and L. Liu (2014), "An Overview of Small Modular Reactors: Status of Global Development, Potential Design Advantages, and Methods for Economic Assessment," *International Journal of Energy, Environment and Economics*. Vol. 22(5), pp. 437-459.

Brown, N. R., B. R. Betzler, J. J. Carbajo, A. J. Wysocki, M. S. Greenwood, C. Gentry and A. L. Qualls (2017), "Preconceptual Design of a Fluoride High Temperature Salt-Cooled Engineering Demonstration Reactor: Core Design and Safety Analysis," *Annals of Nuclear Energy*. Vol. 103, pp. 49-59 DOI: https://doi.org/10.1016/j.anucene.2017.01.003.

Busco, G., E. Merzari and Y. A. Hassan (2019), "Invariant Analysis of the Reynolds Stress Tensor for a Nuclear Fuel Assembly with Spacer Grid and Split Type Vanes," *International Journal of Heat and Fluid Flow*. Vol. 77, pp. 144-156 DOI: https://doi.org/10.1016/j.ijheatfluidflow.2019.04.006.

Chang, S.-K., D.-J. Euh, H. S. Choi, H. Kim, S. R. Choi and H.-Y. Lee (2016), "Flow Distribution and Pressure Loss in Subchannels of a Wire-Wrapped 37-Pin Rod Bundle for a Sodium-Cooled Fast Reactor," *Nuclear Engineering and Technology*. Vol. 48(2), pp. 376-385 DOI: https://doi.org/10.1016/j.net.2015.12.013.

Chen, H. C. and V. C. Patel (1988), "Near-Wall Turbulence Models for Complex Flows Including Separation," *AIAA Journal*. Vol. 26(6), pp. 641-648 DOI: https://doi.org/10.2514/3.9948.

Chen, J., D. Zhang, P. Song, X. Wang, S. Wang, Y. Liang, S. Qiu, Y. Zhang, M. Wang and G. H. Su (2018), "CFD Investigation on Thermal-Hydraulic Behaviors of a Wire-Wrapped Fuel Subassembly for Sodium-Cooled Fast Reactor," *Annals of Nuclear Energy*. Vol. 113, pp. 256-269 DOI: https://doi.org/10.1016/j.anucene.2017.11.023.

Cheng, S.-K. (1984). *Constitutive Correlations for Wire-Wrapped Subchannel Analysis under Forced and Mixed Convection Conditions*. PhD Thesis, Massachusetts Institute of Technology.

Cheng, S.-K. and N. E. Todreas (1986), "Hydrodynamic Models and Correlations for Bare and Wire-Wrapped Hexagonal Rod Bundles—Bundle Friction Factors, Subchannel Friction Factors and Mixing Parameters," *Nuclear engineering and design*. Vol. 92(2), pp. 227-251 DOI: https://doi.org/10.1016/0029-5493(86)90249-9.

Cheng, X. and N. I. Tak (2006), "CFD Analysis of Thermal–Hydraulic Behavior of Heavy Liquid Metals in Sub-Channels," *Nuclear Engineering and Design*. Vol. 236(18), pp. 1874-1885 DOI: https://doi.org/10.1016/j.nucengdes.2006.02.001.

Collin, B. P. (2015). "AGR 3/4 Irradiation Test Final as Run Report," Idaho National Lab.(INL), Idaho Falls, ID (United States), INL/EXT-15-35550.

COMSOL (2018). *COMSOL Multiphysics*, Version 5.4. COMSOL AB, Stockholm, Sweden.

Dave, A. J., K. Sun and L. Hu (2018), "Numerical Simulations of Molten Salt Pebble-Bed Lattices," *Annals of Nuclear Energy*. Vol. 112, pp. 400-410 DOI: https://doi.org/10.1016/j.anucene.2017.10.037.

EIA (2022). "Annual Energy Outlook 2022 (AEO2022)," U.S. Energy Information Administration.

Eiff, O. and M. Lightstone (1997). *On the Modelling of Single-Phase Turbulent Energy Transport in Subchannels*. 1997 CNA/CNS Annual Conference on Powering Canada`s Future, Toronto, Ontario, Canada, Vol. 2.

El-Wakil, M. M. (1978). *Nuclear Heat Transport*. American Nuclear Society.

EPRI (2015). "Computational Fluid Dynamics Benchmark of High Fidelity Rod Bundle Experiments: Industry Round Robin Phase 2 - Rod Bundle with Mixing Vane Grids," Electrical Power Research Institute (EPRI), 3002005401.

Folsom, C. P. (2012). *Effective Thermal Conductivity of Tri-Isotropic (TRISO) Fuel Compacts*. MS Thesis, Utah State University.

Fricano, J. W. and E. Baglietto (2014), "A Quantitative CFD Benchmark for Sodium Fast Reactor Fuel Assembly Modeling," *Annals of Nuclear Energy*. Vol. 64, pp. 32-42 DOI: https://doi.org/10.1016/j.anucene.2013.09.019.

Ge, J., C. Wang, Y. Xiao, W. Tian, S. Qiu, G. H. Su, D. Zhang and Y. Wu (2016), "Thermal-Hydraulic Analysis of a Fluoride-Salt-Cooled Pebble-Bed Reactor with CFD Methodology," *Progress in Nuclear Energy*. Vol. 91, pp. 83-96 DOI: https://doi.org/10.1016/j.pnucene.2016.01.011.

George, T. L., K. L. Basehore, C. L. Wheeler, W. A. Prather and R. E. Masterson (1980). "COBRA-WC: A Version of COBRA for Single-Phase Multiassembly Thermal Hydraulic Transient Analysis," Battelle Pacific Northwest Labs., United States, PNL-3259.

Gnielinski, V. (1976), "New Equations for Heat and Mass Transfer in Turbulent Pipe and Channel Flow," *Int. Chem. Eng.* Vol. 16(2), pp. 359-368.

Gontard, R. and H. Nabielek (1990). "Performance Evaluation of Modern HTR TRISO Fuels," Forschungszentrum Jülich GmbH, Jülich, Germany, KFA-HTA-IB--5/90.

Gonzo, E. E. (2002), "Estimating Correlations for the Effective Thermal Conductivity of Granular Materials," *Chemical Engineering Journal*. Vol. 90(3), pp. 299-302 DOI: https://doi.org/10.1016/S1385-8947(02)00121-3.

Gorman, J. M., E. M. Sparrow, J. P. Abraham and W. J. Minkowycz (2016), "Evaluation of the Efficacy of Turbulence Models for Swirling Flows and the Effect of Turbulence Intensity on Heat Transfer," *Numerical Heat Transfer, Part B: Fundamentals*. Vol. 70(6), pp. 485-502 DOI: https://doi.org/10.1080/10407790.2016.1244390.

Greene, S. R., J. C. Gehin, D. E. Holcomb, J. J. Carbajo, D. Ilas, A. T. Cisneros, V. K. Varma, W. R. Corwin, D. F. Wilson, G. L. Yoder Jr, A. L. Qualls, F. J. Peretz, G. F. Flanagan, D. A. Clayton, E. C. Bradley, G. L. Bell, J. D. Hunn, P. J. Pappano and S. M. Cetiner (2011). "Pre-Conceptual Design of a Fluoride-Salt-Cooled Small

Modular Advanced High Temperature Reactor (SmAHTR)," Oak Ridge National Laboratory, ORNL/TM-2010/199.

Greenwood, M. S., B. R. Betzler, A. L. Qualls, J. Yoo and C. Rabiti (2020), "Demonstration of the Advanced Dynamic System Modeling Tool Transform in a Molten Salt Reactor Application Via a Model of the Molten Salt Demonstration Reactor," *Nuclear Technology*. Vol. 206(3), pp. 478-504 DOI: https://doi.org/10.1080/00295450.2019.1627124.

Gunter, A. and W. Shaw (1945), "A General Correlation of Friction Factors for Various Types of Surfaces in Cross Flow," *Trans. ASME*. Vol. 67(8), pp. 643-660.

Guo, Z., D. Zhang, Y. Xiao, W. Tian, G. Su and S. Qiu (2013), "Simulations of Unprotected Loss of Heat Sink and Combination of Events Accidents for a Molten Salt Reactor," *Annals of Nuclear Energy*. Vol. 53, pp. 309-319 DOI: https://doi.org/10.1016/j.anucene.2012.09.009.

Henry, R. E. (1992). "Severe Accident Management Guidance Technical Basis Report Volume 2: The Physics of Accident Progression," Electric Power Research Institute (EPRI), Palo Alto, California, TR-101869.

IAEA (2014). "Advances in Small Modular Reactor Technology Developments," International Atomic Energy Agency, Vienna, Austria.

Ilas, D., D. E. Holcomb and J. C. Gehin (2014), "SmAHTR-CTC Neutronic Design," *Proceedings of PHYSOR 2014 – The Role of Reactor Physics Toward a Sustainable Future*, Kyoto, Japan

INL (2012). "RELAP-3D Code Manuals Revision 4.0.3," Idaho National Laboratory, INEL-95/0174.

INL (2017). "SAM Theory Manual," Idaho National Laboratory, ANL/NE-17/4.

Johannsen, K. (1983). Longitudinal Flow over Tube Bundles. *Low Reynolds Number Flow Heat Exchangers*. S. Kakac, R. K. Shah and A. E. Bergles. Hemisphere Publ. Corp., New York.

Johnson, R. W., H. Sato and R. R. Schultz (2009). "CFD Analysis of Core Bypass Phenomena," Idaho National Laboratory, INL/EXT-09-16882.

Kakac, S., R. K. Shah and W. Aung (1987). *Handbook of Single-Phase Convective Heat Transfer*. John Wiley and Sons Inc, United States.

Kamide, H., G. Rodriguez, P. Guiberteau, N. Kawasaki, B. Hatala, A. Alemberti, S. Bourg, Y. Huang, F. Serre, M. A. Fuetterer, D. Shropshire, M. Moore, F. Reilly, P. Paviet, G. Cojazzi, L.-Y. Cheng, T. Sofu, L. Edwards, R. Garbil and E. Loewen (2021). "Generation IV International Forum - GIF, Annual Report 2020," Nuclear Energy Agency of the OECD (NEA).

Kawahara, A., M. Sadatomi, H. Kudo and K. Kano (2006), "Single-and Two-Phase Turbulent Mixing Rate between Subchannels in Triangle Tight Lattice Rod Bundle," *JSME International Journal Series B Fluids and Thermal Engineering*. Vol. 49(2), pp. 287-295 DOI: https://doi.org/10.1299/jsmeb.49.287.

Kays, W. M., M. E. Crawford and B. Weigand (2004). *Convective Heat and Mass Transfer*. 4th Ed. McGraw-Hill Higher Education.

Khan, E. U., T. L. George and C. L. Wheeler (1979). "COBRA and CORTRAN Code Thermal-Hydraulic Models for LMFBR Core Wide Temperature Distribution During a Natural Convection Transient," International Atomic Energy Agency (IAEA), IWGFR--29.

Kim, Y., M. Kim and W. Kim (2013), "Effect of the Fukushima Nuclear Disaster on Global Public Acceptance of Nuclear Energy," *Energy Policy*. Vol. 61, pp. 822-828 DOI: https://doi.org/10.1016/j.enpol.2013.06.107.

Kraus, A., E. Merzari, T. Norddine, O. Marin and S. Benhamadouche (2021), "Direct Numerical Simulation of Fluid Flow in a 5x5 Square Rod Bundle," *International Journal of Heat and Fluid Flow*. Vol. 90, p. 108833 DOI: https://doi.org/10.1016/j.ijheatfluidflow.2021.108833.

Lahey Jr., R., B. Shiralkar and D. Radcliffe (1970). "Two-Phase Flow and Heat Transfer in Multirod Geometries: Subchannel and Pressure Drop Measurements in a Nine-Rod Bundle for Diabatic and Adiabatic Conditions," General Electric Co., San Jose, Calif. Atomic Power Equipment Dept., GEAP-13049.

Lin, C. X. and M. A. Ebadian (1999), "The Effects of Inlet Turbulence on the Development of Fluid Flow and Heat Transfer in a Helically Coiled Pipe," *International Journal of Heat and Mass Transfer*. Vol. 42(4), pp. 739-751 DOI: https://doi.org/10.1016/S0017-9310(98)00193-8.

Liu, F.-R., X.-W. Chen, Z. Li and N.-X. Wang (2017), "DEM–CFD Simulation of Modular PB-FHR Core with Two-Grid Method," *Nuclear Science and Techniques*. Vol. 28(7), p. 100 DOI: 10.1007/s41365-017-0246-3.

Lodi, F., G. Grasso, D. Mattioli and M. Sumini (2016), "ANTEO+: A Subchannel Code for Thermal-Hydraulic Analysis of Liquid Metal Cooled Systems," *Nuclear Engineering and Design*. Vol. 301, pp. 128-152 DOI: https://doi.org/10.1016/j.nucengdes.2016.03.001.

Lundberg, R. E., W. C. Reynolds and W. M. Kays (1963). "Heat Transfer with Laminar Flow in Concentric Annuli with Constant and Variable Wall Temperature with Heat Flux," National Aeronautics and Space Administration (NASA), Washington, NASA-TN-D-1972.

M-Tech Industrial (2013). *Flownex SE: Nuclear*.

Manservisi, S. and F. Menghini (2015), "CFD Simulations in Heavy Liquid Metal Flows for Square Lattice Bare Rod Bundle Geometries with a Four Parameter Heat Transfer Turbulence Model," *Nuclear Engineering and Design*. Vol. 295, pp. 251-260 DOI: https://doi.org/10.1016/j.nucengdes.2015.10.006.

Masterson, R. E. (2019). *Nuclear Reactor Thermal Hydraulics: An Introduction to Nuclear Heat Transfer and Fluid Flow* 1st Ed. CRC Press.

MATLAB (2020). *MATLAB*, Version 9.9.0.1467703 (R2020b). The MathWorks Inc., Natick, Massachusetts.

Menter, F. R. (1994), "Two-Equation Eddy-Viscosity Turbulence Models for Engineering Applications," *AIAA Journal*. Vol. 32(8), pp. 1598-1605 DOI: https://doi.org/10.2514/3.12149.

Merzari, E. and H. Ninokata (2011), "Proper Orthogonal Decomposition of the Flow in a Tight Lattice Rod-Bundle," *Nuclear Engineering and Design*. Vol. 241(11), pp. 4621-4632 DOI: https://doi.org/10.1016/j.nucengdes.2010.12.005.

Novak, A. J., R. W. Carlsen, S. Schunert, P. Balestra, D. Reger, R. N. Slaybaugh and R. C. Martineau (2021), "Pronghorn: A Multidimensional Coarse-Mesh Application for Advanced Reactor Thermal Hydraulics," *Nuclear Technology*. Vol. 207(7), pp. 1015-1046 DOI: 10.1080/00295450.2020.1825307.

NRC (2010). "TRACE V5.0 Theory Manual," U.S. Nuclear Regulatory Commission, ML120060218.

OECD (2018). "Benchmark of the Modular High-Temperature Gas-Cooled Reactor (MHTGR)-350 MW Core Design," OECD Nuclear Energy Agency, NEA/NSC/R(2017) 4.

PACE (2017). "Partnership for an Advanced Computing Environment (PACE)," http://www.pace.gatech.edu.

Palomino, L. M. and M. S. El-Genk (2019a), "CFD and Thermal-Hydraulics Analyses of Liquid Sodium Heat Transfer in 19-Rod Hexagonal Bundles with Scalloped Walls," *International Journal of Heat and Mass Transfer*. Vol. 144, p. 118637 DOI: https://doi.org/10.1016/j.ijheatmasstransfer.2019.118637.

Palomino, L. M. and M. S. El-Genk (2019b), "Friction Factor Correlation for Hexagonal Bundles of Bare Tubes/Rods and with Flat and Scalloped Walls," *Nuclear Engineering and Design*. Vol. 353, p. 110230 DOI: https://doi.org/10.1016/j.nucengdes.2019.110230.

Patankar, S. (2018). *Numerical Heat Transfer and Fluid Flow*. CRC press.

Petrunik, K. (1973). *Turbulent Interchange in Simulated Rod Bundle Geometries for Genetron-12 Flow*. PhD Thesis, University of Windsor.

Podila, K. and Y. Rao (2016), "CFD Modelling of Supercritical Water Flow and Heat Transfer in a 2×2 Fuel Rod Bundle," *Nuclear Engineering and Design*. Vol. 301, pp. 279-289 DOI: https://doi.org/10.1016/j.nucengdes.2016.03.019.

Podila, K. and Y. F. Rao (2018), "CFD Simulation of Heated Tight-Lattice Rod Bundles for an IAEA Benchmark," *Progress in Nuclear Energy*. Vol. 108, pp. 222-232 DOI: https://doi.org/10.1016/j.pnucene.2018.06.001.

Rahnema, F. and D. Zhang (2021). *Continuous Energy COMET Solution to a Small Modular Advanced High-Temperature Reactor Benchmark Problem (SmAHTR)*. PHYSOR2020 – International Conference on Physics of Reactors: Transition to a Scalable Nuclear Future. EPJ Web of Conferences, Vol. 247.

Reed, K. (2021). *Stylized Benchmark Description and Reference Solutions for the Pin-Fueled Small Modular Advanced High Temperature Reactor*. Georgia Institute of Technology, Atlanta.

Rehme, K. (1972), "Pressure Drop Performance of Rod Bundles in Hexagonal Arrangements," *International Journal of Heat and Mass Transfer*. Vol. 15(12), pp. 2499-2517 DOI: https://doi.org/10.1016/0017-9310(72)90143-3.

Romatoski, R. R. (2017). *Fluoride-Salt-Cooled High-Temperature Test Reactor Thermal-Hydraulic Licensing and Uncertainty Propagation Analysis*. PhD Thesis, Massachusetts Institute of Technology.

Salko, R., M. Avramova, A. Wysocki, A. Toptan, J. Hu, N. Porter, T. S. Blyth, C. A. Dances, A. Gomez, C. Jernigan and J. Kelly (2019). "CTF 4.0 Theory Manual," Oak Ridge National Laboratory (ORNL), United States, ORNL/TM-2019/1145.

Salko, R. K., T. S. Blyth, C. A. Dances, J. W. Magedanz, C. Jernigan, J. Kelly, A. Toptan, M. Gergar, C. Gosdin and M. Avramova (2016). "CTF Validation and Verification Manual," Oak Ridge National Laboratory (ORNL), ORNL/TM-2016/433.

Salko, R. K., C. Gosdin, M. N. Avramova and M. Gergar (2015). "CTF Void Drift Validation Study," Oak Ridge National Laboratory (ORNL), United States, ORNL/TM-2015/641.

Scarlat, R. O. and P. F. Peterson (2014), "The Current Status of Fluoride Salt Cooled High Temperature Reactor (FHR) Technology and Its Overlap with HIF Target Chamber Concepts," *Nuclear Instruments and Methods in Physics Research Section A: Accelerators, Spectrometers, Detectors and Associated Equipment*. Vol. 733, pp. 57-64 DOI: https://doi.org/10.1016/j.nima.2013.05.094.

Serp, J., M. Allibert, O. Beneš, S. Delpech, O. Feynberg, V. Ghetta, D. Heuer, D. Holcomb, V. Ignatiev, J. L. Kloosterman, L. Luzzi, E. Merle-Lucotte, J. Uhlíř, R. Yoshioka and D. Zhimin (2014), "The Molten Salt Reactor (MSR) in Generation IV: Overview and Perspectives," *Progress in Nuclear Energy*. Vol. 77, pp. 308-319 DOI: https://doi.org/10.1016/j.pnucene.2014.02.014.

Shah, R. K. (1978), "A Correlation for Laminar Hydrodynamic Entry Length Solutions for Circular and Noncircular Ducts," *Journal of Fluids Engineering*. Vol. 100(2), pp. 177-179 DOI: https://doi.org/10.1115/1.3448626.

Shams, A., A. De Santis, L. K. Koloszar, A. Villa Ortiz and C. Narayanan (2019), "Status and Perspectives of Turbulent Heat Transfer Modelling in Low-Prandtl Number Fluids," *Nuclear Engineering and Design*. Vol. 353, p. 110220 DOI: https://doi.org/10.1016/j.nucengdes.2019.110220.

Shang, Z. (2009), "CFD Investigation of Vertical Rod Bundles of Supercritical Water-Cooled Nuclear Reactor," *Nuclear Engineering and Design*. Vol. 239(11), pp. 2562-2572 DOI: https://doi.org/10.1016/j.nucengdes.2009.07.021.

Shih, T.-H., W. W. Liou, A. Shabbir, Z. Yang and J. Zhu (1995), "A New K-ϵ Eddy Viscosity Model for High Reynolds Number Turbulent Flows," *Computers & Fluids*. Vol. 24(3), pp. 227-238 DOI: https://doi.org/10.1016/0045-7930(94)00032-T.

Sieder, E. N. and G. E. Tate (1936), "Heat Transfer and Pressure Drop of Liquids in Tubes," *Industrial & Engineering Chemistry*. Vol. 28(12), pp. 1429-1435 DOI: https://doi.org/10.1021/ie50324a027.

Sohag, F. A., L. Mohanta and F.-B. Cheung (2017), "CFD Analyses of Mixed and Forced Convection in a Heated Vertical Rod Bundle," *Applied Thermal Engineering*. Vol. 117, pp. 85-93 DOI: https://doi.org/10.1016/j.applthermaleng.2017.02.020.

Stewart, C., J. Cuta, S. Montgomery, J. Kelly, K. Basehore, T. George and D. Rowe (1989). "VIPRE-01: A Thermal-Hydraulic Code for Reactor Cores," Pacific Northwest Laboratory, EPRI-NP-2511-CCM-Vol.5.

Stewart, C. W., C. L. Wheeler, R. J. Cena, C. A. McMonagle, J. M. Cuta and D. S. Trent (1977). "COBRA-IV: The Model and the Method," Pacific Northwest Laboratory, BNWL-2214.

Stocker, B. and H. Niessen (1997). "Data Sets of the SANA Experiment 1994–1996," Forschungszentrum Julich, JUEL-3409.

Todreas, N. E. and M. S. Kazimi (2001). *Nuclear Systems II: Elements of Thermal Hydraulic Design* 1st Ed. Taylor and Francis.

US DOE and GIF (2002). "A Technology Roadmap for Generation IV Nuclear Energy Systems," Generation IV International Forum (GIF), GIF-002-00.

Varma, V. K., D. E. Holcomb, F. J. Peretz, E. C. Bradley, D. Ilas, A. Qualls and N. M. Zaharia (2012). "AHTR Mechanical, Structural, and Neutronic Preconceptual Design," Oak Ridge National Laboratory, ORNL/TM-2012/320.

Wang, C., K. Sun, L.-W. Hu, S. Qiu and G. H. Su (2016a), "Thermal-Hydraulic Analyses of Transportable Fluoride Salt–Cooled High-Temperature Reactor with CFD Modeling," *Nuclear Technology*. Vol. 196(1), pp. 34-52 DOI: https://doi.org/10.13182/NT15-42.

Wang, C., K. Sun, L.-w. Hu, D. Zhang, W. Tian, S. Qiu and G. H. Su (2017), "Transient Safety Analysis of a Transportable Fluoride-Salt-Cooled High-Temperature Reactor Using RELAP5-3D," *Nuclear Technology*. Vol. 198(1), pp. 1-16 DOI: https://doi.org/10.1080/00295450.2017.1294011.

Wang, C., Y. Xiao, J. Zhou, D. Zhang, S. Qiu, G. Su, X. Cai, N. Wang and W. Guo (2014), "Computational Fluid Dynamics Analysis of a Fluoride Salt–Cooled Pebble-Bed Test Reactor," *Nuclear Science and Engineering*. Vol. 178(1), pp. 86-102 DOI: 10.13182/NSE13-60.

Wang, X., K. D. Huff, M. Aufiero, P. F. Peterson and M. Fratoni (2016b). *Coupled Reactor Kinetics and Heat Transfer Model for Fluoride Salt-Cooled High-Temperature Reactor Transient Analysis*. 24th International Conference on Nuclear Engineering (ICONE), Charlotte, NC.

Wang, Y., S. Schunert, J. Ortensi, V. Laboure, M. DeHart, Z. Prince, F. Kong, J. Harter, P. Balestra and F. Gleicher (2021), "Rattlesnake: A MOOSE-Based Multiphysics Multischeme Radiation Transport Application," *Nuclear Technology*. Vol. 207(7), pp. 1047-1072 DOI: 10.1080/00295450.2020.1843348.

Wolfshtein, M. (1969), "The Velocity and Temperature Distribution in One-Dimensional Flow with Turbulence Augmentation and Pressure Gradient," *International Journal of Heat and Mass Transfer*. Vol. 12(3), pp. 301-318 DOI: https://doi.org/10.1016/0017-9310(69)90012-X.

Yoder, G., A. T. Bopp, D. E. Holcomb, W. D. Pointer and D. Wang (2014). "Advanced High Temperature Reactor Thermal Hydraulics Analysis and Salt Clean-up System Description," Oak Ridge National Laboratory, ORNL/TM-2014/499.

Yoo, Y. J. and D. H. Hwang (1998). "Development of a Subchannel Analysis Code MATRA (Ver. A)," Korea Atomic Energy Research Institute, KAERI/TR-1033/98.

Zhang, D., L. Liu, M. Liu, R. Xu, C. Gong, J. Zhang, C. Wang, S. Qiu and G. Su (2018), "Review of Conceptual Design and Fundamental Research of Molten Salt Reactors in China," *International Journal of Energy Research*. Vol. 42(5), pp. 1834-1848 DOI: https://doi.org/10.1002/er.3979.

Zhang, D. and F. Rahnema (2018), "Continuous-Energy COMET Solution to the Stylized AHTR Benchmark Problem," *Annals of Nuclear Energy*. Vol. 121, pp. 284-294 DOI: https://doi.org/10.1016/j.anucene.2018.06.032.

Zhang, Y., P. Gao, X. He, C. Chen, Q. Wang and C. Tian (2020), "Numerical Analysis of Flow Resistance Characteristics in an Inclined Rod Bundle Channel," *Progress in*

Nuclear Energy. Vol. 122, p. 103247 DOI: https://doi.org/10.1016/j.pnucene.2020.103247.

Zhu, X., S. Morooka and Y. Oka (2014), "Numerical Investigation of Grid Spacer Effect on Heat Transfer of Supercritical Water Flows in a Tight Rod Bundle," *International Journal of Thermal Sciences*. Vol. 76, pp. 245-257 DOI: https://doi.org/10.1016/j.ijthermalsci.2013.10.003.

Zweibaum, N. (2015). *Experimental Validation of Passive Safety System Models: Application to Design and Optimization of Fluoride-Salt-Cooled, High-Temperature Reactors*. PhD Thesis, University of California, Berkeley.